Computational modelling of information processing in deep cerebellar nucleus neurons

Johannes Luthman

A thesis submitted to the University of Hertfordshire
in partial fulfilment of the requirements for the degree of
Doctor of Philosophy

The programme of research was carried out
in the School of Computer Science
Faculty of Engineering and Information Sciences
University of Hertfordshire

April 2012

Abstract

The deep cerebellar nuclei (DCN) function as output gates for a large majority of the Purkinje cells of the cerebellar cortex and thereby determine how the cerebellum influences the rest of the brain and body. In my PhD programme I have investigated how the DCN process two kinds of input patterns received from Purkinje cells: irregularity of spike intervals and pauses in Purkinje cell activity resulting from the recognition of patterns received at the synapses with the upstream parallel fibres (PFs).

To that objective I have created a network system of biophysically realistic Purkinje cell and DCN neuron models that enables the exploration of a wide range of network structure and cell physiology parameters. With this system I have performed simulations that show how the DCN neuron changes the information modality of its input, consisting of varying regularity in Purkinje cell spike intervals, to varying spike rates in its output to the nervous system outside of the cerebellum. This was confirmed in simulations where I exchanged the artificial Purkinje cell trains for those received from experimental collaborators.

In pattern recognition simulations I have found that the morphological arrangement present in the cerebellum, where multiple Purkinje cells connect to each DCN neuron, has the effect of amplifying pattern recognition already performed in the Purkinje cells. Using the metric of signal-to-noise ratio I show that PF patterns previously encountered and stored in PF - Purkinje cell synapses are most clearly distinguished from those novel to the system by a 10-20 ms shortened burst firing of the DCN neuron. This result suggests that the effect on downstream targets of these excitatory projection neurons is a decreased excitation when a stored as opposed to novel pattern is received.

My work has contributed to a better understanding of information processing in the cerebellum, with implications for human motor control as well as the increasingly recognised non-motor functions of the cerebellum.

List of Figures

59. Readout by the DCN neuron model of asynchronous pattern presentation to Purkinje cells
60. Effect of how many of the total 147,400 parallel fibre inputs to the associative net are active in a pattern
61. Pattern recognition at varying settings of the number of patterns presented to the associative net
62. Pattern recognition effects of feed-forward inhibition onto the Purkinje cell
63. Raster plot of the DCN neuron model response to receiving pattern inputs to only 30% of its $GABA_A$ synapses
64. Pattern recognition capacities at different percentages of the Purkinje cell – DCN neuron model synapses receiving pattern readouts
65. Voltage trace responses to mossy-fibre collateral bursts to the DCN neuron model during pattern recognition
66. Signal-to-noise ratios as the DCN neuron model recognises Purkinje cell pattern outputs accompanied by mossy fibre collateral firing; 6.8 ms delay
67. Same as Figure 63 but with a 12.6 ms delay between the inputs
68. Interspike interval distributions of Purkinje cells recorded in vivo
69. The short term depression (STD) element of the Purkinje cell to DCN neuron synapse
70. Examples of ISI distributions of the artificial spike generator GammaStim
71. DCN neuron model firing as a function of Purkinje cell irregularity
72. DCN neuron model firing rate at Purkinje cell inputs of different rate and irregularity
73. Effects of STD at different Purkinje cell to DCN neuron model convergence ratios
74. Samples of tottering and wild-type PC spike trains
75. Tottering and wild-type Purkinje cell spike trains: raw versus selected to give equal firing rates

76. The DCN neuron model response to tottering and wild-type inputs in the presence and absence of STD at different levels of PC-DCN convergence: firing rate and $GABA_A$ conductance
77. DCN neuron model firing rate response to GammaStim inputs where spike rate and irregularity has been set to imitate the real tottering and wild-type trains
78. $GABA_A$ conductance and voltage traces of the DCN neuron model as it receives input from tottering (left) and wild-type (right) Purkinje cells
79. Effects on the DCN neuron model of synchronised pauses in Purkinje cell firing
80. Membrane potential (top traces) and summed $GABA_A$ conductance (bottom) of the DCN neuron model as it receives input from tottering PC trains at convergence ratios 5 (A) and 150 (B). STD was in use at both convergence ratios.
81. DCN neuron model firing as it receives completely regular PC firing at 61.8 Hz with a convergence ratio of 1
82. Coefficient of variation of ISIs of the DCN neuron model output with wild-type and tottering inputs
83. Results of control simulations using an integrate-and-fire neuron receiving inputs of the same regularity levels used in the simulations with the full model.
84. The phenotype of human cerebellar ataxia

List of Tables

Glossary

- CV: coefficient of variation – the standard deviation divided by the mean
- CV_2: an alternative to the CV, measuring local variation of interspike intervals
- DCN: Deep cerebellar nucleus/nuclei
- GABA: gamma-amino butyric acid – a neurotransmitter, usually acting inhibitorily
- hoc: An interpreted programming language used in NEURON for all coding other than the ion channel and synaptic mechanisms which are implemented in NMODL.
- ISI: interspike interval
- LTD: Long-term depression
- LTP: Long-term potentiation
- NEURON: software for simulating neurons and networks of neurons
- NMODL: a compiled C-like language used in NEURON for coding the ion channel and synaptic mechanisms.
- PC: Purkinje cell
- PF: parallel fibre – the axonal processes of cerebellar granule cells
- STD: Short-term depression

Acknowledgments

I am very thankful to my supervisors Volker Steuber, Rod Adams, Neil Davey, and Reinoud Maex, for their unwavering support and dedication. Volker in particular has provided a very substantial amount of time for teaching me much of what I know about neuronal modelling and has always been available for discussions and comments. Especially impressive has been your careful reading of all the texts I have produced over the years. I never expected to improve my English so much from a German!

To the whole group of supervisors: I will certainly miss our enthusiastic and productive meetings.

Thank you Freek Hoebeek and Chris De Zeeuw for providing me with Purkinje cell recordings.

To the people in the Biocomputation Research Group: thank you all for good times over these years: Angela, Aruna, David, Faisal, Giseli, Johannes, Katja, Karen, Maria, Mark (both of you!), Nicolas, Thiago, Weiliang, Yi. Great thanks also to many others at the university, especially Lorraine Nicholls for helping me find accommodation.

The University of Hertfordshire deserves a big thank-you for generous funding of my research, including making available the use of 2000 clustered student computers. This has allowed these computationally very expensive simulations; the estimated 20 CPU years have enabled parameter explorations without which the thesis work could not have reached the achieved results.

Finally, thank you Stefanie – for everything.

1. Introduction

The cerebellum is a part of the brain that is important for motor control and associative learning, as well as increasingly being implicated in purely cognitive functions. It is well characterised in terms of anatomy, morphology of the constituent cell types, and cellular physiology. The highly stereotypical wiring between its neurons makes it an ideal target for studying the function of neuronal circuits. Yet, understanding of the computations that the cerebellum performs remains elusive.

Cerebellar output to the rest of the brain and body is gated through the deep cerebellar nuclei (DCN). These small assemblies of neurons receive inputs from the Purkinje cells of the cerebellar cortex and from other sources outside of the cerebellum. Their function has often been seen as a relay station for the much studied Purkinje cells. In recent years, however, they have been shown to be involved in learning such as the paradigm of eyeblink conditioning.

This thesis focuses on the connection between DCN neurons and Purkinje cells and how different types of activity in the latter are modified by the DCN neurons and their synapses for communication with targets outside of the cerebellum. For that purpose, the projects underlying the thesis use biological data on the cerebellar circuitry and physiology and integrate these data using the technique of biophysically realistic computational modelling. Two main topics are addressed. The first is how variations in the regularity of Purkinje cell output influence the DCN neuron output. The second regards the role of DCN neurons in interpreting the output of pattern recognition performed by Purkinje cells.

1.1 Contributions to knowledge

Scientific contributions from the work underlying this thesis have been published (Luthman et al., 2009a; Luthman et al., 2009b; Luthman et al., 2011) and include the following:

- In simulations of pattern recognition in Purkinje cells based on long-term depression of synapses with parallel fibres, it has previously been shown that the length of pauses in Purkinje cell firing (Steuber et al., 2007), as well as the firing rate of the Purkinje cell (Steuber et al., 2007; Walter and Khodakhah, 2009) carry information about stored PF patterns. The results in this thesis imply that irrespective of the coding mode of the Purkinje cell, the most effective readout mechanism in the resulting cerebellar output is the length of a burst of DCN neuron spikes.
- The convergence of many Purkinje cells onto each DCN neuron that is a feature of the circuitry has the potential to modify the output of the DCN neurons. One way it does so is by increasing the signal-to-noise ratio of pattern recognition; another is by decreasing the DCN neuron firing rate.
- Short-term depression of the synapse between Purkinje cells and DCN neurons endows DCN neurons with the ability to change the modality of information transfer, from a code based on levels of regularity to a code based on firing rate.
- Efficient pattern recognition is possible in Purkinje cells that are spontaneously active, in addition to Purkinje cells that are quiet in the absence of synaptic inputs.
- Feed-forward inhibition of Purkinje cells may improve the pattern recognition performance of the network.

1.2 Structure of the thesis

This document is structured into chapters: after this introduction, Chapter 2 introduces the neurobiology of the project, followed by an introduction to computational neuroscience (Chapter 3). The interdisciplinary nature of the field has led me to aim at making the biology understandable for readers with a computer science background and vice versa.

Chapter 4 covers the work of translating an existing DCN neuron model to a neuronal modelling environment more suited for the purposes of this work; it also includes the ensuing work of updating parts of the model and making it ready to work in a Purkinje cell and DCN neuron network. Chapters 5 and 6 contain the scientific studies of the project, concerning pattern recognition and irregularity, respectively. While, as mentioned, parts of the projects have been published, the outline used in Chapters 5 and 6 is not one of scientific journal writing but instead brings up methods and materials as they are needed, hopefully giving better readability. The two chapters include discussions of the respective results and are followed by a chapter containing overarching conclusions (Chapter 7). This is followed by the references of the thesis, and appendices that list the simulation and analysis code and contain additional data from the pattern recognition project.

The following flowchart illustrates the work described in the present thesis.

1.3 Flow chart of the main steps of the thesis work

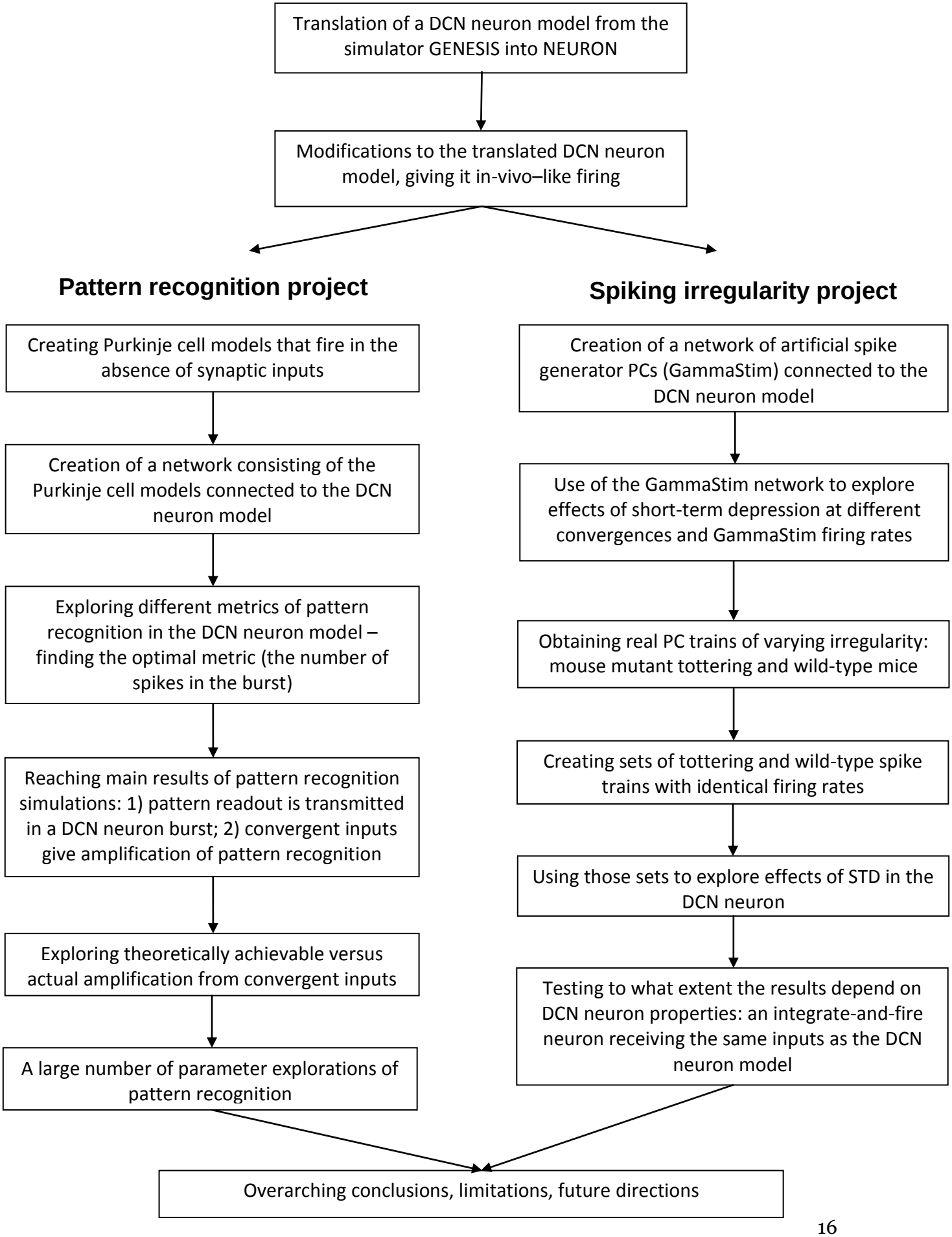

2. Neurobiology

This chapter will deal with introducing the biology of neurons and specifically of the cerebellum and its nuclei.

2.1 Neurons are electrically excitable cells

Neurons are cells with properties setting them apart from other cell types. Among those are:

- Electrical excitability
- Complex morphology, with protrusions from the cell body (the soma) often making up the largest part of the cell (Figure 1)
- One of the extensions, the axon, carries electrical charge from its proximal end at the soma to its branching distal ends, which form connections to other neurons at synapses

Electrical excitability refers to the ability of the membrane to generate varying membrane potentials. These potentials depend on the presence of different concentrations of ions on the inside compared to the outside of the cell. Neurons use four ion species for this purpose: sodium (Na^+), potassium (K^+), calcium (Ca^{2+}), chloride (Cl^-). When the electrical potential on the inside of a neuron is lower than on the outside, it is referred to as hyperpolarisation, while the inverse is called depolarisation.

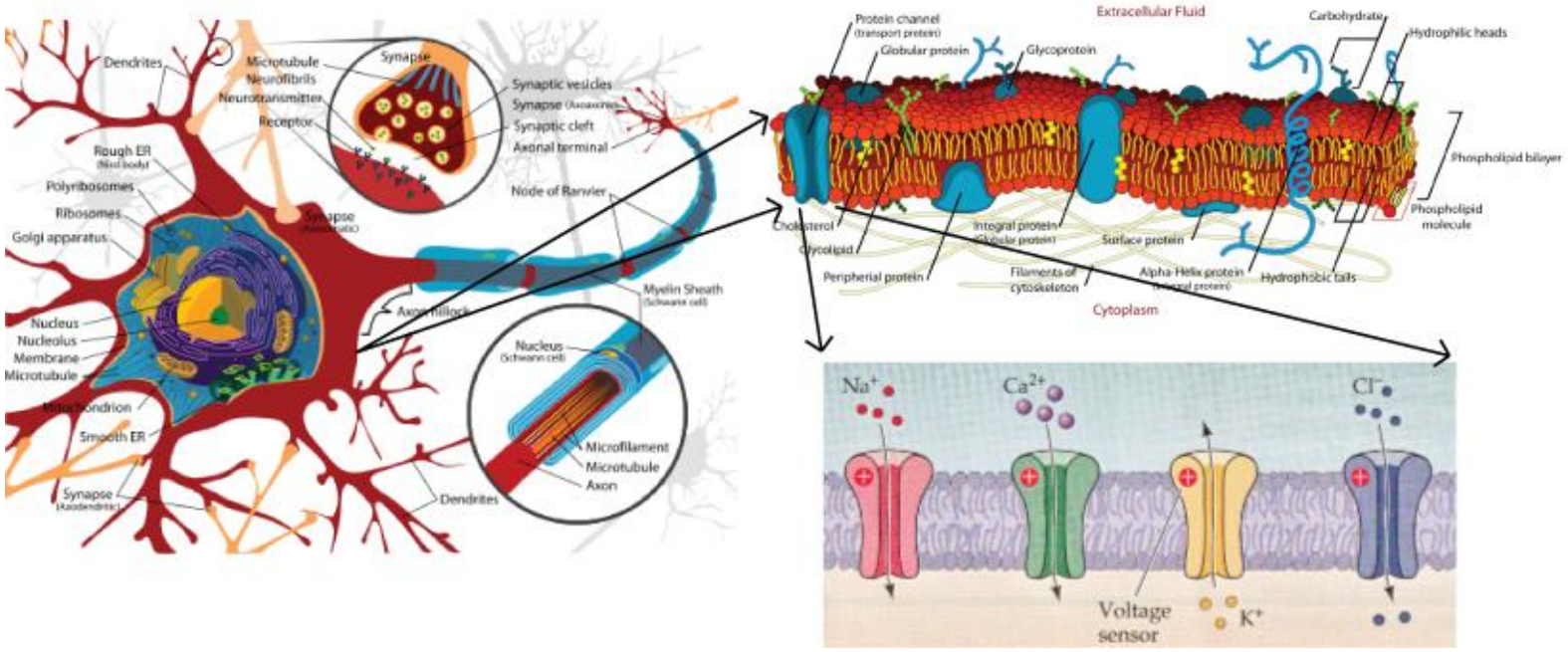

Figure 1 Components of a neuron with zoom-ins on the membrane and its ion channels. From top left: While a neuron contains a multitude of organelles, loose protein and other molecules, and a highly complex cytoskeleton, of relevance for the neuronal modelling done in this thesis is the neuronal membrane (top right) and especially its ion channels (bottom right). Ion channels specific for four ion species used to create membrane current flow are shown with arrows depicting the direction of flow: all but potassium are present at a higher concentration in the extracellular fluid and hence generate inward flow (for positively charged ions, this results in inward currents). Sources: en.wikipedia.org/wiki/File:Complete_neuron_cell_diagram_en.svg (left part of the picture); en.wikipedia.org/wiki/File:Cell_membrane_detailed_diagram_en.svg (top right); lower right: Purves (2004).

Ion-species specific channels are diagrammed in Figure 1 with arrows showing the direction of current flow when the channels open. Note that while all ion species but potassium give rise to inward flows, it is only sodium and calcium that act to depolarise on the neuron; the negative charge of the chloride ion gives a hyperpolarising effect with its inflow.

To maintain different extra- and intracellular concentrations of ions, pumps are located in the membrane and can transport ions in the opposite direction of the ion concentration gradient. The latter is utilised for generating flows of ions through ion channels, thus creating a current.

2.2 Ion channels govern excitability and current flow

Ion channels regulate the membrane potential of a neuron by controlling the in- and outflow of ions across the cell membrane. While some channels are open constantly, most channels regulate the ion flow through their cavity tightly, in a process called gating. The term refers to how the channels are opened to let ions pass through the cell membrane, and closed to prevent further flow. Common types of gating are response to membrane potential (voltage-gating) and to intracellular ion concentrations.

When channels are open, the amount of current carried by an ion species through the channel depends on the electrochemical driving force for the species across the neuronal cell membrane. The electrochemical driving force in turn depends both on the reversal potential E of the ion species and on the potential across the membrane, the membrane potential.

The reversal potential is created by the relative abundance of an ion inside compared to outside of a cell and can be calculated by the Nernst equation:

$$E_x = \frac{RT}{zF} \ln \frac{[\mathrm{X}]_o}{[\mathrm{X}]_i} \quad (1)$$

where R is the gas constant, T is the absolute temperature, z is the valence of the ion (+2 for calcium, +1 for sodium and potassium, and -1 chloride ions), F is the Faraday constant, and $[X]_i$, $[X]_o$ are the ion concentrations inside and outside the cell, respectively.

With the reversal potential determined, the current *I* through a channel is given by:

$$I = g(V - E_x) \quad (2)$$

where *g* is the conductance of the channel; *V* is the membrane potential. The equation shows that the reversal potential, E_x, is the membrane potential where no electrochemical driving force is exerted on the ion species and, thus, no current flows through the channel.

2.3 Signal propagation in neurons

Open ion channels create current flows into the different parts of a neuron; this current response is both passively and actively propagated throughout the parts of the neuron (see Figure 1 for the parts of a neuron). The currents from these parts add up in the soma. The part of the soma connecting to the axon, the axon hillock, contains a large density of sodium channels, which implements a thresholding mechanism: when a certain membrane potential level is crossed, the sodium channel activation at the hillock leads to an all-or-none event, an action potential. The action potential rapidly propagates down the axon by the opening and closing of sodium channels in consecutive axonal segments. This ensures the fast one-way flow of the action potential to the distal parts of the

axonal branches; there, the signal is transferred to the downstream target – a neuron or other cell – via the release of chemical messengers, neurotransmitters, at the synapse.

It should be added that there are exceptions to these general principles; many neuron types are able to generate action potentials that back-propagate into the dendrite, in addition to axonal action potentials. Further, in addition to the more common chemical synapses mentioned above and described in the next section, there are electrical synapses that communicate via direct transfer of ions, and thereby electrical current, to the postsynaptic target.

2.4 The synapse

The ends of an axon are called boutons or axonal end plates. These expansions of the axonal processes (circular inset at the top left of Figure 1) contain vesicles with neurotransmitter, which are used for the signal transfer to the postsynaptic target. After the arrival of an action potential results in the fusion of vesicles with the cell membrane of the bouton, neurotransmitter is released from the presynaptic neuron. For the signal transfer to take place, the transmitter needs to travel the extracellular space (the synaptic cleft) to the postsynaptic density of the downstream cell. The postsynaptic density contains receptors for the transmitter molecule; binding of the transmitter to its receptors may elicit a wide variety of different effects depending on the receptor type, including ion channel opening and signalling cascade initiation.

Many synapses exhibit plasticity, meaning that their strength can depend on prior activity. Long-term synaptic plasticity is regarded as a fundamental mechanism of learning and memory (for review see e.g. Tsukada, 2008) and comprises the opposite events of long-term potentiation (LTP) and long-term

depression (LTD). While long-term synaptic plasticity leads to changes in synaptic strength that persist for hours and longer, there are also short-term forms of synaptic plasticity, which induce changes in synaptic strength that decay back to baseline in less than a second. Short-term synaptic plasticity has been implicated in a number of computational functions. Abbott et al. (1997) show that short-term depression (STD) of synapses allows neurons to dynamically modify the strength of responses to inputs based on the frequencies of the inputs. Thus, a presynaptic neuron that fires very fast results in a decreased synaptic strength compared to a slower-firing neuron, giving the receiving neuron an increased sensitivity to the slower input. Abbott et al. investigated this in neurons of the cerebral cortex, but STD is also present in synapses of the cerebellum including the inhibitory synapse between Purkinje cells (PCs) and DCN neurons. The dependence of STD on the spike rate of the presynaptic PCs is shown for these synapses in Figure 2. These neurons, and the inhibitory connection between them, will be discussed in detail in Section 2.7.

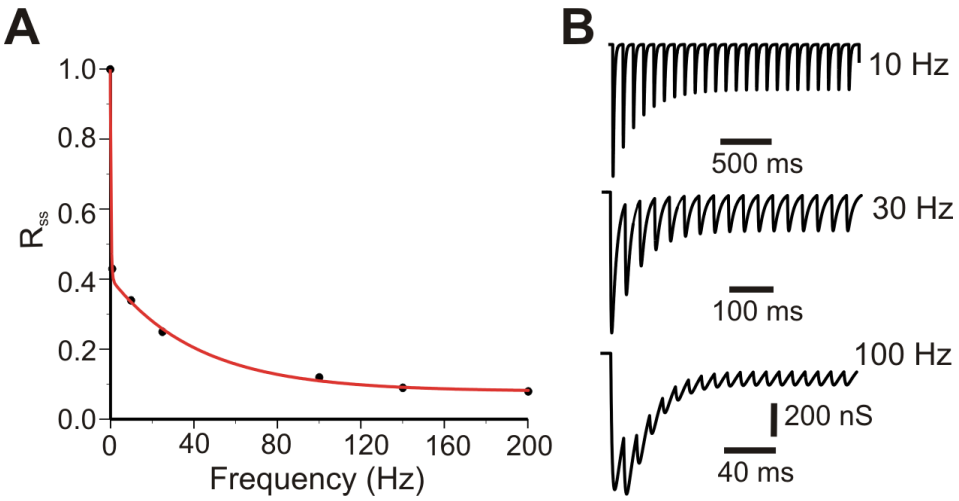

Figure 2 Short-term depression (STD) of the Purkinje cell to DCN neuron synapse (Figure source: Shin et al., 2007a). **(A)** Steady-state probability (R_{ss}) of the Purkinje cell synaptic bouton to release neurotransmitter (GABA) at different spiking rates of the neuron. **(B)** Conductance of the synapse for regular firing at 10, 30, and 100 Hz, respectively.

There is more direct evidence of computational roles of STD, reported by Rothman et al. (2009). They show that single cerebellar granule cells can perform multiplications and divisions on inputs and that this capability is fully accounted for by the presence of STD in the synapses.

2.5 Neuronal coding

Neurons communicate with action potentials, spikes: the way that one neuron signals to another is via the transfer of information from its axonal end plates upon arrival of a spike from the axon hillock. The study of how one neuron communicates with the next is therefore the study of spiking. Relevant to this thesis are these three characteristics of spiking over time:

1. Spike rate
2. Degree of regularity of the intervals between spikes

3. Temporal spike patterns

The first spiking type is often known as a rate code or more precisely, an independent-spike code (Dayan and Abbott, 2001). The second and third can be classified as temporal codes or in the terminology of Dayan and Abbott, correlation codes.

The last item requires explanation: I mean something akin to the Morse code with a hypothetical example being that a neuron sends one spike, followed by a second spike at 23 ms after the first, followed by a ten ms burst of four spikes yet another five ms later.

The three types of code can be combined so that for example a specific degree of regularity at two different rates can be hypothesised to convey two different “messages”.

2.6 Analysis and visualisation of neuronal spiking

A series of neuronal spikes is called a spike train; the analysis of neural coding is based on spike train analysis. Several kinds of metrics of spike trains characteristics have been devised, the simplest being the rate of spiking, usually given as hertz (Hz or 1/s, the unit Hz is used even though a spike train usually cannot be described with a single wave function). The traditional metric of regularity of spiking is the coefficient of variation (CV) of the interspike intervals (ISIs), which is defined as the standard deviation divided by the mean. A high CV may mask parts of more regular firing within a spike train, for which the metric of CV_2 was introduced to spike train analysis (Holt et al., 1996). The CV_2 measures the discrepancy between two consecutive ISIs and is defined as:

$$CV_2 = 2\frac{|\,ISI_{n+1} - ISI_n\,|}{ISI_{n+1} + ISI_n} \tag{3}$$

Figure 3 illustrates the differences between the CV and CV_2 metrics.

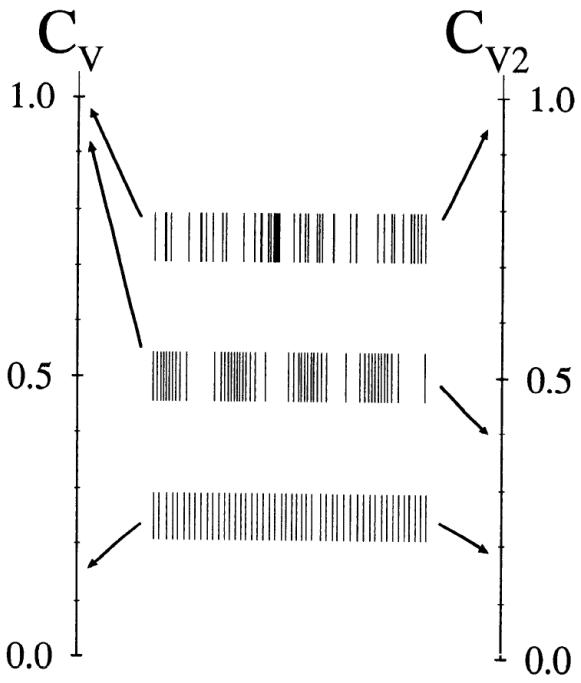

Figure 3 The CV and CV_2 as metrics of neuronal spiking regularity. The upper spike train is a Poisson process and gets a high score on irregularity both by the CV and the CV_2. The lower train is drawn from a gamma distribution of degree 50 (see 2.6.2); such a regular process scores low on both metrics. The middle train is the type of train where the CV_2 metric gives information on the presence of local regularity in the midst of high irregularity of the train as a whole. From Holt et al. (1996).

2.6.1 Interspike interval distributions

Graphing of spike train data is often helpful in their analysis. Two of the most common types of graphing methods are raster plots and ISI distribution plots. An example of each is shown in Figure 4.

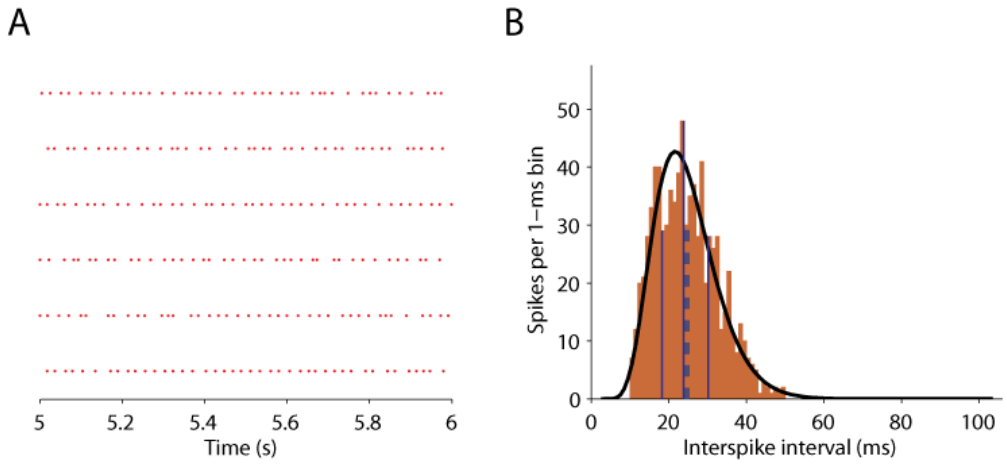

Figure 4 Visualisation of neuronal spiking. A) Sample raster plot of six spike trains over one second of firing. B) ISI distribution for 20 seconds of spiking from the entirety of the top train of A). The black curve is a gamma probability density function of order 7.2 (See text and Figure 5) fit to the data using the gamfit and gampdf functions of MATLAB (v 2006a, MathWorks Inc), which includes 89% of the ISIs of the train. The solid blue lines show the quartiles of the distribution and the thick dashed blue line, the median.

ISI distributions give a compact picture of the overall spike train structure (as opposed to the microstructure, described by the CV_2). For example, Figure 4 B shows that this particular spike train has a rather condensed distribution (50% of the spikes are within the two outer vertical blue lines, at 18 and 30 ms) and a relatively short tail of long ISIs; this would not have been shown conclusively by the CV.

The ISI distribution can be modelled by the fitting of a gamma probability density function, as shown by the black curve in the panel. Section 2.6.2 gives an introduction to gamma probability density functions.

2.6.2 The gamma probability density function and its use in modelling ISI distributions

When the ISI distribution of a spike train is modelled with a gamma probability density function, the probability p of an ISI to be of length x ms can be computed as:

$$p(x) = \frac{1}{b^a \Gamma(a)} x^{a-1} e^{\frac{-x}{b}} \quad (4)$$

where a is the order parameter and b is the scale parameter. Γ(a) is the gamma function with order a and is calculated as:

$$\Gamma(a) = \int_0^\infty e^{-t} t^{a-1} dt \quad (5)$$

The plotting of p (Equation 4) over all ISI values gives the particular gamma probability density function. Examples of gamma distributions with different order and scale values are given in Figure 5.

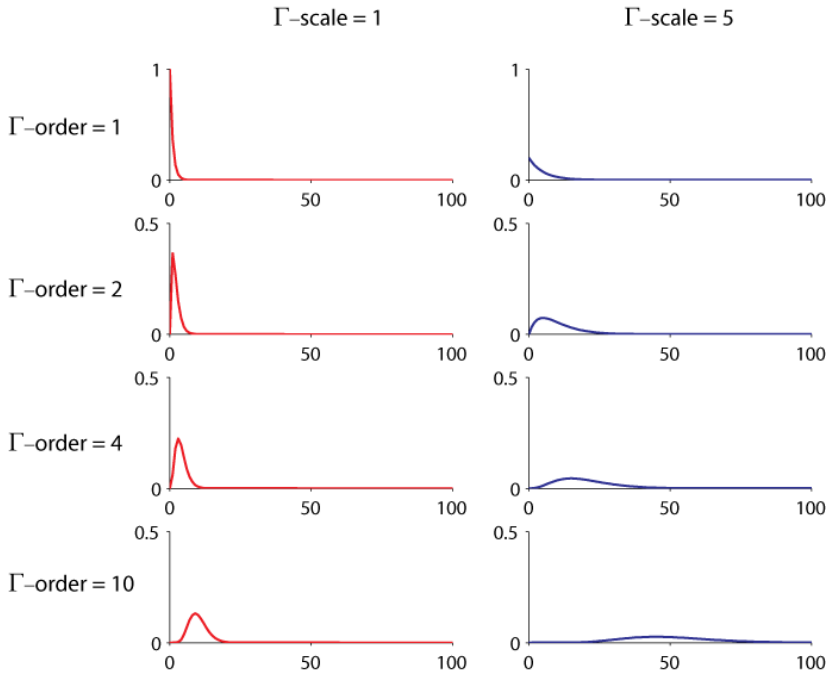

Figure 5 Gamma probability density functions of varying order and scale. The plots were created in MATLAB with the gampdf function.

A gamma distribution of order one (top panels, Figure 5) equals a negative exponential function and can be generated by a Poisson process (Figure 6 A). More regular ISI distributions can often be described by higher-order gamma distributions (Figure 6 D).

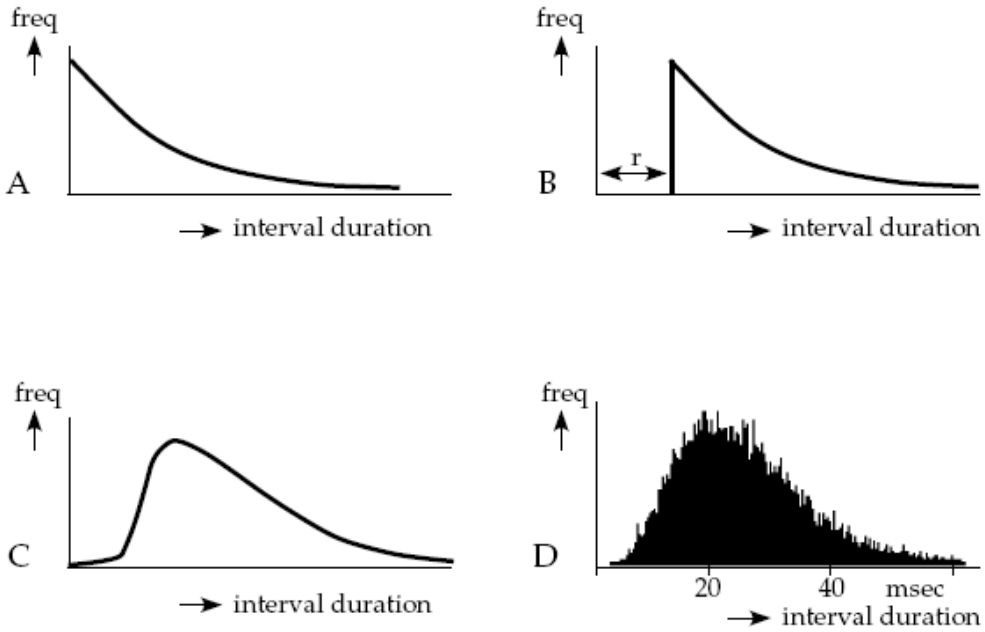

Figure 6 Gamma distributions of interspike intervals. A-C depict theoretical ISI distributions with: A) Poisson distribution; B) the distribution of A, shifted with an (exaggerated) refractory period, illustrating how a higher-order gamma probability density function comes about; C) higher-order gamma distribution; (D) a real neuronal spike train, showing the ability to model spike trains with gamma distributions (approximately gamma order three).

2.7 The cerebellum

Neurons are organised into neuronal circuits where inputs from either other brain areas or sensory neurons are received and processed by neurons of several types, including interneurons that often serve feedback or feed-forward functions within the neuronal circuit. This thesis focuses on the deep cerebellar nuclei (DCN), in particular, on the excitatory DCN projection neurons and their input from the Purkinje neurons of the cerebellar cortex (Figure 9).

The cerebellum is a major part of the vertebrate central nervous system, and contains more than half of the total number of neurons in the human brain (Glickstein, 2007). It is known to play a crucial role in motor functions (reviews

by Middleton and Strick, 1998; Saab and Willis, 2003; Glickstein, 2007), but is increasingly implicated in purely cognitive functions as well (see, for example, Thach, 2007).

An overview of the anatomy of the human cerebellum and its position in the brain is shown in Figure 7.

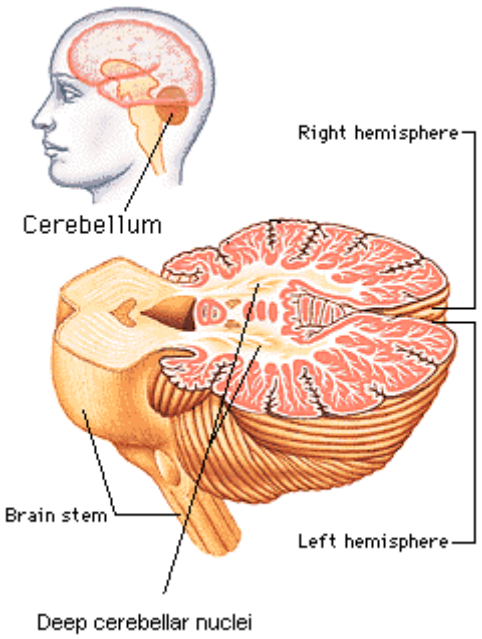

Figure 7 Gross anatomy of the human cerebellum with its position in the brain. Like the cerebrum, the cerebellum consists of a folded cortex (grey matter) and internal white matter. Interior to the white matter are the cerebellar nuclei. These constitute the output region of the cerebellum and connect to the brain stem (leftmost) and further to targets over large parts of the brain. Figure source: www.a2zpsychology.com/images/BIOLOG8.GIF.

The pink areas in Figure 7 constitute the cerebellar cortex; medial to those are the deep cerebellar nuclei (DCN) which form the main cerebellar output region (Thach, 1970; Eccles, 1973).

The cerebellum is characterised by a highly regular circuitry (Thach, 2007), consisting of millions of repeated units of one basic circuit which is almost

identical between different species of mammals (Voogd and Glickstein, 1998). Its anatomy is shown in Figure 8. A simplification of this network structure is illustrated in Figure 9, which depicts the constituent cells of the cerebellar circuit and shows that two types of axons carry the main input to the cerebellum – the mossy fibres and climbing fibres.

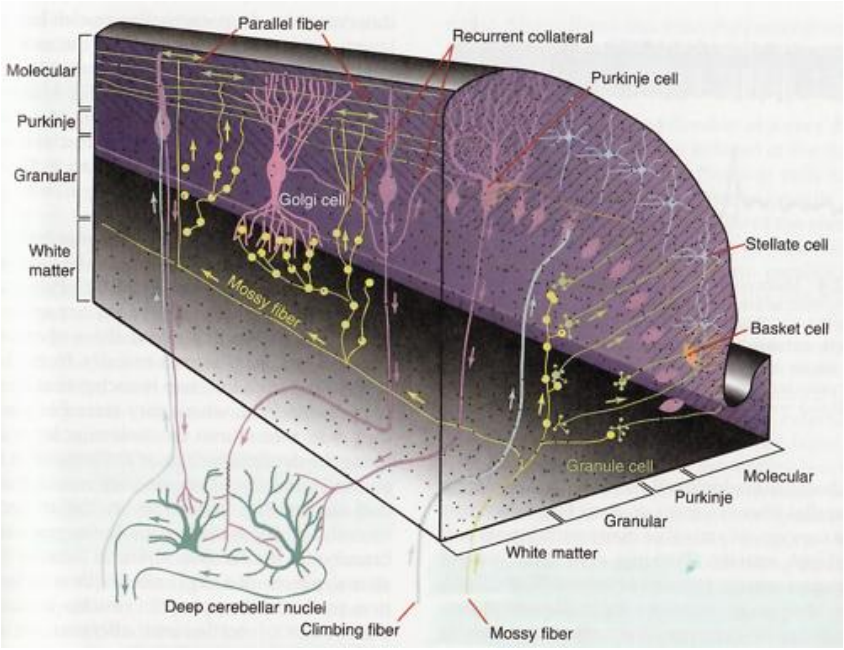

Figure 8 Anatomy of the cerebellum with its principal cell types. The picture shows one of the cortical folds of Figure 7. Arrows point out the direction of axons from soma to boutons. Cerebellar inputs are shown in the lower right part of the picture and its output in the lower left. From Squire et al. (2008).

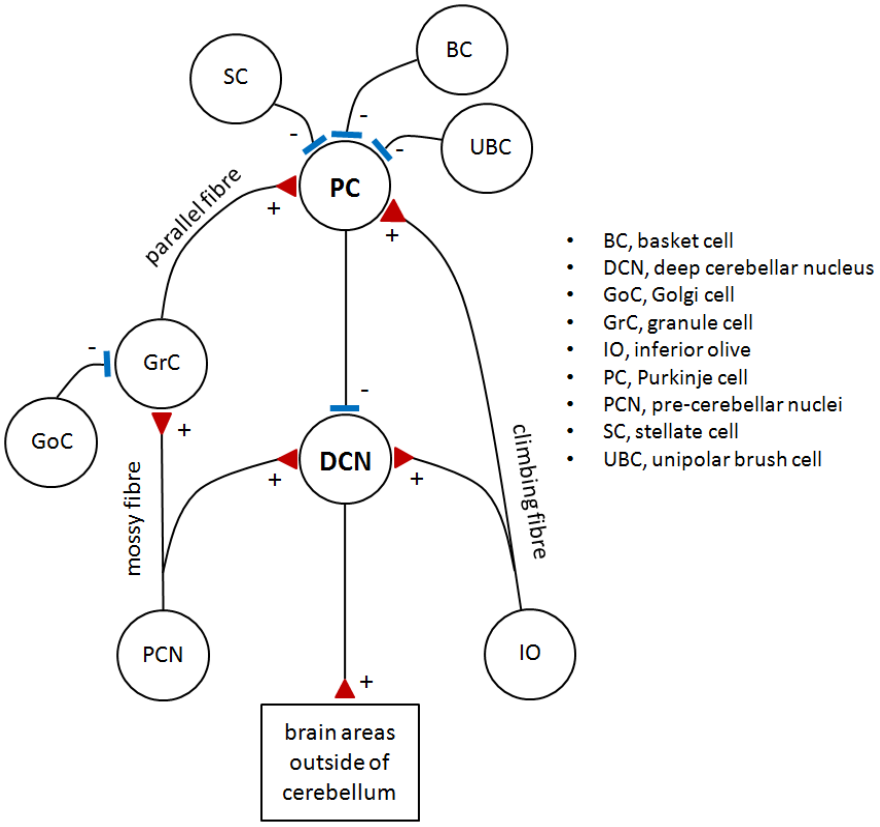

Figure 9 Circuit structure of the cerebellum where the two cells that are central to this thesis are in the middle of the diagram (The Purkinje cell and the DCN neuron). Red arrowheads indicate excitatory synapses; blue, inhibitory synapses.

The mossy fibres originate in cell bodies of multiple precerebellar nuclei in the brain stem and spinal cord. The climbing fibres constitute the other afferent connection and convey information from the inferior olive, which receives input from many brain sites, including the motor cortex.

Mossy fibres connect to the cerebellar granule cells with excitatory synapses, while one of the cerebellar interneuron cell types, the Golgi cell, inhibits the granule cells. The axons of the granule cells form the PFs which connect to the Purkinje cells with excitatory synapses. The climbing fibres also act excitatory on the Purkinje cells, with one climbing fibre surrounding the Purkinje cell like ivy on a tree. Thus, the two main fibres that convey information to the cerebellum

stimulate Purkinje cells and thereby increase their propensity to fire action potentials. This stimulatory effect on the Purkinje cells is counteracted by the inhibitory signalling of the basket cells, the stellate cells, and the unipolar brush cells.

Purkinje cells are at the centre of the cerebellar circuit, directly or indirectly contacted by all the other cell types. With the exception of a minor direct connection from Purkinje cells to the vestibular nuclei, Purkinje cells transmit the output of the cerebellar cortex to the deep cerebellar nuclei (DCN) neurons (Jahnsen, 1986a); this is mediated by inhibitory synapses (Ito et al., 1964).

The DCN neurons constitute the output of the circuit as a whole. In addition to the signals from the Purkinje cells, the DCN receive branches of the mossy and climbing fibres (Chan-Palay, 1973; Sugihara et al., 1999; Wu et al., 1999; Shinoda et al., 2000). Hence, on top of being the main output of the Purkinje cells, the DCN obtain the same signals as the Purkinje cells do, without the processing in the granule cells. This placement of the DCN neurons has been highlighted by Llinas and Muhlethaler (1988): “Indeed, the connectivity of these neurones places them in a truly privileged position.”

2.7.1 Deep cerebellar nuclei neurons

The DCN (Figure 10) contain at least four types of neurons (Czubayko et al., 2001; Sultan et al., 2003; Uusisaari et al., 2007; Uusisaari and Knopfel, 2010). The one classified as large and non-GABAergic is an excitatory projection neuron that uses the neurotransmitter glutamate and carries the main output from the DCN (Batini et al., 1992; Voogd, 2004a). The neuron transmits this output to the brain stem, thalamus, and spinal cord (Voogd, 2004b) and is the main neuron

modelled in this thesis work. The term “DCN neuron” will therefore be used to refer to this neuronal type.

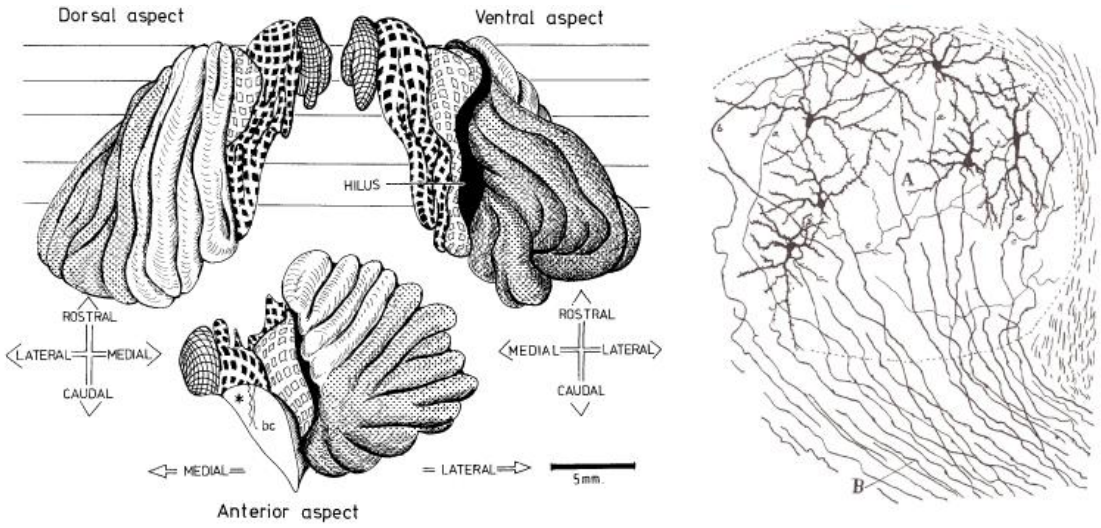

Figure 10 The cerebellar nuclei in humans (left) and a zoom-in on seven DCN neurons of the dentate nucleus of the cat (right). Legend to the left picture: fastigial nucleus: hatched; globose nucleus: filled squares; emboliform nucleus: open squares; the remainder is the dentate nucleus. Right picture: seven nucleus neurons are shown with their axonal projections as they leave the cerebellum. Sources: left picture: Paxinos and Mai (2004); right picture: Cajal (1894).

There are few studies that have characterised only the excitatory projection neurons of the DCN; the majority of studies have investigated a mix of the neuronal types in the DCN, which have similar electrophysiological characteristics (Jahnsen, 1986a). The following paragraphs refer to such a heterogeneous population.

Spontaneous firing rate

Typical for the DCN neurons is that they fire spontaneously even in the absence of synaptic inputs. Studies have shown spontaneous firing rates of ca 25 Hz of DCN neurons in vitro for guinea pig (Jahnsen, 1986a) and rat (Mouginot

and Gaehwiler, 1995). In the presence of synaptic input in vivo, higher firing rates of about 50 Hz have been recorded in rats (LeDoux et al., 1998; Rowland and Jaeger, 2005).

Rebound firing after hyperpolarisation

The term "rebound firing" refers to the situation where a neuron has received an inhibitory stimulus which is subsequently removed, leading to a burst-like response (Figure 11). It is a characteristic response of DCN neurons (Cody et al., 1981; Jahnsen, 1986a; Llinas and Muhlethaler, 1988; Aizenman and Linden, 1999) and its molecular mechanisms have been investigated in several studies. Llinas and Muhlethaler (1988) showed that low-voltage activated calcium channels (CaLVA) participate in DCN neuron rebound firing. Other currents that contribute to the rebound firing are an h current (Aizenman and Linden, 1999) and a persistent sodium (NaP) current (Llinas and Muhlethaler, 1988; Sangrey and Jaeger, 2010).

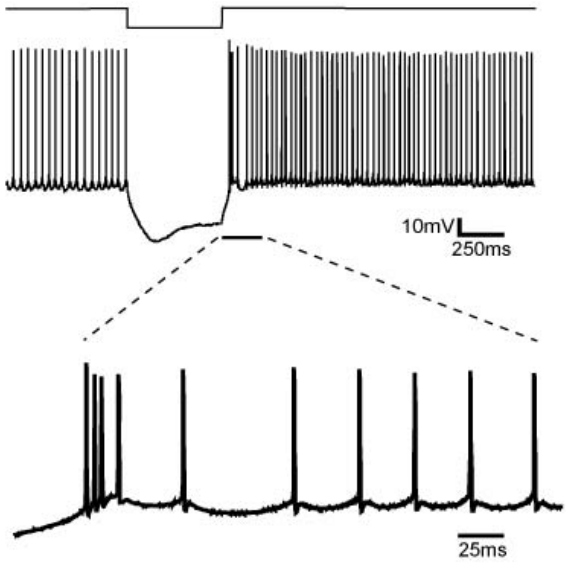

Figure 11 Rebound firing of a DCN neuron. The uppermost line shows the injection of a negative current into the neuron, leading to the membrane hyperpolarisation shown in the second trace. The rebound is the period of enhanced firing rate following the removal of hyperpolarisation, and lasts until the end of the trace in this picture. The first few spikes of the rebound can be of very high frequency, as shown in the enlarged picture at the bottom. Picture source: www.ucalgary.ca/~rwturner/images/dcn_rd_400x454.jpg

2.7.2 Purkinje cells

Purkinje cells (Figure 12) are the principal cell type of the cerebellar cortex; they have flat dendritic trees that receive an unusually large number of synaptic connections. The PFs which arise from the granule cells and run in perpendicular arrays through the Purkinje cell dendritic structure form an estimated 80,000 (Palkovits et al., 1972) to 200,000 (Eccles et al., 1967) synapses (Figure 8).

Figure 12 Human Purkinje cell, showing the large and flat dendritic tree which receives approximately 100,000 synapses from PFs running orthogonally to the tree. From Cajal (1894).

Purkinje cells have a characteristic electrophysiology with two different kinds of spikes: simple and complex spikes, respectively (Figure 13). Simple spikes are the most common ones and consist of single spikes, which occur at frequencies of up to more than 200 spikes per second and are the results of stimulation by PFs (Armstrong and Rawson, 1979). Complex spikes are elicited by stimulation of the single climbing fibre which reaches each Purkinje cell. These spikes are typified by one initial strongly depolarising spike, followed by several spikes of lower amplitude. Complex spikes are normally dispatched at rates of only 1-2 per second (Armstrong and Rawson, 1979). An example of a train of simple spikes and of one complex spike are shown in the following figure.

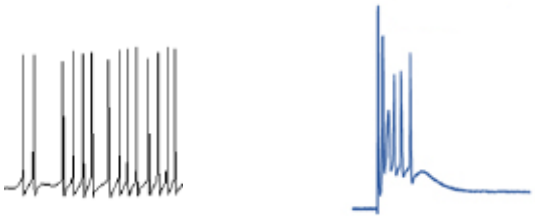

Figure 13 Types of Purkinje cell spikes. The membrane potential trace in black depicts a train of simple spikes (from De Schutter, 1997) while the blue trace shows a complex spike (from Kakizawa et al., 2007), with one forceful depolarisation followed by a number of irregular, less strongly depolarising spikes.

2.7.3 The Purkinje cell to DCN neuron synapse

Purkinje cells connect to the DCN neuron with inhibitory synapses using the neurotransmitter GABA; on binding to the $GABA_A$ receptor of the DCN neuron, chloride ion channels are opened and give a hyperpolarisation. The connection is the dominating input to the DCN with more than ten thousand synapses per DCN neuron (Palkovits et al., 1977). Palkovits et al. also found an average of 26 times more Purkinje cells than DCN neurons and that the synapses from the Purkinje cells make up the majority of synapses on DCN neurons. The number of Purkinje cells converging onto a DCN neuron was estimated at 860, but newer estimates are much lower (Chris De Zeeuw and Indira Raman, personal communication).

The Purkinje cell to DCN neuron synapse (PC-DCN synapse) has the ability to express LTP (Aizenman et al., 1998), LTD (Morishita and Sastry, 1996), and STD (Morishita and Sastry, 1993; Telgkamp and Raman, 2002; Pedroarena and Schwarz, 2003). The plasticity of this synapse is a prominent part of this thesis and will be discussed in some detail in the following paragraphs.

STD of the PC-DCN synapse was introduced in Section 2.4 with the illustration of Figure 2. As shown in the figure, each Purkinje cell spike decreases the strength of the synapse. How large this effect is depends on the interval between spikes, with increasingly large decreases in conductance resulting from shorter intervals.

A high frequency input to the synapse, repeated several times, has the ability to induce LTD (Morishita and Sastry, 1993; Aizenman et al., 1998). A similar stimulus with longer duration induces LTP (Aizenman et al., 1998). Thus, the same kind of stimulus causes either LTD or LTP depending on its length (Figure 14).

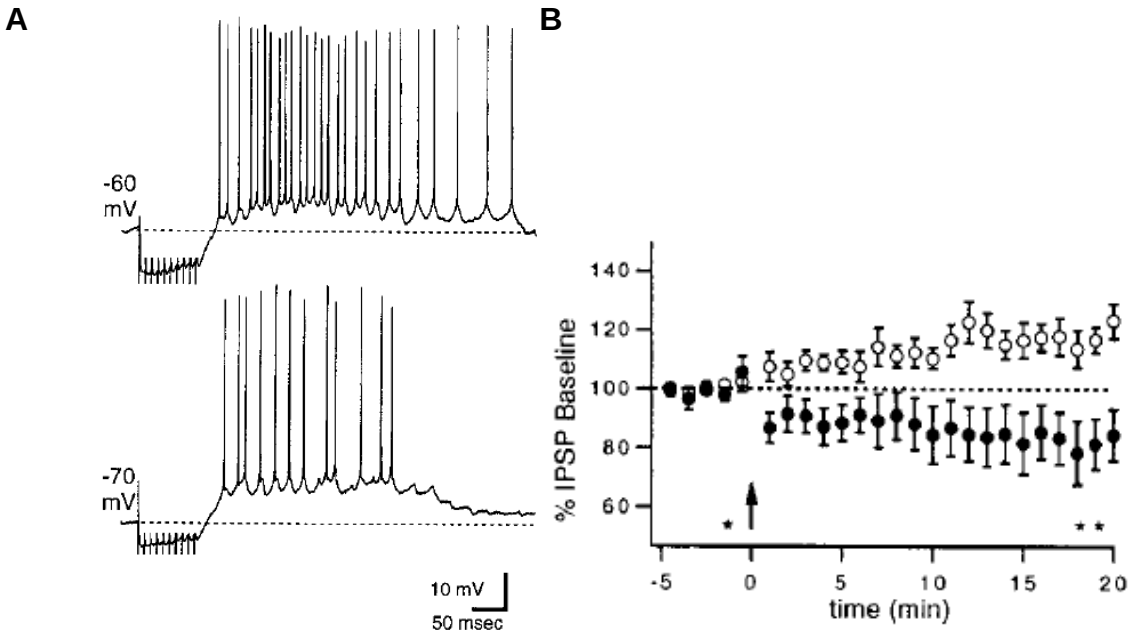

Figure 14 Bidirectional change in strength of the PC-DCN synapse, shown by Aizenman et al. (1998). LTP results from stimulation that evokes a strong rebound firing on its release, while LTD results from stimulation giving slower rebound firing. (A) A pulse train of ten pulses at 100 Hz was applied to the cerebellar cortex directly neighbouring the DCN. The recording electrode was inserted in the DCN, registering inhibitory postsynaptic potentials (IPSPs) following the cortical stimulation. The upper picture shows a sample DCN cell responding to the pulse train by hyperpolarisation from its resting membrane potential (mean = -58mV over 33 cells). The lower picture shows the response to the same train from a point of hyperpolarised membrane potential (mean = -67mV), giving a less intense rebound firing response. (B) The bidirectional change in strengths of subsequent IPSPs following the application of the protocol in (A). The increased IPSP sizes resulting from the protocol applied to cells at resting membrane potential are shown with open circles, while the IPSPs of the tonically hyperpolarised cells are shown with closed circles.

2.7.4 Learning in the cerebellum

The cerebellum is involved in learning of several types of motor behaviour (Mauk et al., 2000). The present section will discuss theories relevant to this

learning and will then exemplify the learning with a famous cerebellar experimental procedure called eyeblink conditioning.

Hebbian and non-Hebbian learning

Most theories of learning in the brain are based on the concept of Hebbian learning (see e.g. Cooper, 2004). Hebbian learning refers to the paradigm outlined by Donald Hebb (1949). The essence of his idea is that neurons that fire together wire together:

"When an axon of cell A is near enough to excite a cell B and repeatedly or persistently takes part in firing it, some growth process or metabolic change takes place in one or both cells such that A's efficiency, as one of the cells firing B, is increased." (Hebb, 1949)

However, not all types of synaptic plasticity that have been implicated in learning can be considered as Hebbian. LTP and LTD at the inhibitory Purkinje cell – DCN neuron synapse result in an increased (decreased) inhibition after increased (decreased) postsynaptic activity and are therefore cases of non-Hebbian synaptic behaviour. Moreover, non-Hebbian LTP and LTD are also found in the cerebellar cortex at the parallel fibre to Purkinje cell synapse (PF-PC synapse), where they are often seen as foundations of memory (Ito, 2001). At this synapse, LTD is induced when the climbing fibre input is active together with parallel fibre input (Ito et al., 1982). Thereby, the synaptic strength is decreased with each such pairing until saturation sets in, which prevents the complete removal of synaptic capacity (Hansel et al., 2001) [but conflicting data indicates that the synapses are completely silenced (Isope and Barbour, 2002)].

The Marr-Albus theory

The perhaps most famous theory of cerebellar computation, the Marr-Albus theory, proposed a central role of the PF-PC synapses and assumed that a

modifiable strength of these synapses would be both necessary and sufficient for motor learning to take place (Marr, 1969; Albus, 1971). The theory was proposed before the experimental evidence of LTD of the PF-PC synapse was discovered by Ito et al.; Subsequently to the discovery, the theory has often been called the Marr-Albus-Ito theory (for example De Schutter, 1997; Hansel et al., 2001).

The Marr-Albus theory was formed on the basis of the structure of the cerebellar circuit (Figure 9) and of the cellular morphology and physiology of the participating cells. The theory has not been conclusively proven, and parts have been shown to be incorrect, such as Marr's assumption that no other cerebellar synapses than the PF synapses are modifiable, but it is an important theoretical framework for the thinking of what the cerebellum does (Ghez and Thach, 2000).

The different Purkinje cell responses to the stimulation of parallel and climbing fibres (Figure 13) together with the wiring differences between the parallel fibres and the climbing fibres play an important part in the Marr-Albus theory, which assumes that the climbing fibres carry information about the intention of a movement, relayed from the motor cortex, while the PFs carry information about the sensory input and other circumstances surrounding the instruction from the cerebral cortex.

The theory, reviewed by Tyrrell and Willshaw (1992), predicts that one single Purkinje cell can convey one particular muscle stimulus. In a non-learned state, the instruction for the Purkinje cell to stimulate a muscle will come from a climbing fibre. In this state, the movement is non-automatic, requiring the participation of input from the motor cortex to the inferior olive.

The Marr-Albus theory hypothesises how the learning of the movement controlled by one Purkinje cell becomes automatic. Through plasticity in the PF-PC synapses, the Purkinje cell learns to associate inputs from mossy fibres with a particular cortical instruction from the climbing fibre. Upon this learning, the set

of sensory inputs from the mossy fibres triggers the movement controlled by the Purkinje cell without the requirement of a simultaneous cortical instruction. Thus, the motor action has become automatic.

Tyrrell and Willshaw give an example of the cerebellum's involvement in motion. When one stretches out an arm and moves it around to form a circle, the cerebellum makes sure that the correct set of muscles comes into play at the correct time – in the arms, the shoulders, trunk, legs, etc. This automatic, smooth, and correctly timed action of the miscellaneous muscles can be explained by the Marr-Albus theory. Each Purkinje cell that controls either of the involved muscles has learnt – through the practice of movement from childhood to adulthood – to react to each combination of sensory state.

As Tyrrell and Willshaw explain, the cerebellum can be seen as a computation device that relieves the consciously thinking cortex of work. This sort of back-up computing that is available after training can be seen in for example the fact that a driver simultaneously can press the brake pedal, release the gas, and steer out of the way of an animal standing on the road. For a beginner driver, where the non-conscious back-up computation has not been learned, merely pressing the brake pedal may in a similar situation take up all processing capacity of the motor cortex.

Evidence that supports the Marr-Albus theory includes that mice with abolished long-term depression of PF-PC synapses have impaired adaptation to the vestibulo-ocular reflex – the following of moving objects with the eyes to stabilise pictures on the retina (Goossens et al., 2004). Additional evidence comes from eyeblink conditioning, a case of associative learning, which is discussed in the following.

However, more recent evidence speaks against the involvement of LTD at the PF-PC synapse in both of these learning tasks (Schonewille et al., 2011).

Eyeblink conditioning – cerebellar associative learning

The cerebellum is today known to be involved in associative learning, such that occurs in eyeblink conditioning (Christian and Thompson, 2003). In this procedure, a subject is first exposed to an *unconditioned stimulus* – for example a puff of air to the eye, leading to a reflexive blink of the eyelid. This air puff is combined with another stimulus, such as a tone, which leads to the subject learning to respond to the second stimulus alone with a reflexive eyeblink (the *conditioned response*), in the same fashion as to the air-puff. The subject has thus been conditioned to the tone – the *conditioned stimulus*.

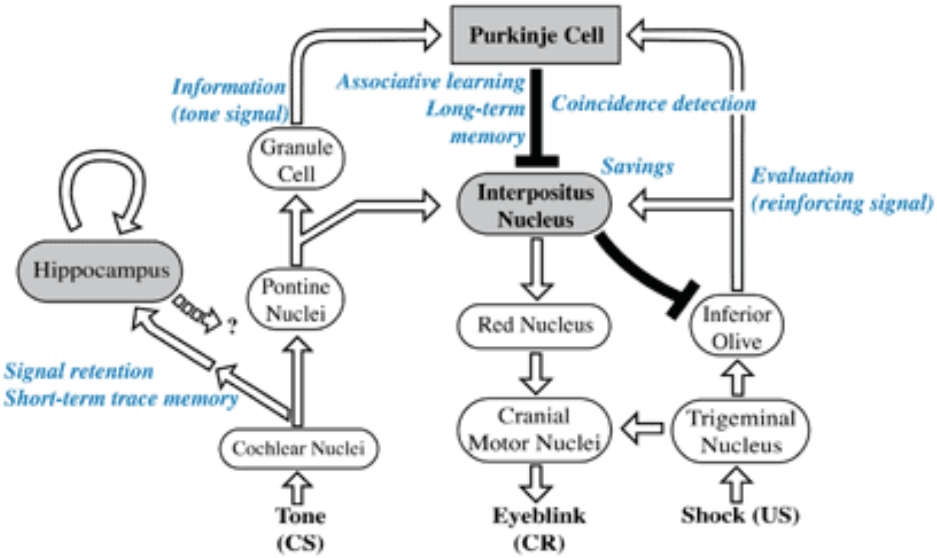

Figure 15 Eyeblink conditioning circuitry. The interpositus nucleus is one of the deep cerebellar nuclei. The figure shows the interactions between several cerebellar locations in the learning of this paradigm. US stands for unconditioned stimulus, CS, conditioned stimulus, CR, conditioned response. Picture source: www.iam.u-tokyo.ac.jp/coe/mishina/index_e.html.

Although there is a large body of evidence for the involvement of the cerebellum in eyeblink conditioning (see Figure 15), the exact locations of the storage of the conditioned behaviour have not been determined conclusively

(reviewed by Lavond, 2002). Abiding by the Marr-Albus-Ito theory, it has been demonstrated that learning the conditioned response involves LTD of the PF-PC synapse (Koekkoek et al., 2003). Jirenhed et al. (2007) in turn demonstrate how single Purkinje cells respond to learning by their paused firing, an effect which disappears upon extinction of the learned response.

In addition to the involvement of Purkinje cells and their afferent synapses, the involvement of the DCN in eyeblink conditioning has been shown in several studies (e.g., Woodruff-Pak et al., 1985; Berthier and Moore, 1990; Christian and Thompson, 2005). The learning of the conditioned behaviour has even been shown to increase the number of excitatory synapses to DCN neurons from mossy fibre and climbing fibre sources (Kleim et al., 2002).

Notably, the involvement of neither Purkinje nor DCN neurons in this learning precludes the involvement of the other neuronal location. Indeed, increasing evidence shows the importance of both sites and their interactions to acquire and display the conditioned eyeblink response (Wada et al., 2007; Woodruff-Pak and Disterhoft, 2008).

As regards the electrophysiological response of the Purkinje cells to learning, the Marr-Albus-Ito theory assumes that as a result of the LTD of the PF-PC synapse, the output of the Purkinje cell is decreased (for example, Hansel et al., 2001). This makes intuitive sense since the synapse is excitatory and the result, according to the theory, is a disinhibition of the DCN neurons. Thus, the presentation of a tone, stored in the weights of the PF-PC synapses, would lead to an increased output from the cerebellar nuclei, which would lead to the execution of the eye-blink response.

2.7.5 A comparison between the cerebellar cortex and the cerebral cortex

The cerebellar cortex has several features that are not seen in the cerebral cortex. While the main cell type of the cerebral cortex – the pyramidal cell – is not spontaneously active, the central cell in the cerebellar cortex – the Purkinje cell – is. This may be required for the cerebellum to function as there is no recurrent excitation as in the cerebral cortex. A baseline level of activity, whether caused by intrinsic mechanisms or by recurrent excitation, can enable inputs to bi-directionally modulate the spiking of a neuron, providing a bigger repertoire of possible neuronal responses.

3. Computational neuroscience and neuronal modelling

In order to understand neural functions, neuroscientists have used a variety of approaches, including the use of morphological techniques such as staining of neural tissue for microscopy (for an example, see the Purkinje cell by Cajal 1894, Figure 12), axonal tracing with radioactive compounds, and more modern imaging techniques like magnetic resonance imaging. Another approach is to record neuronal currents and membrane potentials.

These areas of experimentation have contributed to the understanding of morphology and electrical properties of neurons. Computational neuroscience introduces the possibility of a more holistic understanding of how neurons work. This is achieved by combining data gathered using different experimental techniques and synthesising the facts into models of neuronal behaviour. The

next section will outline how this is undertaken, with a focus on the methodology used for this thesis.

3.1 Neuronal modelling techniques

One of the simplest ways to model neurons is with an integrate-and-fire model (Lapicque, 1907). This type of neuronal model sums up all the electrical inputs to the neuron, integrates the effects they have on the membrane potential of the neuron, and sends out a spike if the threshold voltage has been reached.

Without an additional modification, such an integrate-and-fire model is not realistic in that effects of inputs remain over time (Gabbiani and Koch, 1998). An improvement is the addition of a gradual disappearance of effects of inputs, a feature included in the leaky integrate-and-fire neuron model. However, unrealistic behaviours compared to real neurons remain in the leaky integrate-and-fire neuron model; for example, behaviours such as adaptation and bursting, which depend on the interaction of different ion channels and intracellular calcium, are not represented.

More realistic neuronal firing can be produced with the Izhikevich neuron model (Izhikevich, 2003). It uses a set of differential equations with parameters that can be adjusted to reproduce many types of neuronal firing, such as bursting and tonic spiking. However, the Izhikevich model also does not contain any representation of ion channels or ion concentrations, and like an integrate-and-fire model it treats a neuron as one single compartment without accounting for neuronal morphology.

Neuronal morphology has been shown to be important for computations (review by London and Hausser, 2005), and it has been shown that neuronal spike patterns such as the rebound responses in DCN neurons are shaped by

specific combinations of ion channels (see for example Steuber et al., 2010). Thus, for examining neuronal behaviour in response to new stimuli it can be expected that a neuronal model that captures the neuronal morphology and represents the biophysical mechanisms is better suited (Beeman, 2006a).

For this reason, the work in this thesis was based on the methodology of biophysically and morphologically realistic modelling of neurons. I have assumed that the morphology of the DCN neuron and the ion channels that are present in DCN neurons can potentially affect computational functions such as pattern recognition and the decoding of irregular inputs, and have used a DCN model that includes these features. Although this approach is more computationally expensive than a modelling study that uses an integrate-and-fire or Izhikhevich model, it also enables me to investigate the effect of individual biophysical mechanisms on certain computations by removing them from the model (for example the rebound conductances in Section 5.5.4). In a second set of simulations, the predictions made by a complex model can then be tested against results based on simplified models; I have performed such a control simulation with an integrate-and-fire model (described in Section 6.3).

The ensuing sections will describe how biophysically and morphologically realistic modelling is undertaken in general and are followed by Chapter 4 which gives the details of the setup of the DCN neuron model for the projects in this thesis.

3.2 Morphologically realistic modelling of neurons

One of the tools available for the computational modelling of neurons is GENESIS (Bower and Beeman, 2007), a system which also allows the use of reconstructed neuronal morphologies and provides functions that govern the

electrical behaviour of a neuron: ion channels and membrane properties, along with such matters as the axial resistance along neuronal branches. The technique employed by GENESIS is called biophysically realistic neural modelling and is also the type used in this thesis.

Another widely used neuronal simulator, which shares a lot of functionality with GENESIS and has now overtaken GENESIS in terms of the size of its user base (based for example on the number of published models in ModelDB, http://senselab.med.yale.edu/modeldb/) is NEURON (Hines and Carnevale, 1997). Sections 3.3 and 3.4 in the following will discuss the construction of a conductance-based compartmental model and its implementation in GENESIS and NEURON, both of which have been used in the simulations for this thesis (GENESIS version 2.3, NEURON version 6.1).

The first step in constructing a biophysically realistic neuronal model is to reconstruct the three-dimensional structure of the neuron. The neuron is stained for visualisation; the morphology is then reconstructed using microscopy and custom-made software (Beeman, 2006b).

Secondly, the passive electrical properties of the neuron are identified; these include the membrane and axial resistance and membrane capacitance, which are characterised in electrophysiological experiments performed in the presence of ion channel blockers.

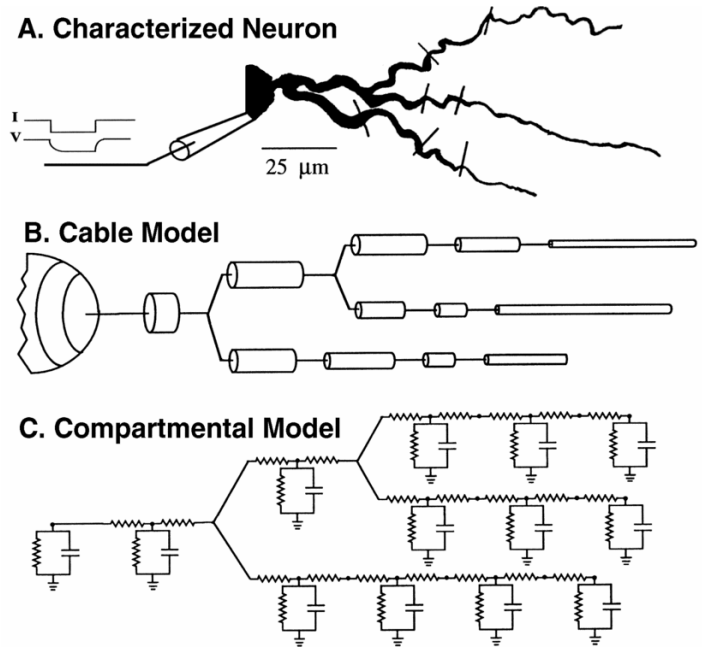

Figure 16 The process of reconstructing neuronal morphology for use in a computer simulation. A) Neuronal morphology and characterisation of the passive electrical properties of a neuron. B) The neuronal morphology is divided into compartments of length and diameters corresponding to distinguishable parts of the original neuron. C) Compartments are represented as electrical circuits, with parameters given from the experiments in A). From Beeman (2006b).

The three dimensional picture of a neuron is then translated into a set of iso-electric compartments. The sizes and numbers of these are determined from the electrical properties, specifically the length constant which gives how voltage decreases over distance in the neuron (Beeman, 2006b). The process of constructing a passive multi-compartmental model of a neuron is illustrated in Figure 16. Figure 17 shows the reconstructed morphology of the DCN neuron and the representation of the morphology in the NEURON implementation of the DCN neuron model that is the subject of the present thesis.

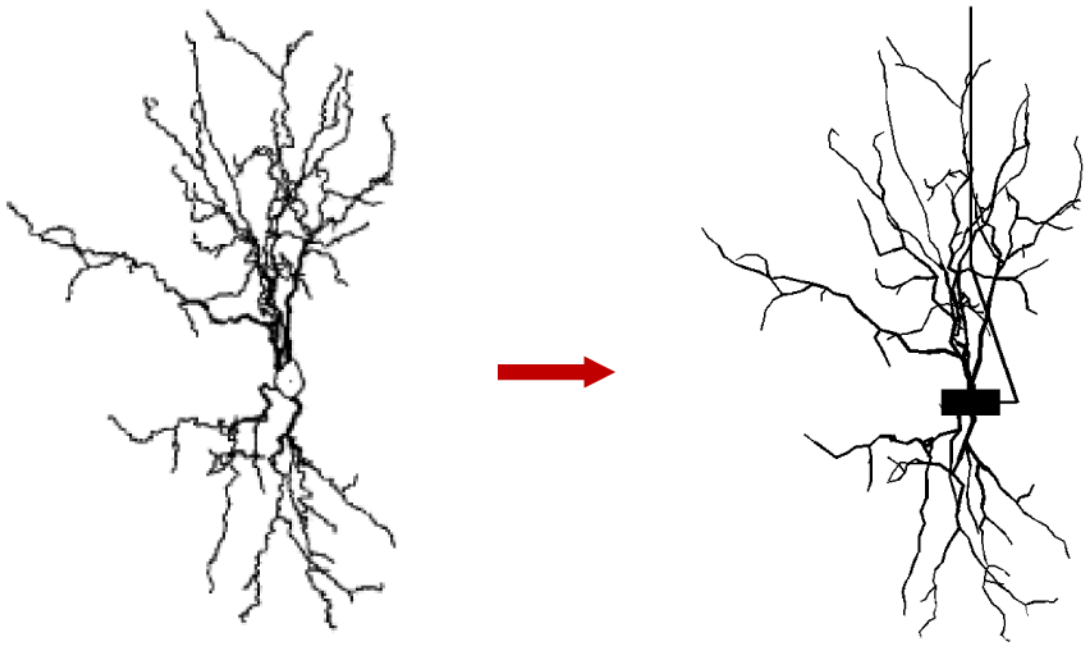

Figure 17 Example of reconstructing a neuronal morphology: at the left is the DCN neuron (Steuber et al., 2004) that is the basis for the DCN neuron model of the present thesis (right). The model contains 517 compartments, most of which constitute the dendritic tree. The most striking visual differences are the soma (centre) and the axon (L-shaped structure emanating from the soma, right picture only). While the soma in the NEURON model is represented by a cylindrical compartment with approximately the same surface as in the reconstructed neuron, the axon was not captured in the microscopy and the axon in the model was added to allow axonal spike initiation.

Taking the next step in the construction of the realistic model – going from a passive to an active neuronal model – requires the assembly of as much information as possible about the ion channels of the neuron (Beeman, 2006b). This involves consulting published literature of the channels in the specific neuron type, where available; where not available, either channels from other neurons in the published literature are used or additional experiments are made to identify the missing channel characteristics. In either case, the result is that

each compartment is constructed as shown in Figure 18 where the passive and active properties are represented by electrical circuit components.

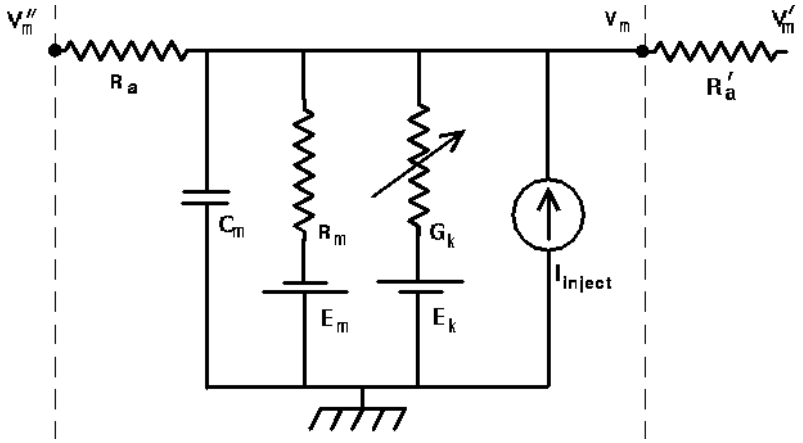

Figure 18 A compartment from the neuronal reconstruction shown in Figure 16. Each compartment is represented by an equivalent neuronal circuit as shown in this picture. C_m is the membrane capacitance; E_m and R_m are the equilibrium potential and resistance of the membrane leak channels; E_k and G_k are the equilibrium potential and the conductance (=1/resistance) of a representative gated ion channel. I_{inject} is current injected into the neuron. V_m is the membrane potential of the compartment, while V_m' and V_m'' are the membrane potentials of the neighbouring compartments. R_a and R_a' are the resistances in the connections to the neighbouring compartments; whether current flows across these and in which direction is determined by the relative values of V_m to V_m', and V_m to V_m'', respectively. From Beeman (2006a).

The change of membrane potential Vm of a compartment can be calculated by:

$$C_m \frac{dV_m}{dt} = \frac{(E_m - V_m)}{R_m} + \sum [(E_k - V_m)G_k] + \frac{(V_m' - V_m)}{R_a'} + \frac{(V_m'' - V_m)}{R_a} + I_{inject} \qquad (6)$$

with explanations to the terms given in Figure 18.

The models of the ion channels are the computationally expensive parts of neuronal modelling. The standard way to model these is to use the formalism that has come to be known as the Hodgkin-Huxley model (Hodgkin and Huxley, 1952).

3.3 The Hodgkin-Huxley model of ion channel kinetics

Voltage-gated ion channels have been modelled since the 1950s using the methodology introduced by Hodgkin and Huxley (1952). The approach is to fit functions to the experimentally identified plots of ion channel conductances as a function of voltage. Hodgkin and Huxley found that this is best achieved with a model that assigns voltage-dependent variables to the activation and, for some channels, inactivation of the channel. Thus, in the Hodgkin-Huxley model, the conductance g of a voltage-gated ion channel is described by

$$g = g_{max} m^a h^b \tag{7}$$

where g_{max} is the maximum conductance of the channel; m is the fraction of activated channels (named the activation variable); h is the fraction of not inactivated channels (inactivation variable); and a and b are constant exponents of the activation and inactivation variables, respectively. Simulation results of the model from the original paper by Hodgkin and Huxley are shown in part (a) of Figure 19; the experimental data from giant squid axon that the model is based on are shown in part (b).

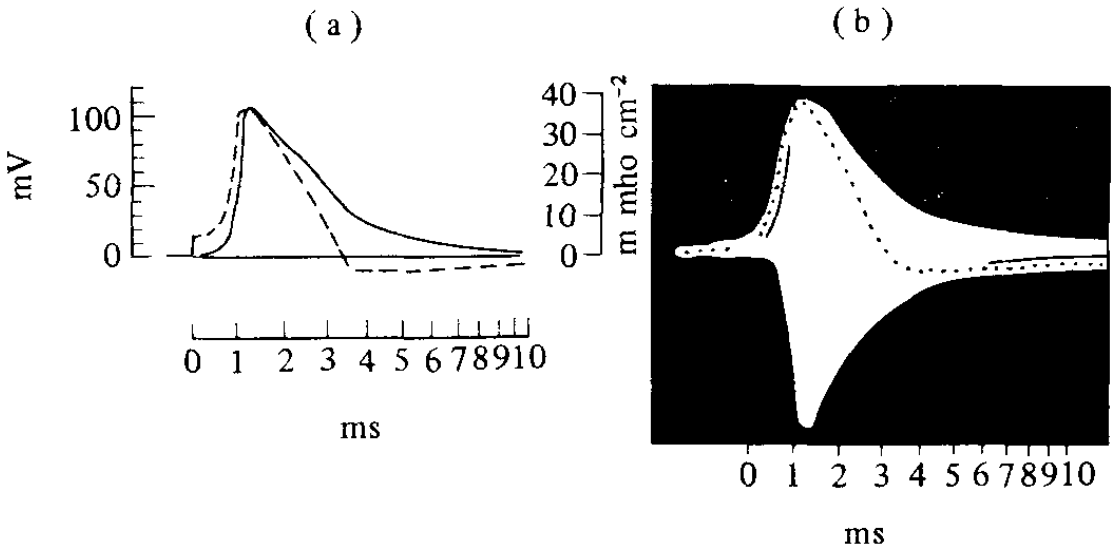

Figure 19 The Hodgkin-Huxley model. The illustration shows how the model of a potassium ion channel together with a sodium ion channel reproduces the behaviour of an actual neuronal action potential. A) The dashed curve (left y-axis) shows the membrane potential relative to the resting membrane potential. The solid line (right y-axis) shows the specific membrane conductance. B) The experimental data of a recording from giant squid axon on which the model was based, with the dotted line showing the membrane potential and the upper black-to-white interface showing the membrane conductance. Note the close to perfect fit of the model in B). Source: Hodgkin and Huxley (1952).

In the following, m and h will be referred to as state variables and the letter x will be used to refer to both m and h.

By its multiplication with g_{max}, the expression $m^a h^b$ gives the actual conductance through the ion channel at any point in time. The exponents a and b of the state variables influence the time course of each channel activation and inactivation; in the original Hodgkin-Huxley model (Figure 19) these are 4, and 0, respectively (for the potassium channel) and 3, and 1, respectively for the sodium channel.

The Hodgkin-Huxley model further assigns each state variable a corresponding steady-state value, x_∞, which depends on the membrane potential. The value of x is determined by x_∞ as well as by the value of x in the previous time step. The following equation shows how a state variable changes value over time (Hille, 2001, page 49):

$$\frac{dx}{dt} = \frac{x_\infty - x}{\tau_x} \tag{8}$$

The equation also contains the time constant of the state variable, τ, which determines how fast the value of x changes with fluctuations of the membrane potential. τ, as x_∞, is voltage dependent and, as for the exponents of the state variables, is chosen for each ion channel model to make the channel kinetics fit electrophysiological data.

The set of Hodgkin-Huxley-like equations describing the set of ion channels for a specific neuron are generally too complex to be solved analytically (Hines and Carnevale, 1997). Thus, in both GENESIS and NEURON, equation 8 is modified to be applied to a neuronal model system which has been discretised in space and time. The discretisation in space consists of the continuous, smooth, morphology of a real neuron being represented by a number of computational compartments as previously discussed. Differential equation (8) can for example be discretised in time using forward Euler integration; this results in equation (9) which is then applied to each state variable of every channel in each compartment.

$$\frac{\Delta x}{\Delta t} = \frac{x_\infty - x}{\tau_x} \tag{9}$$

Having calculated the channel conductance as described above, the channel current can then be derived using Equations 1 and 2 in Section 2.2, and the resulting change of membrane potential is given by Equation 6 (3.2).

As an example for the voltage-dependence of ion channel conductances in the Hodgkin-Huxley model, a channel mechanism of the DCN neuron model will be used: the NaF channel. This is a model of the fast-kinetics sodium current that creates the upstroke of an action potential, using the same state variables and their exponents as the original Hodgkin-Huxley model of Figure 19. In the following equation, the generic Equation 7 has been modified to show the specific case of the NaF channel conductance in the DCN neuron model.

$$g = g_{\max} m^3 h \tag{10}$$

As in Equation 7, g_{max} denotes the maximum conductance of the channel (NaF); m, its activation variable; h, the inactivation variable. Equations 11 and 12 give the voltage dependence of the steady-state values of m and h:

$$m_\infty = \frac{1}{1 + \exp\frac{V + 45}{-7.3}} \tag{11}$$

$$h_\infty = \frac{1}{1 + \exp\frac{V + 42}{5.9}} \tag{12}$$

The suffix "$_\infty$" denotes that the steady-state value of the variable is given; V is the membrane potential in millivolts. Equations 11 and 12 are plotted in Figure 20 for a typical range of membrane potentials encountered in the DCN neuron model.

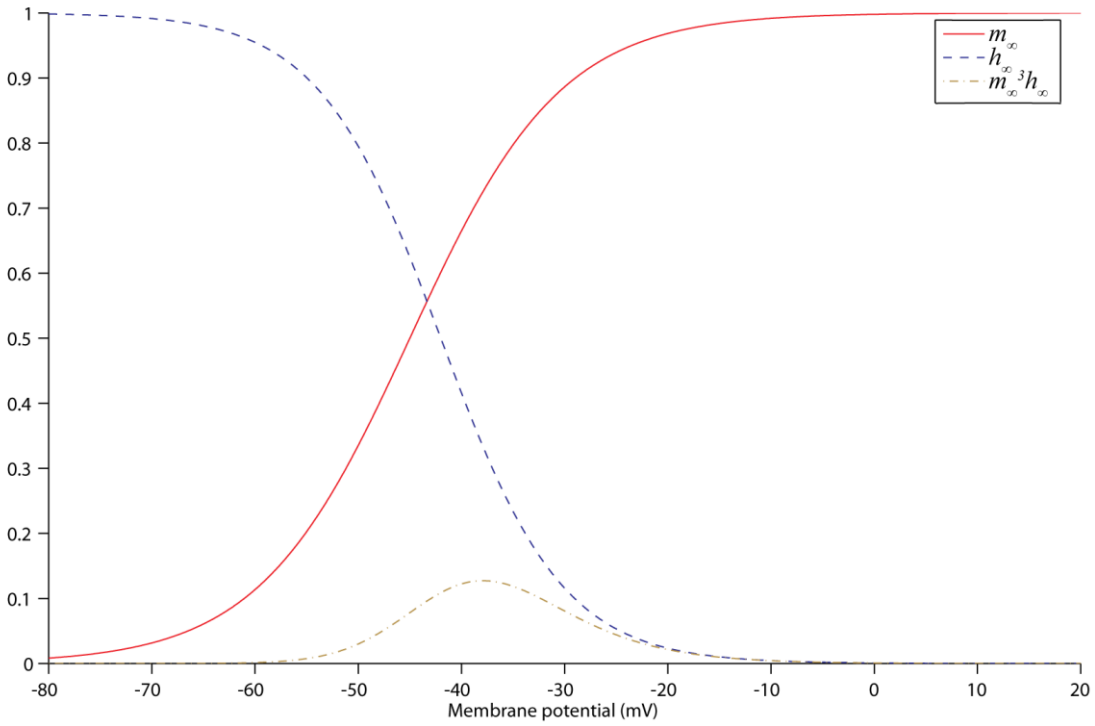

Figure 20 Steady-state values of the activation (m_∞) and inactivation (h_∞) variables of the NaF channel, plotted over the range of typical membrane potentials of the DCN neuron model. The third trace, $m_\infty^3 h_\infty$, gives the degree to which the channel can be persistently open to passage of sodium ions. Due to the longer time constant of the inactivation variable than that of the activation variable, much larger values of m^3h are obtained than those that $m_\infty^3 h_\infty$ reaches in the graph. Thus, during parts of an action potential, the NaF channel is more open to inflow than the up to 0.12 times of maximum conductance shown to be persistently possible for -38mV in the graph.

As described in Section 2.2, what drives current to pass through an ion channel is the difference between the membrane potential and the reversal potential of the ion species (V - E). With E_{Na} of the model being +71 mV, a strong driving force is exerted on the sodium ions to pass through the NaF channel when the membrane potential is close to its negative rest value, in line with what can be expected from an ion channel mechanism driving the action potential. As the gating expression of equation 10 opens the ion channel, the passing sodium

current brings the membrane potential to the height of the action potential – the "spike" in a voltage trace, as shown in Figure 21.

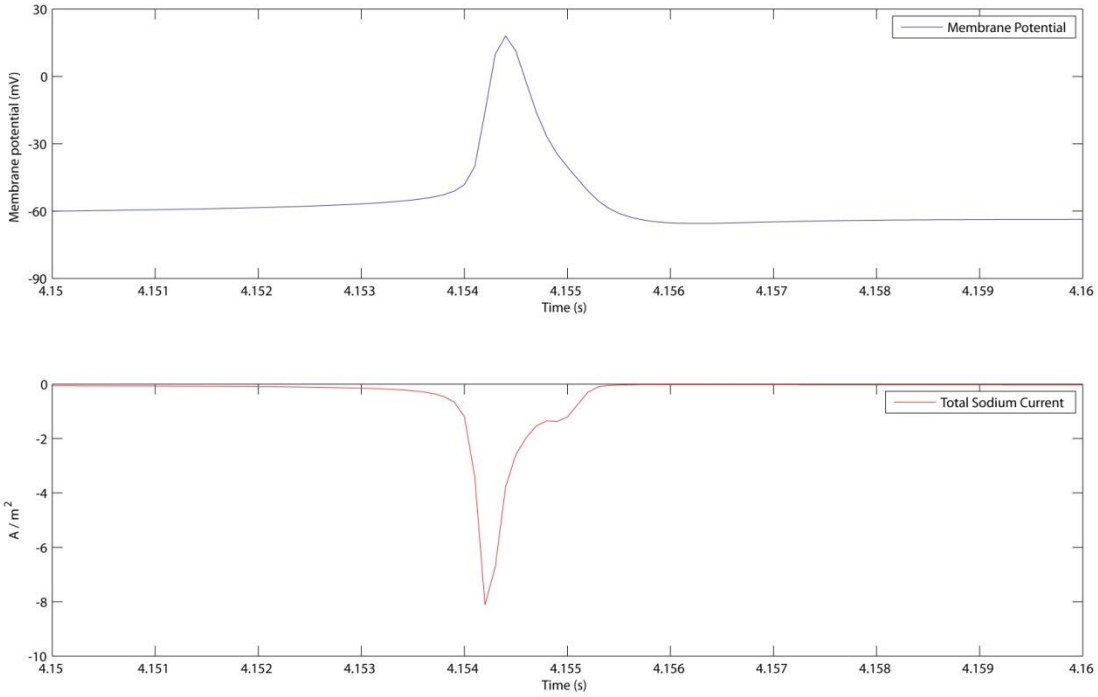

Figure 21 Action potential generation in the DCN neuron model, shown in the absence of synaptic inputs. The top trace shows the deflection of the membrane potential from the resting state at ca -60 mV to the action potential peak at ca 20 mV. The initial increase of the membrane potential is almost completely accounted for by the NaF current (see text). The repolarisation is caused by a combination of potassium channel mechanisms.

3.4 Constructing ion channel models in NEURON and GENESIS

This section describes how an ion channel mechanism can be created in the NEURON and GENESIS simulators. The NaF channel of the DCN model will again be used to illustrate the concepts.

NEURON contains a mechanism-description language, NMODL, which is a modified version of MODL [MOdel Description Language, (Kohn et al., 1994)]. NMODL is used for implementing the computation-intense mechanisms and is compiled before execution, in contrast to the language that describes the model morphology and run system, hoc, which is interpreted. The NaF channel implementation in NMODL is given in Syntax listing 1.

Syntax listing 1. The fast sodium channel (NaF) constructed in NEURON.

```
NEURON {
   SUFFIX NaF
   USEION na READ ena WRITE ina
...
}
BREAKPOINT {
   SOLVE states METHOD cnexp
   ina = gbar * m^3 *h * (v - ena)
}
DERIVATIVE states {
   rate(v)
   m' = (minf - m)/taum
   h' = (hinf - h)/tauh
}
PROCEDURE rate(v(mV)) {
   TABLE minf, taum, hinf, tauh  FROM -150 TO 100 WITH 300
   minf = 1 / (1 + exp((v + 45) / -7.3))
   hinf = 1 / (1 + exp((v + 42) / 5.9))
   ...
}
```

An NMODL mechanism starts with the `NEURON` block, where the names of ions used by the mechanism are specified. The example shows that the NaF channel uses the sodium ion (`USEION na`) and that it reads the reversal potential of sodium (`ena`; its value is set in hoc code elsewhere in the simulation code). Further, the `NEURON` block gives that the NaF channel writes to hoc the calculated value of the sodium current (`ina`) passing through the imaginary pore of the channel ("..." indicates code removed for brevity).

In the `BREAKPOINT` block the integration of the states of the simulation takes place; it is so called because hoc calls the attention of NMODL at each time step (25 μs in the NEURON model of the DCN neuron). The code in the `BREAKPOINT` block calls the `DERIVATIVE` block `states` where the activation and inactivation variables `m` and `h` are updated. The updating is done in the following steps:

1. The steady-state values, `minf` and `hinf`, are read in from the interpolated `TABLE` values calculated in the procedure `rate` at the outset of the simulation. In the code listing above it can be seen that the table contains the values of the steady-state variables at 300 equidistant values of membrane potential (v) between -150 and +100 mV.
2. The time constants, `taum` and `tauh`, at the given membrane potential are read in from a similar interpolated table.
3. The statements `m' = (minf - m)/taum` and the corresponding one for `h'` are calculated to give the present values of `m` and `h`. The expression `m'` takes the time step, Δt, of the simulation into account automatically and is thus the implementation in NEURON of Equation 9 (or a modified form of Equation 8 if another numerical integration scheme than Euler integration is used).
4. The channel current is calculated in the statement `ina = gbar * m^3 * h * (v - ena)`, using the new values of `m` and `h`.

The division by the time constants (`tau`) in the updating of the state variables sets the degree of inertia in the responsiveness of a channel to environmental changes (here, voltage). In the DCN neuron model, the time constants vary greatly between the channels, from a close to instantaneous response of NaF to changed membrane potential (the NaF activation time

constant is shorter than 0.1 ms at all voltages) to the magnitudes slower *h* channel (activation time constant is a constant 400 ms).

Channels in the GENESIS simulator language are part of the main simulation code; the GENESIS NaF channel code is given here, where the inactivation variables have been excluded for compactness:

Syntax listing 2. The NaF channel implementation in GENESIS.

```
create tabchannel NaF
setfield NaF Ek ENa Gbar Ginit Ik 0 Gk 0 Xpower 3 Ypower 1 Zpower 0

call NaF TABCREATE X tab_xdivs tab_xmin tab_xmax

x = tab_xmin
dx = (tab_xmax - tab_xmin)/tab_xdivs

for (i = 0; i <= tab_xdivs; i = i + 1)
    ...
    act = 1.0/(1.0 + exp (x + 0.045)/-0.007324)
    ...
    x = x + dx
end
...
call NaF TABFILL X tab_xfills 0
```

A notable difference is how in GENESIS the code loops explicitly over the values of v (usually given in volts in GENESIS, versus millivolts in NEURON) to assign values to the state variables, while in NEURON this looping is handled automatically with the `TABLE` statement. Another difference is how programming in GENESIS to a large extent relies on function calls to create functionality which in NEURON is coded directly in NMODL. An example in Syntax listing 2 is the call to `setfield`, giving values to the reversal potential of sodium (`Ek ENa`), the maximum conductance of the NaF channel (`Gbar Ginit`), and the exponents of the state variables (`Xpower`, etc).

4. Translation of the DCN neuron model

Note: part of this Chapter has been published as a technical report at the School of Computer Science, University of Hertfordshire (Luthman, 2008).

For the purpose of studying the behaviour of DCN neurons, a biophysically realistic computational model of a DCN neuron (Figure 17) was previously created in the GENESIS simulation environment based on the morphology and functional characteristics of DCN neurons in rats (Steuber et al., 2004; Steuber et al., 2010).

The DCN neuron model contains 517 compartments and ten ion channel mechanisms. An example of the correspondence of the GENESIS implementation of the model to DCN physiology is shown in Figure 22.

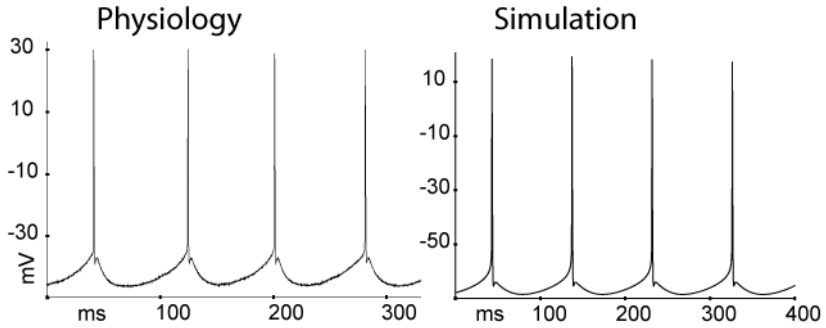

Figure 22 The behaviour of a typical DCN neuron in a brain slice experiment (left) compared to the behaviour of the simulation implemented in GENESIS (right), with spontaneous frequency of firing in both graphs in the range of 10-12 Hz. From Figure 1 in Steuber et al. (2010).

The GENESIS implementation of the DCN neuron model has been used to investigate the dependence of DCN neuron rebound firing on properties of

voltage-gated channels of the DCN neuron and on synaptic input patterns to the neuron (Steuber et al., 2010). In order to use the model for the purposes of the present thesis, the NEURON simulation environment was considered a more suitable one. NEURON allows easier implementation than GENESIS of STD and of the creation of several types of calcium pools, both of which were deemed essential for the thesis work. The importance of STD was discussed in previous chapters; the following section will discuss the need for an additional type of calcium pool.

4.1 Current-voltage relationships of ion channels

In Section 2.2, the current through an ion channel was described as a linear function of conductance and voltage (Equation 2). This is an approximation commonly used in modelling ion channels (Yamada et al., 1998), including the original Hodgkin-Huxley model (Hodgkin and Huxley, 1952) where it was used to accurately model sodium and potassium ion flows (Figure 19).

However, the assumption of a linear (Ohmic) relation between current and voltage is increasingly inaccurate as the ratios of extra- to intracellular ion concentrations increase (Hille, 2001, pp. 445-448). These ratios are up to ca 30 in mammalian neurons for the sodium, potassium, and chloride ions, while the calcium ion ratio is approximately one thousand times larger (Purves, 2004, p. 40). A more correct model for non-linear current-voltage relationships through ion channels was introduced by Goldman (1943) and Hodgkin and Katz (1949), with the Goldman-Hodgkin-Katz (GHK) current equation (Hille, 2001, p. 445):

$$I = p\frac{z^2F^2V}{RT}\frac{[\mathrm{X}]_i - [\mathrm{X}]_o\, exp\left(\frac{-zFV}{RT}\right)}{1 - exp\left(\frac{-zFV}{RT}\right)} \quad (13)$$

where p is the permeability of the ion (in meters/second; the permeability replaces the conductance, g, in Equation 2); z, the valence of the ion; F, the Faraday constant; V, the membrane potential; R, the gas constant; T, the absolute temperature; $[X]_i$, $[X]_o$ are the ion concentrations inside and outside the cell, respectively.

In analogy to the expression used to calculate the conductance in the standard version of the Hodgkin-Huxley model (Equation 7), the permeability can be calculated as the product of a maximal permeability p_{max} and the activation and inactivation variables m and h raised to their respective exponents a and b:

$$p = p_{max} m^a h^b \quad (14)$$

where p_{max} is the maximum conductance of the channel; m is the activation variable; h is the inactivation variable.

It is commonly accepted practice in the computational neuroscience community to use linear current – voltage relationships for modelling sodium, potassium, and chloride ion channels, while calcium channels are often modelled using the computationally more demanding GHK current equation (De Schutter and Smolen, 1998; Yamada et al., 1998). In order to be able to use the GHK formalism to model calcium channels, the internal calcium concentration that influences the channel current has to be calculated using an exponentially decaying calcium pool:

$$\frac{d[Ca^{2+}]}{dt} = I_{Ca} k_{Ca2+} - \frac{[Ca^{2+}] - [Ca^{2+}]_{base}}{\tau_{Ca^{2+}}} \quad (15)$$

where I_{ca} is the calcium current; k_{Ca2+} is a free parameter (tuned for the GENESIS DCN model and kept unchanged in the NEURON version); $[Ca^{2+}]_{base}$, the baseline calcium concentration; τ_{Ca2+}, the decay time constant.

The DCN neuron model channel functions include two calcium channel mechanisms, a low-voltage activated calcium channel (CaLVA) and a high-voltage activated calcium channel (CaHVA); see Table 1. Further, the small-conductance calcium-dependent potassium channel (SK) in the model is activated by the concentration of calcium in its vicinity. This calcium pool is controlled by the CaHVA channel while the CaLVA channel is assumed to be without influence on these membrane-close calcium ions (Alvina and Khodakhah, 2008).

In the GENESIS implementation of the DCN model, the CaHVA channel was modelled using the GHK current equation and coupled to a calcium pool that was linked to SK channel activation, while the CaLVA channel used the linear current equation and was not linked to any calcium pool.

With NEURON allowing the addition of a second calcium pool, the CaLVA channel was modified to use the GHK current equation too. Hence, the CaHVA and CaLVA channels had two separate calcium pool mechanisms so that the CaLVA-controlled calcium would not influence the SK channel conductance.

4.2 Overview of the process of translating the model

The translation of the DCN neuron model from GENESIS to NEURON and its modification followed these main steps:

1. Constructing the ion channels and the calcium concentration mechanisms from their mathematical descriptions.
2. Converting the DCN neuron morphology file from the GENESIS format to that of NEURON.
3. Incorporating the ion channels and the calcium concentration elements into the neuronal morphology.
4. Constructing synapses and synapse-stimulus elements followed by their incorporation in the morphology.
5. Updating the NEURON DCN neuron model.

Each of steps 1-4 was followed by testing to ensure the correct replication of the GENESIS model.

4.3 Construction of ion channels and calcium concentration mechanisms

The construction in NEURON of the channel mechanisms of the DCN neuron was done as described for the NaF channel in Section 3.4.

4.3.1 The ion channels of the DCN neuron model

The DCN neuron model incorporates ten ion channel mechanisms, listed in Table 1. The ten channel mechanisms model the experimentally observed DCN neuron currents; their presence in the model results in the reproduction of the physiological DCN neuron behaviour by the GENESIS simulation (cf. example shown in Figure 22).

Table 1 The ion channel mechanisms of the DCN neuron model. The first seven mechanisms are voltage gated channels, followed by the SK channel and the two passive currents pasDCN and TNC. The latter are not channels in the molecularly identified sense; instead, they correspond to the leak over the membrane, and a collectively modelled range of cation channel currents not accounted for by the other mechanisms. The gating expressions correspond to $m^a h^b$ in Equation 7.

Name of current	Abbreviation	Gating
Fast sodium current	NaF	m^3h
Persistent sodium current	NaP	m^3h
Fast delayed rectifier (potassium current)	fKdr	m^4
Slow delayed rectifier (potassium current)	sKdr	m^4
High-voltage-activated calcium current	CaHVA	m^3
Low-voltage-activated calcium current	CaLVA	m^2h
h current	h	m^2
Small-conductance calcium-dependent potassium current	SK	calcium concentration
Tonic non-specific cation current	TNC	none
Passive current	pasDCN	none

4.3.2 Conversion of the GENESIS morphology into NEURON format

The morphology code specifies the physical dimensions and three-dimensional locations of the compartments of the DCN neuron model and their grouping into different kinds of neuronal parts (soma, proximal/distal dendrites, axonal hillock, etc).

In GENESIS the morphology specification follows the following pattern, repeated for each compartment:

```
compartmentName parentCompartmentName  X  Y  Z  diameter
```

where parameters `X Y Z` specify the position of the end point of the added compartment (`compartmentName`) in the 3-dimensional morphology of the neuron. The start position of `compartmentName` is given by the end position of the parent compartment (`parentCompartmentName`). The shapes of all compartments in GENESIS are cylindrical, except the soma which can also be a sphere. In the GENESIS DCN neuron model, the morphology specification for the soma and one of the dendritic compartments connecting to the soma is:

```
soma  none  0  0  0  21.597
p1[1]  soma  -1.708  15.872  6.12  2.52
```

The soma is treated as the starting point of the neuron, with parent compartment given as `none`.

The GENESIS morphology file was converted into NEURON format using the program neuroConstruct version 1.01 (Gleeson et al., 2007). The visualisation of the GENESIS morphology imported into neuroConstruct is shown in Figure 23 along with the resulting NEURON morphology.

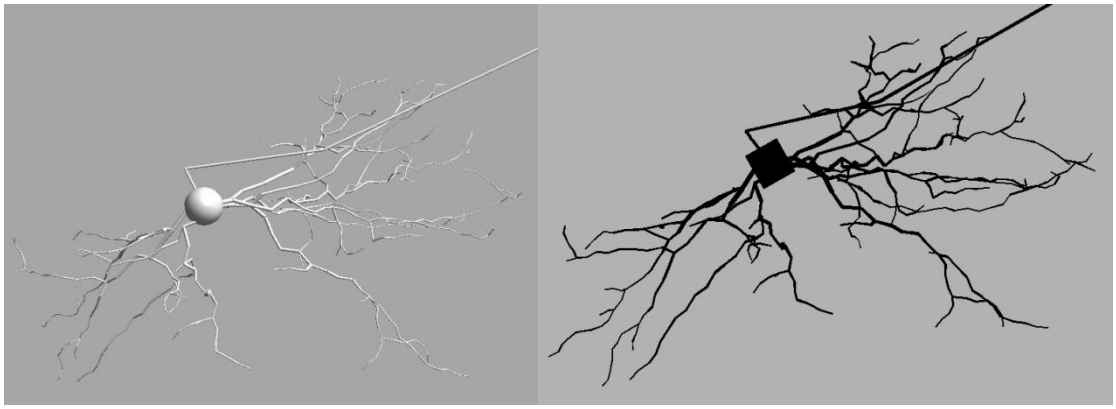

Figure 23 DCN neuron morphology, with the GENESIS morphology displayed in neuroConstruct to the left, and the exported NEURON format morphology, visualised in NEURON, on the right. Note the different shapes of the soma (middle of each picture).

The DCN neuron morphology was exported from neuroConstruct as NEURON hoc code. The following hoc code specifies the same morphology as the GENESIS example:

```
connect p1[1](0), soma(0.5)
soma pt3dadd(0, 0, 0, 21.597) pt3dadd(21.597, 0, 0, 21.597)
p1[0] pt3dadd(0, 0, 0, 2.52) pt3dadd(-1.708, 15.872, 6.12, 2.52)
```

The connection point between two compartments in NEURON can be set to any part of either of the two compartments, using the expression:

```
connect comp1(fractionOfLength), comp2(fractionOfLength)
```

Thus, from the given example, `connect p1[1](0), soma(0.5)` instructs NEURON to connect the beginning of dendrite `p1[1]` to the middle of `soma`.

The next line uses the `pt3dadd` command, which as in GENESIS gives X, Y, Z coordinates followed by the diameter of the compartment. In NEURON this is done twice, first for the position and diameter of the beginning of the compartment, followed by the same for the end.

The translation resulted in one obvious morphological difference. NEURON does not allow spherical compartments and neuroConstruct therefore

translated the soma as a cylinder with equal length and diameter. The cylindrical soma is shown with its side facing the viewer in Figure 23.

4.3.3 Inserting the channel mechanisms into the model

Each compartment of the model belongs to one of the groups in Table 2.

Table 2 Compartments of the DCN neuron model.

Compartment group	Compartments per group
soma	1
axon hillock	1
axon initial segment	10
axonal node	20
proximal dendritic	83
distal dendritic	402

Each of the groups in Table 2 contains a specific set of channels and channel conductances. The insertion of the channels in NEURON required their units to be changed. NEURON uses units commonly used in neurophysiology, for example millivolts and milliamperes/cm^2, while GENESIS allows any consistent set of units. In the GENESIS DCN neuron model, SI units were used throughout (volts and amperes/m^2 for the given NEURON examples).

A complication in the comparison of currents passing through the ion channel mechanisms in GENESIS and NEURON is that while NEURON gives current in units per area, GENESIS gives current in absolute units. Thus, when comparing currents between the two simulators, a correction factor had to be applied individually for each evaluated compartment based on its surface area.

4.3.4 Synaptic mechanisms

Synapses were constructed in NMODL in a manner similar to the one previously described for voltage and concentration gated ion channels. As for ion channels, GENESIS provides functions and objects that enable the creation of synapses (the `synchan` object) and their stimulus elements (the `timetable` and `spikegen` objects), while NEURON requires more programming but offers more flexibility, such as the ability to include STD. The synapses of the NEURON DCN model were constructed with most of their code based on the included `exp2syn` mechanism. The synapse mechanism responds to inputs from afferent neurons; these were created using the NEURON `NetStim` object which corresponds to `timetable` and `spikegen` in GENESIS.

The synapses of the model are located in the soma and the dendritic compartments. Of the inhibitory GABAergic synapses, originating from Purkinje cells, one synaptic mechanism is added to the soma and 400 to randomly selected dendritic compartments. The excitatory inputs to DCN neurons comprise three mechanisms: an AMPA channel, and fast and slow NMDA channel components. The model contains one excitatory synapse on the soma, and 100 on a group of randomly selected dendritic compartments.

The somatic synapses of the original DCN neuron model receive input at a 50 times higher frequency than the dendritic synapses. This is a computationally efficient way of creating the effect of the larger number of synapses that reach the much larger somatic compartment than the dendritic ones. The result is that the soma receives one third of all excitatory and one ninth of all inhibitory synaptic input to the DCN neuron model.

4.3.5 The run system of the NEURON model

The run system is the part of the NEURON model that differs most from GENESIS, with operations such as recording (of membrane potential, currents, state variables, etc), injections of current, and sending stimuli to synaptic compartments. The NEURON DCN neuron model run system was constructed to set up a simulation comprising the following main steps:

- The simulation start file *DCN_simulation.hoc* defines the number of phases of the simulation, the length of time of each phase and what it contains in the form of frequency of synaptic inputs and current injection strength (if any).
- *DCN_simulation.hoc* also defines what compartments to record from and what variables to record and then in turn loads the rest of the files: *DCN_morph.hoc*, *DCN_mechs.hoc*, *DCN_withoutgui.hoc*, and *DCN_recording.hoc*.
- *DCN_morph.hoc* contains the morphology and specifies the compartment groups.
- *DCN_mechs.hoc* inserts the NMODL mechanisms: ion channels, the calcium concentration element, synapses, and synapse-stimulus elements.
- *DCN_withoutgui.hoc* steps through the simulation, time step by time step, controlling when to record variables and save files, tasks it outsources to *DCN_recording.hoc*.

4.4 Results of the model translation

This section will assess the translated DCN neuron model, with a focus on comparisons between the behaviour of the GENESIS and NEURON

implementations. Features that will be evaluated include how the spike shape and spike trains compare and how the models respond to injected current. The behaviour of the model takes a few seconds to stabilise after a simulation is started: in the NEURON version of the DCN neuron model from directly after translation 5 seconds were required for perfect equilibration, while both the GENESIS and NEURON models reached firing rates within 2% of the final firing frequency after 2.5 seconds of equilibration. Analyses of simulation data in this thesis are based on the time following 4 seconds of initial equilibration time. The firing rates given in the ensuing evaluations are means of 15 seconds (i.e., from 4-19 seconds of the simulation output).

The spontaneous firing frequency in the model with no synaptic input and no current injection applied was 11.59 Hz in the translated model (NEURON), compared to 11.79 Hz in the GENESIS original, giving a difference of less than 2%. With 20 Hz excitatory and 40 Hz inhibitory background synaptic inputs, the NEURON model had a firing frequency of 19.45 Hz while the GENESIS model fired at 19.55 Hz (a difference of ca 0.5%).

4.4.1 Shape of spikes and spike trains

The shapes of spikes were correctly reproduced in the NEURON model and are shown in Figure 24.

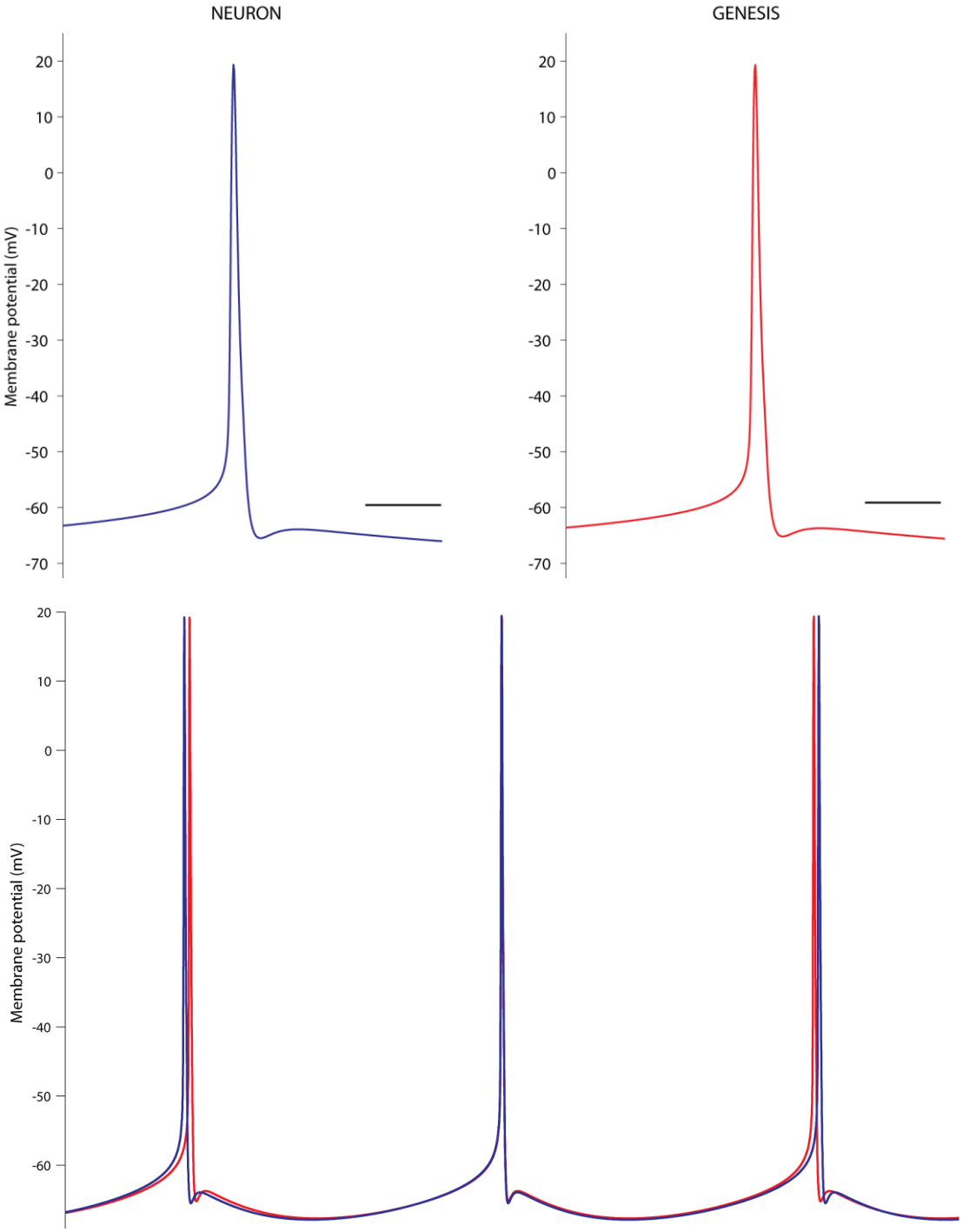

Figure 24 Spike shape on spontaneous firing in the NEURON and GENESIS versions of the DCN neuron model. The lower graph shows the overlay of the parts of the action potential and reveals a remaining 2% difference in spike rate between the models. The bar in the upper two figures indicates 5 milliseconds. Both simulators were set to use the Crank-Nicholson method of numeric integration with an integration time step of 25 µs in NEURON and 5 µs in GENESIS.

The spike shape of the original GENESIS spike, in turn, is a good replication of the physiological spike shape of DCN neurons as shown in Figure 22.

Spiking in the DCN neuron model without synapses was completely regular in both implementations, meaning that each interspike interval (ISI) had an equal length after the end of the initial equilibration period had been reached.

With background levels of synaptic inputs applied, typical spike trains from both implementations are shown in Figure 25.

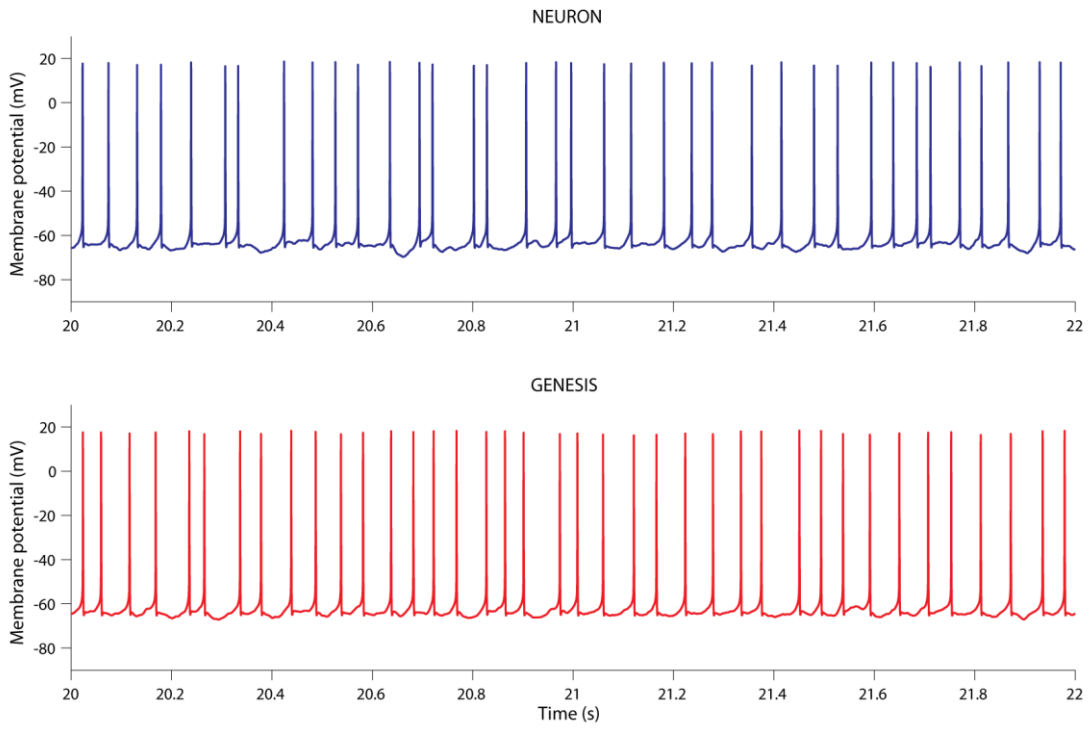

Figure 25 A sample 2-second spike train from the NEURON and GENESIS implementations of the DCN neuron model. The trains are from simulations with background synaptic input (at a level of 20 Hz excitatory and 30 Hz inhibitory inputs). The NEURON model features a firing frequency of 19.45 Hz while the GENESIS version fires at 19.55 Hz (averages of 100 seconds). The GENESIS spike train displays a smaller level of variability in the intervals between spikes (interspike intervals, ISIs), an observation which is confirmed by the ISI distribution plot of Figure 26.

While the average spiking rate of the neuron differed very little between the two models in the presence of synaptic input, the ISI distributions of the two models exhibited clear differences, shown in Figure 26.

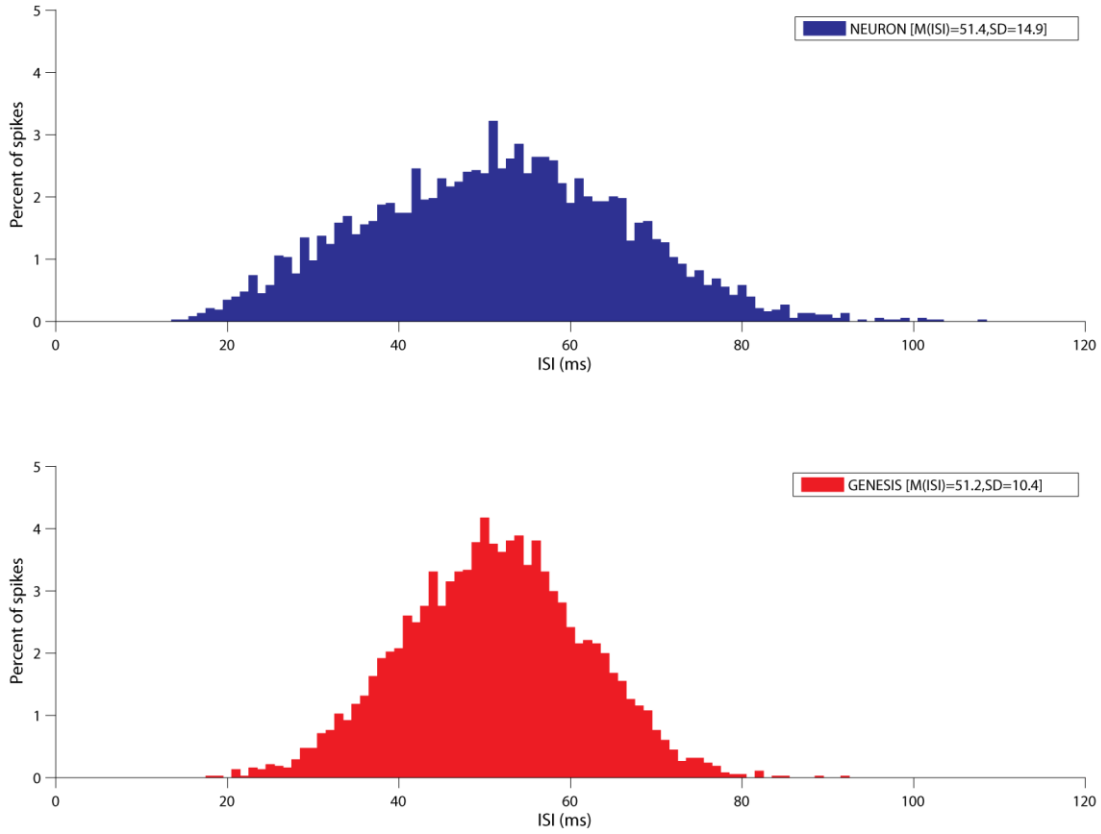

Figure 26 ISI distributions of the NEURON and GENESIS models with background synaptic input applied (20 Hz excitation and 30 Hz inhibition). The histograms show the percentage of ISIs in each 1-ms-bin, for each model based on a sample of ca 3800 spikes over 200 seconds. The ISI distribution of the NEURON model displays a larger standard deviation (14.9 ms) and a non-normal distribution (p-value = 0.002 in the Kolmogorov-Smirnov test for normality of distribution) compared to the GENESIS model's standard deviation of 10.4 ms and its normally distributed ISIs (Kolmogorov-Smirnov p-value > 0.2).

In contrast to the GENESIS model, the ISIs of the spikes fired by the NEURON version of the DCN model did not comprise a normal distribution (see caption to Figure 26 for test of normality). To investigate the cause for these

disparate distributions, the output of the synaptic stimulus elements provided by the simulators (`NetStim` in NEURON, `timetable` and `spikegen` in GENESIS) was analysed. The two synaptic stimulus elements, which generate the time series of input spikes that activate the synapses of the DCN neuron model, had clearly different ISI distributions as shown in Figure 27, below. The attempts to create a modified input-spike ISI distribution that resembles those found in vivo will be discussed in Section 4.5.7.

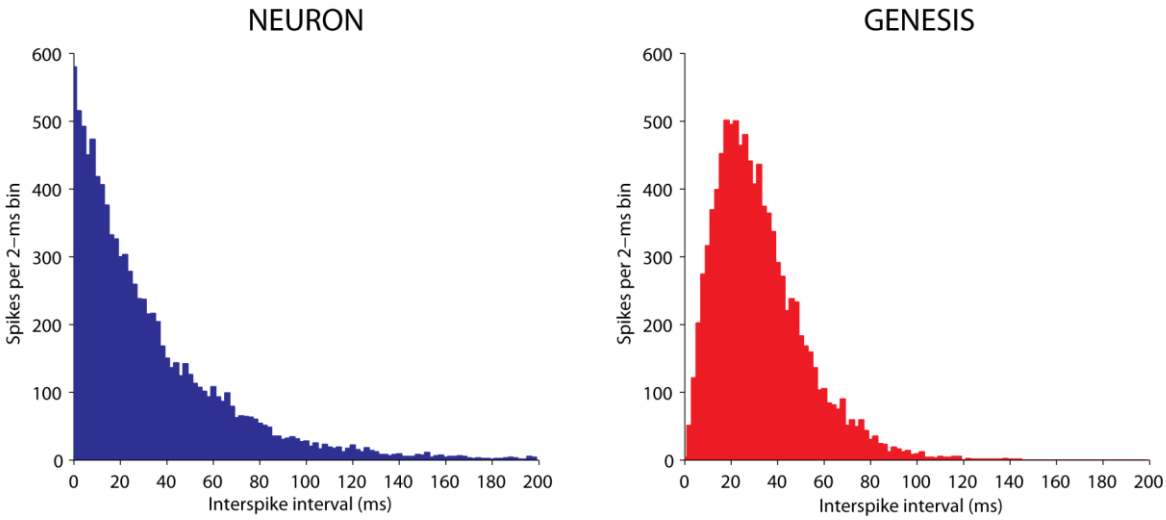

Figure 27 ISI distributions of 30 Hz inhibitory synaptic inputs to the GENESIS and NEURON models. The plotted data are based on ca 10000 input spikes to each model and show how the built-in NEURON synaptic input element, `NetStim`, produces Poisson-distributed inputs while the GENESIS DCN model uses a setting giving gamma distributed input spikes.

4.4.2 Rebound firing

Post-inhibitory rebound firing is a prominent feature of DCN neuron electrophysiology (2.7.1); its reproduction in the model is one of the metrics of successful modelling. Rebound responses comprise a combination of fast rebound bursts and/or slow and prolonged periods of accelerated spiking that are expressed to variable extents (Steuber et al., 2010). The shape of a slow and

prolonged rebound response in a DCN neuron in slice recording is shown in Figure 28, while a similar rebound spike train from each of the GENESIS and NEURON models is shown in Figure 29 (note that the latter shows 0.5 seconds while the recording spans 1.5 seconds, giving the recorded spike train a more compressed appearance than a same-scale comparison would show).

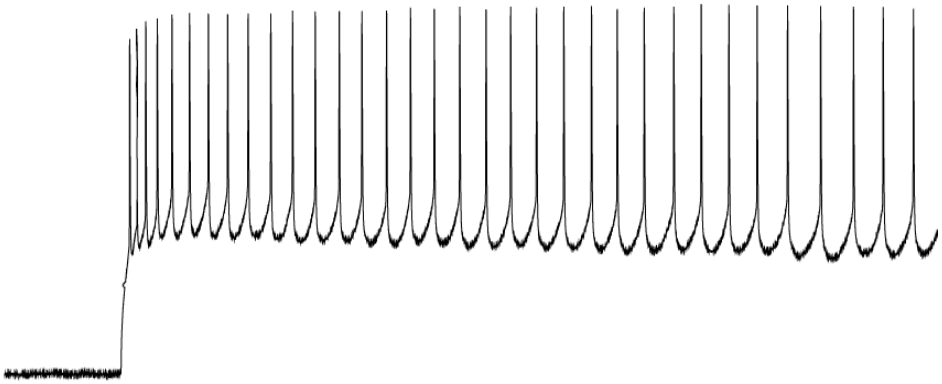

Figure 28 Rebound spike train recorded from a DCN neuron in a cerebellar slice, showing the end portion of 150pA of hyperpolarising current injection to the left. Total time displayed in the figure is 1.5 seconds. Adapted from a figure provided by Dieter Jaeger (unpublished data).

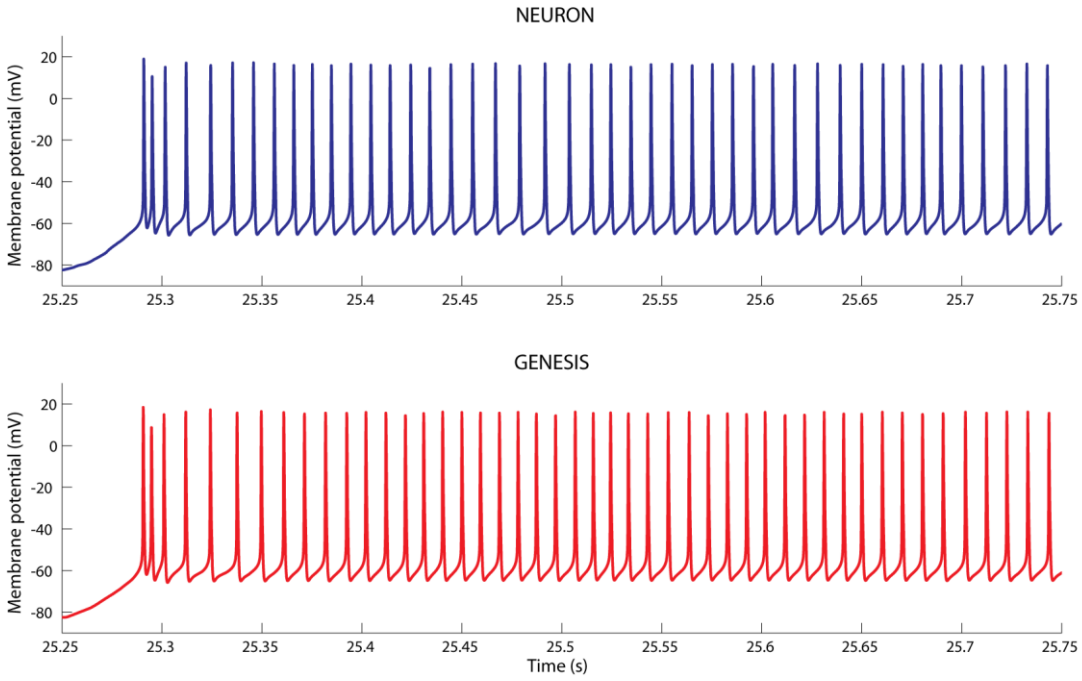

Figure 29 Rebound responses of the NEURON and GENESIS implementations of the DCN neuron model after the offset of 300 Hz of inhibitory synaptic input, showing good correspondence between the two models.

The spike trains of Figure 29 show a satisfactory reproduction of the GENESIS model behaviour in the NEURON translation, with the same triad of tightly spaced spikes followed by longer interspike intervals.

4.4.3 Response to current injection

Another electrophysiological signature of a neuron and thereby necessary to be replicated in a model is its response to current injection. The DCN neuron reacts to increasing levels of positive current injection by firing at increasing rates (Figure 30). The spike rate does not saturate for the range of input currents tested (<= 400 pA), but the f(I) curve resembles the initial part of a sigmoid, which is a commonly observed shape of f(I) curves in real neurons and computational models (see for example Silver, 2010). This response to current injection was well

reproduced in the NEURON translation, with a comparison to the original GENESIS model shown in Figure 31.

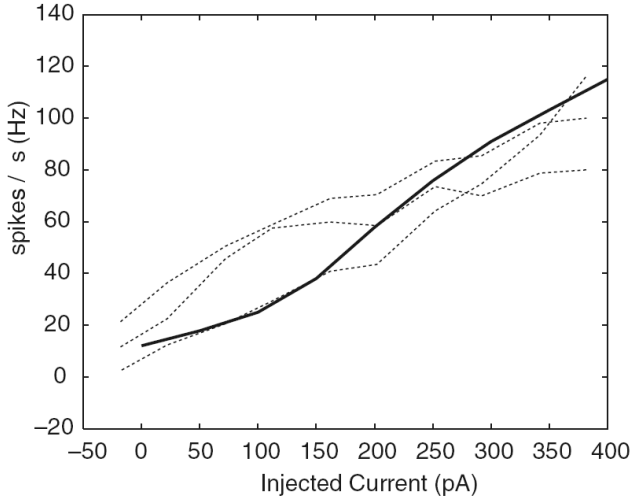

Figure 30 Spike rate in response to current injection into the soma of three DCN neurons (dotted lines) and the GENESIS DCN neuron model (solid line). From (Steuber et al., 2010).

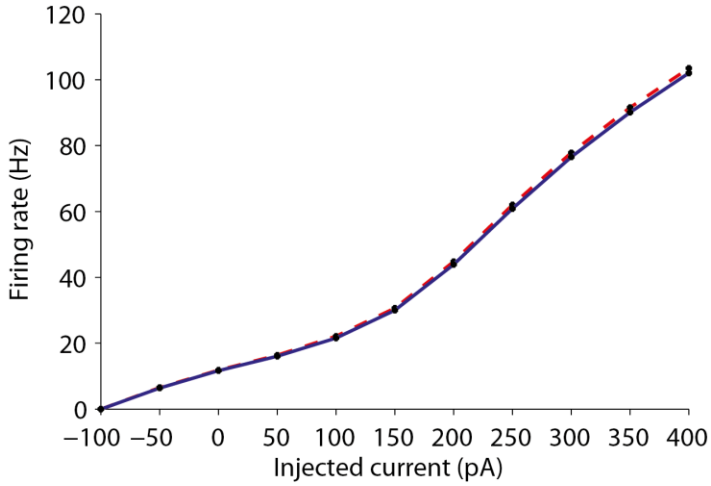

Figure 31 Spike rate in response to current injection into the soma of the DCN neuron model in GENESIS (dotted red line) and in the model after translation into NEURON. The time step of integration was 5 µs and the temperature was 32°C. The GENESIS result corresponds to the solid line of Figure 30.

4.4.4 Effect of integration time step

The length of the time step of integration (Δt) determines the time required to execute a simulation in a directly proportional fashion. While this gives a motivation for using a long Δt, the degree to which the results of a simulation correspond to the exact mathematical descriptions of the modelled mechanisms decreases upon lengthening Δt (Carnevale and Hines, 2006, p 64).

The original DCN model in GENESIS used Δt = 5 μs. The spontaneous firing rate resulting from varying Δt was investigated in the two models, and is presented in Figure 32. Surprisingly, decreasing Δt from the default value of 25 μs down to 1 μs resulted in a slightly larger rather than smaller difference in spontaneous firing rate between the two models. 25 μs was used as the time step of integration in all subsequent NEURON simulations of this thesis.

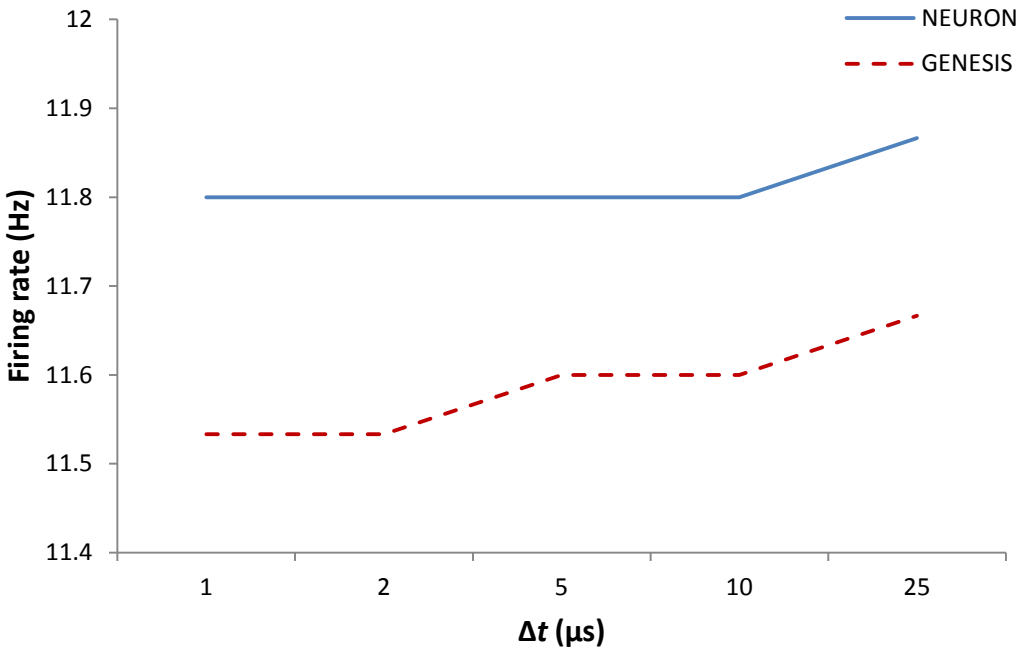

Figure 32 Spontaneous firing rate of the GENESIS and NEURON models as a function of the integration time step, Δ*t*. Note how the results of the GENESIS simulation are more susceptible to changes in Δ*t*, while the firing frequency of the NEURON model remains stable for values of Δ*t* between 1 and 10 μs. Crank-Nicholson integration was used in both models.

4.4.5 Fidelity of reproduction

I have shown how the translated model reproduces several important characteristics of the original DCN neuron model to a satisfactory degree. These metrics include the spike shape, firing frequency with and without background levels of synaptic input and over a range of current injections, and rebound spike train characteristics.

Up to two percent difference in firing rate remained between the models. Several rounds of meticulous proof-reading of the code and of testing of currents, ion concentrations, and state variables from a range of different compartments

failed to reveal any remaining differences in the mathematical descriptions of the models.

Differences in how the simulators compute membrane potential and other variables may account for the remaining differences, although the same numerical integration method has been chosen for the two models (Crank-Nicholson). The GENESIS model uses compartment type `compartment` where the axial resistivity is located at one side of each compartment. The alternative method, dividing the axial resistivity into two components on either side of the midpoint of the compartment, is the only way it can be done in NEURON (De Schutter and Steuber, 2001). This is an additional possible source for the small difference between the two DCN neuron models.

4.5 Modifications to the translated model

The introduction to this chapter discussed the main reasons for the translation of the DCN neuron model to the NEURON simulator. These and additional features to be modified or added are listed in Table 3.

Table 3 Modifications and additions to the translated DCN NEURON model.

- Synaptic short-term depression (STD)
- Calcium channel currents
- Temperature adjustments to run simulations at in vivo temperature
- Synaptic input with gamma distributed spike trains, including the provision of a refractory period
- $GABA_A$ receptor synaptic input from Purkinje cell spike train files
- Synaptic strengths, numbers and activation rates
- Adjusted DCN neuron model output to that of DCN neurons recorded in vivo

The remainder of Section 4.5 will describe briefly how the changes listed in Table 3 were made. “DCN neuron model” hereafter denotes the NEURON version of the model.

4.5.1 STD

The experimental data on STD at the PC-DCN synapse by (Pedroarena and Schwarz, 2003) were mathematically described and modelled by Shin et al. (2007a). In their model, the synaptic depression is assumed to be caused by a decreased probability of presynaptic transmitter release; the steady-state release probability and the ensuing synaptic conductance at different Purkinje cell firing frequencies were shown in Figure 2.

The STD model from Shin et al. was incorporated into the DCN neuron model, using the following equations to calculate the release probability for each input spike n.

$$R_{ss}(r) = 0.08 + 0.60e^{-2.84r} + 0.32e^{-0.02r} \tag{16}$$

$$\tau(r) = 2 + 2500e^{-0.274r} + 100e^{-0.022r} \tag{17}$$

$$R_n = R_{n-1} + (R_{ss} - R_{n-1})(1 - e^{-\frac{ISI_n}{\tau}}) \tag{18}$$

where r is the instantaneous firing rate (in Hz) calculated as the inverse of the preceding interspike interval; R_{n-1} is the release probability for the previous spike; ISI_n is the interspike interval (in ms) between the present spike and the preceding spike; R_{ss} is the steady-state release probability; and τ is the time constant of depression, given in ms.

The computed release probability R_n is used in the DCN neuron model as a scaling factor applied to the synaptic conductance for each input spike. For example, this gives a synaptic conductance of 0.42 times the maximum conductance at regular 1 Hz Purkinje cell firing, and 0.18 times the maximum conductance at 60 Hz (compare with Figure 2).

4.5.2 Modifying calcium channel currents

The change to use the GHK current equation for calculation of current of all calcium channels was implemented with one additional calcium concentration element (CalConc.mod) and a modified CaLVA channel, where the linear current-voltage relationship was changed to use the GHK current equation (Equation 13).

The comparison between the new and old model versions showed no difference. In the presence of background synaptic input (20 Hz excitatory and 30 Hz inhibitory) the DCN neuron firing rates were 20.20 Hz in both versions.

4.5.3 Adjusted kinetics to give physiological behaviour at 37°C

The original GENESIS model was constructed to replicate experimental data obtained in electrophysiology experiments in cerebellar slices performed at 32°C (Steuber et al., 2010). The model used a temperature adjustment mechanism for the voltage-gated channel kinetics with a Q10 of 3, which means that a temperature change of 10 degrees Celsius alters the speed of ion channel gating three-fold (Hille, 2001, page 51). The rise and fall time constants of synaptic channels were not provided with temperature adjustment in the original DCN neuron model.

The aim in this thesis work was to reproduce in vivo neuronal behaviour and therefore to run simulations at 37°C. The DCN neuron model was therefore

modified so that in addition to utilising the same level of temperature adjustment as the GENESIS original, temperature adjustments were added for synaptic channel gating, conductances of all channels and synapses, as well as calcium concentration kinetics. The Q10 of synaptic rise and decay constants was set to 2 based on measurements of temperature sensitivity of the kinetics of inhibitory (Otis and Mody, 1992) and excitatory (Silver et al., 1996) synapses. Conductances are less temperature sensitive than gating kinetics and the conductances of the DCN model were given a Q10 of 1.4, in the middle of the experimentally determined range (Hille, 2001, page 51). Finally, the calcium concentration pools were set to use Q10 = 2. No data on calcium concentration temperature response was found in the published literature; the used value is based on the reasoning that calcium concentration is affected by changes in actions of protein pumps (plausibly with a Q10 in the range of that of channel gating) and by changes in diffusion of the ion species (with a Q10 as of conductances).

4.5.4 Synaptic input with gamma distributed spike trains

Figure 27 showed how the synaptic input in the NEURON model differed from the synaptic input to the GENESIS version; while the former was initially provided by a Poisson process, the latter constituted a higher-order gamma function.

Since Purkinje cell spiking has been quantified to be of gamma order 3.4 (Shin et al., 2007b) the GENESIS model synaptic input was the better match. It was created using the `timetable` object in GENESIS, allowing the setting of synaptic input to a gamma distribution of integer order 1 to 6. The synaptic input generator in NEURON, `NetStim`, can only generate Poisson distributed spikes. Hence, I translated the code of `timetable` from GENESIS and added it as a new mechanism in NEURON: `GammaStim`; this mechanism was uploaded to the

computational neuroscience tools repository, which is part of the ModelDB database curated at senselab.med.yale.edu. Like the GENESIS original, GammaStim can be set to integer gamma orders 1-6. The DCN neuron model used GammaStim with order 3, both for Purkinje cell inputs and for the excitatory mossy fibre inputs.

Another functionality added with GammaStim compared with NetStim is the ability to specify a refractory period between spikes. This was set to a default of 1 ms which has been used for all simulations where a different refractory period is not explicitly given. The inhibitory inputs to the DCN neuron model replicate Purkinje cell firing, which has been shown to be faithfully transmitted down the Purkinje cell axon at a maximum of ca 300 Hz (Monsivais et al., 2005), corresponding to a refractory period of ca 3 ms. Due to the gamma shape of the input distribution, few spike intervals reach below this value when the GammaStim is set to a refractory period of 1 ms; the de facto minimum spike interval in a sample of 1000 input spikes was 2.42 ms at an input spike rate of 30 and 1.84 ms at 50 Hz.

4.5.5 $GABA_A$ receptor synaptic input from Purkinje cell spike train files

For the research projects described in Chapters 5 and 6, it was necessary to be able to use recordings from real Purkinje cells from electrophysiology experiments and from the Purkinje cell model (De Schutter and Bower, 1994b, a).

This functionality was added to the DCN neuron model run system so that up to 450 different spike train files could be read in from a repository of spike trains on the computer running the simulations.

4.5.6 Modified synaptic strengths, numbers and activation rates

The conductances and firing rates of excitatory inputs to the model were kept as in the default setup of the GENESIS version, with 20 Hz excitatory firing. In the original model the synapses to the soma were modelled as one excitatory and one inhibitory synapse, each sped up 50 times compared to the dendritic synapses, yet with the same maximum conductances. While this was computationally efficient, it created close to tonic excitatory and inhibitory input currents. To make this more realistic, in the NEURON version of the model the single excitatory and inhibitory synapses were replaced by 50 synapses each, which were activated at the same rate as the dendritic synapses.

The peak conductance of the $GABA_A$ synapses was drastically increased from the GENESIS model to reflect more recent experimental data (Telgkamp et al., 2004). While Steuber et al. (2010) used $GABA_A$ synaptic conductances in the range of 50 to 200 pS, I set the peak $GABA_A$ conductance to 1.6 nS at 32°C which corresponded to 1.89 nS at the used simulation temperature, 37°C (applying a Q10 of 1.4, see Section 4.5.3). Yet, since the DCN neuron model in GENESIS did not use STD, in that model the actual conductance resulting from an input spike equalled the peak conductance, while in the new $GABA_A$ synapse with STD (Section 4.5.1) the actual conductance was computed for each input according to Equations 16 to 18. Hence the actual conductances depended on the input rate prior to each spike and effectively never reached the peak conductance. Table 4 shows how the actual conductance in the modified DCN neuron model depends on the firing rate, for an input where each interspike interval has the same length (i.e., the input is completely regular).

Table 4 Conductance of $GABA_A$ synapses of the modified DCN neuron model with short-term depression (STD) applied. STD makes the conductance generated by a synaptic input depend on the prior input rate whereas in the GENESIS version each input to the $GABA_A$ synapse created the same conductance. The data in the table are for a peak conductance of 1.89 nS and for inputs with completely regular interspike intervals.

Input rate (Hz)	Conductance (pS)
0.1	1.61×10^3
1	810
10	646
100	233

The reversal potential for the inhibitory inputs is that of the chloride ion that $GABA_A$ receptor channels are selective for; it was changed from -90 mV of the NEURON model directly after translation to -75 mV for all subsequent simulations (Jahnsen, 1986b; Llinas and Muhlethaler, 1988; Morishita and Sastry, 1996; Alvina et al., 2008). The inhibitory input rate was set to a default 40 spikes per second, reflecting the available data on adult rats (Savio and Tempia, 1985; Stratton et al., 1988; LeDoux and Lorden, 2002).

4.5.7 Adjusting the DCN neuron model output to that of DCN neurons recorded in vivo

A literature review revealed two published ISI distributions of in vivo recordings from DCN neurons at spontaneous firing, one from cats (Figure 5 B in Delgado-Garcia and Gruart, 2002) and one from the rat strain (Sprague-Dawley) the DCN neuron model is based on (Figure 2 B in Rowland and Jaeger, 2005).

The ISI distribution of the rat DCN neuron is shown in Figure 33 and is highly similar to the distribution of ISIs in the cat (not shown).

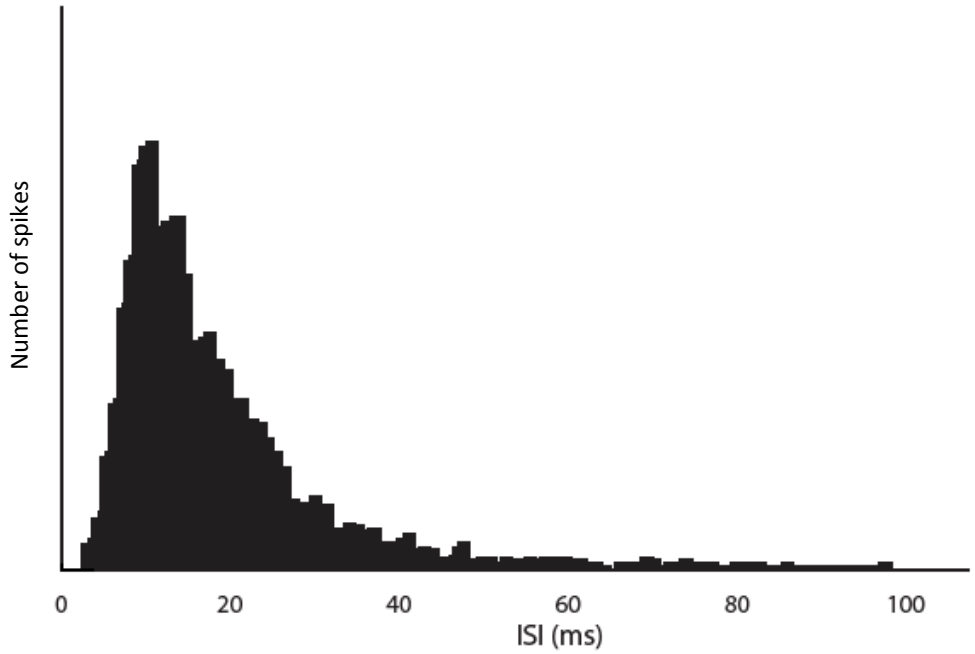

Figure 33 Interspike interval distribution of a spontaneously firing DCN neuron in vivo (Figure 2 B in Rowland and Jaeger, 2005). Compare this distribution with the ISI distributions in the two versions of the DCN neuron model (Figure 26 in Section 4.4.1).

The result of the steps described above was a DCN neuron model output with a firing rate of 50.1 Hz (ISI = 19.9) and an ISI distribution with a gamma order of 6.7 (mean of 11 trains of 20 seconds each). An example ISI distribution of one of the 20 s spike trains that were used to calculate the mean firing rate and gamma order is shown in Figure 34.

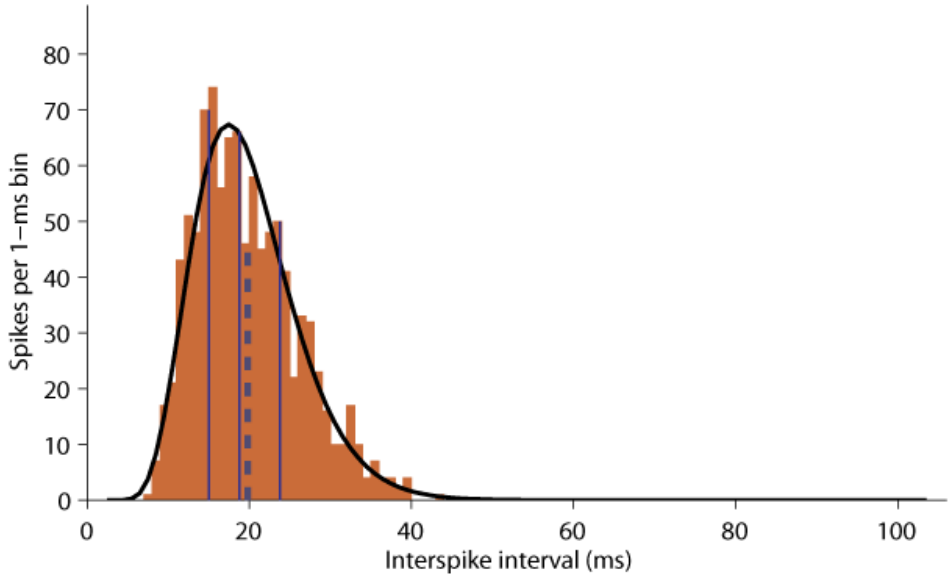

Figure 34 ISI distribution of a 20 second train of the DCN neuron model after introducing the modifications described in Section 4.5. The mean ISI is 19.8 ms (dotted vertical line) and the modelled gamma probability density function is of order 7.05. The solid vertical lines show the quartiles of the distribution.

4.6 Spiking behaviour after modifications

Following the changes detailed above, the firing rate in the absence of synaptic inputs was 26.5 Hz. The response curve to current injections remained slightly sigmoid (Figure 35); the shapes of spikes and spike trains were slightly altered compared to the original model with a shallower interspike hyperpolarisation Figure 36.

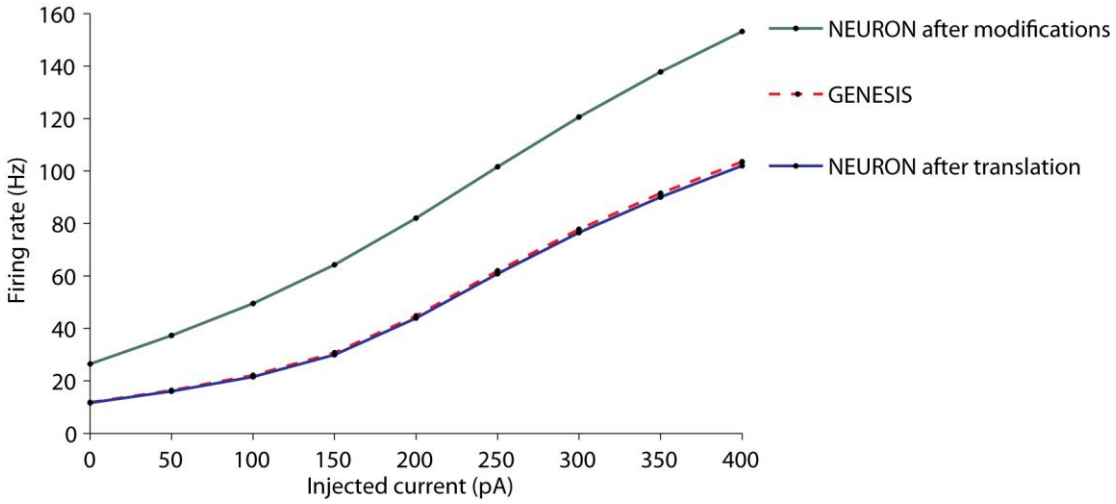

Figure 35 Spike rate in response to current injection into the soma of the DCN neuron model in GENESIS (dotted red line), NEURON directly after translation (blue) and in NEURON after modifications (green). The integration time step was 25 µs in the post-modifications NEURON case and 5 µs in the NEURON version after translation as in GENESIS. The lower two lines of the graph are replicas from Figure 31.

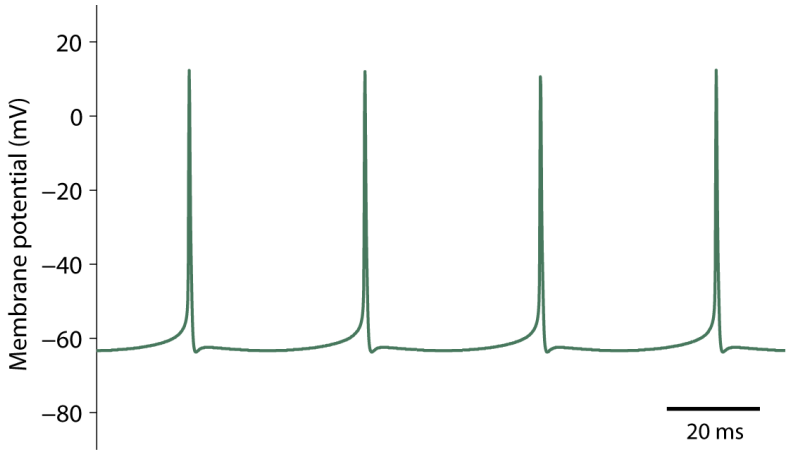

Figure 36 Spontaneous firing of the DCN neuron model after modifications were incorporated. The firing rate increased to 26.5 Hz from 11.6 Hz in the model directly after translation; this was almost exclusively a result of running the simulations at 37°C instead of 32°C (comparison not shown).

The default excitatory synaptic input rate was kept at 20 Hz; together with the increased inhibitory default rate of 40 Hz and the new default temperature of 37°C, the DCN neuron fired at 50.3 Hz (mean of ten 15-second trains; all synaptic inputs were individually randomised). This result reached the above stated goal of producing in vivo firing rates of DCN neurons, replicating the mean of 50 Hz discussed in Section 2.7.1.

4.6.1 No effect of modified calcium kinetics

The lack of effect of the modified CaLVA channel kinetics (Section 4.5.2) on the baseline firing rate was surprising. As mentioned in Section 4.1, the consensus in the field of computational modelling of neurons is that the Goldman-Hodgkin-Katz (GHK) current equation is required for correct modelling of calcium currents. Since the CaLVA channel is involved in rebound firing, I wanted to evaluate the effect of the changed kinetics on such firing. The mean currents at baseline firing of the old and new channels were set to be identical, but if a difference in behaviour of the channel would be seen during rebound firing, the case for using the GHK channel would be strengthened.

Figure 37 shows the CaLVA current inflow to the soma of the DCN neuron model in simulations of rebound, using (left) the original CaLVA model with linear current-voltage response, versus the new GHK current equation (right). While the currents have different shapes, especially during the first rebound spikes, there is no change in the overall number of spikes in the rebound phase. Combined with the lack of changed firing rate at baseline firing, it appears unlikely that the CaLVA channel modifications play any role in the setup of the DCN neuron model used in this thesis.

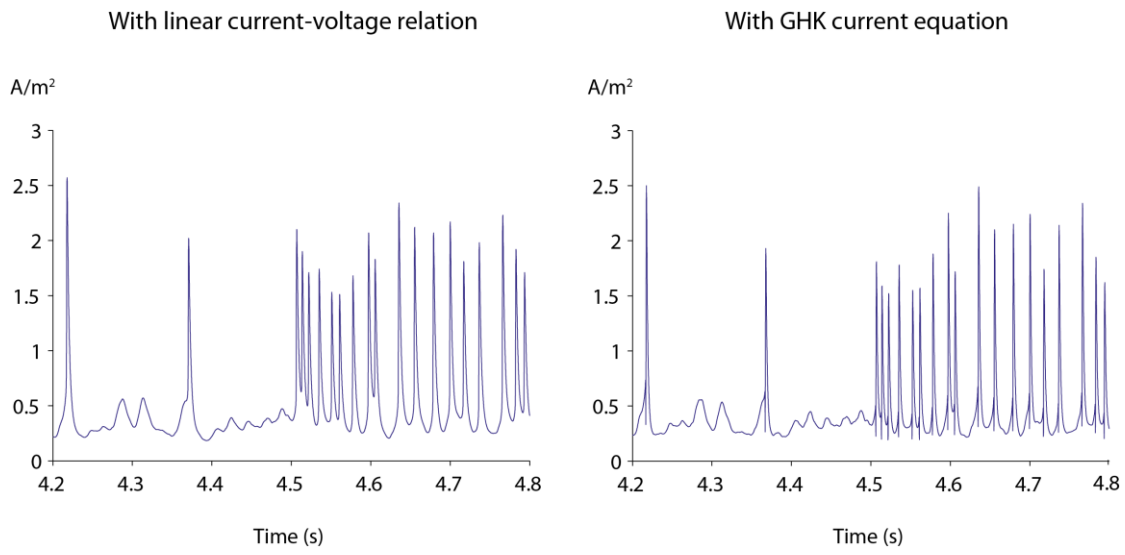

Figure 37 CaLVA channel current during rebound firing. The graphs show the current going through the CaLVA channel in the DCN neuron model soma during high-frequency inhibitory input (150 Hz, from 4 to 4.5 seconds) to the DCN neuron model followed by the return to baseline inhibitory input (40 Hz). The excitatory input remained constant at 20 Hz.

5. Pattern recognition by Purkinje cells and DCN neurons

The computations performed by the cerebellum remain poorly understood. As discussed in Section 2.7.4, a main theory of cerebellar function is the Marr-Albus theory, which predicts a central role for the parallel fibre to Purkinje cell synapses (PF-PC synapses) in storing information. This assumption is tested in the work on cerebellar pattern recognition that will be presented in

this chapter. The investigation involves several steps following the initial modelling of presentation of parallel fibre patterns to Purkinje cells. To simplify the understanding of the project, the flow chart in Figure 1 summarises the main steps of the work.

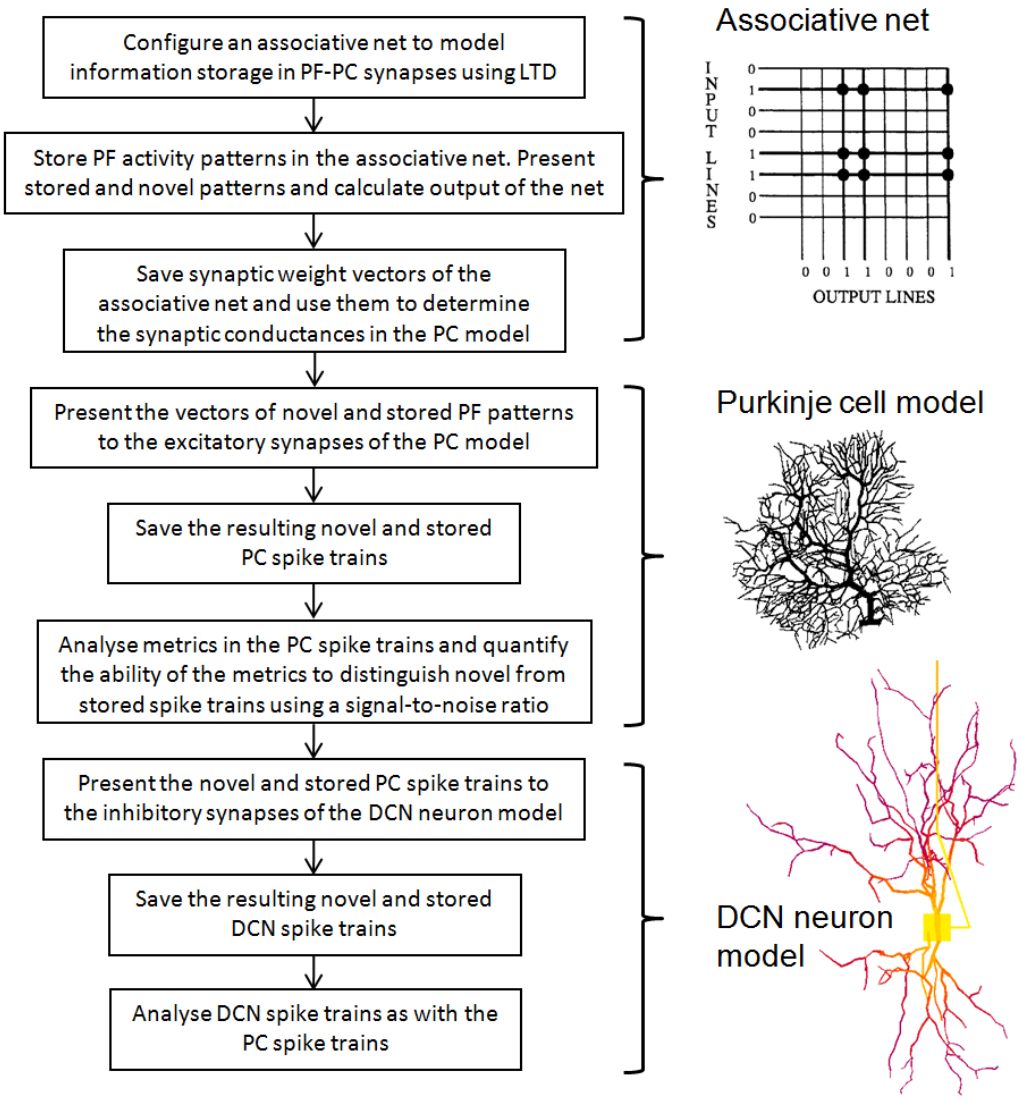

Figure 38 Work flow for the pattern recognition simulations of the present thesis. The performed work is summarised in the boxes to the left and will be presented in detail in the remainder of the chapter. The figures to the right show the locations in the modelled network where the steps to the left were taken. Compare with the outline of the cerebellar circuitry shown in Figure 9 in Section 2.7.

5.1 Past studies of cerebellar pattern recognition

5.1.1 Models of associative memory in cerebellar cortex

The Marr-Albus theory of cerebellar computation has been explored in previous computer simulations. One early example is the work of Tyrrell and Willshaw (1992) where the Marr-Albus theory was implemented and compared to an associative net.

An associative net (Willshaw et al., 1969) is a type of artificial neural network which has the ability to detect and remember simultaneously active inputs and outputs, making it function as a pattern recognition device. The principles of its operation are shown and explained in Figure 39.

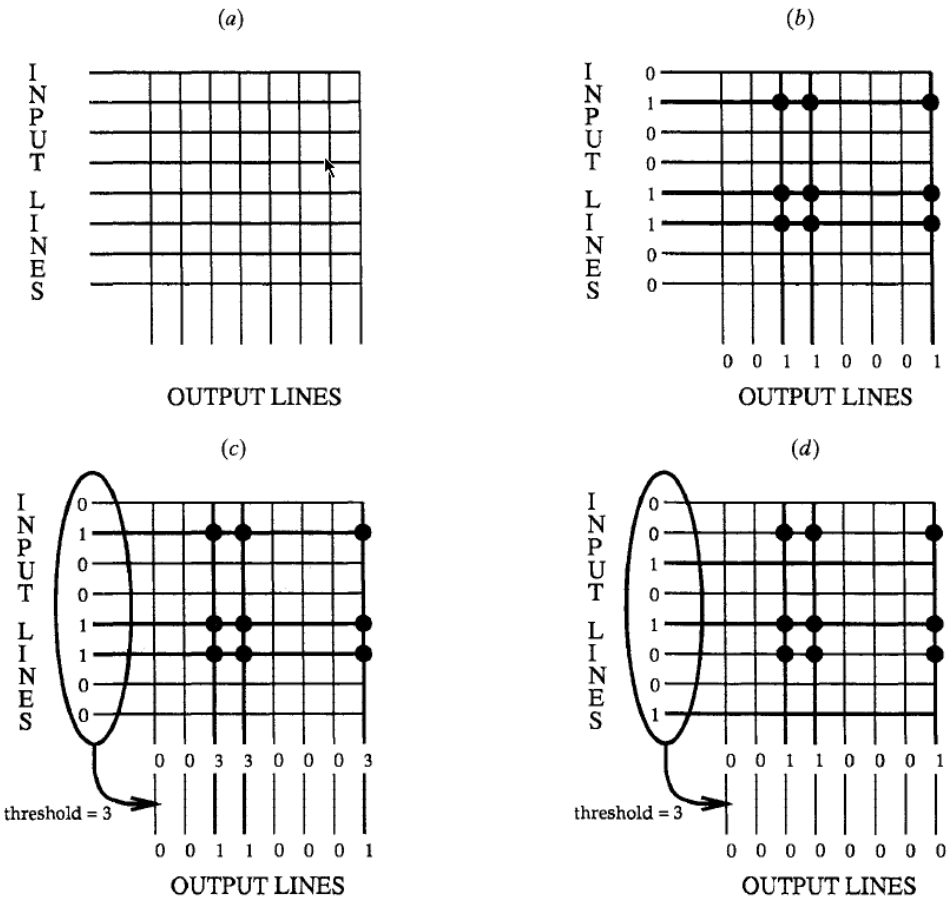

Figure 39 The principles of an associative net. (a) The initial state where no learning has taken place. (b) learning mode: inputs and outputs are presented and the intersections between active inputs and outputs are switched on. (c) and (d) show the retrieval mode, where in (c) the re-presentation of the learned input pattern activates the output lines, whereas in (d) the presentation of a novel pattern does not. Although three output units receive input through an intersection that has been switched on in (d), the threshold is not reached since it is set to the sum of the active input lines. From Tyrrell and Willshaw (1992).

Tyrrell and Willshaw (1992) argue that the Marr-Albus theory can be seen as the representation of the cerebellar cortex as an associative net, where the parallel fibres (PFs) constitute the input lines; the Purkinje cells the output lines; the PF-PC synapses the nodes (intersections) of the net; and the climbing fibres the signal to invoke the learning mode.

Tyrrell and Willshaw created a simulation of the circuitry of the cerebellar cortex based on the Marr-Albus theory. Their results show that the Purkinje cell may be able to distinguish with low error levels approximately one hundred different patterns presented along its parallel fibre input lines. These parallel fibre input patterns involved the activation of 1% of PF-PC synapses; learning in the synapses was coded as a binary event where synapses had weight 0 initially and were set to 1 during learning (Figure 38).

5.1.2 A simple model of cerebellar pattern recognition based on LTD

Steuber and De Schutter (2001) developed a more biologically realistic associative net based on depressing synapses, and they compared pattern recognition in this associative net with results from a Purkinje cell model with a passive soma which did not contain any voltage-gated ion channels and could therefore not generate action potentials. The synaptic strengths of the associative net were set to 1 initially and were halved each time LTD was induced. The principles of the construction of the net was the same as that used for the associative net used in this thesis and will be described in detail in Sections 5.2.1 and 5.2.2. During the learning phase, the net was presented with varying numbers of patterns that the system was instructed to store; this is illustrated schematically in Figure 40. During the recall phase, the net was then presented with the same stored patterns and an equal number of novel patterns, and the responses of the output unit were calculated as inner products of the pattern vectors and the synaptic weight vector.

The weight vectors that resulted from storing the patterns based on the LTD learning rule were saved and used to determine the PF synaptic conductances of a passive soma version of the biophysically realistic Purkinje cell

model (PC model) of De Schutter and Bower (1994a, b). This simulation system consisted of the PC model receiving 147,400 PF-PC synapses, which were synchronously activated by vectors corresponding to novel and stored patterns presented to the associative net. The effect on the model of the pattern presentations was evaluated by measuring the voltage responses in its soma. The main findings of this study were that the associative net outperformed the Purkinje cell model by more than an order of magnitude, and that pattern recognition in the Purkinje cell model benefitted from the presence of active ion channels in the dendrites, which amplified the difference of voltage responses to stored and novel patterns.

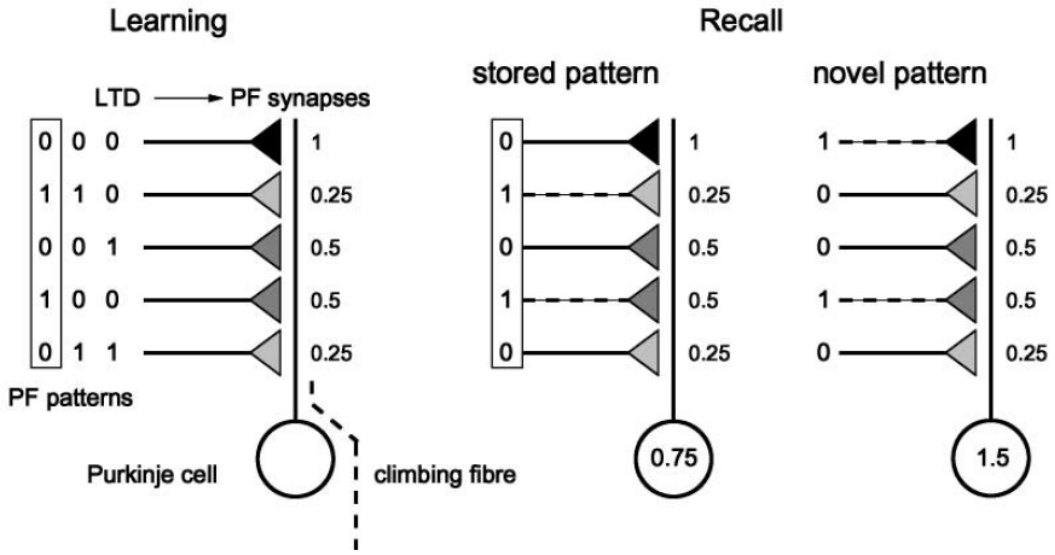

Figure 40 The type of associative net underlying the pattern recognition simulations in this thesis. The illustrations show how a set of five synapses store and retrieve information presented via activity of the parallel fibres. Leftmost, three different patterns are presented to the system, resulting in from zero to two halvings of the synaptic strengths depending on the number of times the synapses receive input. The middle part shows the re-presentation of one of the three patterns, giving a depressed response (summed weight = 0.75) compared to the novel pattern (rightmost) that produces a summed weight of 1.5. From Steuber and De Schutter (2001).

5.1.3 Pauses in Purkinje cell firing are shown to contain information

The work on pattern recognition by Purkinje cells with a passive soma by Steuber and De Schutter (2001) was extended to a more biologically realistic Purkinje cell model with an active soma by Steuber et al. (2007). The results of presenting novel and stored patterns to the active-soma PC model showed that the most sensitive metric for pattern recognition by the Purkinje cell was the length of a pause in firing that followed the PF inputs. Stored patterns gave a shorter pause than the novel ones, in spite of the higher excitatory strength of the

novel patterns. Pause length was thereby identified as a new type of neuronal coding feature. Figure 41 shows the differential pause responses to a set of novel and stored patterns in Steuber et al. (2007). Parenthetically, I will use the term "stored pattern" rather than "learned pattern", so as not to imply an assumption of intention on behalf of the system.

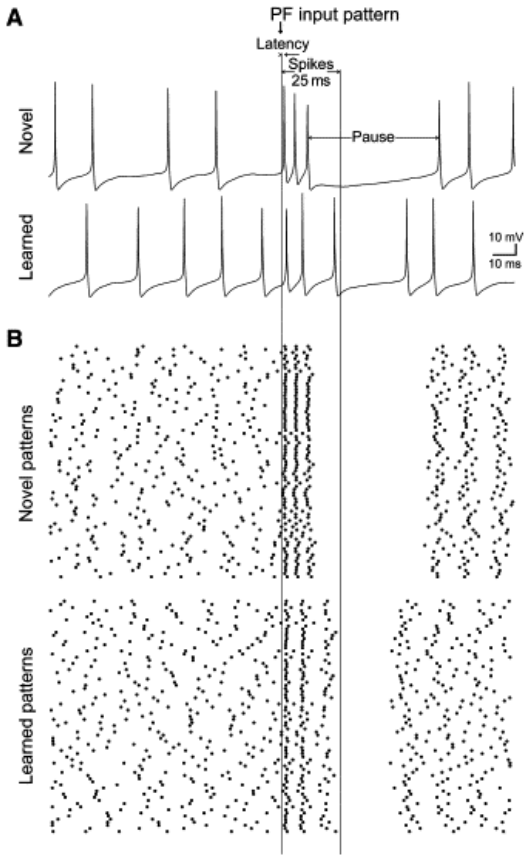

Figure 41 Purkinje cell firing patterns resulting from stored ("learned" in the Figure) and novel patterns. The most characteristic change in Purkinje cell firing on recognition of a stored pattern was found in the length of pause (see top of the picture for the metrics). The recognition of stored patterns led to shorter pauses than those resulting from novel patterns. From Steuber et al. (2007)

The pattern recognition results in the PC model were intriguing and raised the follow-up question of how these differential pause lengths affect the targets of

the Purkinje cells in the cerebellar nuclei. For this thesis the issue was investigated by the creation of a network model where up to 450 instances of one of three different PC models were connected to the DCN neuron model. The responses to the inputs of novel and stored patterns, respectively, to the Purkinje cells were analysed primarily on the DCN level; comparisons with the pattern recognition capability of the PC models were made where deemed interesting.

5.2 Modelling of PC pattern recognition in this thesis

The PC model was used as in Steuber et al. (2007), with a few modifications. These included the change of the inhibitory inputs to the model to be no longer tonic: the 1000 Hz inhibition to the soma of the Purkinje cell of Steuber et al. (2007) was here reduced to 1 Hz, with a concomitant increase of the peak inhibitory synaptic conductances by a factor of 1000. Thus, in the simulations for this thesis, the original PC model inhibitory synaptic conductance of 7 mS/cm^2 was used ("Stellate cell synapses" in De Schutter and Bower, 1994b). The reason for this change was that Purkinje cell output rates could not be titrated with 1000 Hz inhibitory input; this will be described in detail in Section 5.2.8.

All simulations were run at 37°C as in the original PC model.

5.2.1 The configuration of the associative net

The associative net was constructed as in Steuber and De Schutter (2001) and Steuber et al. (2007). As in these studies, the assumption is that patterns of activity among the circa 150,000 actual PF inputs to the Purkinje cell are stored in the values of the conductances of the PF-PC synapses. The storage mechanism

is long-term depression where each time a pattern is stored, conductances of all activated synapses halve.

The full version of the original PC model contained 147,400 spines where each spine head received one PF-PC synapse. While this number of spines was biologically realistic, it was computationally expensive and was simplified to a version where only 1% of spines were explicitly modelled, giving a total of 1474 spines (De Schutter and Bower, 1994b). Steuber et al. (2007) showed that the pattern recognition results of such a simplified model were indistinguishable from those of the full model. During pattern presentation, the PF-PC synapses received a synchronised burst of activity with input strength determined by a 1474-entry vector. The following section will explain how these vectors resulted from the presentation of patterns to the associative net.

5.2.2 Pattern recognition in the associative net

As in the previous studies, simulations to create the PF activity vectors were based on the Marr-Albus theory, which predicts sparseness of coding in the PF-PC synapses. Marr (1969) estimated that a minimum of 0.25% of PF-PC synapses would need to be active for the pattern they make up to be read out by the Purkinje cell, and that the mean number of PFs being active in a pattern must be much closer to that minimum than to the total number of PFs. Accepting a 1% error rate, he predicted that the Purkinje cell could learn to respond to 240 different patterns if a pattern would be made up of the activation of 0.5% of all PF-PC synapses; at 1% activation, the number of patterns would be 119.

The PF-PC synapses were modelled as a vector of size 147,400 where each entry was set to an initial weight of 1 (unitless). PF activity was likewise modelled as a vector of size 147,400 where all entries were set to an initial level of 0. A subset of these entries was activated, modelled by setting them to 1. The default

number of active entries was 1000 (0.7% of PFs); 1000 simultaneously active PFs were previously found to give optimal pattern recognition by the passive soma PC model (Steuber and De Schutter, 2001), and this number will be used in the following explanation. 100 of such PF activity vectors were presented to the synapses in the learning mode, giving a halving of synaptic strength each time at each synapse that received an input (Figure 40, left). In the subsequent retrieval stage, each of these stored patterns was presented to the now modified synapses. The strength of the excitatory effect of a pattern was now given by the inner product of its PF activity vector and the synaptic weight vector; i.e., each of the entries of the PF activity vector (1000 ones, 146,400 zeros) was multiplied by the corresponding synaptic weight (ranging from a theoretical minimum of 0.5^{100} for a synapse that has received input from all 100 patterns, to the maximum being the original weight of 1).

Another 100 PF activity vectors were created with 1000 randomly selected entries set to 1. These vectors were only presented to the synapses in the retrieval mode; they constitute the "novel" patterns.

For the application of these 147,400-entry vectors to the PC model with 1474 spines, the entry-wise products were summed in clusters of 100 each, giving a total of 1474 activation values for each pattern; these vectors will be called final PF activity vectors. For the above given number of 1000 active PFs, a final PF activity vector containing a novel pattern yields a theoretical maximum sum of its entries of 1000, which would be reached if neither of the corresponding PF-PC synapses were depressed by any of the 100 stored patterns. Similarly, the maximum sum of entries of a final PF activity vector of stored patterns would be 500, reached if no synapse was activated by more than one pattern during the learning phase. The actual mean sum of the 100 novel vectors was 712 and for the

stored patterns, 357, resulting from approximately half of all synapses having been included in at least two patterns.

5.2.3 Evaluation of pattern recognition capability

The ability of the associative net to distinguish between novel and stored patterns given by the PF activity vectors was quantified by the calculation of signal-to-noise ratios (Dayan and Willshaw, 1991). These are commonly abbreviated S/Ns or SNRs; the latter will be the choice here to avoid confusion with the subscripts *s* (for stored) and *n* (novel):

$$SNR = \frac{2(\mu_s - \mu_n)^2}{\sigma_s^{\,2} + \sigma_n^{\,2}} \tag{19}$$

where μ_s and μ_n are the population means and σ_s^2 and σ_n^2 the population variances of responses to stored and novel patterns, respectively. For the example with the associative net above, SNR $\approx 2.2\times10^3$.

In the case where the metrics of novel and stored patterns belong to two normal distributions with equal variance, Equation 19 can be rewritten as:

$$SNR = \frac{(\mu_s - \mu_n)^2}{\sigma_{sn}^{\,2}} \tag{20}$$

where σ_{sn}^2 is the variance of the distributions. The probability of correct discrimination (P_c) can now be calculated with the cumulative normal distribution function, which gives (Schultz, 2007):

$$P_c = \frac{1}{2}\left[1 + erf\sqrt{\frac{SNR}{8}}\right] \tag{21}$$

where SNR is the signal-to-noise ratio and *erf* is the error function:

$$erf(x) = \frac{2}{\sqrt{\pi}} \int_0^x e^{-t^2} dt \quad (22)$$

However, not all metrics used for discriminating between novel and stored patterns in this thesis will be normally distributed. With that caveat, the probabilities of correct discrimination for different signal-to-noise ratios are given in Table 5, calculated from Equations 21 and 22.

Table 5 Probability of correct discrimination for different signal-to-noise ratios in a classification task where the incidence of the desired case is 0.5. The symbols SNR and P_c are from Equation 21.

Signal-to-noise ratio (SNR)	Probability of correct discrimination (P_c)
0	0.5
0.3	0.608
1	0.692
3	0.807
10	0.943
30	0.997
50	0.9998

5.2.4 Biological significance of signal-to-noise ratios

The size of the signal-to-noise ratio (Equation 19) is influenced on one hand by the size of the numerator, which depends on the difference of means between the groups; on the other hand, it depends on the denominator, which depends on their corresponding variances. Hence, a large signal-to-noise ratio can be achieved in the extremes by either a large difference in means or small

variances. Considering the inherent noise in biological computing, a very small difference of means is unlikely to carry a relevant signal. For this reason, I will at times present the numerator and denominator of the signal-to-noise ratio in addition to the actual signal-to-noise ratios, where this is needed to understand the likely biological significance of the pattern readouts. The numerator and denominator values will be normalised in a way similar to that done when the coefficient of variation is calculated from a standard deviation: The normalised signal-to-noise numerator and denominator are their raw values divided by the square of the sum of the means of the underlying novel and stored data.

5.2.5 Pattern presentation to the Purkinje cell

The following will explain how the final PF activity vectors were presented to the Purkinje cell in the Steuber et al. (2007) work; the few modifications made for this thesis will be introduced in the next section.

The patterns constituted by the PF activity vectors were synchronously presented to the Purkinje cell, superposed on the background excitatory input. The default excitatory background input to the Purkinje cell was 28 Hz, providing an average of $1{,}474 \times 28 \approx 41{,}000$ input spikes per second. Each input spike activated an AMPA receptor peak conductance $g_0 = 0.7$ nS, while the presentation of a PF activity vector induced peak conductances equal to the elements of the PF activity vectors multiplied by g_0. Hence, for the final PF activity vectors described above, this induced a total AMPA receptor conductance at the time of the pattern presentation averaging 712 input spikes for novel patterns, and 357 spikes for stored patterns, plus an average of 0.8 background spikes for both patterns.

The effects of this input on the Purkinje cell action potential generation was shown in Figure 41 from the work by Steuber et al. (2007). The rest of the present chapter builds on that work by exploring the effects of the PC model

pattern recognition on the DCN neuron model and by exploring pattern recognition by the Purkinje cell and DCN neuron models in networks with spontaneously firing versions of the PC model. The first step in this work was the construction of new, spontaneously active, PC models.

5.2.6 Methodology of creating a spontaneously active PC model

The original PC model did not fire in the absence of synaptic inputs, that is, it was not spontaneously active; however, since it was constructed it has been found that a large majority of Purkinje cells are spontaneously active (Hausser and Clark, 1997; Raman and Bean, 1997). There has been criticism of the Steuber et al. (2007) work based on the lack of spontaneous activity in the PC model (Walter and Khodakhah, 2009), where the authors argue that spontaneous activity of Purkinje cells may be incompatible with efficient pattern recognition. Based on that criticism and the advantage of showing the ability of pattern recognition to exist in alternative biophysically realistic PC models, I created a range of PC models, in the simulator GENESIS, with the original morphology but with modified electric properties that resulted in model variants with spontaneous background firing. The term background firing will be used to refer to the output of the model prior to pattern presentation.

Neuronal models are most often the result of parameter searches within wide ranges of values for constants such as peak ion channel conductances. Often, as with the Purkinje cell, lack of precise and consistent experimental data makes this a reasonable methodology and that is therefore how I proceeded to create a spontaneously firing PC model. The following will describe the main steps of that work; all values of Purkinje cell output variables will refer to their steady-state after three seconds of simulation.

The initial attempt to render the model spontaneously active was made by making the reversal potential of the leak current less negative from its original value of -80 mV. The constant flow of the leak current acts to hyperpolarise the cell membrane; with a less negative reversal potential, the reduced strength of the leak current could be assumed to allow the membrane potential to reach the action potential threshold more often and thereby give increased spiking. Indeed, this modification made the PC model spontaneously active, but either at too fast (> 100 Hz) or too slow (15-20 Hz) rates of firing compared to the rates measured in vitro of ca 50 Hz (for example, Raman and Bean, 1997).

Continuing the methodology of modifying one parameter at a time, I changed several ion channel conductances without causing the firing rate to reach values close to the 50 Hz target rate. For that reason, I changed strategy to perform a combinatorial search where I simultaneously changed up to seven different ion channel conductances together with membrane resistance and leak conductance. Several thousands of combinations were examined. Where published data on Purkinje cell firing characteristics in vitro differed from those of the original model, criteria were based on reproducing the in vitro behaviour rather than that of the original model. Metrics included the response to injected current and to channel blockers, the firing rate in the soma, the level of dendritic excitability, and the lowest membrane potential reached during the spike cycle. Of crucial importance was to eliminate doublet spiking. This repetitive pairing of spikes within a few milliseconds is not a feature of real Purkinje cells and its presence was the cause of failure for the majority of the tested combinations.

5.2.7 Evaluating the in vitro behaviour of the PC models

The lowest possible spontaneous firing rate in a model fulfilling these requirements was 74 Hz, placing it at approximately the 75th percentile of firing

rates of Purkinje cells in vitro (Raman and Bean, 1997). Two spontaneously firing models were chosen for use in pattern recognition simulations; their properties are given in Table 6.

Table 6 Properties of the PC models used in the pattern recognition simulations of this thesis. *non_spontPC* is the original model (De Schutter and Bower, 1994a); *spontPC* and *spontPC_2* are the two spontaneously firing models used in the pattern recognition project of the thesis.

Model name	non_spontPC	spontPC	spontPC_2
Spontaneous firing rate	N/A	73.8	74.6
Firing rate (Hz) with 28 Hz excitatory + 1 Hz inhibitory input	91.9	56.6	59.6
Membrane resistance of soma (Ω m^2)	1	1	0.9
Initialisation membrane potential (mV)	-55	-60	-60
Reversal potential of leak channel mechanism (mV)	-80	-77	-77
Peak ion channel conductances of soma compartment (S/m^2)			
Fast sodium current (NaF)	75,000	72,000	65,000
Slow sodium current (NaP)	10	40	40
Delayed rectifier (Kdr)	6,000	7,500	8,000
Persistent potassium current (KM)	0.4	8	10
A current (KA)	150	600	750
P-type calcium current (CaP)	45	46	45

The response to current injections of various amplitudes gives the f(I) curve of a neuron, where firing rate is plotted as a function of the current injected into the soma compartment, in the absence of synaptic input to the neuron.

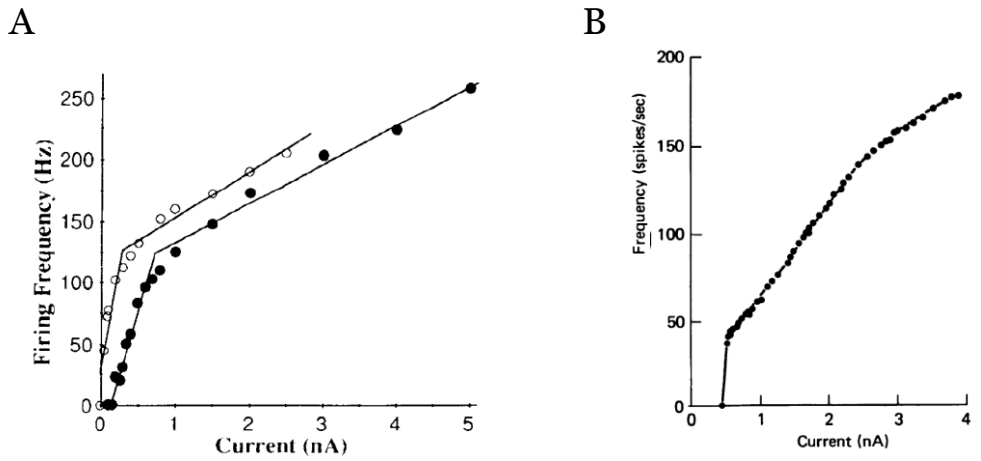

Figure 42 Purkinje cell firing rate response to current injection in the soma. (A) Two PC models with different ion channel conductances, rendering them differently responsive to current injection; neither is spontaneously active. The filled circles are the version that has been used in this thesis with the name non_spontPC. From De Schutter and Bower (1994a). (B) In vitro experiments underlying the models of (A). From Llinas and Sugimori (1980).

The f(I) curves of the original PC model (Figure 42, A) plot the firing rates in the interval 300-700 ms of the simulations (De Schutter and Bower, 1994a). In analysing the behaviour of the model, I noticed that the simulations did not reach equilibrium until later; see for example Figure 43, where the injection of 1.5 nA into the soma of the original PC model results in burst firing only after ca 500 ms. At injections below 1.5 nA no burst firing resulted but stable firing rates were not reached until after approximately 1 second of simulated neuronal time for all examined current values. Therefore the interval of 4-15 seconds was used to construct the f(I) curves in this thesis, with results shown in Figure 44.

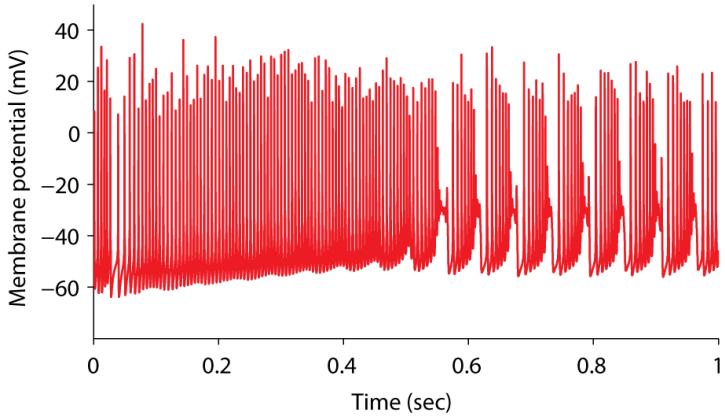

Figure 43 Current injection into the soma of the original PC model (non_spontPC). Injection of 1.5 nA shows how burst firing begins at ca 500 ms. The metrics for the f(I) curves in (Figure 44) are based on the interval of 4-15 seconds (not displayed).

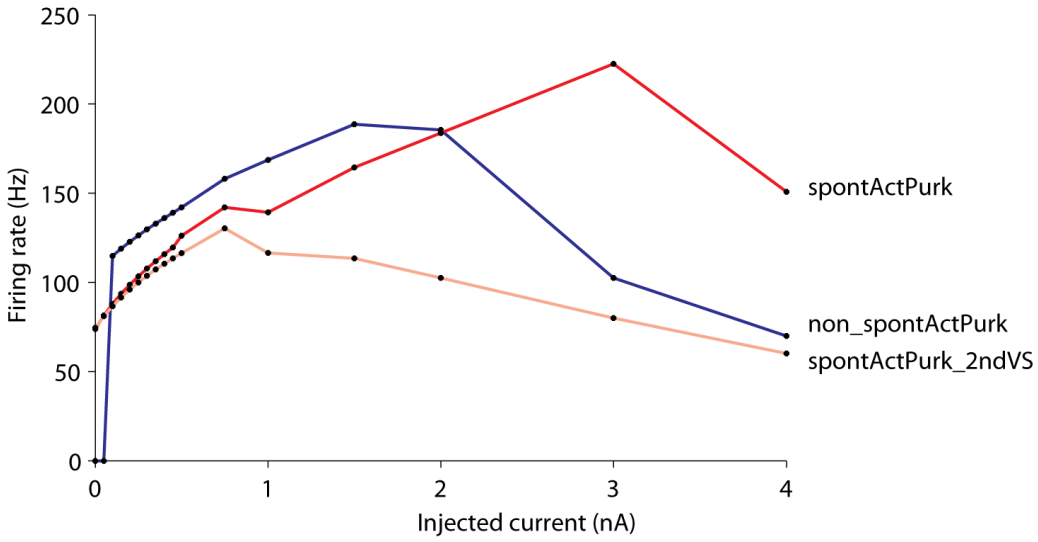

Figure 44 The three versions of PC models used in the pattern recognition work of this thesis. The different shape of the f(I) curve of non_spontPC compared with that from the original publication (Figure 42) is caused by the measurement here of stable firing, whether regular or burst firing, in the interval of 4-15 seconds. In the original f(I) curve the measurements were made in 300-700 ms, where the firing has not yet reached steady-state. The initial monotonically increasing parts of the curves correspond to currents below the levels that induce burst firing, which begins at 1 nA for the two spontaneously firing models and at 1.5 nA for non_spontPC.

5.2.8 Tuning the in vivo firing rate of the PC model

Similarly to the effect of modifying the amount of current injected to a neuronal model to achieve different output rates in the absence of synaptic inputs, when modelling the in vivo behaviour of a neuron the background synaptic inputs can be used to reach a desired background firing rate.

The first PC pattern recognition studies I performed – before having created the spontaneous PC models – suffered in that I could not slow down the PC firing rate as I desired. The solution was to reinstate a non-tonic inhibitory input to the PC model as in De Schutter and Bower (1994b) and will be described in the following.

I wanted to make sure that the pattern presentation was always done after full equilibration had taken place. As shown for the current injections to the PC models (5.2.7), the PC models require a second or more to fire stably. The tonic inhibition used by Steuber et al. produced 48 Hz firing in the first 200 ms of the simulation, while at steady-state firing in the interval 3-4 seconds, the firing rate was 84 Hz with a coefficient of variation (CV) of 0.10. Purkinje cells of adult rats have an in vivo firing rate of 35-40 Hz, with a CV of approximately 0.4-0.5 (Savio and Tempia, 1985; Stratton et al., 1988; LeDoux and Lorden, 2002) (but see Shin et al., 2007a). Hence, I considered the PC model setup to give too high and too regular a firing rate to correctly model in vivo behaviour and therefore attempted to decrease the firing rate by decreasing the excitatory input from its initial setting of 28 Hz. This, however, revealed an instability of the PC model with firing rates only possible to be lowered to ca 59 Hz: excitatory inputs set to 25.70315 Hz gave 1.67 Hz output, while a 0.00001 Hz higher rate gave 58.65 Hz. In addition to 59 Hz remaining too high as the lower output limit, it gave too low CVs for realistic modelling of in vivo conditions.

The solution was to change the inhibitory input from 1000 Hz – in effect giving a tonic inhibition – to 1 Hz, while simultaneously increasing the maximum conductance of the inhibitory synapses by a factor of 1000. The result was a no-longer unstable PC model which could be titrated to any desired output rate by the manipulation of its excitatory input rate.

The input rate of 1 Hz had previously been used in the Purkinje cell model (De Schutter and Bower, 1994b); since this input rate worked to create good output characteristics, I judged that the much more laborious undertaking of titrating the Purkinje cell model to fire in a satisfactory way at either 1000 Hz or intermediate rates was an unnecessary procedure.

1 Hz inhibitory input was subsequently used with the spontaneously firing PC models which, likewise, could be titrated to any output rate, exemplified with the first version of the spontaneously active model (spontPC) in Table 7.

Table 7 Firing rates of PC model spontPC. The inhibitory input rate was 1 Hz while the excitatory input rate was titrated to reach different rates of firing to be used in the subsequent pattern recognition modelling. The data are mean values for background firing of 750 trains (see Section 5.2.9).

Excitatory input rate (Hz)	Output rate (Hz)	CV of interspike intervals
26	35.3	0.76
28	56.6	0.56
37	98.6	0.16

56.6 Hz was used as the default in vivo output spike rate, since although this rate is slightly higher than those of rats at rest, the mean CV of the trains (0.56) is closer to the mean in vivo (0.4-0.5). The other two train types shown in Table 7 were used in parameter explorations.

To allow comparisons between the PC models in pattern recognition trials, the excitatory input to the other two models (non_spontPC and spontPC_2) was titrated to give the default background output rate of spontPC, 56.6 Hz. With the inhibitory input rate kept static at 1 Hz, the excitatory input rates were titrated to 24.034 Hz for non_spontPC and 27.548 Hz for spontPC_2.

5.2.9 Creating a repository of spike trains resulting from pattern recognition by PC models

To supply spike trains resulting from pattern recognition by the PC model as input to the DCN neuron model, a repository of PC model spike trains was created. The pattern recognition simulations followed the methodology outlined in Section 5.2; here I will describe the implementation details.

The associative net implementation of Steuber et al. (2007) was translated into Microsoft Visual C++ and was run for many different settings of number of patterns and size of patterns in order to provide for the range of simulation settings used in Section 5.6.

For comparability with previous work (Steuber et al., 2007), I created the same type of setup as there, with each simulation of PC pattern presentation consisting of the presentation of 75 novel PF patterns and 75 stored PF patterns to the PC model, randomised for each run to create varying background activity at the moment of pattern presentation. This simulation setup was run ten times, resulting in a total of 750 each of spike trains from Purkinje cells receiving novel and stored patterns. For each of the ten runs, a new set of associative net pattern recognition output vectors (PF activity vectors, as described above) was created and the Purkinje cell simulation was initialised with different randomised settings. Signal-to-noise ratios of pause lengths and other parameters were calculated for each run of 2×75 simulations; results were presented as the mean

signal-to-noise ratio of the ten runs, with standard errors of that mean based on its sample size of ten. The 2×750 spike trains resulting from the ten runs were stored as a spike file repository to be used as input to the DCN neuron model in the next step.

The setup was different from the Steuber et al. (2007) work in two respects: the inhibitory input was non-tonic (described in Section 5.2) and the PC model simulation was run for a four second equilibration time followed by four seconds of background firing. The PF patterns were presented after these eight seconds of simulation, and the simulation was continued for one second after pattern presentation. In the Steuber et al. work the pattern was presented after 200 ms of equilibration time.

5.2.10 Testing correctness of the PF-PC implementation

The Steuber et al. (2007) publication on PC pattern recognition forms much of the foundation for the pattern recognition work in this thesis. To validate my implementation of PC pattern recognition, I ran simulations with their original setup, and calculated signal-to-noise ratios for four spike train metrics described by the authors: the latency to the first spike after pattern presentation; the number of spikes in the 25 ms following pattern presentation; the firing rate of those burst spikes (measured as the inverse of the mean interspike interval); the length of the pause after the burst spikes.

The resulting mean signal-to-noise ratio of the pause equalled 18 as in Steuber et al. (2007), but the best metric for pattern recognition was in my hands the firing rate of the burst phase. The mean burst spike rate was 198 Hz for novel patterns and 118 Hz for stored patterns, with a mean signal-to-noise ratio of 41. The corresponding mean signal-to-noise ratio in Steuber et al. (2007) was 1.4

which was not possible to reproduce in the present work, perhaps due to different methodologies of calculating the burst phase firing frequency.

5.2.11 Pattern recognition by the modified PC models

The Purkinje cell firing rate after PF input is the best metric in most settings

For the calculations of signal-to-noise ratios in the three PC models with many different settings of output rate, synchronicity of PF pattern presentation, and other features, I modified the definitions of spike response metrics from Steuber et al. (2007) to ensure that the pause would be found even if occurring later than 25 ms following pattern presentation. The minimum ISI classified as pause was extended to 30 ms and a number of alternate metrics were introduced; those are listed in Table 8.

Table 8 Spike train metrics of the outputs of PC models presented with stored and novel PF patterns. The metrics are relative to the time of PF pattern presentation (See Figure 46 in Section 5.4).

Metric
Time of first spike
ISI of the first two spikes
Number of spikes in the burst following pattern presentation (i.e., before the pause)
Length of the burst
Firing rate of the burst
CV of ISIs in the burst
Time at start of the pause
Length of the pause
Time of the first spike after the pause

By a wide margin, the best pattern recognition metrics were (1) the interval between the first two Purkinje cell spikes following the PF pattern presentation, and (2) the spike frequency of the burst these spikes were part of. This was true at all but the highest of the four examined Purkinje cell firing rates (36 Hz, 57 Hz, and 77 Hz). The highest firing rate (99 Hz) resulted in the length of the pause being the best metric. The metrics of Table 8 were measured in each analysis of PC pattern recognition.

The best five metrics of PC pattern recognition at 56.6 Hz baseline firing are plotted for each of the three PC models in Figure 45. Note the much lower pattern recognition results compared to those of Steuber et al. (2007), accounted for by the change here to non-tonic inhibition and longer equilibration time.

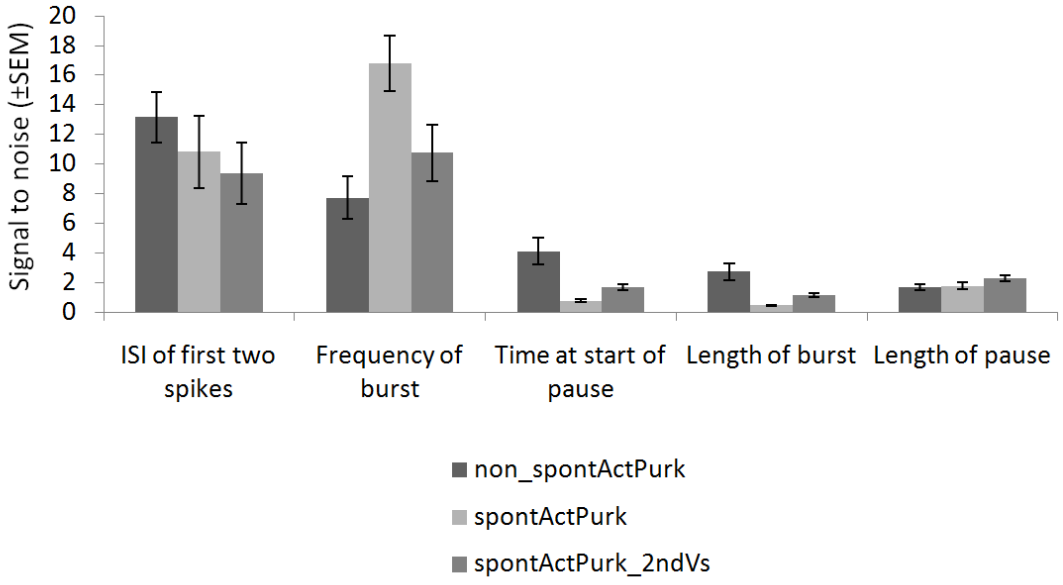

Figure 45 Pattern discrimination with the five best metrics in the examined PC models when simulated with a background firing rate of 56.6 Hz. These metrics were the best in all three models, but the internal ranking differed between the models.

5.2.12 Spontaneous Purkinje cell firing activity is compatible with pattern recognition

As can be seen in Figure 45, the two spontaneously active PC models are both capable of pattern recognition, with some metrics being better than in the non-spontaneous model while others are worse. It is therefore hard to state which of the models is best for pattern recognition. In any case, as Purkinje cell output is interpreted by DCN neurons before it affects any systems outside of the cerebellum, PC pattern recognition is likely to be of lesser importance than pattern recognition in the DCN. The exception, which is not covered by this thesis work, is the effect of Purkinje cell firing on the vestibular nuclei, the only Purkinje cell target outside of the cerebellar nuclei (De Schutter and Steuber, 2009). Hence, the interpretation of the outputs of pattern recognition by the DCN neuron is the important question which will be the focus in the following; the corresponding Purkinje cell signal-to-noise ratios will be given but will not be analysed exhaustively.

5.3 Simulations of pattern recognition in a network of PFs, Purkinje cells, and a DCN neuron

With three biophysically realistic PC models created, the next step was to analyse the DCN neuron model responses to Purkinje cell trains generated by novel and stored PF pattern presentations (these will henceforth be called *novel* and *stored* trains, respectively).

For that purpose, I needed to feed the DCN neuron with the outputs from the PC models, as described in Section 4.5.5. Since the PC models were made in GENESIS, the easiest solution was to first run the simulations with PF pattern presentation to the PC model, save the Purkinje cell outputs to spike time files,

and then run the NEURON-based DCN neuron model simulation where the files were read in and their spike times were sent to the DCN neuron synapses.

While the simulations of PC pattern recognition were divided into 10 runs to be able to average out variations in the signal-to-noise ratios, for providing inputs to the DCN neuron model, the Purkinje cell spike trains were pooled into two groups, one with the 750 novel trains and the other with the 750 stored trains.

The number of Purkinje cells that each DCN neuron receives input from is not well characterised. Section 2.7.3 introduced the data from Palkovits et al. (1977) which remains the only published study of this convergence ratio of Purkinje cells to DCN neurons, giving the value 860. Others argue that the convergence ratio is lower (Chris De Zeeuw and Indira Raman, personal communication); further, synchronisation of nearby Purkinje cells (Ebner and Bloedel, 1981) would lower the effective convergence ratio from that of the physical convergence ratio. Therefore the DCN neuron model was designed so it could be run with different convergence settings, allowing the exploration of convergence effects on pattern recognition. However, the model always received input to its full set of inhibitory synapses. Thus, with the simplest case of a convergence level of one PC per DCN neuron, each of the 450 PC-DCN synapses received input from the same single Purkinje cell, while at the other extreme of convergence 450 independently firing Purkinje cells provided input to the 450 synapses. These two extremes of convergence as well as the intermediate values were created by the randomised selection of the required number of Purkinje cell trains from the pool of 750 trains of novel or stored trains, with no duplicate train selections.

As with the simulations of PC pattern recognition, 75 simulations were run with Purkinje cell novel pattern readout presented to the DCN neuron model,

followed by 75 simulations with stored pattern readouts. A new random selection of Purkinje cell trains was drawn from the 750-train pool for each simulation, and the randomiser was differently initialised. As in PC pattern presentation, the simulations were repeated in 10 such runs, and the signal-to-noise ratios were calculated and averaged as described for the Purkinje cell simulations.

When the DCN neuron is said to receive a novel (stored) pattern, all Purkinje cells providing input to its synapses have been presented with novel (stored) PF patterns, unless otherwise specified.

5.4 Analysis of DCN neuron pattern recognition

The presentation of PF patterns to the network resulted in the PC model burst-pause response causing a characteristic spike response in the DCN neuron model, comprising a short pause that was followed by a burst and then another pause. Typical raster plots showing these responses in a Purkinje cell and DCN neuron are shown in Figure 46. The plots show that the number of spikes in the novel pattern DCN neuron burst is larger than in the stored burst, corresponding to the longer pause in PC firing in response to novel PF patterns. This is true in all examined cases in this thesis.

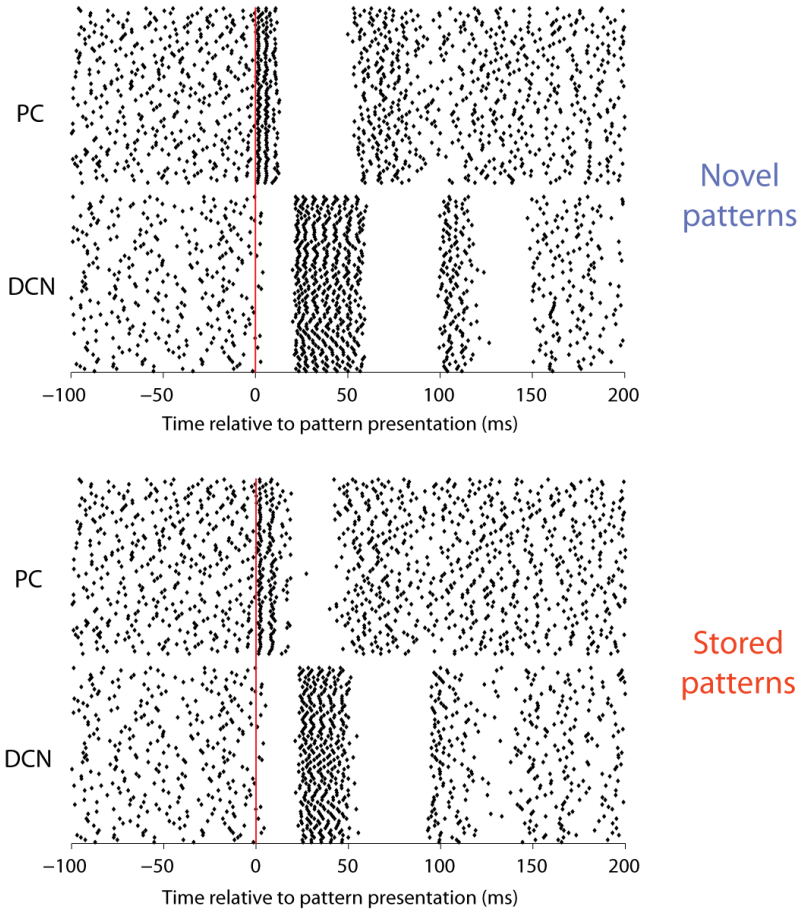

Figure 46 Novel (top) and stored (bottom) pattern readouts in the PC model spontPC and the DCN neuron model with the raster plots aligned in time. Both of the graphs display 75 trains of PC and DCN pattern readouts. In all cases, the convergence is 450 Purkinje cells to 1 DCN neuron; the DCN trains in the plots are not the result of the particular Purkinje cell trains that are shown but are instead responses to PC spike trains drawn from the entire 750+750 pools of Purkinje cell trains as in all simulations (see method description in Section 5.2.9). The scale of the graphs shows the time in milliseconds relative to the PF pattern presentation (the actual simulation time is the default of 4 seconds).

The high-convergence case shown in Figure 46 was the default network setup, meaning that the DCN neuron received the outputs of 450 different Purkinje cells firing at a background rate of 56.6 Hz and that those Purkinje cells

had been presented with PF weight vectors resulting from the learning of 100 patterns with 1000 active units at the associative net stage.

5.4.1 Defining characteristics of DCN responses to patterns

While Steuber and collaborators (2007) defined a minimum length of the pause response in the Purkinje cell after PF input to detect and measure pauses in spiking, the DCN responses are not amenable to such an algorithm. This is exemplified by the low convergence case in Figure 48 which shows that the burst phase often has no clear end. Conversely, other simulation settings created trains where the preceding pause phase was hard to define while the end of the burst was clear. To enable the largest possible number of analyses of pattern recognition, I found that the most successful alternative was to define the burst as a DCN rebound response, that is, a response that follows a period of inhibitory input of such strength that the neuron temporarily stops firing. A published definition of DCN rebound gives that all spikes in the rebound have an instantaneous firing rate equal to or larger than the previous mean firing rate plus 25 Hz (Molineux et al., 2006). Using this requirement to identify the burst phase made it possible to analyse a number of different characteristics of the spike responses of the DCN neuron model and quantify their contribution to pattern recognition. The different metrics for the DCN neuron response are shown in Figure 47. The bar plot shows that the best metric for pattern recognition in the DCN is the number of spikes in the burst; this is discussed in more detail in Section 5.6.

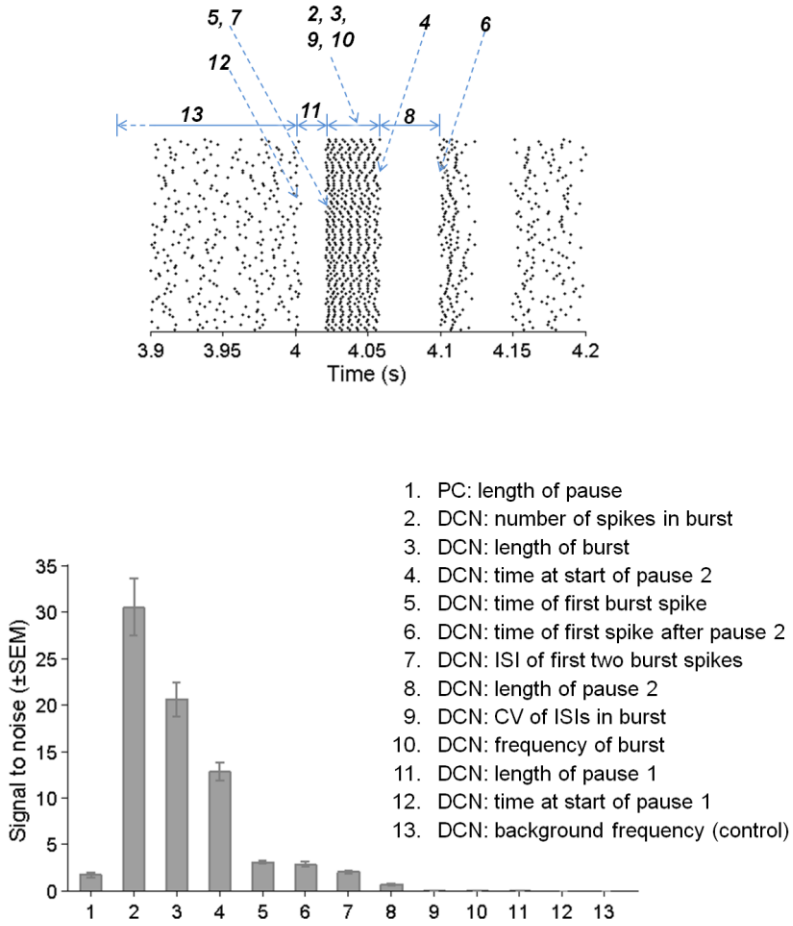

Figure 47 Pattern recognition capability of different metrics of the DCN readout. The top graph shows the twelve different characteristics of the DCN neuron spike trains that were measured for novel and stored trains in each simulation setup; the inset explains the meaning of each metric. The bar graph shows the pattern discrimination power – determined by signal-to-noise ratios – of the metrics when applied in the high convergence setup of Figure 48; the Purkinje cell pause value is added for comparison.

5.4.2 Modified and additional spike train metrics

While I was analysing some of the simulation results it was clear that the raster plots of the kind shown in Figure 48 in some cases showed an obvious difference between novel and stored responses which did not show up in the

signal-to-noise ratios. For example, some DCN burst phase responses were visually distinguishable without fulfilling the rebound definition.

This made me develop an alternative set of metrics, based on the types of neural coding listed in Section 2.5: (1) spike rate; (2) degree of regularity of spike intervals; (3) temporal spike patterns. The metrics were designed to capture each of these coding modalities in different time windows of the DCN neuron output following pattern presentation, with the quantification in each window of: (1) number of spikes; (2) CV_2 of spike intervals; (3) time of first spike.

Based on the visual evaluation of raster plots from dozens of different simulation setups, I chose to examine those three metrics for differences between the DCN neuron response to novel and stored trains in the following consecutive intervals:

- eight 10-millisecond intervals
- nine 20-millisecond intervals
- four 50-millisecond intervals

As starting point for all intervals I chose the point in time where the hyperpolarising effect of the PF pattern presentation could be seen in the DCN neuron soma.

The metrics will be referred to as interval-based metrics and they have been used in a subset of simulations, mainly where the original metrics could not be used because their requirements were not fulfilled.

In order for any metric – original or alternative – to be used with the results of a simulation, I required that less than 5 percent of the calculated values were missing; such missing data occurred for metrics CV_2 and the *time of first spike* when there were no spikes in the interval; *number of spikes* was still used with the value 0.

With less than 5 percent missing data allowed, a total of 75×10 data meant that the maximum number of data points allowed to be missing was 37 in the novel and 37 in the stored DCN neuron outputs. As it turned out, all signal-to-noise ratios included for the analyses in the present work were based on metrics where all measurements could be made.

5.5 Main results of DCN readout of PC pattern recognition

The modelled cerebellar network has many parameters open to exploration. I identified more than a dozen such explorations that I judged to be biologically relevant and interesting. Before proceeding to the entire range of those investigations, I will discuss what I see as the two main results of the pattern recognition project, followed by questions they pose and simulations run to answer those questions. The first is that the DCN neuron model reads out the PC output of pattern recognition in a clearly defined burst firing. The second is that the signal-to-noise ratio of the readout is highly dependent on the convergence ratio of PCs onto the DCN neuron.

5.5.1 The modelled DCN neuron is highly proficient at discriminating between novel and stored patterns and transmits this information in a burst of spikes

As can be seen in Figure 47, the best metric of pattern recognition readout in the DCN neuron model at maximum convergence is the number of spikes in the burst phase. Figure 46 showed that this burst phase corresponds in time to the period where the Purkinje cell pauses.

In the default setup, novel trains give a mean of 6.8 spikes in the DCN neuron burst while stored trains give 5.0. The difference is read out with a signal-to-noise ratio of 30.2±3.1, while the next best metric – the length of the burst in time – gives a lower signal-to-noise ratio (20.5±1.9) due to its larger variance rather than a smaller normalised difference between the mean of novel trains compared to the mean of stored trains.

5.5.2 Pattern recognition depends on the convergence ratio of PCs onto the DCN neuron

Eccles (1973) proposed the cerebellar arrangement of multiple Purkinje cells conducting signals to one DCN neuron to function as a device to average Purkinje cell signals so as to decrease noise and thereby increase the reliability of the cerebellar output. The idea was confirmed in an artificial neural net by Walter and Khodakhah (2009).

I investigated the effect of such averaging by varying the convergence ratio of the Purkinje cell inputs (spontPC at 56.6 Hz) to the DCN neuron model. The 450 synapses were divided randomly into groups where synapses within each group received the same Purkinje cell train, synchronised in time. The group sizes were divisors of 450 and resulted in simulations with convergence ratios of 1, 3, 9, 18, 50, 90, 150, and 450.

The extremes of convergence ratios are illustrated in Figure 48. The Figure shows how the low convergence setting gives a high variability of DCN neuron responses from trial to trial while the high convergence setting gives a more reproducible point in time where the DCN neuron starts to fire a burst following its readout of the Purkinje cell pause – supporting Eccles' idea of increased reliability of signals at high convergences.

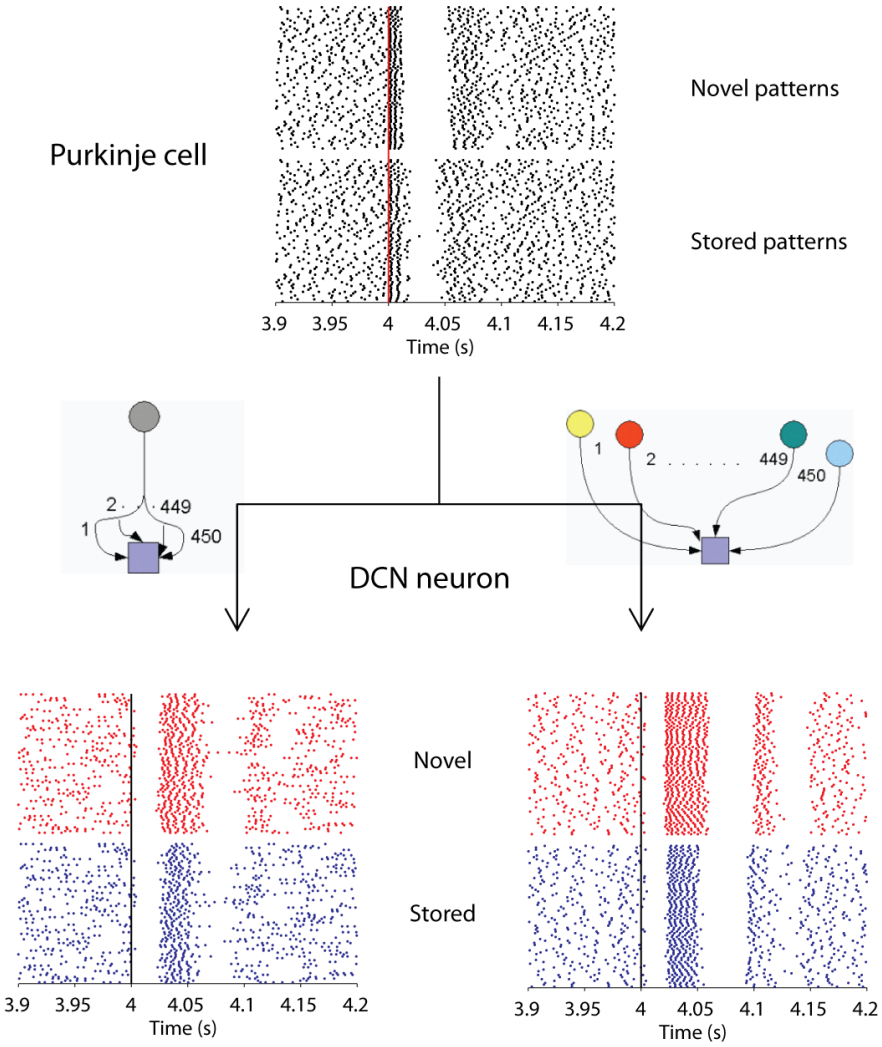

Figure 48 Pattern presentation from PFs (at the time of the vertical red or black line at 4 seconds) to the PC model spontPC and its subsequent readout in the DCN neuron model at the two extremes of convergence settings. Top: 75 each of novel and stored patterns are presented to the PC model with one simulation per line, with an SNR of 2.0 for the duration of pauses. Bottom: 75 novel and stored readouts in the DCN neuron model when all its 450 synapses receive input from the same PC (left: convergence = 1, SNR = 0.90), and when all synapses receive input from different PCs (right: convergence = 450, SNR = 48.3). Each SNR here is the result of one 2×75 simulation each; therefore these SNRs differ from those of Figure 49 which are means of ten 2×75 simulations. The background firing was kept constant in the two convergence settings via titration of the excitatory input to the DCN neuron.

The initial simulations (not shown here) suffered from a problem of comparability. With constant excitatory input rates the DCN neuron background firing was 67.8 Hz when the PC inputs were provided at a convergence of 1 while a convergence of 450 gave a background rate of 39.3 Hz. At intermediate levels of convergence, the background firing rate was decreasing with increasing convergences ratio. The cause of the dependence of the background firing rate on the convergence is, at least partly, explained with the following example of the extreme convergences.

At a convergence of 1, each of the 450 synapses receives input from the same Purkinje cell whose spiking thereby activates hyperpolarising currents at all synapses simultaneously. Hence, this input mode results in a powerful inhibition of the DCN neuron at the times of Purkinje cell input, while the intervals between Purkinje cell spikes provide a window of enhanced firing ability. With the short rise and fall time constants of the GABA conductance (0.2 and 3.6 ms, respectively, at 37°C), the average Purkinje cell ISI of 18 ms allows for several DCN spikes.

At the other end of the convergence spectrum, 450 independently firing Purkinje cells provide input to the synapses, making the likelihood of drastic deviations from the mean hyperpolarising effect on the spike generation mechanisms in the axon hillock unlikely.

The DCN neuron background rate affects the pattern recognition capacity as will be shown in Section 5.6.3. Thus the simulation was rerun with excitatory input rates to the DCN neuron titrated so as to keep its background firing rate constant. The resulting trains are shown in Figure 48 and give the signal-to-noise ratios plotted in Figure 49. The Figure shows that the DCN neuron signal-to-noise ratio goes up with every increase in the convergence ratio and rises above that for the Purkinje cell burst frequency as the convergence reaches 30 or more. While

the burst frequency metric of PC pattern recognition gives a signal-to-noise ratio of 16.8±1.9, the Purkinje cell pause gives 1.8±0.2. This value is similar to the signal-to-noise ratio for the DCN burst at the convergence ratio of 1, which is 1.2±0.1 for the burst length and 1.0±0.1 for its number of spikes (this is the only convergence setting where the number of spikes is not the best metric).

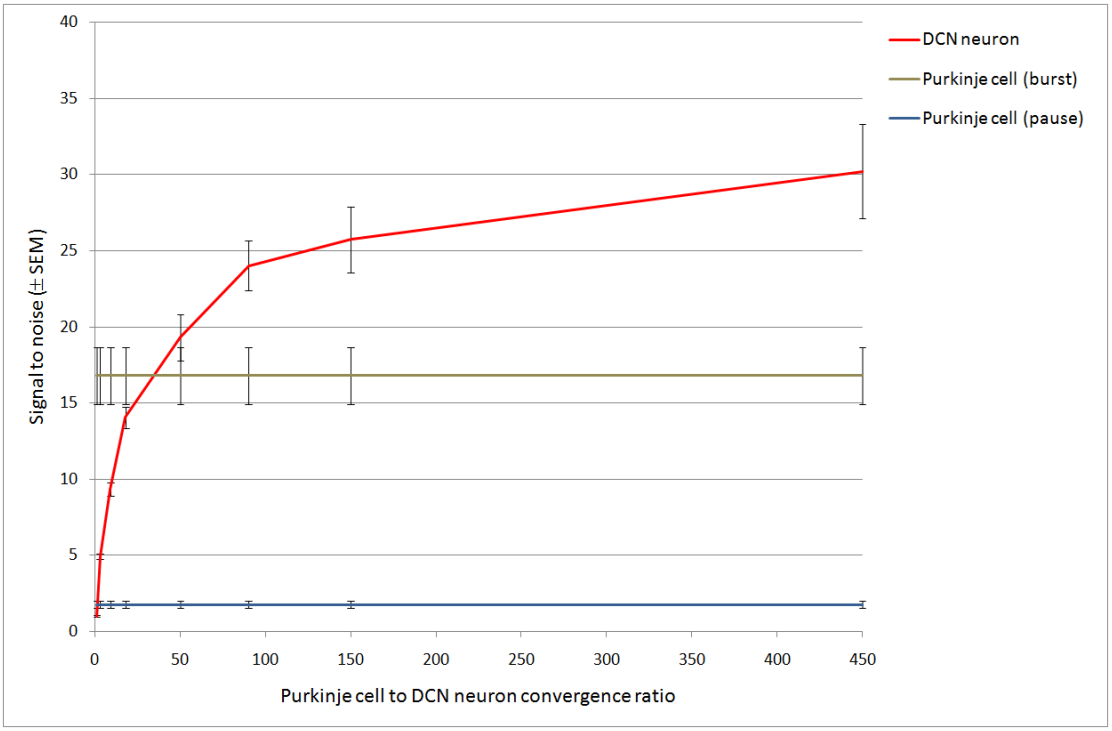

Figure 49 Effects of convergence on the readout of patterns by the DCN neuron. The diagram shows how the pattern recognition performance of the DCN neuron (number of spikes in the burst) goes up as the Purkinje cell to DCN convergence increases. The background firing rate was kept constant at all convergence settings via titration of the excitatory input to the DCN neuron.

As it appears improbable that the cerebellar circuitry wastes a large amount of information in the Purkinje cell to DCN neuron information transfer (convergence 1 is the "raw" measurement where no averaging takes place to enhance pattern discrimination), it is reasonable to assume that the length of the pause – which is a likely candidate for determining the number of spikes in the

burst in the DCN neuron – is the actual information-containing metric for the PC. The simulations in 5.5.4 will show the likelihood of this being the case; I will use the Purkinje cell pause as the reference metric for DCN pattern recognition and will refer to the ratio of the Purkinje cell pause SNR to the best DCN SNR as the amplification of the circuitry. With the given SNRs, the amplification equals 17.0 at a convergence of 450 and 0.68 at a convergence of 1.

5.5.3 Cause of amplified pattern recognition by the DCN neuron

Walter and Khodakhah (2009) showed that the signal-to-noise ratio in an artificial neural net model of the PC-DCN neuron circuitry scales linearly with the convergence ratio. This contradicts the results above which can more clearly be seen in Figure 50 where the DCN SNRs and the inverse of its denominator have been re-plotted at different convergences along with plots of scaling with the convergence and with the square root of the convergence. The Figure shows that the SNR of the readout in the biophysically realistic DCN neuron model scales sub-linearly with the convergence ratio and even approaches the square root of the convergence for large convergence ratios.

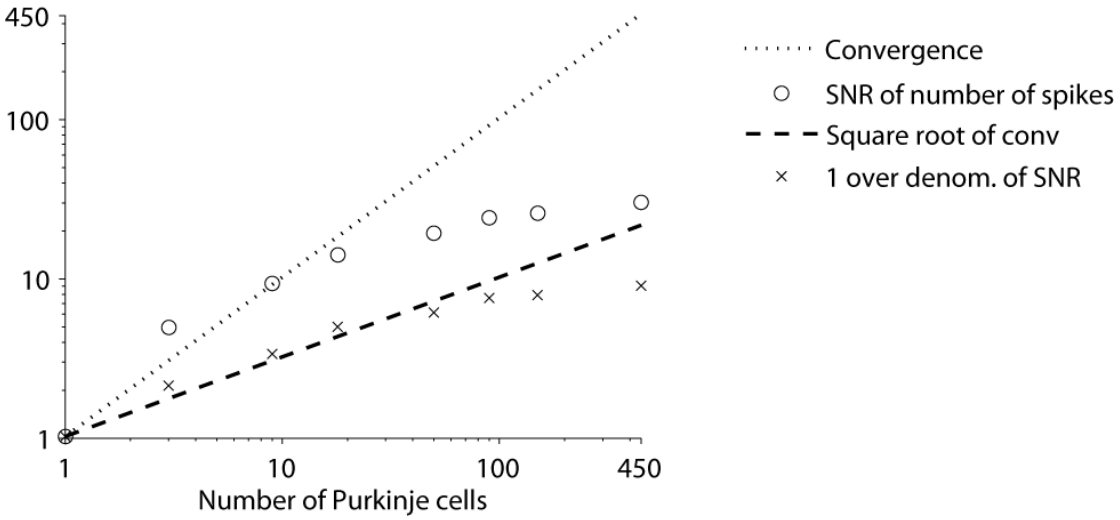

Figure 50 Normalised plots of convergence effects; data were normalised by division with the SNR at convergence 1 (=1.02). The circles give the SNRs and the crosses give 1 divided by the denominator of the SNR, thereby ignoring the effect of changing differences of novel to stored means (see definition of SNR in 5.2.3). The dotted black line is the result of linearly scaling the SNR for a convergence of 1 by the convergence ratio, while the dashed black line is the same for scaling by the square root of the convergence.

The study by Walter and Khodakhah demonstrated that the standard deviations of the means of metrics decreased with the square root of the convergence ratio; the linear scaling of the signal-to-noise ratio follows from the definition of the signal-to-noise ratio since the denominator consists of the squares of the standard deviations (Equation 19).

To clarify this scaling, my primary supervisor and I conducted a set of simple calculations using MATLAB. The results are illustrated in Figure 51 which contains the results of calculations based on 450 matrices of size 100 × n, where n equals the serial number of the matrix (1-450). Each of the 100 rows of a matrix corresponds to one pattern presentation, and each of the n columns to one Purkinje cell synapsing with a DCN neuron. Each entry in the matrices contains a response metric for that particular pattern and PC, which for the purposes of the

present argument was a value randomly drawn from a normal distribution with mean 0 and standard deviation 1.

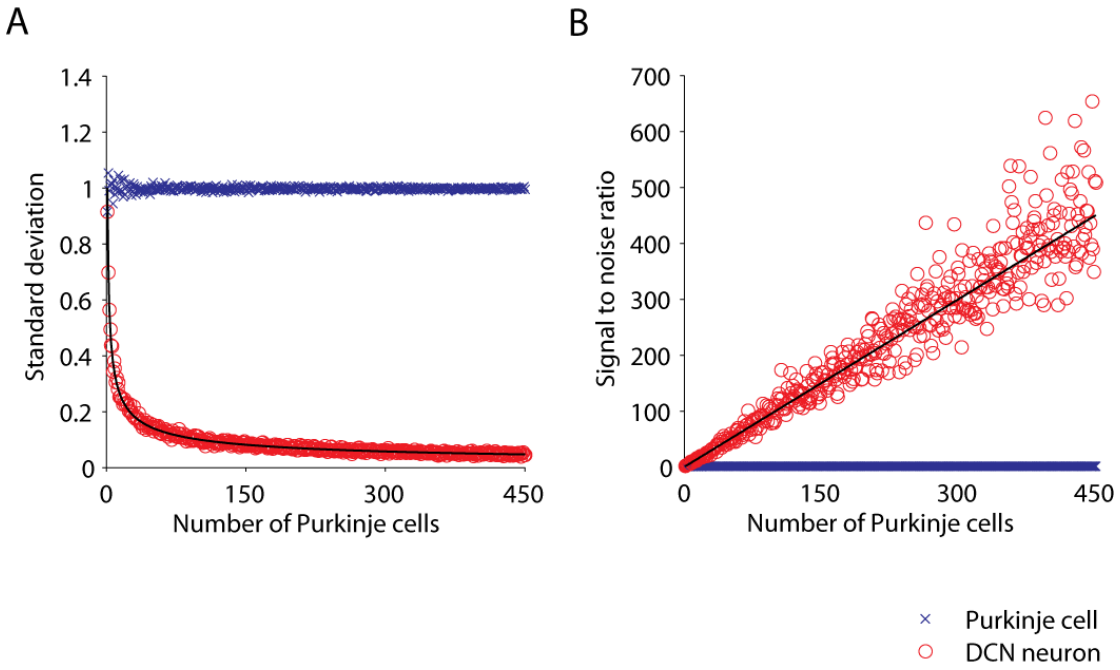

Figure 51 Simulations of how the Purkinje cells to DCN neuron convergence ratio influences standard deviations of observed metrics (A) and the resulting signal-to-noise ratios (B). The black curve in A is a plot of 1 divided by the square root of the convergence ratio; in B, the black line plots the convergence ratio. See text for details.

In Panel A, the blue crosses show the results of first calculating the standard deviation of the 100 values for each of the n Purkinje cells (where n is the convergence, the value on the x-axis) and then taking the average of the n standard deviations. The result is that at 1 on the x-axis, there has been no averaging of the standard deviation of the 100 pattern presentations, while at 450 the standard deviation value is the mean of 450 raw standard deviations.

The red circles in A are the corresponding observations of the Purkinje cell data from the point of view of the DCN neuron. For each convergence, the DCN neuron has effectively calculated the mean of the n Purkinje cells for each of the

100 pattern presentations, and then taken the standard deviation of the 100 resulting sample means. This makes it the standard error of the mean which is defined as the standard deviation of sample means and is calculated as in Equation 23 (Field, 2005).

$$SEM = \frac{s}{\sqrt{n}} \tag{23}$$

where s is the sample standard deviation and n is the sample size. The standard error of the mean was calculated for each of the convergences and was plotted in graph A as the black line, which shows that the standard deviation of the DCN neuron readout indeed develops as the square root of the convergence in this simulation.

In the case of constant differences between means, signal-to-noise calculations scale with one divided by the square of the standard deviation. Panel B of the Figure 50 gives the squares of the standard deviations of graph A and shows that the DCN neuron signal-to-noise ratio in this simulated data set develops linearly with n, as in the Walter and Khodakhah data.

The matrix calculations were then rerun with the random numbers exchanged for pause lengths from the pattern recognition trials with PC model spontPC, and with the number of patterns changed to 75 (the number of repetitions performed in each pattern recognition simulation with the DCN neuron model). With this modified setup of the matrix, the convergence-driven amplification as seen from the DCN neuron would be demonstrated using biophysically realistic PC model data.

However, neither in this simple calculation nor in the biophysically realistic DCN neuron simulations could the convergence be simulated without correlated Purkinje cell outputs being fed to the DCN neuron. The PC model spike

trains were the results of 750 independent presentations each of novel and stored PF patterns, while the DCN neuron simulations with inputs of 75 pattern combinations where each contained up to 450 Purkinje cells would require 33,750 Purkinje cell simulations each for novel and stored pattern presentations. This was impossible given the computational constraints; the solution that I settled on (for the DCN neuron model simulations as well as the present matrix calculations) was instead to create randomly drawn sets from the pool of 750 trains. For the n = 450 settings of convergence explored in the matrix calculations, 75 individually randomised sets of n = 450 Purkinje cell trains each were drawn from the pool. This procedure meant that at convergence 450, 60% of all trains were used for each set, giving a very high degree of correlated pause lengths, while the lower convergences resulted in increasingly diminishing amounts of correlated inputs.

The results are displayed in Figure 52 where Panels A and B show the standard deviations from novel and stored pattern presentations, respectively, as in the previous figure; the black curves show the standard deviation of the Purkinje cell at each convergence ratio divided by the square root of that convergence. Panel C gives the calculated signal-to-noise ratios for each convergence ratio based on the means and standard deviations from the matrix simulations. The black line is the Purkinje cell signal-to-noise ratio at each convergence ratio multiplied by that convergence. Panel D shows an enlarged display of convergences 1-90 from graph C.

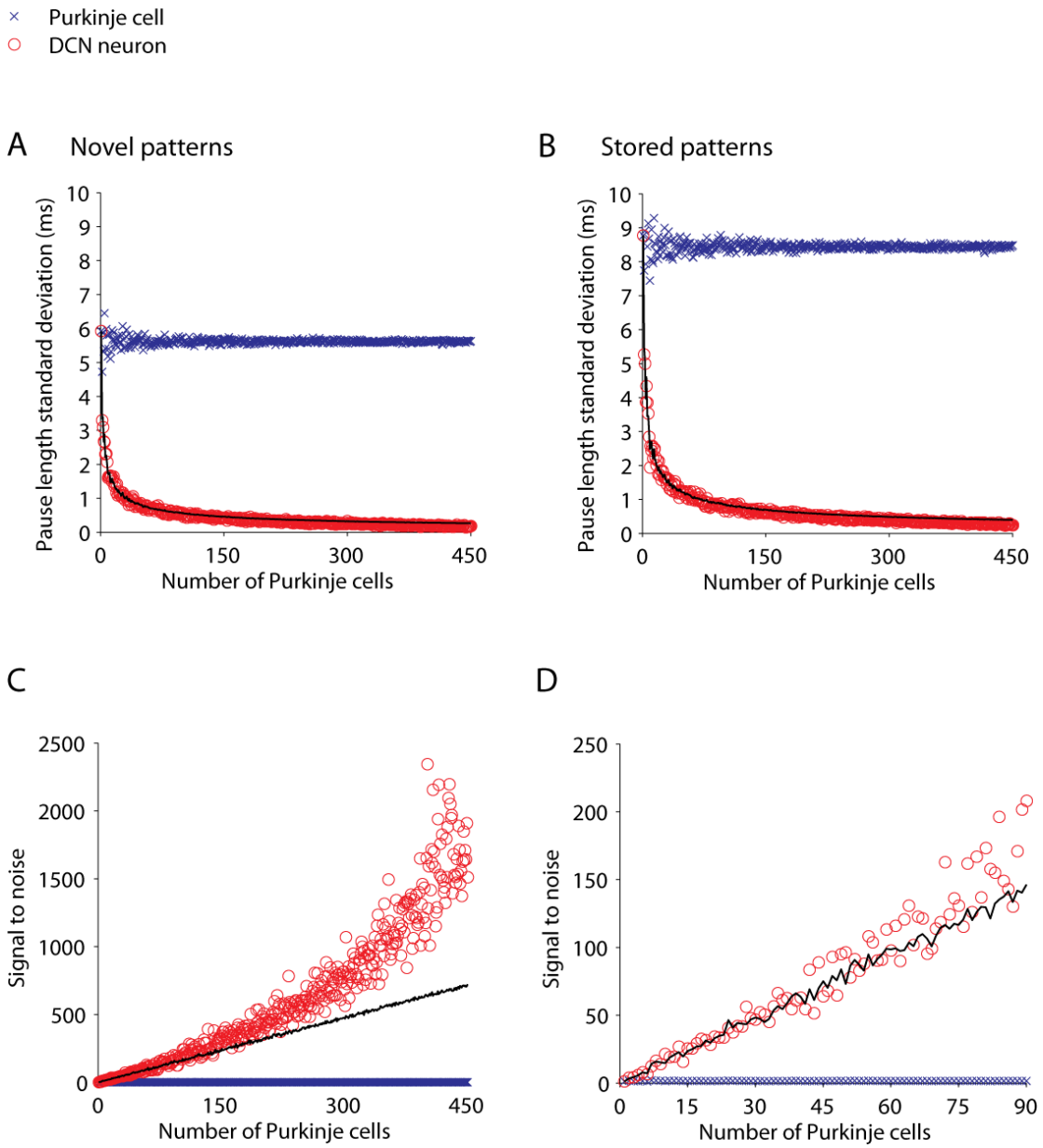

Figure 52 Replication of the calculations of Figure 51, here using the PC model pause lengths instead of random numbers. The calculation uses the pauses resulting from novel (A) and stored (B) pattern presentations; C gives the signal-to-noise ratio calculated for the novel and stored response at each convergence setting; D shows only convergences 1-90 from C and displays the close-to-linear scaling of signal-to-noise ratios in this range.

The graphs of signal-to-noise ratios in C and D show that the signal-to-noise ratios scale supralinearly with the convergence ratio, but only at the higher

convergences. Up to a convergence of about 50, the scaling is linear; the differential results are probably caused by the increasingly correlated pause lengths in the higher convergence cases. Independent of the causation, the linear scaling at the lower convergences is comforting in that most of the amplification effect in the biophysically realistic simulations has already happened by a convergence of 50 (Figure 50). At a convergence of 50, the SNR is 19.3±1.5 while a convergence of 450 gives SNR = 30.2±3.1. Thus, at a convergence of 50, the amplification equals 10.9.

The linear SNR scaling with convergence has therefore been confirmed to be theoretically valid for PC model pause lengths (up to a convergence of 50) while the biophysically realistic DCN neuron model readout scales much slower; the causes of this discrepancy will be discussed in Section 5.7.3.

5.5.4 Investigation of the contributions of rebound excitation to pattern recognition

The following simulations aimed to show how the DCN burst response relates to the initial fast spikes of the Purkinje cell. As shown in Section 5.5.1, the burst is the part of DCN trains that gives the highest signal-to-noise ratio from comparisons of novel and stored trains, but it follows 20-30 ms after the best Purkinje cell metric, which is the frequency of the initial spikes of the Purkinje cell.

Note that with the Purkinje cell transferring a strong inhibitory stimulus to the DCN neuron following synchronised PF inputs, the only DCN output spikes that could possibly carry information about the PF event are those in the burst – the neuron does not fire any spike prior to those (see raster plots in Figure 48 where the few DCN spikes before its pausing are within the synaptic delay time). While the fastest information transfer thereby would be based on the length of the

DCN pause, this feature carries close to no information (SNR = 0.07±0.00). Naturally, the length of a pause can only carry information towards its end where the length of the pause differs between the novel and stored patterns. Thus, the time of the first burst spike of the DCN neuron could perhaps be as fast a feature as the DCN pause length. This feature does carry information (SNR = 3.14±0.14) which, however, is far less than the number of spikes in the burst (SNR = 30.2±3.1). For this reason I will assume that the biologically important feature of the DCN neuron spiking in pattern recognition is the burst length (in number of spikes and/or length in time).

Here I aimed to elucidate what ability the Purkinje cell initial burst could have in affecting the pattern recognition capacity of the DCN burst. If the initial PC burst has little or no influence on the length of the DCN burst, we can limit ourselves to considering the PC pause length when comparing the PC and DCN pattern recognition capacities.

The frequency of its burst is the best discriminator of the PC model spontPC (which will be the one referred to when using the term "PC model" without specification). The *number* of spikes is not a good discriminator, however (SNR = 0.22±0.04). Hence, in order for the fast Purkinje cell burst phase to influence the readout in the DCN, the relative timing of the two or three spikes of the Purkinje cell burst would have to influence the length or number of spikes of the DCN burst.

A possible mechanism for the timing of the Purkinje cell burst spikes to influence the generation of differential DCN burst responses to novel and stored patterns is by contributing to rebound responses in the DCN neuron (see Section 2.7.1). Thus, the simulations to be described below examined DCN pattern recognition under block of channels implicated in the DCN rebound response: the

CaLVA, h, and NaP currents. Figure 53 shows the membrane voltage and the currents flowing through the rebound channels of the DCN neuron during a typical pattern presentation trial. Note the lack of a large difference in hyperpolarisation prior to bursting, where the novel pattern induces a minimum membrane potential of -69.3 mV while the stored pattern reaches -68.9 mV.

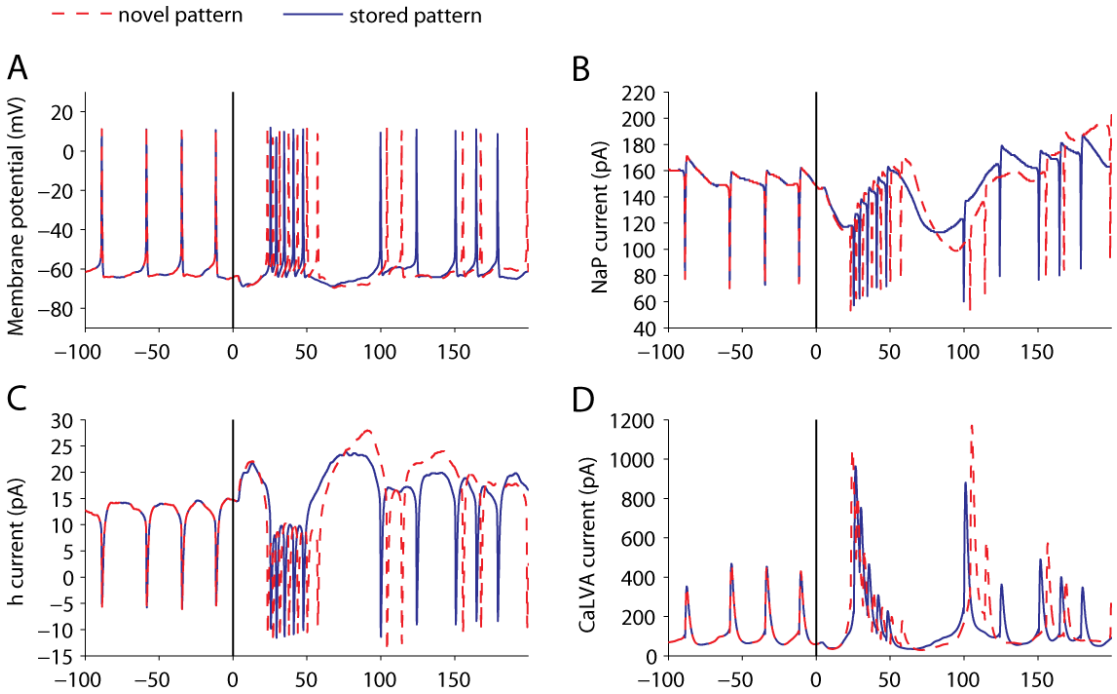

Figure 53 DCN neuron currents that are implicated in the rebound response following membrane hyperpolarisation. The graphs show a representative response to the standard DCN setup, with dashed red lines the novel pattern response and the solid blue lines the stored response. A) The membrane potential of the DCN neuron; B) Persistent sodium current (NaP); C) the hyperpolarisation activated cation current (h); D) low-voltage activated calcium current (CaLVA). Note the different y-axis scales.

To simulate the effect of blocking the ion channels in vivo, the rebound conductances were set to zero. This procedure affected the background firing rates of the neuron; to prevent this from affecting the pattern recognition

capacity, the excitatory inputs to the DCN were titrated as previously described, giving equal firing rates prior to pattern presentation.

The standard setup of 10×75 runs each with novel and stored pattern inputs was performed once for each of the three rebound channels blocked in isolation and once for all blocked in combination. Neither of these simulations resulted in a removed burst response or even a much decreased firing rate in it. In the original setup with all channels included, the mean firing rate of the DCN neuron burst was 179 Hz for the novel patterns and 182 Hz for the stored ones; the number of spikes in the burst was 6.81 vs. 5.02. In the four simulations simulating blocking of channels involved in rebound, these values stayed within ±1.5% of the originals and the SNRs were 20 or above for all cases while the default version gave 30.2 (Table 9).

Table 9 Pattern recognition simulations where channels involved in the DCN neuron rebound response have been blocked. The first line shows the baseline case of the default simulation setup, followed by the blocking of all three rebound channels and finally the channels blocked individually. In all cases the background firing rate of the DCN neuron has been titrated via the excitatory inputs to remain at the baseline level of 39.3 Hz.

Channels blocked	SNR (number of burst spikes)	Number of spikes in novel burst	Number of spikes in stored burst
None	30.2	6.81	5.02
CaLVA, h, and NaP	25.0	6.78	5.01
CaLVA	20.0	6.71	4.97
H	27.7	6.80	5.00
NaP	30.0	6.82	5.00

The most decreased SNR – that of the CaLVA knock-out – was caused by slight decreases in normalised summed variances (the denominator of the SNR calculation) rather than changed normalised differences of means (numerator).

5.5.5 Split novel and stored Purkinje cell trains

An additional way of examining the different contributions of the PC burst versus its pause would be to create synthetic Purkinje cell spike trains containing parts of the output from recognition of stored patterns and parts from novel patterns. As the Purkinje cell response following pattern presentation includes a pause whether the cell is presented with novel or stored patterns, the synthetic spike trains can be made by identifying the last spike in the PC burst response and then have the following time contain the pause of the opposite pattern type. An example of such a procedure is shown in Figure 54, where the lowest third shows a synthetic PC train with the burst response resulting from novel PF patterns while the pause and the following response from stored patterns. Such trains will be referred to as N+S trains in the following, while the inverse splicing and synthesis of trains will be called S+N trains. The original trains are N+N and S+S, respectively.

I ran simulations of the standard setup with N+S and S+N trains fed to the DCN neuron model and calculated signal-to-noise ratios for all combinations of real trains versus synthetic trains: N+N versus N+S, N+N versus S+N, etc.

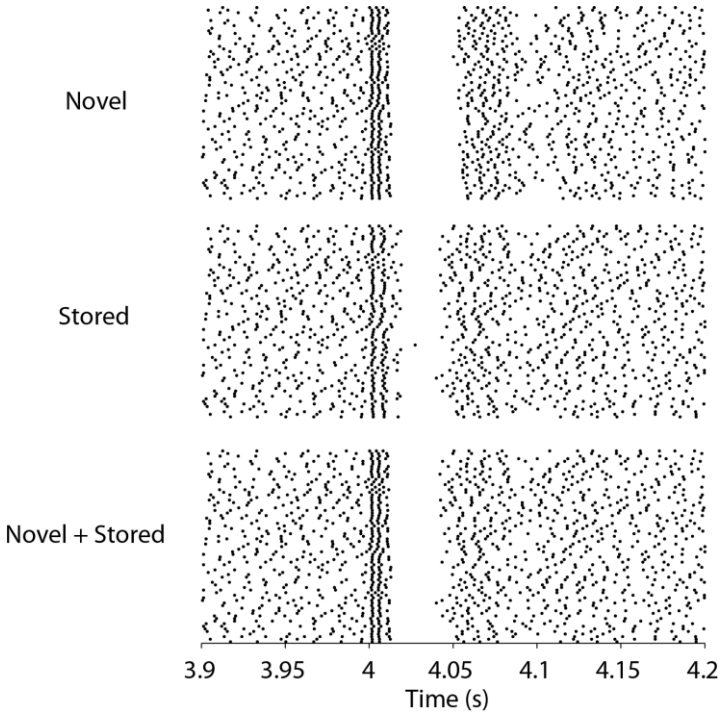

Figure 54 Synthetic Purkinje cell spike trains with parts from recognition of both novel and stored patterns. The top third shows a sample of 75 Purkinje cell trains resulting from presentation of novel PF patterns; the middle third, 75 trains with stored pattern presentation; the lowest third, the same novel and stored PC trains, split and synthesised so that the part before the pause consists of the novel response while the time following the pause is the stored response.

The readout in the DCN neuron model of 75 runs where the input was made up of N+S Purkinje cell trains is shown in the bottom third of Figure 55. The comparison with the rasters where input was made up of N+N trains and S+S trains, respectively (the top and middle thirds), indicates that the DCN neuron burst response was very similar with S+S compared with N+S, while N+N versus N+S gave a larger difference. This was confirmed with the calculations of signal-to-noise ratios of the number of spikes in the burst where N+N versus N+S gave the second highest SNR (8.51±0.39) of all the combinations while S+S versus N+S gave the lowest (1.50±0.18).

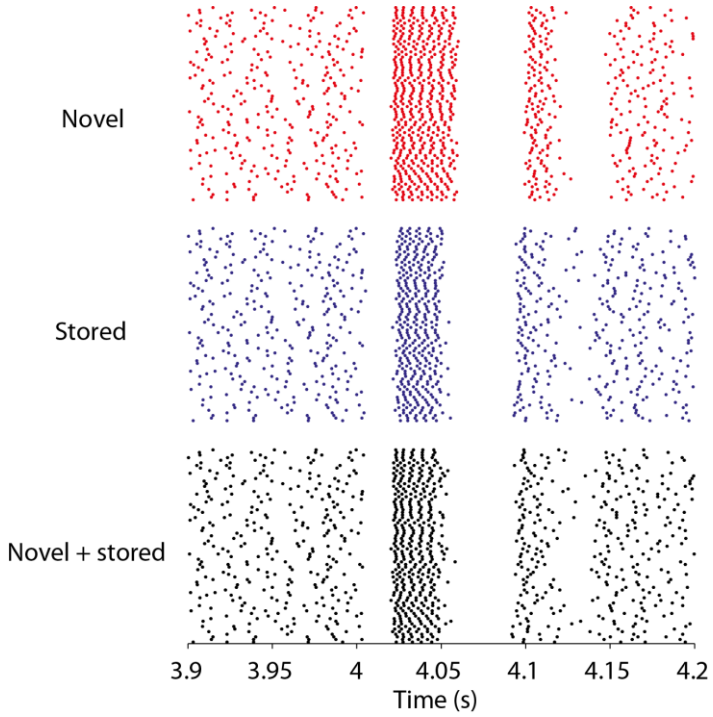

Figure 55 75 readouts in the DCN neuron model of synthetic novel+stored Purkinje cell trains (bottom third) with ordinary novel and stored (75 each) DCN readouts above added for reference.

The SNRs of all combinations are listed in Table 10.

Table 10 Signal-to-noise ratios of the number of spikes in the DCN neuron model burst phase during input of stored and novel PC trains versus synthetic trains with portions of novel and of stored. S=stored, N=novel; see previous text for explanation of the procedure for synthesising trains.

Comparison	Signal-to-noise ratio
N+N vs. N+S	8.51±0.39
N+N vs. S+N	1.86±0.18
S+S vs. N+S	1.50±0.18
S+S vs. S+N	11.57±0.71
N+S vs. S+N	2.52±0.15
N+N vs. S+S (vanilla)	30.23±3.11

With hindsight, these results were very difficult to interpret, however, as the initial burst response in the PC was of different length for novel and stored pattern inputs. Thus, the splicing of the initial burst phase from one type (stored/novel) of trains with the pause response of the other type gave an influence on the pause length from the burst phase.

A cleaner way of creating the spliced trains would probably have been to follow this procedure:

1. Find the last spike in the burst response in one type – train A.
2. Identify the length of the pause in a train of the other type – train B.
3. Shift the spikes in the post-pause part of train B by the difference of the length of the burst phase in train B and A.
4. Splice the burst response of train A with the shifted post-pause part of train B.

With the evidence for the overwhelming importance of the PC pause phase in comparison with its burst phase presented previously and with additional backup in the following set of parameter explorations, such a modified splicing procedure was deemed to be outside of the scope of this thesis project.

5.6 Further DCN pattern recognition investigations

Following the presentation of the main DCN pattern recognition results and their causes, this section will deal with parameter explorations of the Purkinje cell to DCN neuron network, introduced in Table 10.

Table 11 Further parameter explorations of pattern recognition, described in this section. For each exploration, the default value (i.e., the value used in all other parameter explorations) is marked in bold.

1. The DCN neuron model receiving pattern readouts from the not-spontaneously-active PC model (non_spontPC) versus the two spontaneous models: **spontPC** and spontPC_2.
2. Firing rate of the Purkinje cell in the absence of pattern presentation: 35, **57**, 99 Hz.
3. Firing rate of the DCN neuron in the absence of pattern presentation: 22, **39**, 60, 92, 127, 165, 198 Hz.
4. Asynchronous versus **synchronous** pattern presentation to the Purkinje cell. Asynchronous pattern presentation means that the PF-PC synapses are activated at a random time point over an interval of 2, 5, 10, and 25 ms, respectively.
5. The number of PFs (out of the total of 147,400) that participate in presenting a pattern to the associative net: 18 settings in the range 50 - 25,000. The default setting is **1000**.
6. The number of PF patterns presented to the associative net: 7 settings in the range 50 - 1,500. The default setting is **100** (100 novel + 100 stored patterns).

7. Feed-forward inhibition to the Purkinje cell during pattern presentation, with 1.4 ms post-pattern-presentation stellate cell input. Default is to have **no** feed-forward inhibition.
8. Limitation to the frequency with which spikes propagate down the Purkinje cell axon: no limit versus **330 Hz**.
9. Sensitivity of the DCN neuron to the PC pattern outputs. Here the number of DCN neuron synapses that receive the PC pattern is titrated down from **450** to the level where the signal-to-noise ratio falls below 1.
10. $GABA_A$ receptor synaptic short-term depression: **in use** or not.
11. Mossy fibre collateral connections to the DCN neuron. The default simulations **ignore** the direct connection between the mossy fibres and the DCN (Figure 9 in Section 2.7) during pattern presentation. In this simulation I examine the effects of transmitting a synchronised excitatory input to the DCN neuron, a few milliseconds before the output of PC pattern recognition reaches the neuron.

5.6.1 Readout in DCN of patterns presented by the non-spontaneous versus the spontaneous PC models

In Section 5.2.11 I evaluated the pattern recognition performance at the Purkinje cell stage with non_spontPC and the two spontaneously firing models. While I argued that no conclusive differences in pattern recognition capabilities could be seen, we are now interested in the effects on the DCN neuron and will therefore focus on the Purkinje cell pause length. The SNRs of that feature differed slightly between the models, with the SNRs shown in Table 12.

Table 12 Signal-to-noise ratios of the length of the pause in the three PC models.

Model version	Signal-to-noise ratio
non_spontPC	1.64 (SEM=0.17)
spontPC	1.78 (SEM=0.24)
spontPC_2	2.29 (SEM=0.23)

The corresponding results in the DCN neuron are given in Figure 56 and show that there is no clear correspondence between the SNRs of the pause length in the Purkinje cell and any of the five best features of the DCN neuron readout (this would show as a gradual increase in signal-to-noise ratios from non_spontPC over spontPC to spontPC_2).

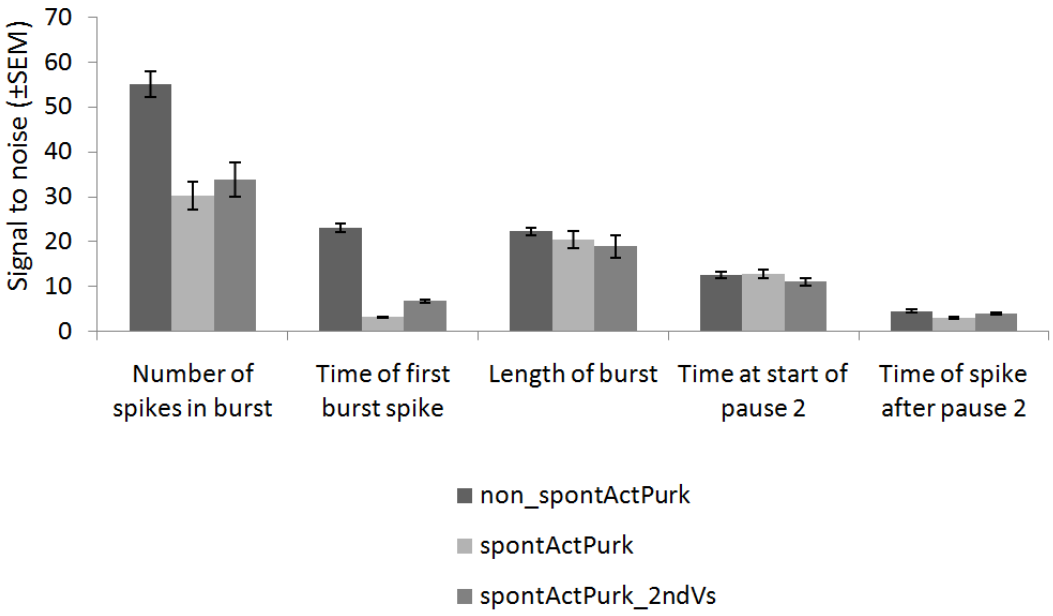

Figure 56 DCN readout of the three PC models, with the five best metrics using the original PC model (non_spontPC) and the spontaneously active models. In all models, the number of spikes in the burst was the best metric and the length of the burst was second. The PC background rate was 56.6 Hz and the convergence was 450.

The number of burst spikes gives the best signal-to-noise ratio with all models, and it is highest using non_spontPC. Figure 57 displays the pattern separation ability for non_spontPC and spontPC with histograms of numbers of spikes in the burst. Compare this with the table of the probability of correct discrimination (Table 5 in Section 5.2.3): this table gives a numerical correlate to the observed complete separation at a signal-to-noise ratio of 55 while a minor overlap remains at SNR = 30.

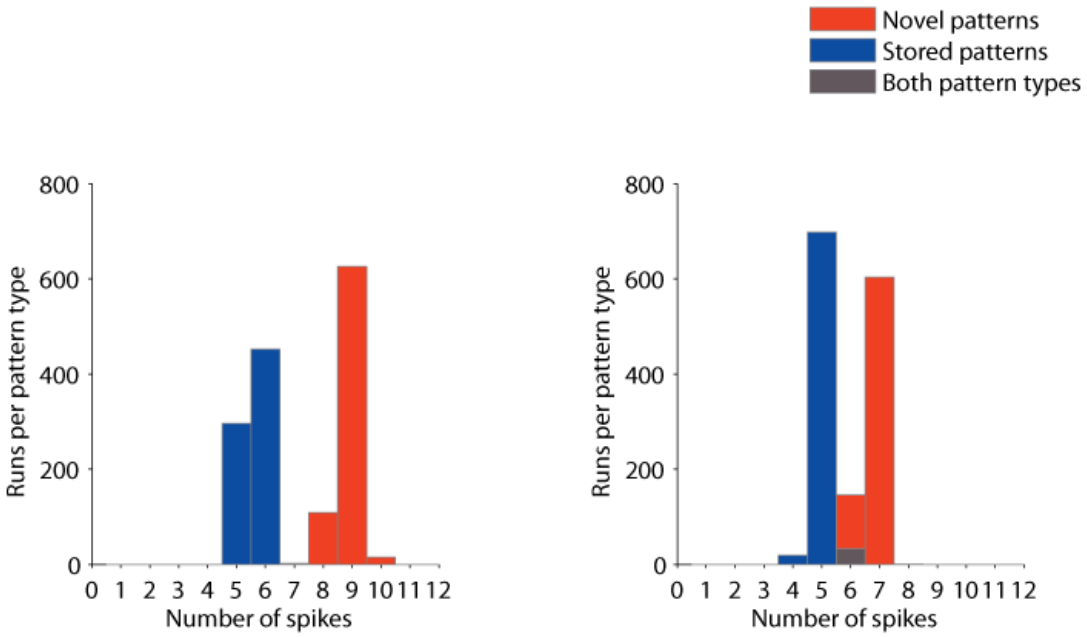

Figure 57 Readout of PC pattern recognition by the DCN neuron as number of spikes in the burst phase, using PC model non_spontPC (left) and spontPC (right). Signal-to-noise ratios: 55.1 for non_spontPC, 30.2 for spontPC. The PC background rate was 56.6 Hz and the convergence was 450 (the default settings).

5.6.2 Background firing rate of the Purkinje cell

In this set of simulations, I examined how the Purkinje cell background firing rate affects the pattern recognition capacity of the DCN neuron. For this purpose I created PC models with three different background firing rates (35, 57,

and 99 Hz) in spontPC and the higher two of those in non_spontPC. A complication is that the DCN neuron pattern recognition capability is affected by its background firing rate (shown next, in parameter exploration 3). Therefore, the different Purkinje cell rates were compensated for via the excitatory inputs to the DCN; those were titrated as previously to keep the DCN firing rate constant at all levels of Purkinje cell background rate.

Table 13 shows that with spontPC as input the DCN neuron pattern recognition capacity increases as the Purkinje cell receives patterns on a higher background rate. This is not seen with inputs from non_spontPC, which however gives almost twice the SNR of spontPC at the default Purkinje cell rate and stays at that level. With both PC models, the number of spikes in the DCN burst remains the best metric at all settings.

Table 13 Effects on pattern recognition from using different Purkinje cell background firing rates. The best metric for the DCN neuron is in all cases the number of spikes in the burst and is the one given in the table. Abbreviations for metrics of PC pattern recognition are: *FBu = firing rate of the initial burst; ISI = interspike interval of the first two spikes of the burst; LPa = length of the pause.*

	Purkinje cell firing rate (Hz)	Purkinje cell SNR of the best metric and of the pause length	DCN neuron SNR
spontPC	35.3	23.2 / 0.24 (ISI / LPa)	11.9
	56.6	16.8 / 1.8 (FBu / LPa)	30.4
	98.6	7.6 (LPa)	39.6
non_spontPC	56.6	13.2 / 1.7 (ISI / LPa)	63.0
	98.6	9.7 (LPa)	60.5

This parameter exploration shows that the pattern recognition principles of the DCN neuron are likely to hold over a broad range of Purkinje cell firing

rates. This is a comforting result in the light of the wide ranges of mean firing rates reported for Purkinje cells in awake animals in vivo, with some examples given in the following list.

- Young rats: 41 Hz (LeDoux and Lorden, 2002)
- Adult rats: 36 Hz (Savio and Tempia, 1985)
- Young/aged mice: 66/43 Hz (Schiffmann et al., 1999)

5.6.3 Background firing rate of the DCN neuron

DCN neurons also display a wide range of firing rates, with 10-80 Hz spontaneous firing reported in behaving animals and much higher rates in rebound bursts (Jaeger, 2011). As in the previous simulation for Purkinje cells, it is therefore of interest to see whether pattern recognition persists at different background firing rates of the DCN neuron model. Here, the excitatory synaptic inputs were set to a range of different levels: 15, 20, 25, 31, 37, 45, and 54 Hz (default is 20 Hz). The resulting DCN neuron background firing rates were 22, 39, 60, 92, 127, 165, and 198 Hz. The pattern recognition results at these firing rates are plotted in Figure 58 and show that pattern recognition is possible at all these DCN neuron firing rates, with a signal-to-noise ratio above 15 at all but the highest rate.

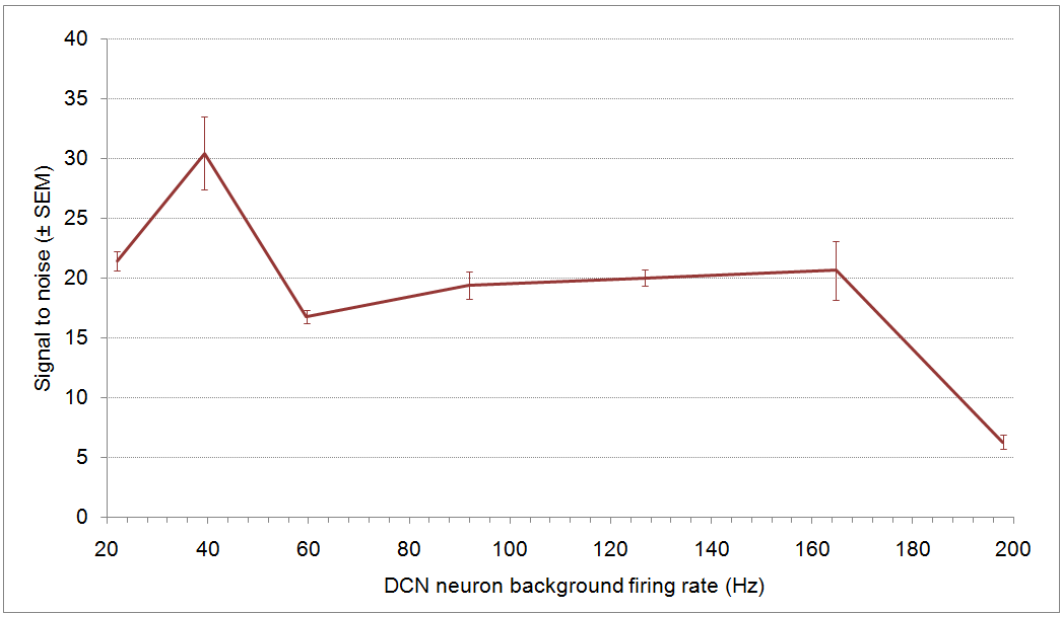

Figure 58 Effect of background firing rates of the DCN neuron on the SNR of its number of burst spikes. The PC spike trains were firing at a mean of 56.6 Hz in all simulations; the firing rate of the DCN neuron was varied over its dynamic range by changing its excitatory inputs.

5.6.4 Asynchronous pattern presentation

In this simulation, PF patterns were presented to the PC model asynchronously, as a control simulation to check that the Purkinje cell / DCN neuron circuit would perform pattern recognition even in the absence of perfect synchronisation of pattern inputs.

To this end, new sets of Purkinje cell spike trains were created by feeding PF patterns randomly dispersed over 2, 5, 10, and 25 ms time intervals respectively, which included the intervals examined by Walter and Khodakhah (2009). The Purkinje cell trains were then used as input to the DCN neuron in the usual way. A robust pattern recognition capability was maintained at up to 10 ms of pattern dispersion: while the fully synchronised presentation gave 30.2 as signal-to-noise ratio for the number of spikes in the burst, the 2 ms asynchronous

presentation gave 23.4±2.0; 5 ms gave 24.9±2.4; 10 ms, 17.0±0.6. Only the 25 ms interval gave a much declined pattern recognition result, with SNR = 2.1±0.1; this result is displayed in Figure 59 with one of the ten repeats each of the DCN neuron readouts for temporal spreads of 10 and 25 ms.

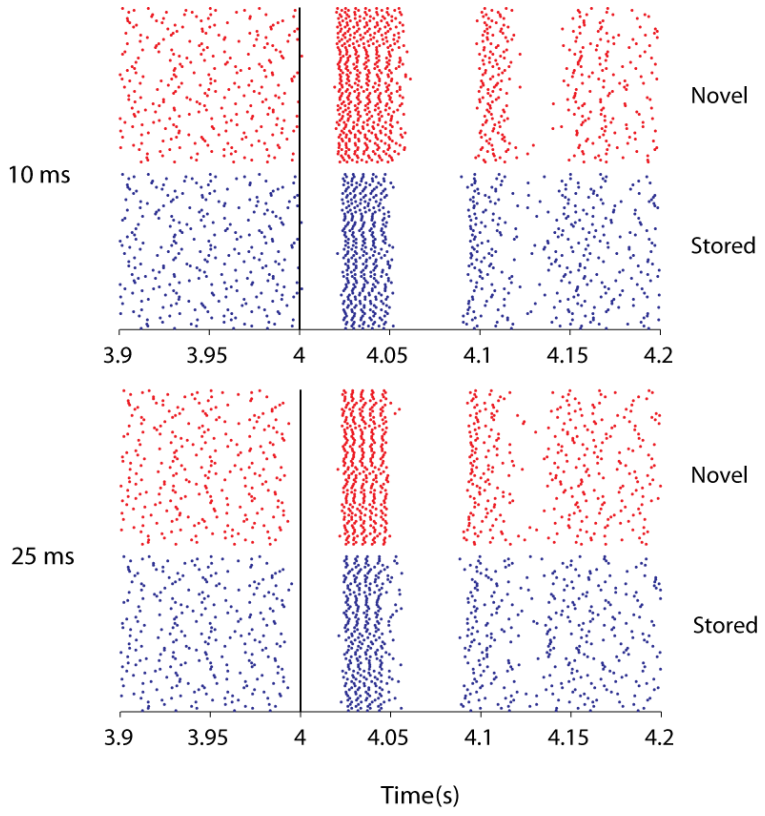

Figure 59 Readout by the DCN neuron of asynchronous PF pattern presentation to upstream Purkinje cells. The figure shows the results of 75 trials each for 10 ms (top) and 25 ms (bottom) intervals of pattern presentation. Note the almost removed difference of burst characteristics in the 25 ms situation, which is accompanied by an almost ten-fold decrease in the SNR for the number of spikes in the burst phase with 19.1 and 2.3, respectively in these trains (means of ten repeats were 17.0 and 2.1).

Pattern recognition was preserved in the Purkinje cell as well: the pause gave a signal-to-noise ratio of 1.8±0.2 at synchronous pattern presentation; 2 ms asynchronous presentation gave 2.1±0.2; 5 ms, 2.4±0.3; 10 ms, 2.1±0.2; 25 ms, 0.24±0.04. In contrast, the SNRs of the firing rate of the initial burst fell quickly

with increasing asynchronicity (16.8, 13.5, 7.2, 3.4, and 0.65). This parallel development of the pause SNRs but not of the burst frequency SNRs with the readout in the DCN is another indicator of the relative lack of importance of the Purkinje cell burst in DCN pattern recognition. Furthermore, these results argue against the previous claim of severely limited pattern recognition ability of pause-based PC pattern recognition with asynchronous pattern presentation (Walter and Khodakhah, 2009).

5.6.5 Number of active PFs

In these simulations the number of PFs that are active in a pattern – the sparseness of patterns – was varied, below and above the default of 1000. Steuber et al. investigated this, with 250 to 10,000 simultaneously active PFs (Steuber et al., 2007, Supplemental Data). Their finding was that PC pattern recognition using the pause length as a metric is robust to this variation, with signal-to-noise ratios of 5 and above, from a PF pattern size of 750 up to and including 7000.

With my modified, spontaneously firing, PC model (spontPC), I sought to repeat those tests and to investigate how the DCN neuron could distinguish the Purkinje cell readout at the different sparsity levels. While the Purkinje cell modifications that I have made – described previously in this document – have worsened the pattern recognition performance of the Purkinje cell pause, the discovery that DCN neuron averaging over many Purkinje cell inputs improves the pattern recognition capability made me decide to examine a broader range of PF numbers than Steuber et al.

The procedure for the presentation of the PF activity vectors to the Purkinje cell was as previously described except that the large number of Purkinje cell simulations made me limit the number of runs to 2×90×1 instead of the usual

2×75×10 runs. The errors of the mean for the Purkinje cell pause length SNR could therefore not be calculated.

The DCN neuron was presented with the 90 resultant spike trains at the maximum possible convergence of 90; this was run the usual 10 times for 75 novel and 75 stored Purkinje cell spike trains and SEMs of the SNRs were calculated. Figure 60 A shows the best DCN neuron pattern recognition results over the examined range of 50 – 25,000 active PFs. The graph shows the robustness of pattern recognition in that a wide range of differently sized patterns could be presented with well-preserved DCN neuron ability to discriminate between novel and stored patterns. Only when the number of pattern-carrying inputs went below 200 or above 10,000 did the signal-to-noise ratio go below 5. The range of 900-5000 PFs resulted in the number of spikes in the burst being the best metric; the best metrics at the other settings are listed in the appendix.

Graph B presents the ratios of the SNR for the best DCN metric to the SNR for the Purkinje cell pause lengths, that is, the amplification of the circuitry. It shows an intriguing property of increased amplification at the extremes of sparseness/denseness: the smaller differences between the novel and stored readouts in the Purkinje cell pause length are read out at approximately 100 times amplification for 200 and 15,000 active PFs, compared with the value of 14.1 for the default number of active PFs (this value, which has been obtained at a convergence ratio of 90, differs from that in the standard simulation setup where it was 17.0).

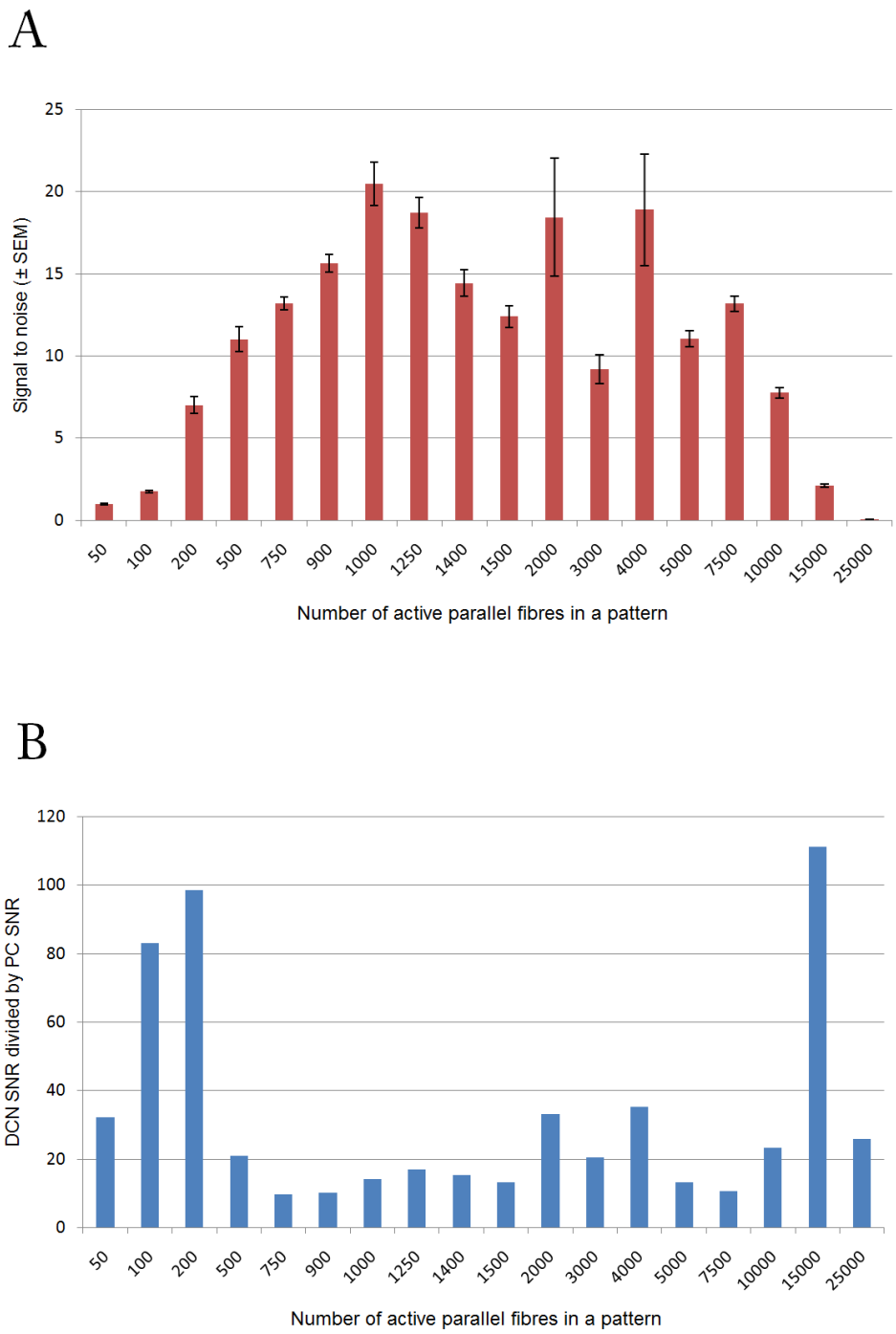

Figure 60 Effect of how many of the total 147,400 PF inputs to the associative net are active in a pattern. The patterns were presented to Purkinje cells converging in a 90:1 ratio on the DCN neuron. Due to the large number of Purkinje cell simulations required, these simulations are based on 90 repeated simulations rather than the standard 750, giving minor differences in SNRs; see text for details. A) The signal-to-noise ratios of the best DCN neuron metrics, all of which are metrics of the burst phase. B) The ratios at each PF setting of the SNR for the best DCN metric and the SNR for the Purkinje cell pause length; the ratio gives the amplification performed by the Purkinje cell to DCN neuron circuitry.

5.6.6 Number of stored patterns

Another important PF pattern parameter is how many different patterns can be stored so that there is still a clear distinction between novel and stored patterns in the Purkinje cell and, more pertinently, in the DCN neuron. To investigate this, the number of different patterns that were presented to the associative net and stored in its weights was varied in the range 50 – 1500, including the default 100. All were based on the default number of PFs active in a pattern (1000). This simulation was performed in the same way as the previous investigation of the number of active PFs per pattern: 90 Purkinje cell runs were presented with unique PF activity vectors; the resultant spike trains were transmitted to the DCN neuron at a convergence of 90.

The best SNRs at the different settings are plotted in Figure 61; the best metric at each setting is given in the appendix.

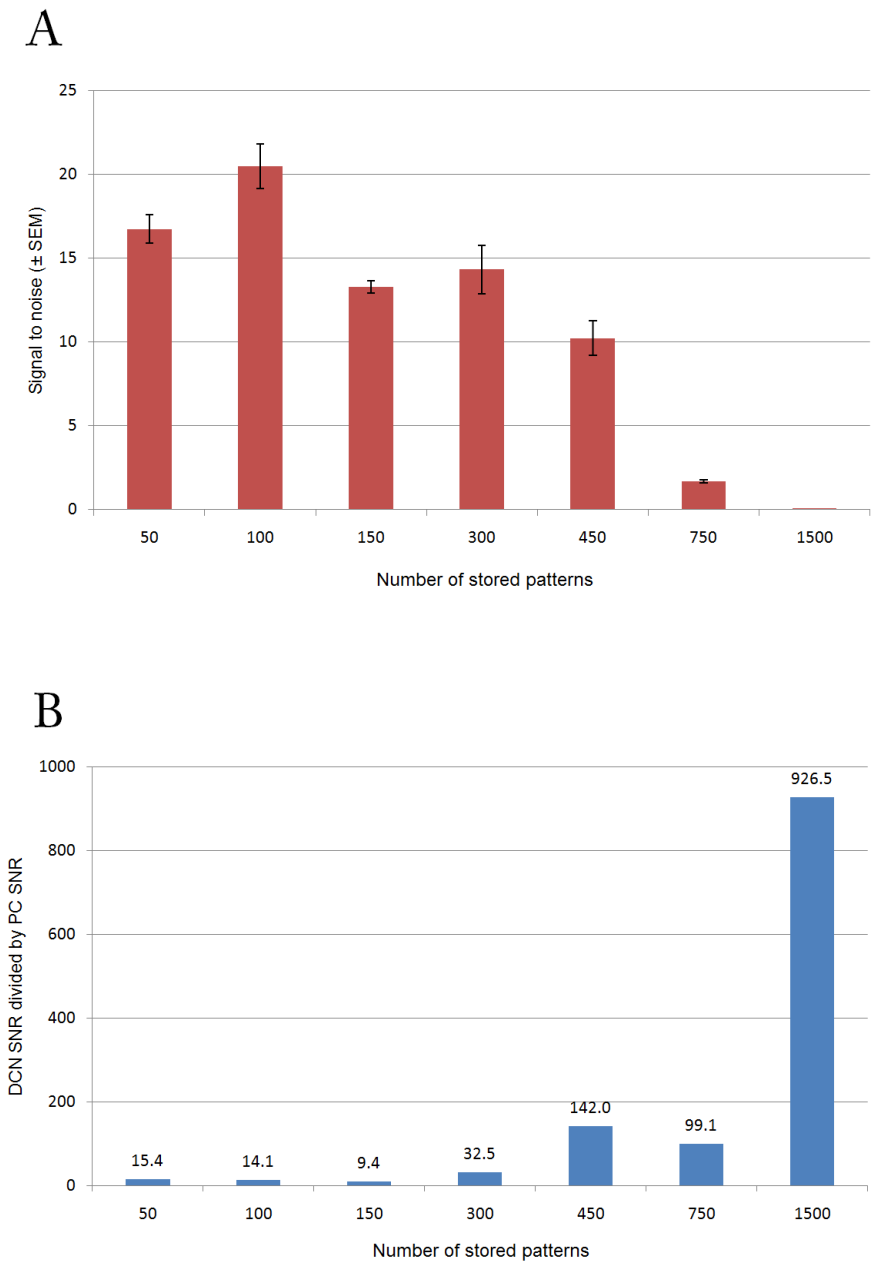

Figure 61 Pattern recognition at varying settings of the number of patterns presented to the associative net. A) Best signal-to-noise ratios in the DCN neuron; B) the amplification of the PC-DCN circuitry at each setting.

As with the simulations in 5.6.5, these results show that DCN pattern recognition suffers only modestly as the number of patterns is changed from the default of 100 patterns. Only at the highest setting, 1500 stored patterns, is the ability of the DCN readout of questionable value to downstream systems. Note

that at this stage, 1,500,000 changes of synaptic weight have taken place (1500 stored patterns, with each pattern of size 1000), meaning that the average PF-PC synapse has been halved in strength more than 10 times. Even so, the DCN neuron gives different means for the novel and stored patterns with the best metric – the time of the first spike after pattern presentation – at 19.1 ms and 17.0 ms, respectively, albeit with a very low signal-to-noise ratio of 0.07.

5.6.7 Feed-forward inhibition to the Purkinje cell during pattern presentation

Apart from their role of exciting Purkinje cells, PFs excite inhibitory interneurons (stellate and basket cells) which in turn synapse onto Purkinje cells. Thus, when a beam of PFs is stimulated, a Purkinje cell connected to this beam is initially excited by the PFs, and is a short time thereafter inhibited by stellate and basket cell inhibitory synapses (Eccles et al., 1967; Bao et al., 2010).

The timing of this *feed-forward inhibition* was quantified by Mittmann et al. (2005) as having a mean of 1.4 ms relative to the PF excitation of the Purkinje cell.

Steuber et al. (2007) examined the effects of feed-forward inhibition modelled based on the Mittmann et al. data and found that as the ratio of the delayed inhibition to the synchronised excitation exceeded approximately 1, the signal-to-noise ratio of the Purkinje cell pause started going down, from 18 without feed-forward inhibition, to 15 at a feed-forward inhibition ratio of 1, and 7 at a ratio of 2.

In the simulations presented here, feed-forward inhibition was added to the PC model in order to investigate its influence on the pattern recognition ability of the Purkinje cell – DCN neuron circuitry. The ordinary 75 × 10 setup was created with the PC model receiving feed-forward inhibition at different

inhibition/excitation ratios and the resultant spike trains were fed to the DCN neuron.

As in the Steuber et al. (2007) work, the ratio of feed-forward inhibition to the excitatory stimulus was calculated using the mean excitatory conductance in response to stored and novel patterns. As the conductances evoked by stored patterns on average were lower than those from novel patterns (approximately half, see Section 5.2.2) the actual ratio of inhibition to excitation was higher for stored patterns. Although it is possible that the storage of PF patterns by PF LTD could also lead to LTD at the inhibitory synapses onto Purkinje cells (Mittmann and Hausser, 2007), it has been shown previously that pattern recognition in Purkinje cells is unaffected by this inhibitory synaptic plasticity (De Sousa et al., 2009), and the inhibitory synaptic conductance was therefore kept the same for presentations of stored and novel patterns.

The Purkinje cell and DCN neuron pattern recognition results are presented in Figure 62, with A, the data for the signal-to-noise ratio of the Purkinje cell pause; B, the best metric of PC pattern recognition – the initial burst frequency at all ratios; C, the readout in the DCN where the best metric was the number of spikes in the burst at all settings.

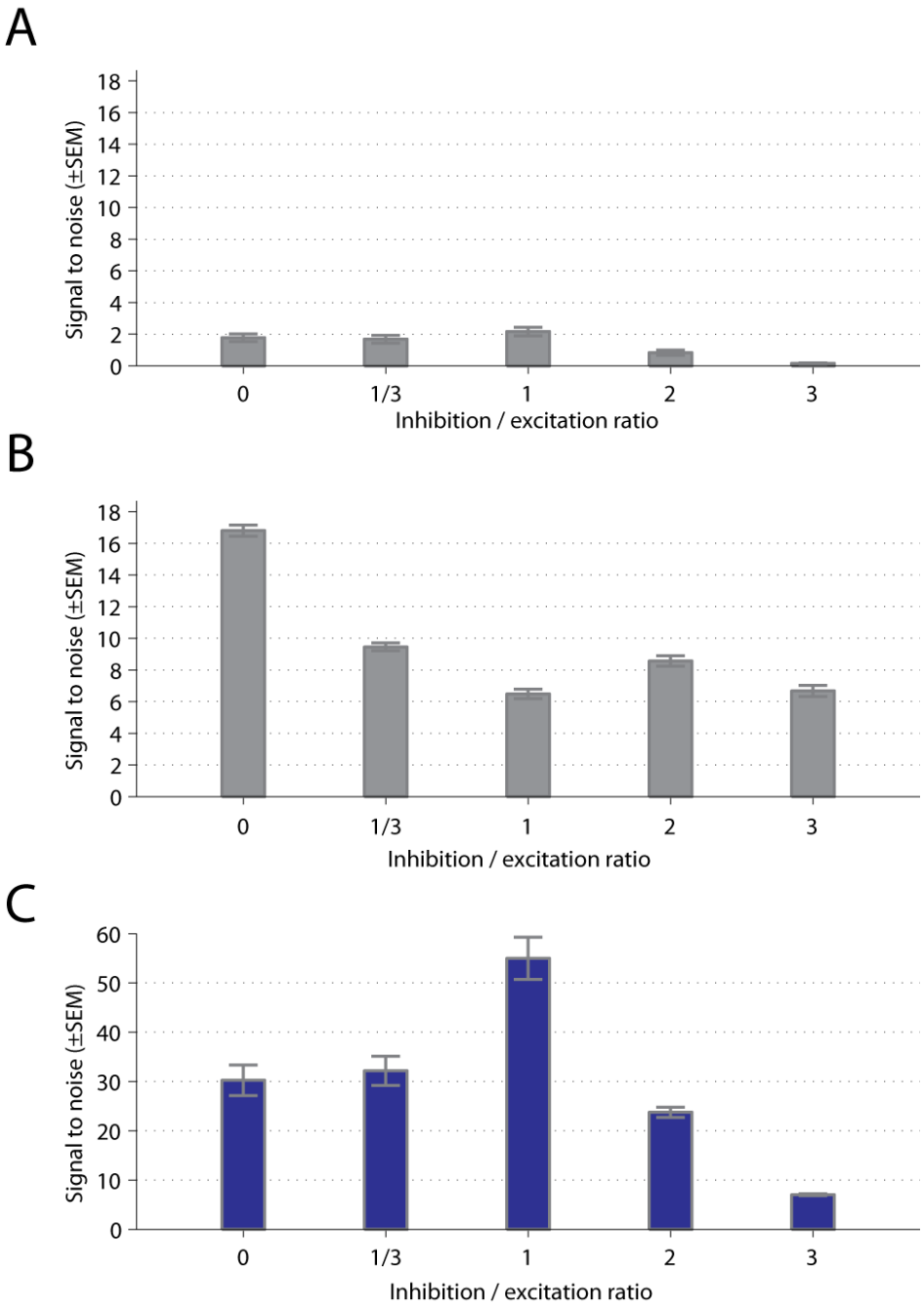

Figure 62 Pattern recognition effects of feed-forward inhibition onto the Purkinje cell. A) The Purkinje cell pause length signal-to-noise ratio; B) The best Purkinje cell metric, the frequency of spikes in the burst following the pattern presentation; C) the signal-to-noise ratio of the best DCN neuron model metric, the number of spikes in the burst.

It is an interesting finding that pattern recognition actually improves as a result of feed-forward inhibition at strengths up to equality with the excitatory

inputs. This is achieved both by an increased difference of means and a decrease in the normalised denominator of the signal-to-noise ratio, both in the Purkinje cell and the DCN neuron.

The best Purkinje cell metric was included in Figure 62 in order to give another indication that the SNR of the DCN neuron burst is largely determined by that of the pause length in the Purkinje cell. Comparing graphs (A) and (C) shows that the signal-to-noise ratios display the same trend of increasing up to the inhibition / excitation ratio of 1 and decreasing thereafter; this trend is not seen with the signal-to-noise ratios of the Purkinje cell burst frequency (B).

While it is well established that feed-forward inhibition of the Purkinje cell occurs, I judged that there are too many unknowns and complexities in the feed-forward inhibition network for it – within the scope of this project – to be so realistically modelled as to allow a 1.4 ms delayed feed-forward inhibition to be added as a default feature of the network. There are uncertainties in the timing: the 1.4 ms figure is the mean of a range of 11 neurons with a range of delays at 0.7-2.5 ms (Mittmann et al., 2005). Further, there is the complexity of different characteristics of the basket and stellate cell inhibitory effects (Bao et al., 2010). Hence, no simulations apart from this parameter exploration utilised feed-forward inhibition.

5.6.8 Limitation to the speed of Purkinje cell axonal transmission

In 4.5.4 I introduced the finding of Monsivais et al. showing that the Purkinje cell axon cannot reliably transmit somatic firing rates above approximately 300 Hz. This was used as the default setting in the pattern recognition simulations; before being used to provide inputs to the DCN neuron model, all Purkinje cell spike trains were filtered with an algorithm that examined

each spike interval and removed the second spike if it occurred less than 3 ms after the first spike, corresponding to a firing rate of 333 Hz. The Purkinje cell SNRs were always calculated using these filtered trains since the main interest was to compare the results of readout from the DCN with that of the readout of the Purkinje cell as seen from another cell – not from an electrode in its soma.

In this simulation, I have examined the pattern recognition capacity of the DCN model when presented with raw Purkinje cell trains. The simulation was only run for PC model non_spontPC, where 726 out of the total 750 novel trains had one or more spikes removed while no stored trains had any interspike intervals shorter than 3 ms. The first spontaneous PC model, spontPC, could not be used since no ISIs were shorter than 3 ms; I chose not to use spontPC_2 either – with only 81 of the novel trains filtered the results would probably not be very revealing.

The DCN model was run with the standard parameter values. The capacity of PC pattern recognition was analysed using its "raw", non-filtered trains. The results are slightly decreased signal-to-noise ratios in the absence of filtering both in the Purkinje cell (SNR of raw trains = 1.64±0.17; of filtered, 1.69±0.17) and in the DCN neuron (55.1±2.8 versus 59.6±3.8).

5.6.9 Reduced number of DCN neuron synapses receiving pattern inputs

A sign of the sensitivity of DCN neuron pattern recognition is how many of the 450 synapses of the neuron would need to receive Purkinje cell inputs resulting from PF pattern presentation of the same pattern type to create a DCN neuron output in which it is possible to distinguish a novel pattern from a stored pattern. In this simulation the DCN neuron was supplied with novel and stored

Purkinje cell trains as usual, but with increasing numbers of its synapses receiving pure background firing of Purkinje cells instead of pattern outputs.

A remaining high signal-to-noise ratio with a large proportion of the DCN synapses fed irrelevant information would allow pattern recognition to operate in a very noisy environment and thus make it more probable to function in real neuronal circuits.

The results of the simulations supported such a narrative. With inputs from spontPC, the DCN neuron stayed above a signal-to-noise ratio of 7 for the best metric with as few as 30 percent of its Purkinje cell synapses receiving a stored or a novel pattern (with all synapses from Purkinje cells receiving patterns, the convergence 450 setup has SNR = 30.2). The readout at this level is shown in Figure 63, which also serves to illustrate the utility of what I have called the interval-based metrics, as described in the caption of the Figure (see also Section 5.4.2).

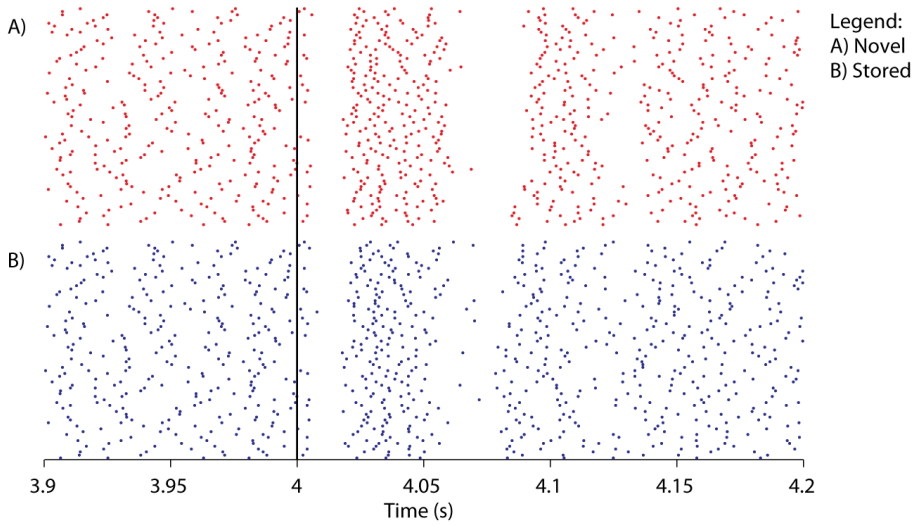

Figure 63 Result of the DCN neuron receiving pattern inputs to 135 of its 450 GABAergic synapses (convergence = 450). With only 30 percent of synapses receiving the pattern, the end of the burst can no longer be identified in several of the runs. Instead, the number of spikes in the first 50 ms after pattern presentation is the best metric, with means 5.0 versus 4.0 (novel/stored), giving a signal-to-noise ratio of 8. The number of spikes in the burst averages 2.9 versus 2.5 but the high variances caused by the ill-defined ends of the bursts make the signal-to-noise ratio only reach 0.5.

The simulation was repeated with all three PC models as inputs, with a fine-grained variation of the number of pattern-presenting synapses revealing several jumps in the signal-to-noise ratios, yet showing an overall trend of the SNR remaining above 9 in all models for 60% or more of synapses receiving pattern inputs (Figure 64), while showing that the active and/or passive electric properties of the three PC models create quite different trajectories of pattern recognition sensitivity.

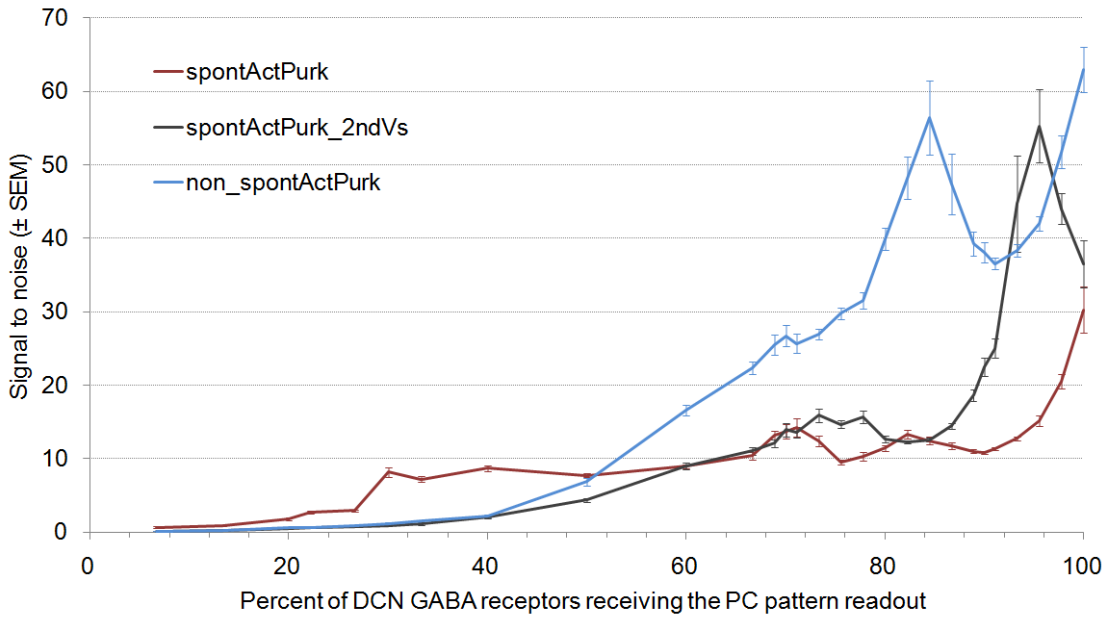

Figure 64 Effect of having different percentages of the Purkinje cell – DCN neuron synapses receive the pattern output, while the remainder receives background firing. At all points, the best metric has been used ; for all three PC models it is the number of burst spikes down to 50-60% of GABA receptors receiving patterns. For the lower percentages, see appendix.

5.6.10 Short-term depression of Purkinje cell synapses

Section 4.5.1 discussed short-term depression (STD) at the PC-DCN synapse and its incorporation into the network model. As it is well established that STD is present in the synapses, its range of neuronal coding functions (Section 2.4) made it interesting to evaluate whether it may be implicated in pattern recognition as well.

To be able to evaluate the contribution of STD at PC-DCN synapses to the pattern recognition performance of the DCN neuron, simulations with and without STD had to inject the same mean inhibitory conductance into the DCN neuron model before the pattern presentation. This relates to the discussion in Section 4.5.6 where I showed how the peak conductance is never reached when

STD is applied. If the peak conductance would not be adjusted in the absence of STD, the total inhibitory conductance in the background firing phase of the DCN neuron would be higher in the absence of STD and thereby the effect of background firing rate would interfere with the effects of STD.

To avoid this bias, I measured the mean conductance of the PC-DCN synapse in a sample of simulations both with STD switched on and off. Based on those measurements I decreased the peak $GABA_A$ conductance of the simulations with STD turned off to give the same mean $GABA_A$ conductance (76 pS) in the time before pattern presentation when STD was turned off as with STD on.

The results of the simulations with the default simulation setup in all other respects apart from STD being switched off and the $GABA_A$ peak conductance adjusted, revealed that STD worsens the pattern recognition performance. The number of spikes in the burst remained the best metric in the absence of STD, giving a signal-to-noise ratio of 43.6±3.0 (the default gave 30.2±3.1). The mean number of burst spikes increased by 0.3 to 7.1 for novel trains and by 0.1 to 5.1 for stored trains.

5.6.11 Projections of mossy fibres both to PCs and the DCN neuron during pattern presentation

The final investigation looks at the cerebellar circuitry on a larger scale. In Section 2.7 the collateral connections of the mossy and climbing fibre systems to the DCN were described. For the purposes of the simple spikes that we assume make up the PC pattern output, the mossy fibres are the relevant collaterals.

The granule cells that project PFs to Purkinje cells receive excitatory inputs from mossy fibres. At least two in vivo recording studies have characterised excitatory and inhibitory responses in the soma of DCN neurons (in the interpositus nucleus) as a result of sensory stimulation of the animal (Cody et

al., 1981; Rowland and Jaeger, 2005). Both studies found the expected inhibitory response that PC firing onto the DCN neuron would cause; in addition, some of the cells responded with a short-latency excitation, followed by the inhibitory effect. A possible explanation for this phenomenon is that those DCN neurons receive input from one or more mossy fibres that are involved in exciting the Purkinje cells that connect to the DCN neuron. It is known that the circuitry of climbing fibres to the Purkinje cell and the DCN neurons maintains somatotopy and there are indications that this holds for the mossy fibre system as well (Manni and Petrosini, 2004).

Published quantifications of the latency and their use in these simulations

The Cody et al. (1981) study found the excitatory response at a mean of 13.0 ms after paw stimulation in awake cats, and the inhibitory response at a mean of 25.6 ms, giving a latency for the inhibitory response relative to the excitatory at a mean of 12.6 ms. Rowland and Jaeger (2005) performed experiments in anaesthetised rats where air puffs to the upper lip evoked the excitatory and inhibitory responses at mean times of 15.1 ms and 21.9 ms, respectively, giving a mean latency of 6.8 ms.

While the DCN neuron model is primarily based on rat recordings and on rat morphology, the cat study of Cody et al. was made in awake animals and therefore of special interest. In either case, the pattern recognition study would benefit from showing effects at two different realistic settings. Hence I created simulations where the default setup of Purkinje cells and DCN neuron was modified so that the excitatory inputs to the DCN neuron provided a synchronised burst, apart from their usual randomised background firing. This synchronised burst was designed so that it could be seen as a membrane potential

deflection in the DCN neuron soma 6.8 or 12.6 ms prior to the onset of the inhibitory response in the DCN neuron soma (based on the two experimental studies mentioned above). A typical membrane potential response to this excitation of the DCN neuron before pattern presentation is shown in Figure 65 (bottom, shown for a delay of 6.8 ms).

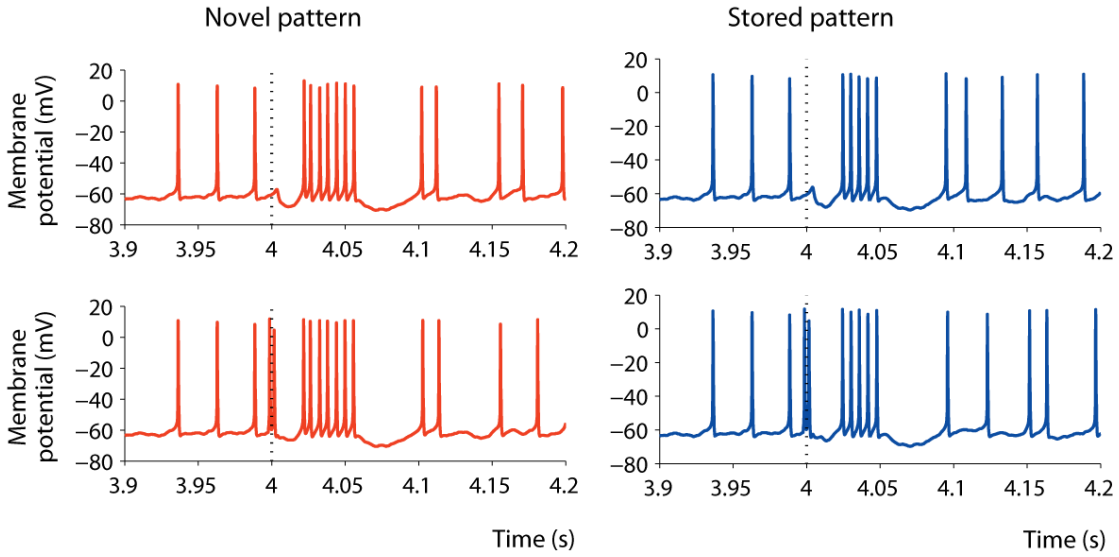

Figure 65 Mossy-fibre collateral bursts to the DCN neuron concomitant with PF pattern presentation to the Purkinje cells (spontPC) that connect to the DCN neuron. The upper voltage traces show the default simulation setup where the excitatory inputs to the DCN provide mere background stimulation, while the lower traces show the same setups but with the addition of a synchronised input to 100 out of all 150 excitatory synapses; this happened 6.8 ms before the effect of the synchronised PF firing reached the DCN via the Purkinje cell inhibitory firing. Note how the modified setting gives a decreased hyperpolarisation during the DCN pause before its burst.

The lower traces of Figure 65 show the DCN neuron response at the setting giving the best SNR, at 49.2±4.9; a similar improvement from the default setup (SNR = 30.2±3.1) was present at several proportions of the excitatory synapses receiving collateral inputs.

As the sample traces show, the mossy fibre collateral firing is accompanied by a decreased hyperpolarisation, both when novel and stored patterns are presented. With the 100 out of 150 excitatory synapses active as in Figure 65, the mean membrane potential minimum in the DCN pause phase changed from on average -69.0 to -66.6 mV for novel patterns and from -68.5 to -66.2 mV for stored patterns. The increased SNR in the face of decreased DCN neuron hyperpolarisation is yet another indicator of the relative irrelevance of the Purkinje cell burst response in evoking a differential burst response in the DCN neuron.

Examinations to show if improved pattern recognition results are local extremes or general trends

I decided to investigate whether improved pattern recognition results observed at some settings constituted local extreme values or were part of a general trend of improved pattern recognition in the presence of mossy fibre collateral inputs. For this purpose I made a detailed characterisation of the intervals around these points and repeated all simulations in non_spontPC and spontPC_2. The results, shown in Figure 66, are that the mossy fibre collateral firing only gives improved pattern recognition in one particular range of the number of active PFs (recognisable from the density of data points) , and only in model spontPC.

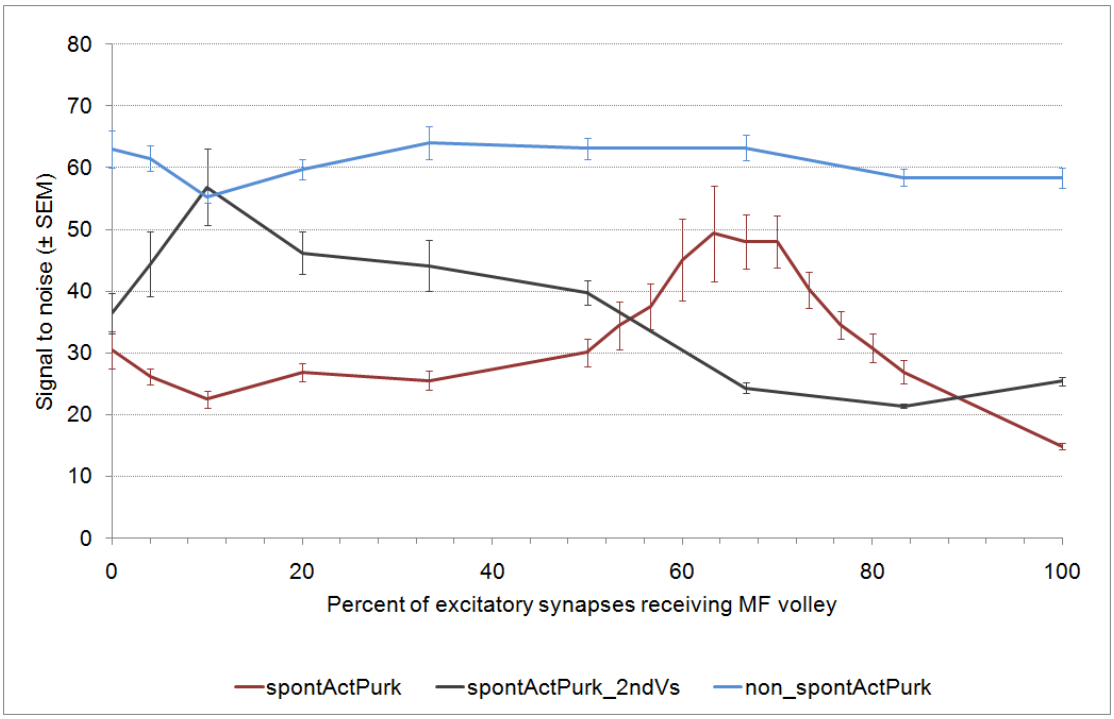

Figure 66 The DCN neuron model recognising PC pattern outputs accompanied by increasing proportions of mossy fibre collateral inputs firing 6.8 ms prior to the DCN receiving the PC pattern output.

Additionally, I ran the full set of simulations with the 12.6 ms delay found in the Cody et al. study (1981). This resulted in the spontPC model no longer being the one improving with collateral firing, but this performance increase was now present in spontPC_2, and at any examined setting of the number of these active collaterals (see Figure 67).

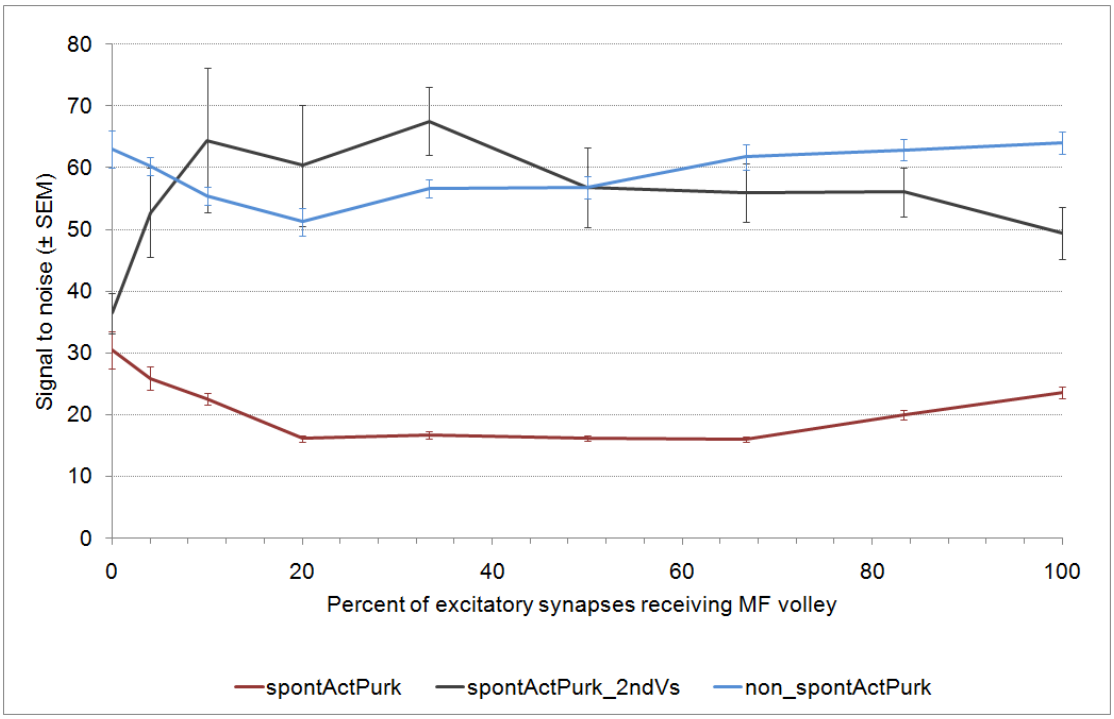

Figure 67 Same as Figure 66 but with 12.6 ms delay between the synchronised inputs.

In sum, the addition of the biologically probable mossy fibre collateral firing to the DCN neuron, prior to the PF to PC pattern presentation, does not consistently decrease or increase pattern recognition capacity overall in these examined models with realistic delay times. That is another reassuring result which rounds off the pattern recognition results part.

5.7 Discussion and limitations of the pattern recognition project

I will here address some of the limitations of my studies of cerebellar pattern recognition. Several of the parameter exploration studies raise more questions than they answer and many suffer from lacking physiological data. For example, the study of mossy fibre collateral firing shows that with the right level

of excitation, there is an amplification of pattern recognition resulting from the collateral connection. If we were to assume that this connection plays a role as amplifier, are there physiological mechanisms to ensure that the inputs reach such optimal levels? To answer this, it would first need to be more precisely established to what extent the mossy fibres providing the granule cell input for the pattern presentation actually connect to the excitatory DCN neurons, and how many different mossy fibres reach each DCN neuron. Following this, recordings of such connected neurons would have to be undertaken simultaneously with granule cells, Purkinje cells, and DCN neurons.

A limitation to my approach to analysing pattern recognition data is that of the lacking statistical significance testing of pattern recognition metrics. The interval-based metrics added 63 new metrics to the original 12 ones, in principle necessitating that results of significance (the SNRs) be corrected for the 75 multiple observations. Although most of both the original and the interval-based metrics turned out to be of no use, it raises the problem that a multitude of tests tends to find something, even if that something is not causal to the phenomenon observed.

Yet, the original metrics were developed based on the inspections of the raster plots of DCN neuron pattern readout and it was clear that the burst was an, or *the*, essential feature before the signal-to-noise ratios confirmed it. The metrics that do not relate to the burst give a high SNR in many cases, but the highest SNRs have always been those relating to the burst, even when the interval-based metrics were the best. For example, in the study with different numbers of Purkinje cell synapses being provided with PC pattern readout, many of the lower percentages (see appendix) gave best results for “3rd 20 ms, number of spikes”; this metric of the number of spikes in 40-60 ms following pattern presentation is in effect a metric of the burst length.

The simulations in this chapter have all assumed that patterns are presented in a distributed fashion over the Purkinje cell dendritic tree. If it were to turn out that the 1000 out of 147,400 parallel fibres that were active during pattern presentation were localised to specific parts of the dendritic tree, the simulation results would likely turn out differently. For example, if clusters of active PFs would be firing onto the same dendritic branch, saturation of the current flow in the dendrite would likely set in and therefore, the difference in responses to stored and novel patterns would likely be much less pronounced.

The remaining sections of this chapter will discuss specific results in terms of their importance and the new questions they raise.

5.7.1 The shortened burst of the DCN neuron upon pattern recognition contradicts earlier theories

Section 5.5.1 described how the DCN neuron responded with a burst of spikes when a PF pattern was presented to the PCs of the network. The burst was shortened when the PC recognised a previously stored pattern (see for example Figure 48) and the number of spikes in the burst was the best metric of pattern recognition in the DCN neuron.

The result stands in contrast to the commonly held theory of how LTD-based learning in the PF-PC synapses would affect cerebellar output. As discussed with regard to eye blink conditioning at the end of Section 2.7.4, it is often assumed that learning would lead to increased DCN neuron output, which in the case of a motor behaviour such as conditioned eye-blink responses would help initiate movement. Note however that even a decreased DCN neuron output upon pattern recognition could fit with the theory of movement induction if an inhibitory interneuron in the chain of neurons leading from the DCN neuron to

the muscles would be found to be spontaneously active, thereby recoding a decreased DCN output to an increased firing rate.

5.7.2 Mechanism of the modulation of the burst duration

The shortened length of the DCN burst was most likely caused by the similarly shortened pause in PC firing, as opposed to being caused by changes in the PC burst following pattern presentation. This was shown in Section 5.5.4 and in several of the pattern recognition explorations of Section 5.6 with evidence that the SNR of the DCN readout changed in concert with changes in the SNR of the PC pause length rather than with SNRs of metrics of the PC burst phase.

Steuber et al. (2007) showed that the pause of the PC resulting from input to the PF-PC synapses could be caused by intracellular Ca^{2+} rises that activated calcium-dependent potassium channels (KCa). These channels create an afterhyperpolarisation (AHP), that is, a period of lowered membrane potential following the PF-triggered spikes, and thereby prevent further spikes following a strong PF input. Steuber et al. (2007) further suggested that the stronger input caused by a novel PF pattern increased the Ca^{2+} influx and the AHP and thereby caused a longer pause (see Figure 41 A).

5.7.3 Convergence causes amplification of pattern recognition

The results of exploring PC to DCN convergence showed that the network produced a much lower than theoretically possible averaging effect. This can be expected to happen in any biological pattern recognition device since such devices operate with inherent noise that digital computations can filter out. Possible sources of noise that could decrease the averaging effect include the introduction of spatial noise by the distribution of synapses over the DCN neuron dendritic

tree. The ideal averaging device would have equally fast transmission times from all points of the dendritic tree, while the DCN neuron has variable transmission delays from the dendritic synapses to the soma reaching up to a couple of milliseconds. This spread of delays will increase the variance of somatic responses to stored and novel patterns, which will decrease the signal-to-noise ratio and result in a diminished pattern recognition performance.

A severe limitation of the convergence study was shown in the matrix simulations of theoretical convergence effects. Those indicated that with the random drawing of spike trains from the pools of Purkinje cell spike trains, correlations between Purkinje cell spike trains were introduced, driving noise lower and giving higher SNRs at the higher convergences. However, the supralinear scaling only began for convergences above 50 at which point the averaging function of the network had already been established; at convergence = 50 the amplification was 10.9 (DCN neuron number of burst spikes / Purkinje cell pause length).

5.7.4 Pattern recognition amplification is independent of linear coding

Walter and Khodakhah (2009) imply that the Purkinje cell to DCN neuron convergent connectivity is ideally suited for amplifying what they call a linear code, that is, with information provided in the frequency of the Purkinje cell burst following pattern presentation. The pattern recognition study in this thesis has shown that not only is this linearly coded information unlikely to significantly contribute to the pattern recognition capability of the cerebellar circuitry, but also that the pause-based pattern recognition opposed by the same authors can be amplified in a convergence-based manner.

5.7.5 Averaging in the efferent connections of DCN neurons

It is interesting to note that many of the pattern recognition results presented here predict that the targets of DCN neurons should be able to distinguish between novel and stored pattern presentations particularly well should there be mechanisms in place to effect a second stage of averaging – of the outputs of DCN neurons themselves. It is not clear how the DCN projection neurons that I have modelled are connected to create eventual outputs in the forms of, for example, muscle contractions.

As a hypothetical example, I briefly discuss the study where only 50 PFs were active in each pattern presentation. This resulted in a mean SNR of 1.0, which was shown to correspond to 31% faulty classification (Table 5). If 30 DCN neuron outputs would be averaged via relay neurons in the brain stem and spinal cord to reach motor neuron targets, the percent of incorrect responses would decrease in a supralinear fashion to 0.3% (also Table 5). Hence, were such post-DCN averaging mechanisms to be found, they would drastically extend the pattern discrimination capabilities of the cerebellum.

5.7.6 Information content in the DCN neuron burst

The DCN neuron burst was shown to contain the most information in the number of spikes it contains rather than in its length in units of time (Section 5.5.1). This was caused by a larger variance of the length of the burst in time – that is, there was more noise present in the signal, giving a lower mean signal-to-noise ratio. It is tempting to speculate that the number of spikes generally is a more noise-resistant metric than the duration of a spike train or burst, given that the thresholding mechanism of neurons means that adding an extra spike to the output of the neuron likely requires more changes in the amount of synaptic

inputs (and other mechanisms that influence the membrane potential) than merely shifting the timing of a spike.

5.7.7 Marr's predictions

In relation to the discussion of the results of the number of active PFs during pattern presentation, it is worthwhile to revisit the predictions made by David Marr (1969). His expectation was that a minimum of 0.25% of PF-PC synapses need to be active for the pattern they make up to be read out by the Purkinje cell, corresponding to approximately 600 PFs presenting patterns to the associative net of these studies. In my parameter exploration, 500 such PFs gave an SNR of 0.53 while the next setting of 750 gave an SNR of 1.36. The corresponding data for the DCN readout are 11.0 and 13.2. Marr did not include DCN neuron averaging in his theory, but its presence proves his minimum to be a realistic estimate.

6. DCN neuron readout of irregularity in Purkinje cell firing

Note: part of this chapter has been published as a journal article (Luthman et al., 2011).

This project investigates the irregularity of timing of Purkinje cell (PC) spikes and its effects on the DCN neuron. The concept of irregularity was introduced in Section 2.6 together with its quantification using the coefficient of variation (CV), CV_2, and gamma probability functions (gamma functions for short) for describing the ISI distributions.

PC spike trains typically show a wide variation in the interspike intervals (Figure 68), giving CVs of approximately 0.4-0.5 for PCs in adult rats (Savio and Tempia, 1985; Stratton et al., 1988; LeDoux and Lorden, 2002). It has, however, been shown that the seemingly irregular firing of PCs masks periods of regular firing and that those periods coincide with behavioural states (Shin et al., 2007a).

Purkinje cells are bistable; the membrane potential and spike output switches between two states, the up- and down-states, where the downstate is characterised by hyperpolarisation of the membrane potential and lacks simple spike firing. Via sensory stimulation, activity in the climbing fibres can switch PCs between the two states (Loewenstein et al., 2005; Rokni et al., 2009).

In the study of Shin et al. (2007a), regular firing only occurred during the up state of the membrane potential and Rokni et al. (2009) showed that the up state is intrinsically made up of high-frequency regular firing that is modulated into more irregular firing by inhibitory synaptic inputs.

Thus, the property of bistability inherently gives an irregularity to the output of the Purkinje cell.

For any kind of difference in PC irregularity to affect the behaviour of the animal, it must be assumed to change the output from the DCN neurons. Short-term depression (STD) of the PC-DCN synapses can be expected to contribute to how the DCN neuron output is modified.

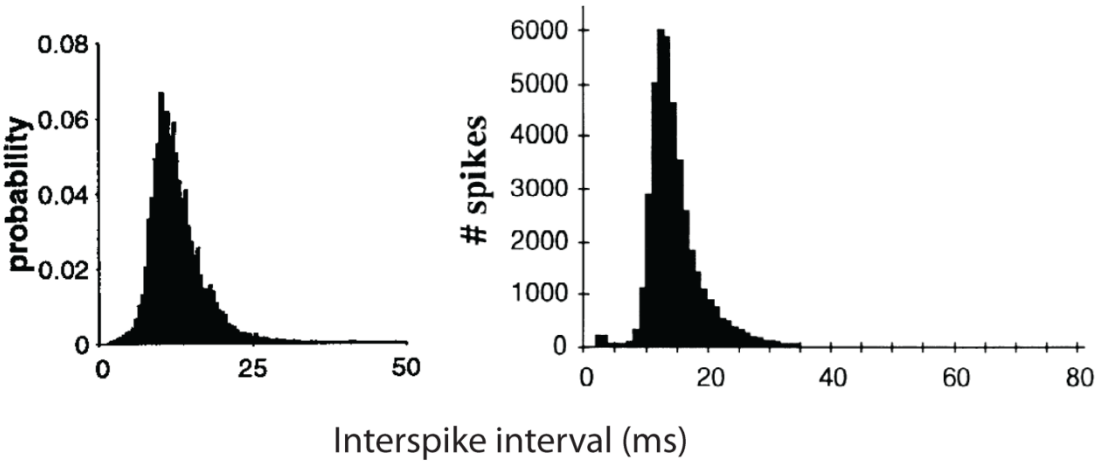

Figure 68 Interspike interval distributions of Purkinje cells recorded in vivo. The left figure is from Goossens et al. (2001); the right, from De Schutter and Bower (1994b).

STD of the PC-DCN synapse was described in Section 2.4 and its incorporation into the DCN neuron model in 4.5.1. As discussed there, STD makes the unitary conductance of the PC-DCN synaptic channel depend on the prior firing rate of the connecting Purkinje cell. Figure 69 shows how STD decreases the inhibitory conductance to the DCN neuron that results from a PC spike when it receives PC input that fires with a high rate compared to that with a lower firing rate. Since irregularity of PC firing implies variations in the instantaneous firing rates it can be expected that irregular inputs lead to modified conductances of the PC-DCN synapse; those changes should influence the firing of the DCN neuron.

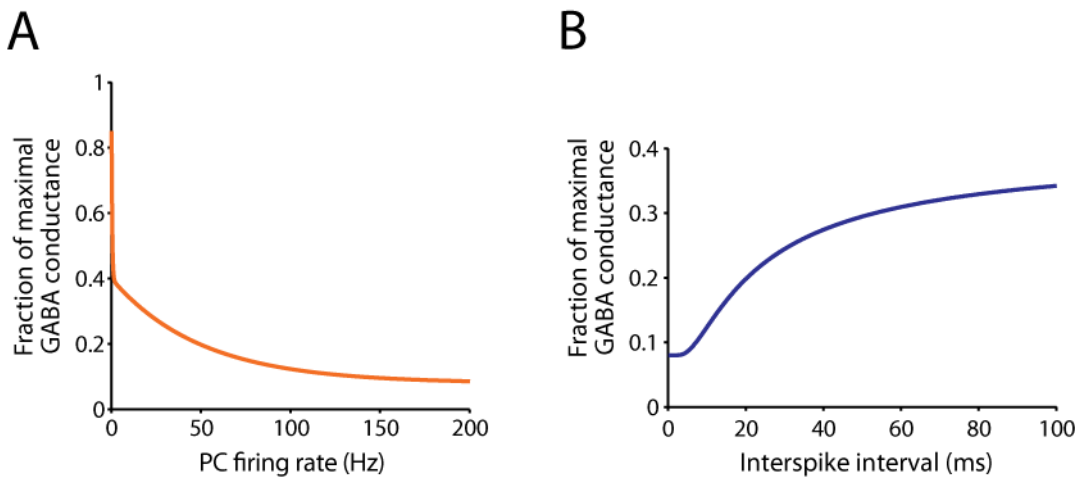

Figure 69 The short term depression (STD) element introduced in Chapter 2 (Figure 2). It is here depicted both depending on firing rate (A) and its inverse, the interspike interval (B).

Another factor that can be expected to be of importance is the convergence ratio of PCs to DCN neurons. I discussed in Section 5.5.2 how high convergence ratios of desynchronised firing of PCs would lead to a more tonic hyperpolarising effect than inputs of low convergence or inputs that are synchronised. In the latter case one can therefore expect longer windows where the inhibitory stimulus is reduced and where the spontaneous firing of the DCN neuron would combine with the excitatory inputs to cause a fast firing. On the other hand, naturally, the periods of enhanced inhibitory input would decrease DCN neuron firing. Taken together, low-convergence inputs should give a more varying output than high-convergence input.

The present project aimed at elucidating the effects of STD and of convergence in the presence of different levels of irregularity of PC firing. I did this by modelling PC firing of varying irregularity and firing rate using the artificial spike generator element GammaStim (Section 4.5.4); later, I repeated simulations using real PC recordings of different levels of irregularity to confirm observations in a more biologically realistic setting. Thus, this project did not use

the PC model as input. Further, the inhibitory input rate to the DCN neuron model was 60 Hz instead of the 56.6 Hz of the PC model. In other respects, the simulation setup equalled that of the pattern recognition project.

6.1 Simulations of irregularity using the GammaStim spike generator

In this part of the present project, the GammaStim spike generator was used to model PC input to the DCN neuron model. Based on personal communication by Chris de Zeeuw (Erasmus MC Rotterdam) I chose 90 as the default convergence ratio in this part of the project.

As when the contribution of STD to pattern recognition was evaluated (Section 5.6.10), the $GABA_A$ conductances needed to be identical in the case of full regularity of PC firing when STD was used as when it was not. With this baseline equality of conductances, the contribution of STD to the conductances and to the DCN neuron firing could be evaluated. The equalising of baseline conductances was done in the same manner as in the pattern recognition project and was described in Section 5.6.10.

6.1.1 Modelling irregularity of PC firing

Different levels of irregularity of PC firing were modelled with the GammaStim synaptic element, using irregularity settings from 0 to 1 where 0 was completely regular input – that is, ISIs of constant length – and setting 1 gave ISI lengths drawn from a gamma distribution of specified order. Equation 24 describes how the ISI lengths were calculated:

$$ISI = (1-x)\,y + xyz \tag{24}$$

where x is the irregularity setting, y is the desired mean of the ISIs, and z is a random number between 0 and 1, drawn from a third degree gamma distribution. Figure 70 shows some examples of ISI distributions resulting from different irregularity settings sampled over 15 seconds of GammaStim firing.

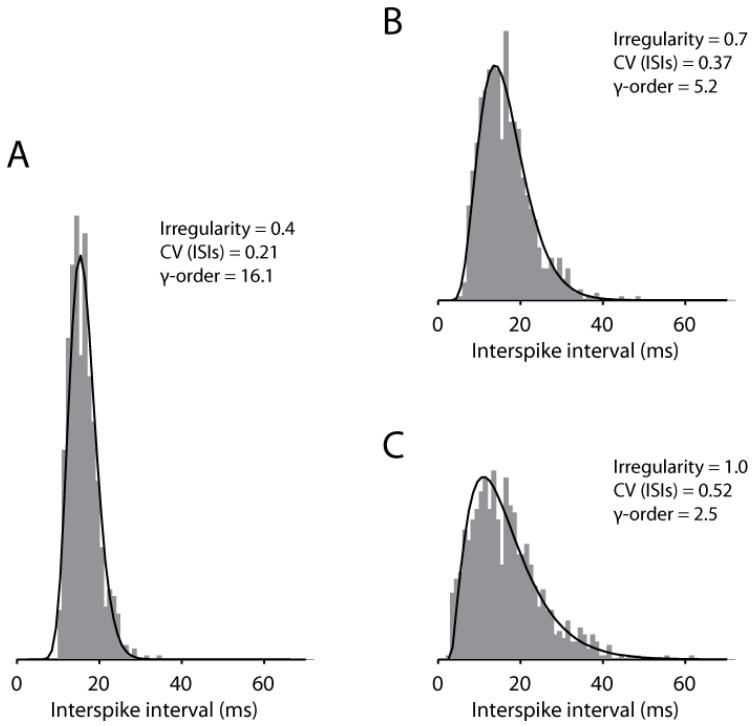

Figure 70 Examples of ISI distributions of GammaStim outputs with an irregularity setting (Equation 24) of 0.4 in (A), 0.7 in (B), and 1.0 in (C). (B) has a similar gamma order as that of the wild-type real PCs used in Section 6.2, while (C) in the same way corresponds to the *tottering* PCs (compare with Figure 74).

6.1.2 First results

The first set of simulations was with GammaStim firing at 60 Hz at a range of settings of increasing irregularity: 0 (fully regular trains), 0.2, 0.4, 0.6, 0.8, and 1. This PC output was sent to the PC-DCN synapses, with and without STD. The DCN neuron was allowed to equilibrate for 5 seconds and simulations were then run for 90 seconds of neuronal time. The results of these simulations are plotted

in Figure 71: with STD switched on, the DCN neuron firing rate increased from 33.3 Hz at regular PC firing to 40.6 Hz at the highest irregularity, an increase of 22.0%. This was in contrast to the situation with STD switched off where firing only increased by 1.4%, from 33.3 Hz to 33.8 Hz. Thus, at this firing rate and convergence ratio, irregular inputs speed up the DCN neuron spiking and STD is the main cause of it.

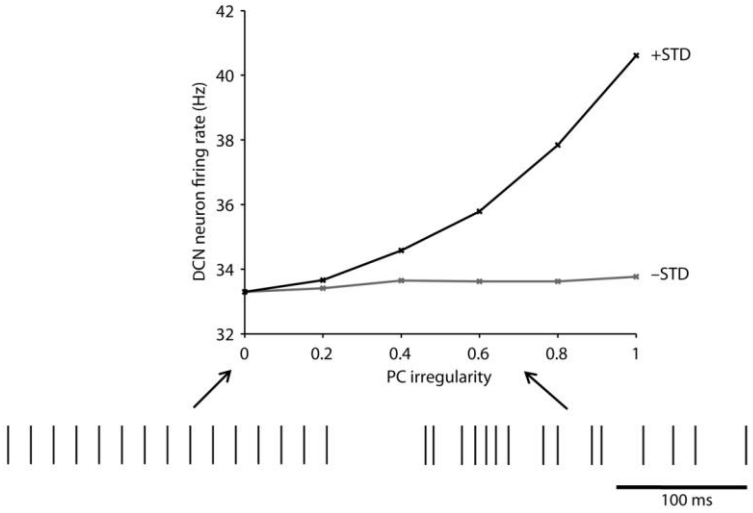

Figure 71 DCN neuron firing as a function of PC irregularity, in the presence and absence of short-term depression (STD), showing how the DCN neuron responds with increasing firing rates as the irregularity of its $GABA_A$ synaptic inputs increases. The insets below the graph are of two spike trains, both with a frequency of 60 Hz. The left train has constant ISI lengths, resulting from an irregularity setting of 0. The right train illustrates the effect of increasing the irregularity setting to 0.7 (corresponding to ISI distribution B in Figure 70).

The increased firing rate in the presence of STD was accompanied by a decreased $GABA_A$ conductance, with the mean $GABA_A$ input over all synapses decreasing by 11.2% from 38.0 nS at fully regular inputs to 33.7 nS at inputs of irregularity = 1. In the absence of STD, the conductance was unchanged at 38.0 nS.

The decreased $GABA_A$ conductance with irregular firing in the presence of STD is understandable from the shape of the curve of the STD function in Figure 69. As irregularity is introduced, the previously constant ISI length of 16.7 ms changes to a mix of ISI lengths, still with a mean of 16.7 ms. Graph B in Figure 69 shows that for example a one-millisecond decrease in the length of an ISI from 16.7 ms (or anywhere else from ca 5 ms to 100 ms, i.e., a firing rate of 10–200 Hz) creates a larger decrease in the $GABA_A$ conductance than the *increased* conductance resulting from the same *increase* in the length of an ISI. The graph shows how this relationship covers most of normally occurring PC firing rates; this means that the decreased $GABA_A$ conductance from STD during irregular firing can be expected to be a general feature at the PC-DCN synapse.

However, the larger range of PC ISI lengths that results from irregular firing may have another effect. If the PCs fire synchronously or if the physical convergence is low, the longer ISIs may allow an increased number of spontaneously generated DCN neuron spikes, just like the shorter ISIs may allow fewer spikes. I discussed this in Section 5.5.2 together with its implications for pattern recognition and it could be part of the explanation for the effects of irregularity too, at low levels of synchronicity/convergence.

To evaluate these hypotheses, I designed experiments to test the effects of PC firing irregularity in the presence and absence of STD, at different PC firing rates and levels of convergence.

6.1.3 Parameter exploration 1: GammaStim firing rate

The first parameter exploration was of GammaStim firing rate, in the range 10–150 Hz with 10 Hz intervals. The same irregularity levels as previously were used and all simulations were run with a convergence setting of 90. Results are shown in Figure 72.

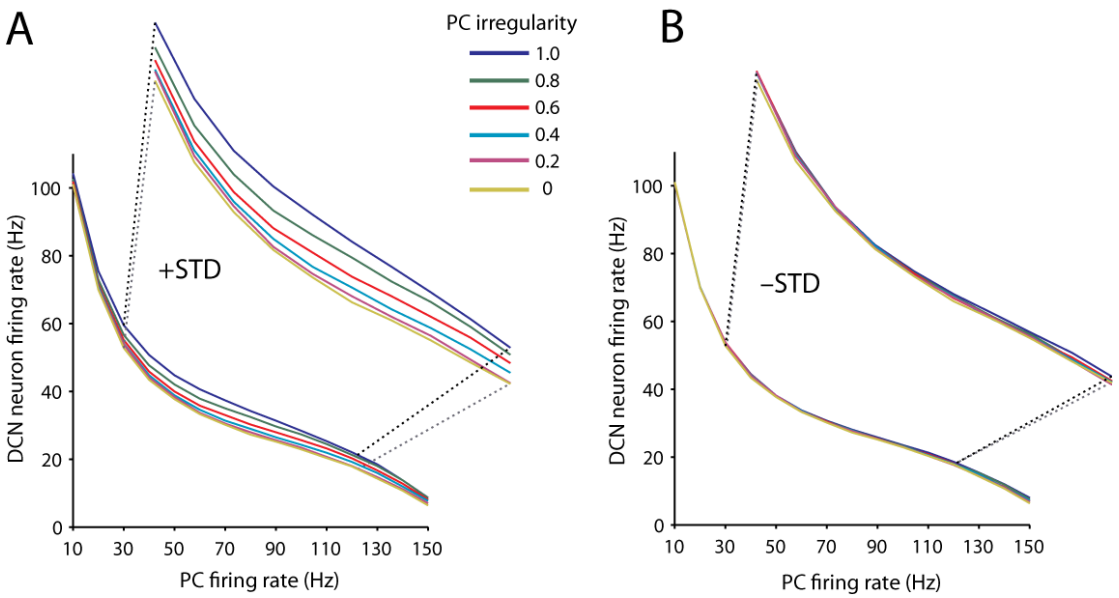

Figure 72 DCN neuron firing at PC inputs of different rate and irregularity. A) The results of STD switched on, with higher PC irregularity causing higher DCN firing rates across the spectrum of PC firing rates. B) Without STD, little of the speedup occurs.

The irregularity-induced speedup from STD remained at all PC firing rates in the range, but was most pronounced at the intermediate ranges (Figure 72, A), covering the most commonly occurring rates in vivo (Figure 68).

6.1.4 Parameter exploration 2: convergence ratios

In another parameter exploration I investigated the effect of different convergence ratios on the STD-dependent speedup for increased irregularity values. The following divisors of the total number of $GABA_A$ synapses (450) were used as convergence ratios: 1, 3, 9, 18, 45, 90, and 450. The simulations were run with GammaStim firing at 60 Hz, at the previously used irregularity settings, and in the presence and absence of STD. The results are shown in Figure 73.

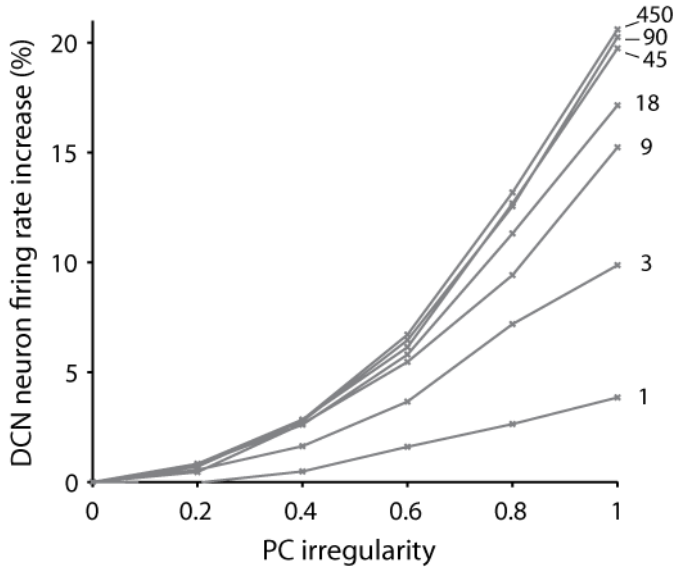

Figure 73 Exploration of different convergence ratios of PCs to the DCN neuron: the STD-based acceleration of firing for irregular inputs goes up with increasing convergence ratios. The graph plots results of the equation $(STD_{on}\text{-}STD_{off})/STD_{off}$.

As was the case with the pattern recognition effects of convergence (Section 5.5.2), a saturation of the effect (here, increased DCN firing; in pattern recognition, signal-to-noise ratios) sets in at the highest convergence ratios. Below the point of relative saturation of effects – at convergence of 45 – the speedup from STD abates as the convergence ratio is lowered. With full synchronicity or with a convergence of 1, the presence of STD led to an increase of DCN neuron firing rate by only 3.8% with maximally irregular input compared to with fully regular input, while the $GABA_A$ conductance decreased by 9.3%. In comparison, convergence 450 gave a 21% increased firing rate together with a larger $GABA_A$ conductance decrease, at 11%. The diminished effect of STD at low convergence ratios will be discussed in detail in the following section.

6.2 Investigating effects on the DCN neuron of real PC inputs of varying irregularity

Understanding the two potential effects of irregularity – the decreased conductance in the presence of STD and the changed firing opportunities which result from irregular ISI lengths – should benefit from being studied for spike trains recorded from real Purkinje cells in mice.

In addition to the normal variation in the firing rate of PCs, there are mutated strains of mice with an increased irregularity of PC spiking. One of these strains is *tottering*, which has a mutation in the Cacna1a gene that encodes the pore-forming α1A-subunit of P/Q-type voltage-gated calcium channels. *Tottering* mice have poor motor control; some of this phenotype can be rescued by decreasing the irregularity of PC firing (Hoebeek et al., 2005; Walter et al., 2006).

I made contact with experimental neuroscientists at Erasmus MC, Rotterdam: Freek Hoebeek and Chris de Zeeuw, who kindly provided recordings from awake and head-restrained mice of *tottering* as well as wild-type mice. The total number of neurons recorded from was 37 *tottering* and 28 wild-type Purkinje cells, with a total time of approximately 5000 and 4000 seconds, respectively. Figure 74 shows the firing characteristics of these *tottering* and wild-type mice.

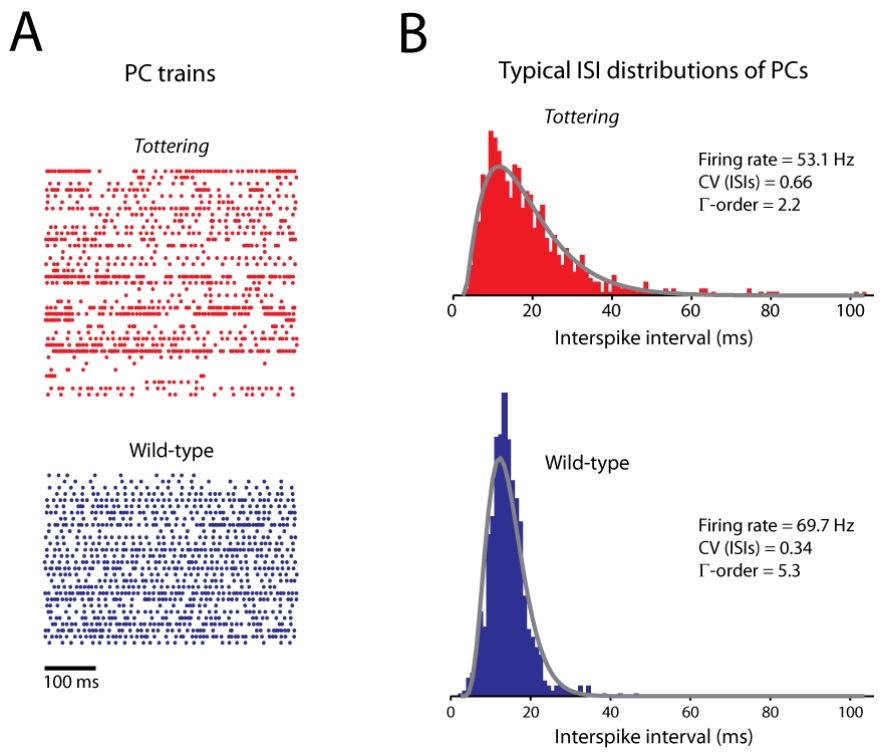

Figure 74 Samples of *tottering* and wild-type PC spike trains. A) 500 ms of firing from each of the 37 *tottering* and 28 wild-type trains. B) ISI distributions of the 15-second trains used as input to the $GABA_A$ synapses of the DCN neuron model. The panel shows a typical case each of *tottering* and wild-type; the given firing rates, CVs of ISIs, and gamma function orders are close to the respective mean values (Table 14).

6.2.1 Selecting PC spike trains for use as DCN neuron input

To use the Purkinje cell spike trains in simulations with the DCN neuron model, I divided the raw spike trains into 15-second stretches, yielding 326 *tottering* and 251 wild-type trains. Of those, the *tottering* trains had a mean firing rate of 54.5 ± 33.4 Hz (SEM) while the wild-type trains had an average of 70.4 ± 21.1 Hz. Figure 74 shows samples of *tottering* and wild-type trains.

As in the pattern recognition project, a spike-removal algorithm was applied which eliminated the second spike of each ISI that was shorter than 3 ms. The procedure reduced the mean firing rates to 52.2 ± 29.6 Hz for *tottering* versus 70.1 ± 21.0 Hz for wild-type.

In order to allow the results of simulations using wild-type trains to be compared with those of *tottering*, the mean firing rates of the trains were made equal. I did this with a biased selection procedure: of the raw *tottering* trains I used the trains with higher firing frequencies more often than the slower ones. Inversely, for the wild-type, I used slower trains more often than faster ones.

150 trains each of *tottering* and wild-type were drawn from the pools of 326 and 251 fifteen-second trains, respectively, to allow simulations with a PC-DCN convergence level of up to 150. I created 204 sets with each 150 *tottering* and 150 wild-type trains where the mean of a set was confined to the interval 61.3–62.3 Hz. The groups were analysed using the same metrics as for the pool of raw trains and revealed a good consistency of variability metrics pre- versus post-selection (Table 14).

Table 14 Statistics of spike trains from *tottering* and wild-type Purkinje cells before and after selection.

	Firing rate	CV of ISIs	Gamma order	CV_2 of ISIs	Percent of time in long patterns
			Raw Purkinje cell spike trains		
Wild-type (n=251)	70.1	0.45	4.56	0.39	18.4
St. Dev.	21.0	0.16	2.40	0.10	12.5
Tottering (n=326)	52.2	1.72	2.23	0.56	7.8
St. Dev.	29.6	1.28	1.57	0.18	9.6
			After selection: per-set means		
Wild-type (n=204x150)	61.8	0.46	4.87	0.38	20.0
Min	61.3	0.44	4.59	0.37	18.5
Max	62.3	0.47	5.13	0.39	21.5
Tottering (n=204x150)	61.8	1.70	2.18	0.53	8.3
Min	61.3	1.52	1.98	0.50	6.6
Max	62.3	1.91	2.42	0.55	10.0

The distributions of firing rates of *tottering* and wild-type trains before and after the selection mechanisms are shown in Figure 75.

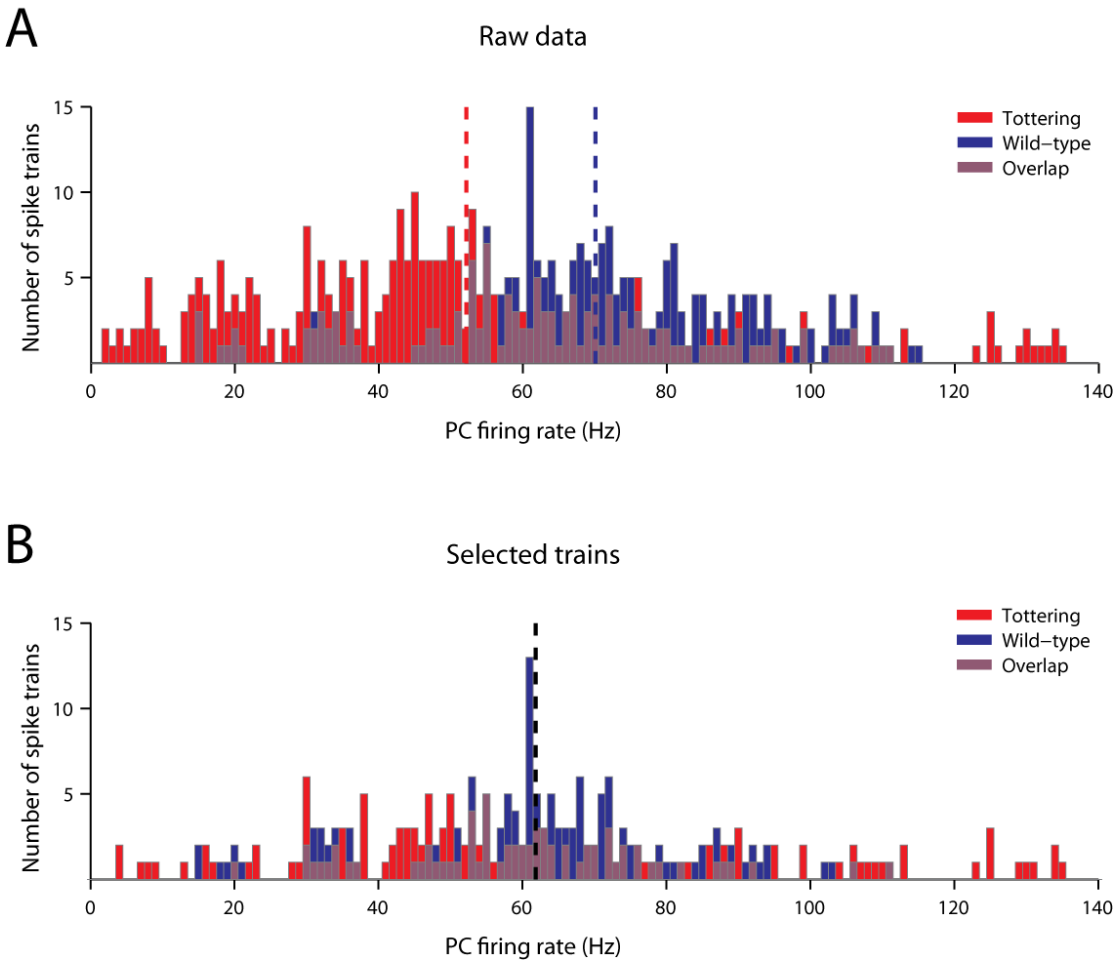

Figure 75 Purkinje cell spike trains before and after using a biased selection method to create train sets where the *tottering* and wild-type trains had the same mean frequency, yet retained the characteristics of increased variation of firing within the group of *tottering* trains. A) All original 326 *tottering* and 251 wild-type trains (mean spike rates indicated by dashed lines). B) One each of the 204 paired sets of 150 *tottering* and 150 wild-type trains where each set in the pair had the same mean firing rate, here 61.8 Hz (dashed line).

6.2.2 Simulations using wild-type and tottering PC trains

The studies using the GammaStim elements were repeated with the real PC trains as input, to the extent possible. Thus, while the effects of different PC firing rates could not be explored in a practical manner using real PC trains, the following set of convergence ratios were used to examine effects of the different

levels of irregularity that *tottering* and wild-type corresponded to, in the presence and absence of STD: 1, 2, 3, 5, 15, 50, and 150. The convergence setting of 150 used all spike trains in each 150 + 150 pool, while for the lower convergence ratios, trains were drawn randomly from the pool without duplicate drawings. Simulations were run for a 5 second calibration period during which artificially generated trains with the mean firing rate of the 204 sets – 61.8 Hz – were used. Thereafter, the simulations were continued for a simulated neuronal time of 15 seconds where the real PC trains were used.

Statistical data were calculated for each of the resulting 204 + 204 wild-type + *tottering* DCN spike trains and then averaged over the 204 simulations. The firing rates and $GABA_A$ conductances are presented in Figure 76.

6.2.3 Effects on DCN neuron firing rate

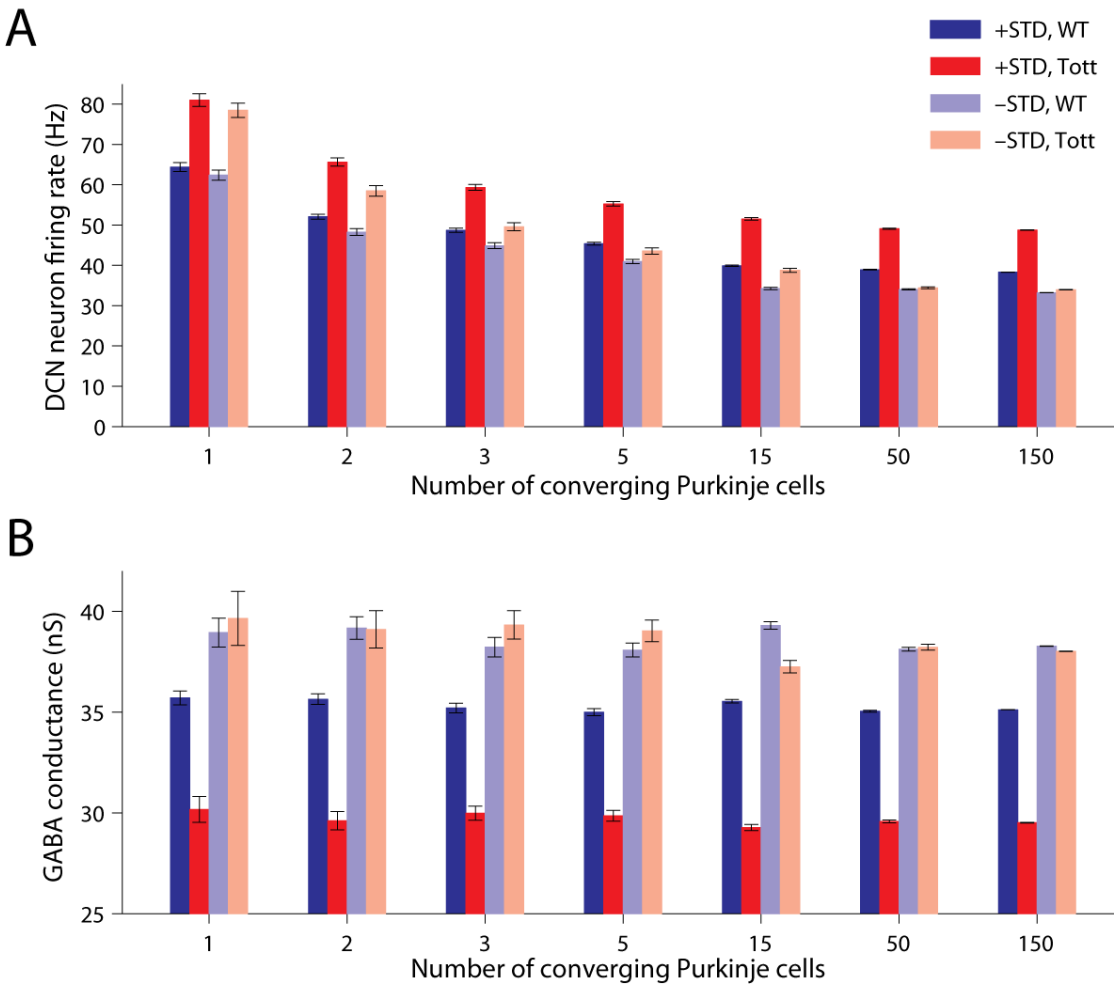

Figure 76 The DCN neuron model response to *tottering* and wild-type inputs in the presence and absence of STD at different levels of PC-DCN convergence. Data are presented ± standard error of the mean (n=204). A) This graph of spike rates shows that the irregularity-driven acceleration depends on the presence of STD for high convergence ratios, but becomes less dependent of STD for low convergence ratios. B) Means of the $GABA_A$ conductance to the DCN neuron model injected by the spike trains used in (A), showing consistency across the convergence spectrum.

As in the results from the GammaStim simulations with varying convergence (Section 6.1.4), the DCN neuron firing rates and the STD dependent firing rate increases were very similar at the highest convergences (here, 50 and

150), supporting the validity of comparing these results with those of convergence 90 where GammaStim inputs were used (Figure 71).

In these simulations in the presence of STD, at a convergence of 150 the DCN neuron model responded with a 27.4% higher firing rate to the irregular spike trains from *tottering* Purkinje cells than to the more regular trains from wild-type cells (48.8 Hz versus 38.3 Hz). In the absence of STD, the difference in DCN neuron firing rate in response to *tottering* and wild-type Purkinje cells was reduced to 2.4% (34.0 Hz versus 33.2 Hz).

However, at lower convergence ratios the irregular inputs from *tottering* mice resulted in an accelerated spike rate in the DCN neurons, which was less dependent on STD, and the STD dependence of the irregularity based spike rate acceleration disappeared completely at a convergence ratio of 1 (Figure 76 A), mirroring the situation with GammaStim inputs (Figure 73). The mechanism for this STD-independent acceleration will be explored in Section 6.2.6.

6.2.4 $GABA_A$ conductance changes

The changes in $GABA_A$ conductance caused by STD were more pronounced than in the GammaStim case: at a convergence ratio of 150, the presence of STD resulted in a 16.0% reduction of the mean $GABA_A$ conductance injected into the DCN neuron model by the *tottering* spike trains compared to the wild-type trains (*tottering*: 29.5 nS, wild-type: 35.1 nS). Without STD, the difference between the mean conductances from *tottering* and wild-type spike trains at a convergence ratio of 150 was reduced to 0.8% (*tottering*: 38.0, wild-type: 38.3 nS).

Note that the difference between wild-type and *tottering* in terms of gamma order of ISI distribution were smaller than the differences between fully regular and maximally irregular trains in the GammaStim simulations (from

Table 14: mean gamma order of a wild-type 150-set is 4.9, *tottering*, 2.2; GammaStims: an irregularity setting of 0 gives an infinite gamma order, while 1.0 gives 2.5). In spite of this, the DCN neuron firing rate increase caused by the irregularity of inputs was larger with *tottering* as compared with wild-type than in irregular GammaStims compared with regular GammaStims (27.4% versus 22.0%, with convergence 150 vs. 90). The corresponding values for the $GABA_A$ conductance were 16.0% for real PC trains and 11.2% for GammaStims.

However, the metric of gamma order does not capture other irregularity features of *tottering* spike trains. The *tottering* ISI distributions are characterised by a larger variation of interspike intervals than the GammaStim element produces even at the highest irregularity setting (Figure 74 and Figure 70, respectively). This is quantified with the CV of the ISI distributions, which has an average of 0.46 for wild-type and 1.7 for *tottering* (Table 14) and 0 vs. 0.52 for fully regular GammaStim trains versus those of irregularity setting 1.0.

6.2.5 Exploring differences in DCN responses to spike generators compared to real PC spike trains

To understand why the real PC trains gave a stronger effect than the spike generators, I performed simulations with GammaStim elements where I created the same mean firing rate as that of the real PC trains – 61.8 Hz – and as close as possible a gamma order of the GammaStim spikes to replicate wild-type and *tottering* PC trains (2.8 and 5.2, respectively). These simulations were run with the same convergence ratios as those with real PC trains had been. In addition, I ran simulations where the GammaStim output was fully regular, also at 61.8 Hz. The result is shown in Figure 77.

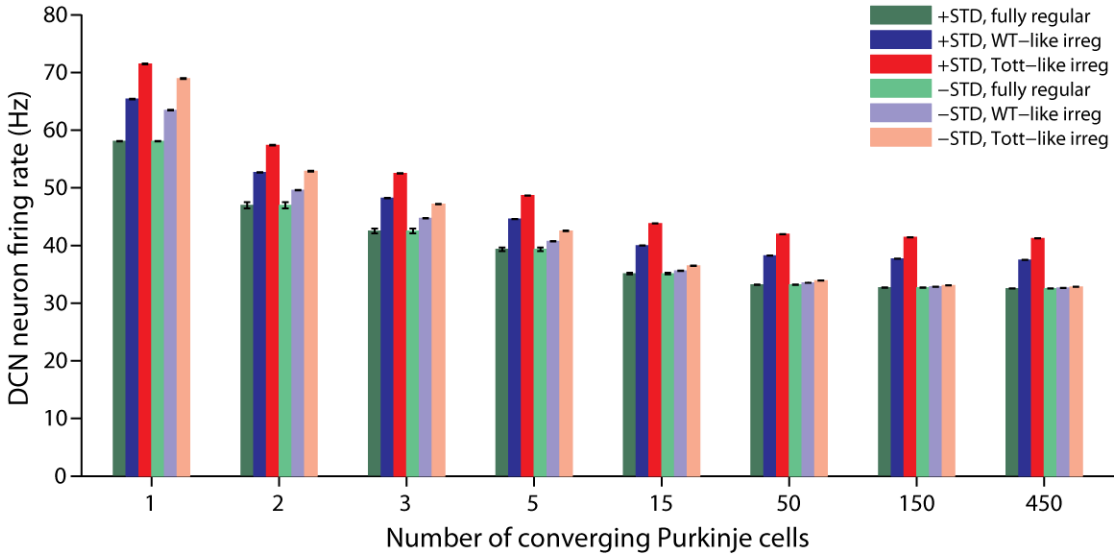

Figure 77 Firing rate of the DCN neuron when receiving GammaStim inputs where spike rate and irregularity has been set to imitate the real PC trains from *tottering* and wild-type, as well as fully regular trains. Data are presented ± standard error of the mean (n=204).

At a convergence ratio of 150 and in the presence of STD, the acceleration caused by irregularity in the *tottering*-like trains compared with the wild-type–like trains was 8.9% (wild-type-like: 37.7 Hz, *tottering*-like: 41.4 Hz). The mean summed $GABA_A$ conductance decreased by 6.6%, from 35.3 nS to 33.1 nS. Thus, the STD-caused firing rate acceleration with *tottering*-like inputs compared with wild-type–like inputs was lower than that caused by real *tottering* versus wild-type trains (27.4%) and was accompanied by a lower $GABA_A$ decrease than seen with the real trains (16.0%). Unsurprisingly, the fully regular PC trains gave no difference in DCN neuron output rate in the presence versus absence of STD (Figure 77).

Further, I examined samples of $GABA_A$ conductance and membrane potential traces from the wild-type and *tottering* trains. Figure 78 shows how the $GABA_A$ conductance varies more for *tottering* inputs and how STD works as a low-pass filter, decreasing the conductances when inputs arrive at short intervals.

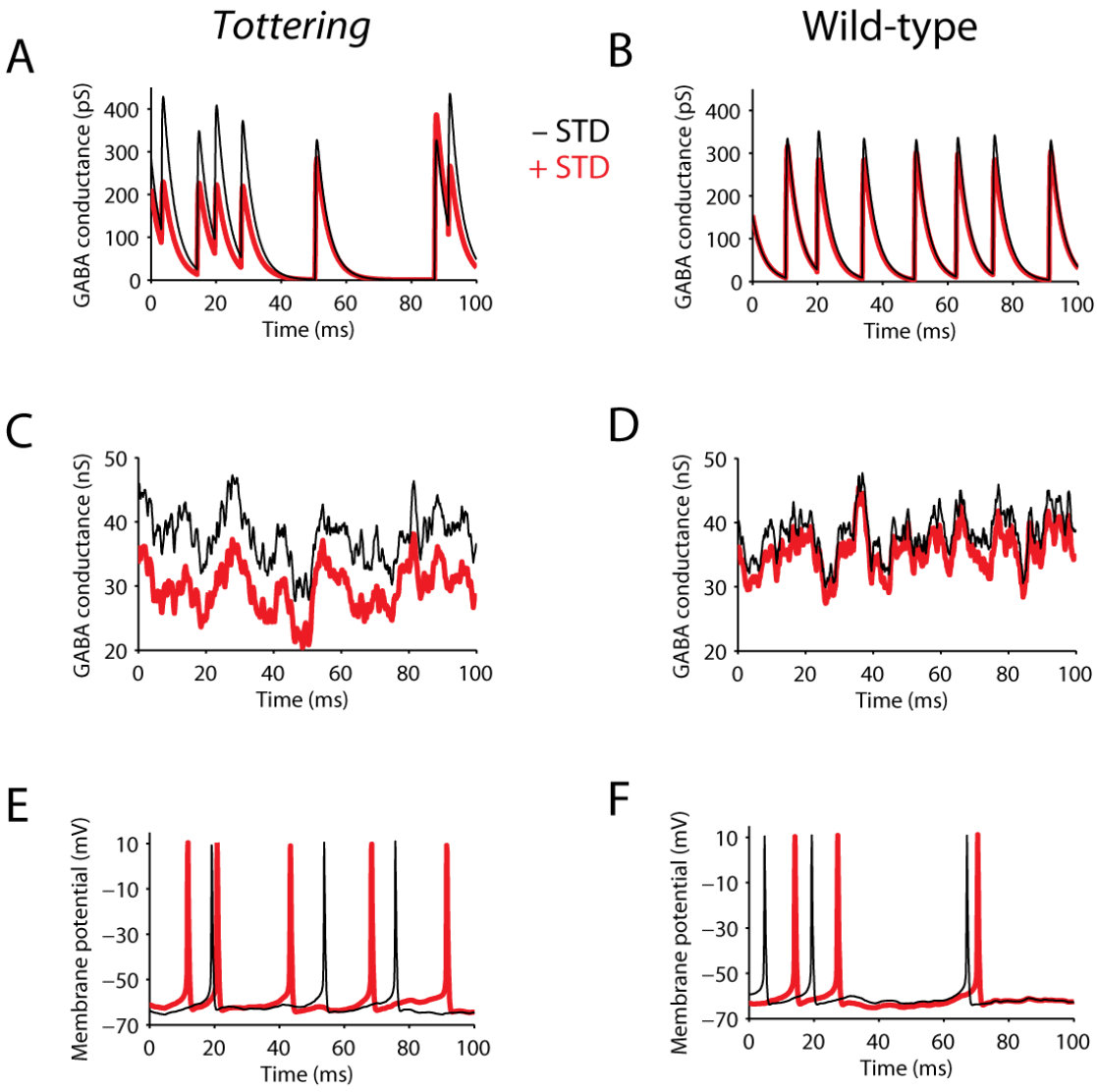

Figure 78 Sample traces of the DCN neuron model as it receives input from *tottering* (left) and wild-type (right) PCs at a convergence of 150, with STD (red traces) and without (black). The traces are 100 ms long and are from the same time point in the 15 second long simulations. (A) and (B) show the conductance of one $GABA_A$ synapse, while (C) and (D) show the conductance sums of all 450 $GABA_A$ synapses. Note the larger fluctuations in conductance when *tottering* inputs are received, especially on the level of one synapse. Also note how the higher instantaneous input rates of *tottering* leads to a larger effect of STD (A). (E) and (F) show the membrane potential of the DCN neuron (red traces). The firing rate of the DCN neuron is increased with *tottering* input in the presence of STD; the additional spikes with *tottering* coincide with periods of decreased $GABA_A$ conductance sums.

The graph in Figure 78 A shows that the larger variability of ISIs in the *tottering* trains compared to the wild-type trains leads to a forceful depression of $GABA_A$ conductance when spikes are closely spaced, yet not to a correspondingly strong recovery of conductance when spikes are far apart (see difference between the +STD and -STD traces). This effect is also expected to occur more strongly for *tottering* trains than for *tottering*-like trains and is the most likely explanation for the lowered $GABA_A$ conductance with real PC trains compared with spike generators; the lowered $GABA_A$ conductance in turn causes the increased firing rate of the real PC trains. This is supported by the lack of difference in firing rate between the regular, the wild-type-like, and the *tottering*-like trains at the highest convergences when STD is not used (Figure 77).

At a convergence of one, input from *tottering* Purkinje cells led to accelerated DCN neuron spiking both in the presence and absence of STD, and both for the real PC trains and for GammaStim inputs (Figure 76 A and Figure 77), whereas the reduction of the inhibitory conductance only occurred when STD was present (Figure 76 B). This implies that other mechanisms must be involved in the irregularity-based spike rate acceleration at a convergence ratio of one. One such potential mechanism could be the contribution of the spontaneous firing of the DCN neuron and its excitatory inputs when the single *tottering* PC that provides input to the DCN neuron at a convergence ratio of one pauses.

6.2.6 Synchronised pauses in PC firing

The effects that *tottering* and wild-type trains have on the DCN neuron output at a convergence of 1 is exemplified in Figure 79, A and B. The endogenous spike generation mechanism, in combination with the excitatory inputs and the likely generation of rebound responses at the offset of inhibitory input (not shown), is activated in the longer PC input pauses caused by the *tottering* trains

(A), giving instantaneous firing rates during those pauses of up to 170 Hz. This is a sufficiently high rate to drive up the *tottering* firing rate to its mean of 81.0 Hz when STD is in use, and to a similarly high rate when STD has been switched off (78.6 Hz). Most of the difference between DCN firing rate when receiving *tottering* input through the STD-enabled compared to STD-disabled synapse that is present at higher convergence ratios has thereby been swamped by these fast regular firing periods which are unaffected by STD. This conclusion is confirmed by the frequent presence of periods of long regular patterns in the output of the DCN neuron receiving *tottering* input at convergence 1 (Figure 79, C). Long regular patterns are defined as periods of firing where four or more consecutive ISIs have a $CV_2 \leq 0.2$ (Shin et al., 2007a).

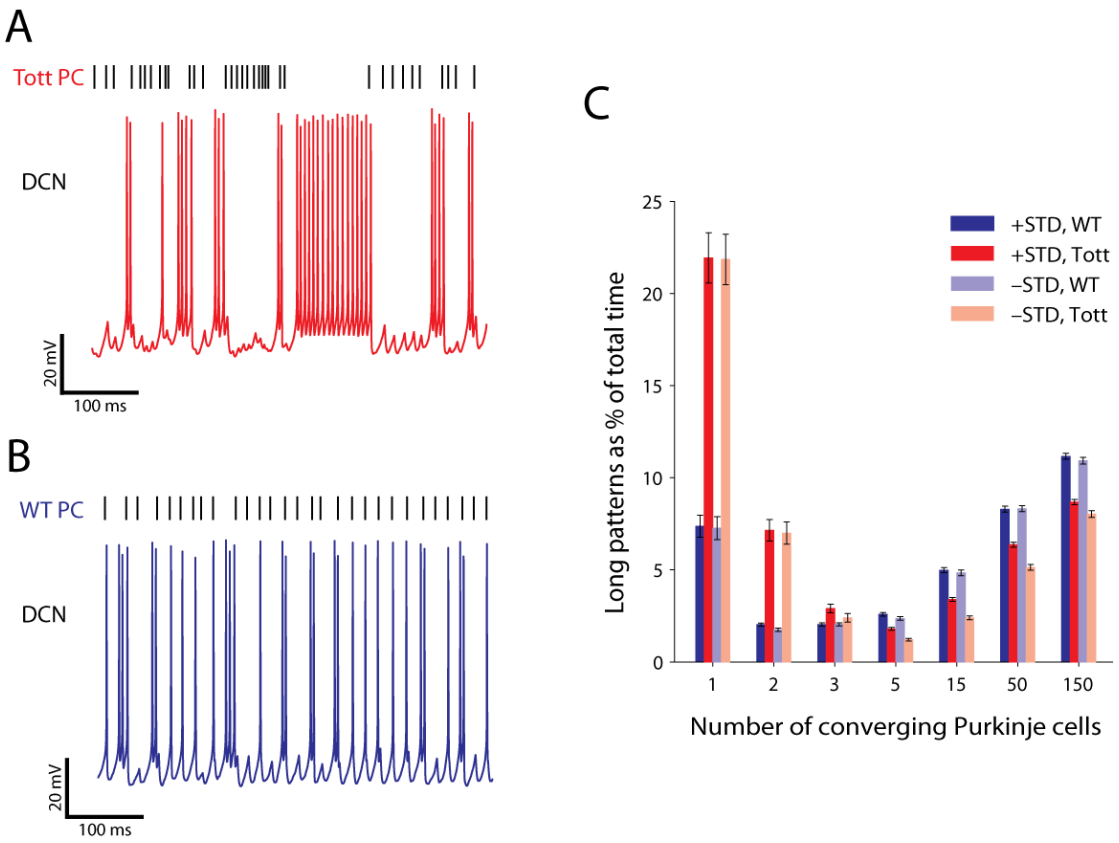

Figure 79 Periods of pauses in PC firing allow regular high-frequency firing to be generated by the spontaneous firing of the DCN neuron in combination with its excitatory inputs and rebound responses. **A, B)** 500 ms of DCN neuron spiking resulting from input from *tottering* and wild-type real PC trains (vertical black lines), respectively, at a convergence ratio of 1, with STD active. The DCN neuron model membrane potential is plotted below the PC spikes; note that there is a slightly delayed effect of PC spikes (approximately 3 ms) which is caused by synaptic delays as well as the time required for the membrane potential to spread down the PC axon and, for dendritic DCN synapses, from the DCN dendrites to the DCN soma. **C)** The extent of long regular patterns (see text) of DCN firing at different convergence ratios of real PCs to the DCN neuron. The error bars show standard error of the mean (n=204).

The proportion of DCN spike trains that comprise long regular patterns as determined by the CV_2 metric (Figure 79 C) shows two trends as the convergence ratio changes, with the highest proportion given at a convergence ratio of 1, but

only in *tottering*. Using +STD for exemplification, this proportion decreases quickly, from 21.9% at a convergence of 1 to 1.8% at a convergence of 5. As the convergence ratio increases further, the percentage of long patterns goes up again, to 8.7% at a convergence of 150. To understand the mechanism underlying this change, I plotted the membrane potential and the summed $GABA_A$ conductance for the *tottering* trains at convergence 5 and at convergence 150. The results, where STD has been in use, are shown in Figure 80.

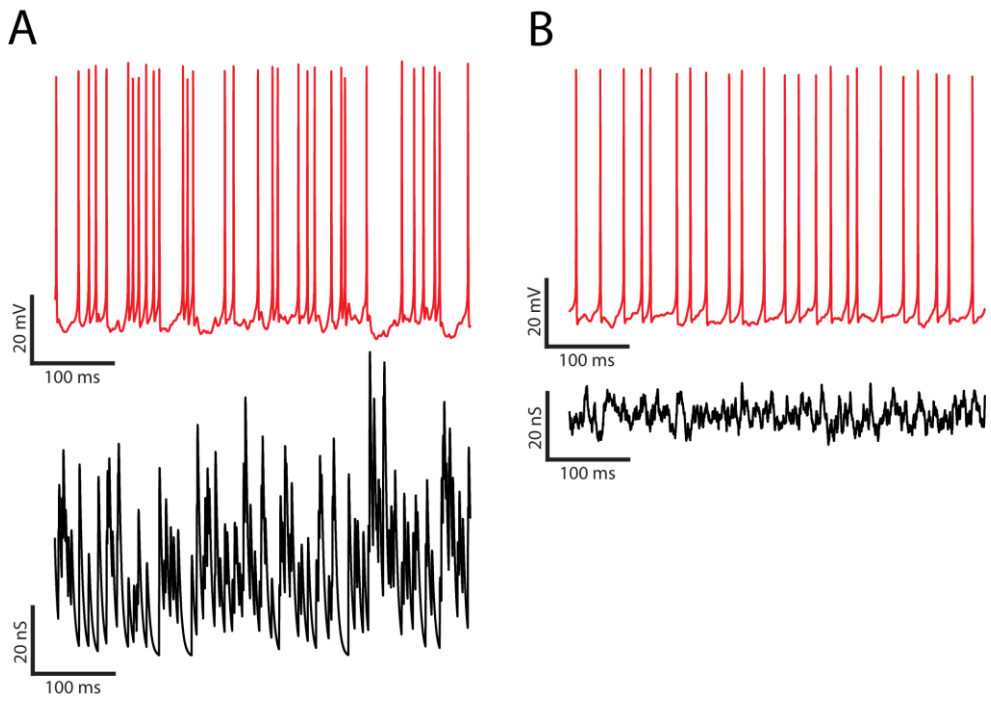

Figure 80 Membrane potential (top traces) and summed $GABA_A$ conductance (bottom) of the DCN neuron model as it receives input from *tottering* PC trains at convergence ratios 5 (A) and 150 (B). STD was in use at both convergence ratios.

Combined with the membrane potential plot of the DCN neuron receiving *tottering* input at a convergence of 1 (Figure 79 A), the trains of Figure 80 suggest an explanation for the non-monotonic dependence of the percentage of long patterns in *tottering* (+STD) on the convergence ratio. The minimum of the percentage of long patterns at a convergence of 5 could be caused by the absence

of long periods of sufficiently low $GABA_A$ conductance to allow continuous spiking driven by the combination of the spontaneous firing of the neuron and its excitatory inputs; those stretches are much diminished at a convergence of 5 (Figure 80 A) compared to a convergence of 1.

With convergence 150, on the other hand, there are no longer any periods without significant $GABA_A$ conductance (Figure 80 B). Instead, the averaging effect of the 150 independently firing PCs that connect to the DCN neuron leads to a more tonic $GABA_A$ conductance; the result is that there are no periods of such spontaneous firing at a convergence of 150. The long regular patterns are there instead made up of the longer ISIs seen, for example, in the middle of the membrane potential trace of Figure 80 B.

This interpretation is supported by the similar dependence of the percentage of long regular patterns on convergence ratio in wild-type, with a third of the percentage of long patterns of *tottering* at the lowest convergence ratio (wild-type, +STD: 7.4%). As for *tottering*, the percentage of long pattern first decreases and then increases with increasing convergence ratios, with an increase in regular patterns from convergence 5 up to a convergence of 150 (Figure 79 C). The three times lower percentage of long patterns in wild-type compared to *tottering* at a convergence of 1 is explained by its lack of long silent periods of PC activity, while the higher percentage than in *tottering* at the higher convergence ratios is explained by its evenly spaced PC spikes and thereby higher tonicity of $GABA_A$ conductance injected into the DCN neuron.

6.2.7 Another mechanism sets output rate at regular PC firing with full synchrony

The results of the simulations using tottering- and wild-type–like PC trains as input were shown in Figure 77 together with a control simulation using

GammaStim spike generators that fired at the same rate as the tottering- and wild-type–like PC trains. The firing rate of the DCN neuron when receiving those regular trains at a convergence of 1 was 58.1 Hz, very similar to the input rate (61.8 Hz). Further, the DCN neuron output was highly regular with 64.2% of simulation time consisting of long regular patterns as compared to 4.6% for tottering-like inputs (+STD). Such a high proportion of long regular periods at 58.1 Hz could not plausibly originate from the 170 Hz firing that was mediated by spontaneous firing combined with excitatory inputs (Section 6.2.6), especially since the strong inhibitory inputs arrived every 1000/61.8 = 16.2 ms. This indicated that another type of regular firing than that caused by synchronised PC pauses was present here.

The plot of the membrane potential of the DCN neuron under these circumstances in Figure 81 shows that the cause most likely was that the DCN neuron becomes phase locked to the inhibitory input, with a few omitted spikes likely due to the randomised nature of the excitatory inputs.

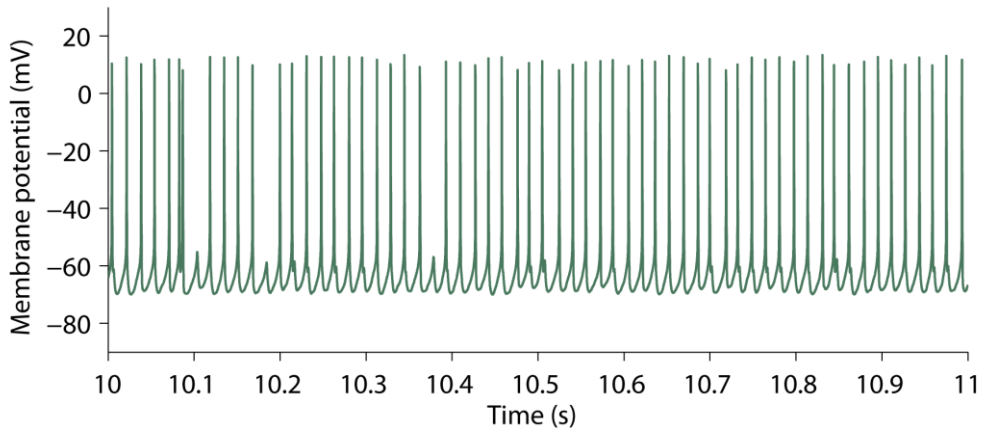

Figure 81 DCN neuron firing as it receives completely regular PC firing at 61.8 Hz with a convergence ratio of 1.

6.2.8 Effects of PC irregularity on DCN neuron irregularity

The main result of this project is the increased firing rate of the DCN neuron as it receives inputs of higher irregularity. Were this accelerated firing the only modification of the DCN neuron output, we would have a case of pure information modality change. However, the graph of percentages of long patterns (Figure 79 C) shows that there is an effect on the regularity of the DCN neuron output from varying the input regularity. As mentioned above, at a convergence of 1 the DCN neuron output from wild-type PCs contains only a third as much of long regular periods as the output with *tottering* input; this gives an inverse correlation between the irregularity of inputs and outputs. Yet, in the absence of PC synchronisation, the actual convergence ratio of the network (see Section 5.3) makes the situation at the higher part of the convergence spectrum of larger interest; for large convergence ratios regular inputs give more of long regular stretches of DCN neuron output (+STD: wild-type: 11.2%, *tottering*: 8.7%).

In addition to the CV_2 metric of local regularity, I quantified the effect of the increased irregularity of spike trains from *tottering* Purkinje cells on a global metric of irregularity – the CV of the DCN neuron spike output (Figure 82).

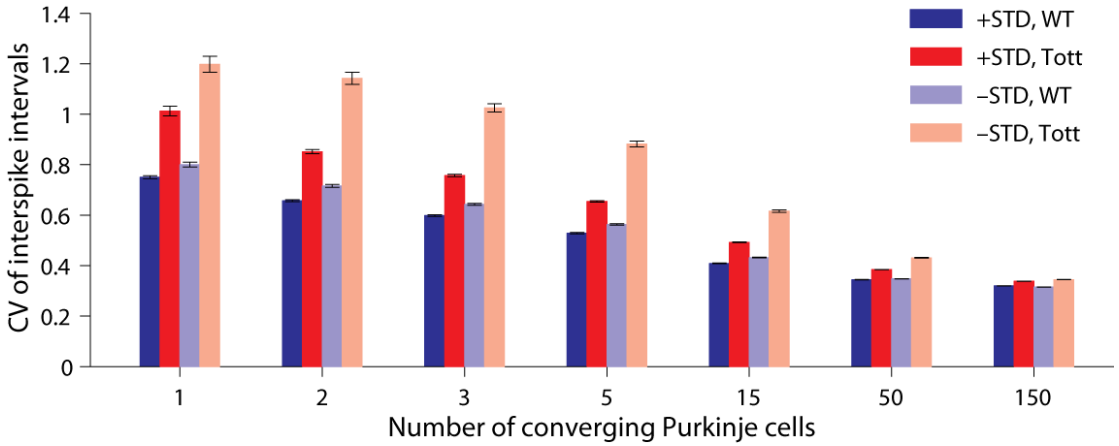

Figure 82 CV of interspike intervals of DCN neuron output when receiving PC spike trains from wild-type and *tottering* in the presence and absence of STD, at different convergence ratios. Error bars show standard error of the mean (n=204).

In all cases, the increased irregularity of the inhibitory input resulted in an increased CV of the DCN neuron spike trains. This effect was most pronounced for a convergence ratio of one (+STD: tottering: 1.01 ± 0.28, wild-type: 0.75 ± 0.08, n = 204; -STD: tottering: 1.20 ± 0.46, wild-type: 0.80 ± 0.13, n = 204) but still present for a convergence ratio of 150 (+STD: tottering: 0.34 ± 0.01, wild-type: 0.32 ± 0.00, n = 204; -STD: tottering: 0.34 ± 0.01, wild-type: 0.32 ± 0.01, n = 204).

Thus, although STD adds a coding modality in the form of increased firing rate to the irregular inputs, differences in irregularity remain in the DCN output, as reported in the experimental literature (Hoebeek et al., 2008).

6.3 Control simulations with an integrate-and-fire neuron model

With a biophysically and morphologically realistic model such as the DCN neuron model used in this thesis, the complexity of the dendritic tree and the voltage and ligand gated ion channels can be expected to influence results. For this reason, I carried out control simulations where the DCN neuron model was replaced with an integrate-and-fire neuron model. This control model was made up of a single compartment which contained 45 GABA synapses and 15 AMPA synapses, whereas the original model contained 450, and 150 synapses, respectively. The input rates to the synapses were kept at those used as default in the GammaStim based simulations with the full model, with 60 Hz for the inhibitory synapses and 20 Hz for the excitatory synapses. The kinetics of the synapses also remained as in the full model. The maximum GABA conductance was kept as in the original model (1.6 nS at 32°C, adjusted to 1.89 nS at the used temperature of 37°C), while the AMPA synapse conductance was titrated to give the same firing rate as the original model, with 33.3 Hz at fully regular GABA input.

The resting membrane potential was set to -63 mV and the threshold for firing was -45 mV. When the threshold was reached, a spike was counted and the membrane potential was reset to -63 mV and kept there during the 2.5 ms refractory period.

The model was supplied with input at the same irregularity levels as the full model and the effect on the neuronal output rate was examined. The results are depicted in Figure 83.

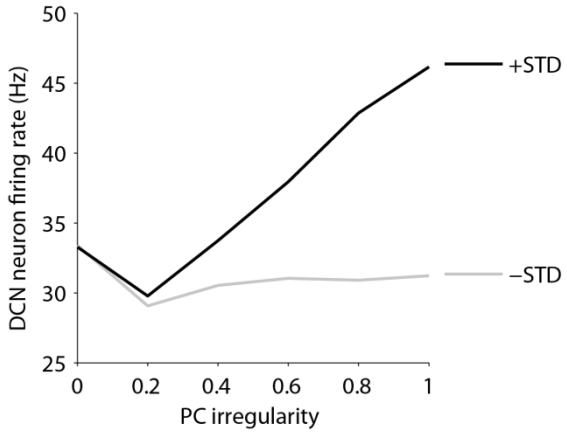

Figure 83 Results of control simulations using an integrate-and-fire neuron receiving inputs of the same regularity levels used in the simulations with the full model. The result of increased DCN neuron output rate as the GABAergic input irregularity increases remains with this simplified model, where the speedup is more pronounced; compare with the results of the full model (Figure 71).

As with the full model, the general trend with the integrate-and-fire neuron model was that the application of GABA STD gave an increased firing rate as irregularity increased (Figure 83). Also as in the full model, only the +STD case gave a decreased GABA conductance as irregularity increased, with an 8.0% lower summed conductance at irregularity 1 compared to irregularity 0 (sum of all 45 GABA synapses: 6.25 nS vs. 5.75 nS). The firing rate increase from irregularity 0 to 1.0 was 38.7% in the +STD case, vs. -6.5% without STD.

Thus, the effects of irregular and regular inputs to the integrate-and-fire neuron version of the DCN neuron model are very similar to those seen in the full model (Figure 71 and surrounding text). This shows that the effects are based on the synaptic properties of STD and are not dependent on a complex neuronal morphology or physiology.

6.4 Additional discussion

6.4.1 The convergence ratio determines the relative contributions of different mechanisms of irregularity-caused speedup

The results of this project showed that a function of STD at the PC-DCN synapse may be to recode irregularity of inputs from the Purkinje cells into differences in DCN neuron firing rate. The observation that this effect is strongest at the most common PC firing rates (Figure 72 A) argues for the usefulness of this function of STD at the PC-DCN synapse.

Further, the data support different mechanisms behind irregularity-induced accelerated firing. Both with the tottering versus wild-type PC trains and with tottering-like versus wild-type–like artificial PC trains, high convergence ratios show an irregularity-induced acceleration that is STD-dependent, and is caused by the lowered $GABA_A$ conductance that results from irregular compared to regular trains. Without STD the firing rate acceleration disappears at the highest convergence ratio (Figure 76 and Figure 77). However, as the convergence ratio is decreased, the contribution from STD to the irregularity-caused speedup is lowered; at a convergence ratio of 1, it is a relatively unimportant contributor. One likely reason for the STD-independent speedup at low convergence ratios is the presence of synchronised pauses of PCs that fire irregularly. These pauses allow the spontaneous firing of the DCN neuron to combine with the excitatory inputs to produce a high-frequency firing that is not dependent on the presence of STD. Moreover, the journal article this project has been described in (Luthman et al., 2011) includes an analysis of another likely contributor to the STD-independent speedup at low convergences: the $GABA_A$ conductance variance is higher at lower convergence ratios, which causes increased membrane potential

variations and therefore an increased propensity of the DCN neuron to fire. In the interest of brevity, the investigation was not included in the present thesis.

6.4.2 Different metrics of irregularity give opposing results

At a convergence of 1, the global regularity metric of coefficient of variation (Figure 82) and the local regularity metric, CV_2 (Figure 79), gave opposite results: while the global metric showed that the regularity of DCN output is decreased from receiving tottering inputs, the CV_2 showed that the percentage of periods of regular firing were increased by the irregular inputs. This result shows the importance of analysing the local regularity since the effects on downstream targets of the DCN neurons very likely will respond to moment-to-moment changes in regularity rather than the mean of many seconds of firing.

7. Conclusions

7.1 Results and their implications

This thesis programme set out to further the state of knowledge about computations of the excitatory projection neurons of the deep cerebellar nuclei. The most important of the novel findings achieved in the work will be discussed here, with the goal of placing them in the framework of the field of cerebellar studies. The less important results will not be commented here as they have already been discussed in the respective chapters.

7.1.1 DCN burst length is the best criterion for parallel fibre pattern recognition

The Purkinje cell output during parallel fibre pattern recognition was shown in Chapter 5 (Section 5.5.1) to be most efficiently read out by the number of spikes in a burst of DCN neuron firing. This burst was decreased in length when Purkinje cells recognised previously stored patterns.

The cerebellum is known to be important in timing of motor behaviours (review by Ivry et al., 2002). In Section 2.7.4 I described how the cerebellum can be seen as a device to ensure that the right muscles are active at the right time during the execution of movement. I gave the example of the drawing of a circle with one's arms and how successive groups of muscles need to be activated at precise times, with the relevant body parts in the correct positions, to perform this in a smooth manner. Since any smooth, goal-directed, movement can be seen as a result of learning (newborns are not capable of performing such movements), the following discussion attempts to place the pattern recognition results of this thesis in the context of such motor behaviour. For the purpose of this argument, let us assume that the Purkinje cells are provided with the positional information of the relevant body parts via the pattern presented by parallel fibre activity. As long as novel patterns are presented (that is, the current positional state has not been stored) the long DCN neuron bursts that result could comprise signals for muscular contractions to be executed. If those contractions lead to the desired positional state, the parallel fibres will present the Purkinje cells with the information that a stored pattern has been encountered; the result is, as Chapter 5 showed, a shortened burst and a removed error correction signal.

While the above clearly is speculative, the state of knowledge in 2011 of the involvement of the DCN in controlling the muscle activity that underlies complex

movements is still to a large extent not conclusive (Ebner et al., 2011). The major projections of the cerebellar nuclei were briefly introduced in Section 2.7.1 as the brain stem, thalamus, and spinal cord. To my knowledge only for very simple movements, such as conditioned eye-blink reflexes, has it been possible to trace the output of DCN neurons to motor neurons, thus making it possible to determine the final result of DCN neuron firing. The issue is complicated by the indications that the diverse targets of DCN neurons are contacted by collaterals of branching axons from single DCN neurons (Voogd, 2004b). Thus, the output of a DCN neuron could simultaneously activate targets in the ventral lateral nucleus of the thalamus, in the red nucleus (a part of the mesencephalon, in the brain stem), and in parts of the spinal cord. The spinal cord target may be only a few relay neurons from a motor neuron target; yet, with several steps of relays where each relay may have several other inputs than the one originating in the DCN neuron, the complexity can be assumed to be large. When the collateral targets, and their further connections, are taken into account, the DCN neuron output can be expected to influence the activity of a large number of neurons, including neurons involved in conscious motor planning, since the motor and premotor cortices are the targets of the ventral lateral nucleus of the thalamus (Nieuwenhuys et al., 2008).

7.1.2 Convergence of PCs to DCN neurons amplifies DCN neuron pattern recognition performance

Chapter 5 showed how the pattern recognition signal-to-noise ratio increases as the convergence ratio of Purkinje cells to DCN neurons increases. In Section 5.5.3 it was demonstrated how this could be theoretically proven based on the decreased error of the sampled means of the spike train metrics used for pattern recognition. However, the simulations using the biophysically and

morphologically realistic DCN neuron model showed that the amplification was much lower than that theoretically achieved. With the DCN neuron model, signal-to-noise ratios scaled approximately with the square root of the convergence ratio while the calculations resulted in scaling that was linear with the convergence ratio. The reasons for this remain unexplored, but can be expected to include the variable delays from the synapses to the soma that a dendritic tree imposes.

7.1.3 Irregularity of Purkinje cell firing and its ability to function as a neural code

The main result of the study of different levels of irregularity of Purkinje cell firing and the effects that those have on the DCN neuron output was that irregular input firing caused an increased output firing rate. At the most likely high convergence ratios, this accelerated firing was caused by the decreased $GABA_A$ conductance that short-term depression induced. In this way, I showed that short-term depression of the synapse between Purkinje cells and DCN neurons endows DCN neurons with the ability to change the modality of information transfer, from a code based on levels of regularity to a code based on firing rate.

7.2 Limitations

A great obstacle in the study of computations in the cerebellar nuclei is the lack of available connectivity data, which in this thesis has been highlighted by the range of broad parameter explorations that I performed. For example, the convergence ratios of Purkinje cells to DCN neurons was shown to be of great importance in determining the pattern recognition efficiency (Section 5.5.2), firing rate (Section 6.2.3), and firing regularity (Section 6.2.6) of the DCN neuron

model, but in the absence of firm evidence of the actual convergence ratios, it is only possible to give a range of different effects as the study outcome. However, recent evidence suggests that most Purkinje cell input to the DCN is tonic during behaviour (implying high convergence ratios, see the $GABA_A$ conductance of Figure 80 B) and that the low-convergence or high-synchrony relationship explored in this thesis is found seldomly and is restricted to synchronous complex spikes in response to inferior olivary input (Bengtsson et al., 2011).

Another gap in the state of knowledge regards whether branching mossy fibres project both to Purkinje cells and to the same DCN neuron that receives the Purkinje cell output during pattern presentation (Section 5.6.11). Generally, the interplay between the excitatory and inhibitory inputs to the DCN has not been much explored in the projects of this thesis. This leads to another limitation of the studies herein: the DCN neuron has been viewed in isolation from the interneurons of the DCN. The connections from those to the excitatory DCN projection neuron examined in the thesis are poorly known, comprising a great obstacle to an understanding of the DCN (Uusisaari and De Schutter, 2011).

7.3 Future directions

Several questions about the computations performed by DCN neurons have been raised in this thesis. Apart from the need for a general advancement of the knowledge of anatomy and connectivity within the DCN that was discussed in the previous section, this section presents some ideas about future work to continue the research in this area.

7.3.1 Inhibitor of STD as a treatment for cerebellar ataxia

Tottering PCs fire more irregularly than wild-type PCs, while their firing rates during optokinetic stimulation is indistinguishable from that in wild-type littermates (Hoebeek et al., 2005). Since they also show impaired motor function including an abnormal optokinetic reflex, the data indicate that the regularity of Purkinje cell spiking is relevant for motor control. At the same time, the data raise the question of how the degree of regularity in Purkinje cell activity can be read out by neurons downstream. As the postsynaptic target neurons of the Purkinje cells in the DCN fire at higher rates in anesthetised tottering mice than in wild-type ones (Hoebeek et al., 2008), the effect of the increased Purkinje cell irregularity on impaired motor control might be caused by an increased DCN neuron spike rate. The results of the simulations in this thesis predict that the increased DCN neuron spike rate in tottering mice can be caused directly by the increased irregularity in the Purkinje cell activity. This argues for the possibility that the motor abnormalities of tottering mice depend at least to an extent on STD at PC-DCN synapses. It also argues for the possibility of lessening the motor deficiencies by inhibiting STD pharmacologically.

The short-term depression of the PC-DCN synapse appears to be presynaptic in origin (Pedroarena and Schwarz, 2003). To alleviate the symptoms of tottering mice, and more pertinently, of the human cerebellar ataxias (Figure 84) that tottering serves as a model for, an inhibitor of this process would need to show specificity for STD at the PC-DCN synapse. As mentioned in Section 2.4, STD is found in other parts of the brain and has been implicated in computational functions of neurons; blocking those functions can be expected to lead to possibly grave side-effects.

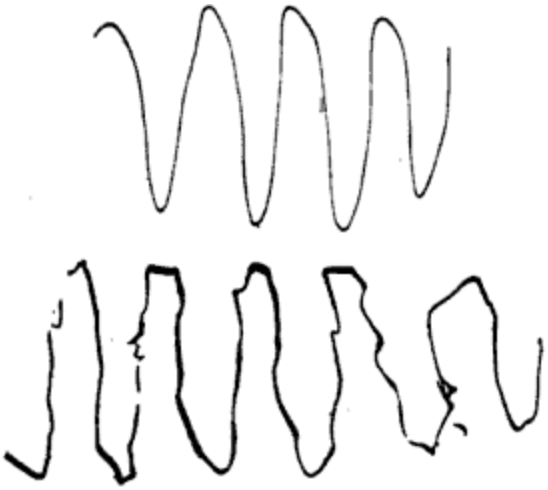

Figure 84 The phenotype of human cerebellar ataxia, with a diagnosing physician's drawing at top; below: the attempt by a cerebellar ataxia patient to reproduce the drawing. From Thomas (1912).

While the simulations of Chapter 6 show that differences remain between DCN neuron output in tottering versus wild-type also in the absence of STD, especially in the length of regular periods of firing (Figure 79 C), the increased firing rate with DCN neurons receiving tottering inputs has almost disappeared at the higher, and more likely to be predominant, convergence ratios with STD absent.

7.3.2 The effect of feed-forward inhibition to Purkinje cells on pattern recognition

The pattern recognition work revealed that feed-forward inhibition of Purkinje cells with strength equal to the excitatory input to the Purkinje cell could cause an improved pattern recognition performance, both of the Purkinje cell and in the DCN neuron readout (Section 5.6.7). Lower or higher ratios of inhibition to excitation did not achieve this amplification of signal-to-noise ratios.

In the DCN neuron, the increased signal-to-noise ratio was caused both by a decreased trial-by-trial variation of the metric (the number of spikes in the burst) and an increased difference of means of the metric. It would be interesting to investigate what the mechanism is that underlies this effect in the Purkinje cell model and what, if any, the behavioural effects would be of blocking the feed-forward inhibition in vivo, if technically feasible.

7.3.3 The effect of different $GABA_A$ reversal potentials on pattern recognition

One parameter that was not varied in the simulations was the $GABA_A$ reversal potential. As discussed in Section 4.5.6 this value was set at -75 mV for all simulations, based on the majority of the evidence for adult animals. The $GABA_A$ reversal potential changes drastically during growth of an animal; one study showed a value of -54 mV in 2-day old rats while the mean membrane potential was -63 mV (Ouardouz and Sastry, 2005). This illustrates why the transmitter substance, GABA, has an excitatory effect in young animals instead of an inhibitory one as investigated in this thesis; the electrophysiological effect of activating the $GABA_A$ receptor depends on the relationship between the membrane potential and the reversal potential of the chloride ions used by the channel of the receptor. Animal experiments that record both these two parameters at different stages of development and in different species could be of great value in clarifying the effects of Purkinje cell input to DCN neurons.

Moreover, the computational implications of different $GABA_A$ reversal potentials could be studied in additional computer simulations.

7.3.4 In search of a holy grail: species-, strain-, age-, and sex-specific modelling

The studies underlying the neuronal modelling of this thesis were performed in several different species of mammals: rats, mice, guinea pigs, and cats. While all mammals share much of their brain structure and even more so, the basic cellular mechanisms underlying neuronal physiology, there are many important differences in function even on the single neuron level. For example, the mean firing rates of Purkinje cells are higher in mice (55-65 Hz; Schiffmann et al., 1999; Goossens et al., 2001; Yoshida et al., 2004) than rats (35-40 Hz; Savio and Tempia, 1985; Stratton et al., 1988; LeDoux and Lorden, 2002). These data are from adult yet not aged animals: while the young adult mice in the study by Schiffmann et al. (1999) fired with a mean rate of 66.2 Hz, aged mice fired at 42.9 Hz. These data serve to exemplify the dependence on species and age of neuronal electrophysiology. In order to minimise such natural variation, when intervention studies are undertaken on laboratory animals (for example in testing pharmaceuticals), it is preferable to standardise the samples so that in addition to originating from the same species, the used animals are of the same inbred strain and are thus genetic copies of one another. Further, one aims at only using age- and sex-matched animals.

A similar approach would be highly desirable for computational neuroscience. Thus, in the ideal world of greater funding opportunities, a DCN neuron model would be created with a keen eye on the published electrophysiology of DCN neurons, but with subsequent replication of the identified studies in similarly standardised animals. Many recordings and hence many different neurons are needed for characterising the many different types of ion channels in a neuron; the neurons used for those characterisations would be

limited to those found within a small area of stereotaxic coordinates in the DCN in order to minimise variation. Moreover, several different neurons would be reconstructed to allow the examination of effects of morphological variation.

References

Abbott LF, Varela JA, Sen K, Nelson SB (1997) Synaptic depression and cortical gain control. Science 275:220-224.

Aizenman CD, Linden DJ (1999) Regulation of the rebound depolarization and spontaneous firing patterns of deep nuclear neurons in slices of rat cerebellum. J Neurophysiol 82:1697-1709.

Aizenman CD, Manis PB, Linden DJ (1998) Polarity of long-term synaptic gain change is related to postsynaptic spike firing at a cerebellar inhibitory synapse. Neuron 21:827-835.

Albus JS (1971) A theory of cerebellar function. Math Biosci 10:25-61.

Alvina K, Khodakhah K (2008) Selective regulation of spontaneous activity of neurons of the deep cerebellar nuclei by N-type calcium channels in juvenile rats. J Physiol 586:2523-2538.

Alvina K, Walter JT, Kohn A, Ellis-Davies G, Khodakhah K (2008) Questioning the role of rebound firing in the cerebellum. Nat Neurosci.

Armstrong DM, Rawson JA (1979) Activity patterns of cerebellar cortical neurones and climbing fibre afferents in the awake cat. Journal of Physiology (London) 289:425-448.

Bao J, Reim K, Sakaba T (2010) Target-dependent feedforward inhibition mediated by short-term synaptic plasticity in the cerebellum. J Neurosci 30:8171-8179.

Batini C, Compoint C, Buisseret-Delmas C, Daniel H, Guegan M (1992) Cerebellar nuclei and the nucleocortical projections in the rat: retrograde tracing coupled to GABA and glutamate immunohistochemistry. J Comp Neurol 315:74-84.

Beeman D (2006a) Introduction to Computational Neuroscience, retrieved from http://www.genesis-sim.org/GENESIS/cnslecs/cns1.html#IntroCNS

Beeman D (2006b) Modeling Dendrites and Synapses, retrieved from http://www.genesis-sim.org/GENESIS/cnslecs/cns2a.html

Bengtsson F, Ekerot CF, Jorntell H (2011) In vivo analysis of inhibitory synaptic inputs and rebounds in deep cerebellar nuclear neurons. PLoS One 6:e18822.

Berthier NE, Moore JW (1990) Activity of deep cerebellar nuclear cells during classical conditioning of nictitating membrane extension in rabbits. Exp Brain Res 83:44-54.

Bower JM, Beeman D (2007) GENESIS. Scholarpedia 2(3):1383.

Cajal Ry (1894) Les nouvelles idées sur la structure du système nerveux chez l'homme et chez les vertébrés.

Carnevale NT, Hines ML (2006) The NEURON Book: Cambridge University Press.

Chan-Palay V (1973) Axon terminals of the intrinsic neurons in the nucleus lateralis of the cerebellum. An electron microscope study. Anat Embryol (Berl) 142:187-206.

Christian KM, Thompson RF (2003) Neural substrates of eyeblink conditioning: acquisition and retention. Learn Mem 10:427-455.

Christian KM, Thompson RF (2005) Long-term storage of an associative memory trace in the cerebellum. Behav Neurosci 119:526-537.

Cody FW, Moore RB, Richardson HC (1981) Patterns of activity evoked in cerebellar interpositus nuclear neurones by natural somatosensory stimuli in awake cats. J Physiol 317:1-20.

Cooper SJ (2004) Donald O. Hebb's synapse and learning rule: a history and commentary. Neurosci Biobehav Rev 28:851-874.

Czubayko U, Sultan F, Thier P, Schwarz C (2001) Two types of neurons in the rat cerebellar nuclei as distinguished by membrane potentials and intracellular fillings. J Neurophysiol 85:2017-2029.
Dayan P, Abbott LF (2001) Theoretical neuroscience: computational and mathematical modeling of neural systems: MIT Press.
Dayan P, Willshaw DJ (1991) Optimising synaptic learning rules in linear associative memories. Biol Cybern 65:253-265.
De Schutter E (1997) A new functional role for cerebellar long-term depression. Prog Brain Res 114:529-542.
De Schutter E, Bower JM (1994a) An active membrane model of the cerebellar Purkinje cell. I. Simulation of current clamps in slice. J Neurophysiol 71:375-400.
De Schutter E, Bower JM (1994b) An active membrane model of the cerebellar Purkinje cell. II. Simulation of synaptic responses. J Neurophysiol 71:401-419.
De Schutter E, Smolen P (1998) Calcium Dynamics in Large Neuronal Models. In: Methods in Neuronal Modeling: From Ions to Networks (Koch C, Segev I, eds), pp 211-250: MIT Press.
De Schutter E, Steuber V (2001) Modeling simple and complex active neurons. In: Computational neuroscience: realistic modeling for experimentalists (de Schutter E, ed). Boca Raton: CRC Press.
De Schutter E, Steuber V (2009) Patterns and Pauses in Purkinje Cell Simple Spike Trains: Experiments, Modeling and Theory. Neuroscience.
De Sousa G, Adams R, Davey N, Maex R, Steuber V (2009) The effect of different forms of synaptic plasticity on pattern recognition in the cerebellar cortex. Adaptive and Natural Computing Algorithms:413-422.
Delgado-Garcia JM, Gruart A (2002) The role of interpositus nucleus in eyelid conditioned responses. Cerebellum 1:289-308.
Ebner TJ, Bloedel JR (1981) Correlation between activity of Purkinje cells and its modification by natural peripheral stimuli. J Neurophysiol 45:948-961.
Ebner TJ, Hewitt AL, Popa LS (2011) What Features of Limb Movements are Encoded in the Discharge of Cerebellar Neurons? Cerebellum.
Eccles JC (1973) The cerebellum as a computer: patterns in space and time. J Physiol 229:1-32.
Eccles JC, Ito M, Szentágothai J (1967) The cerebellum as a neuronal machine: Springer-Verlag.
Field A (2005) Discovering statistics using SPSS, 2nd Edition: SAGE publications Ltd.
Gabbiani F, Koch C (1998) Principles of Spike Train Analysis. In: Methods in Neuronal Modeling: From Ions to Networks (Koch C, Segev I, eds), pp 313-360: MIT Press.
Ghez C, Thach WT (2000) The Cerebellum (Ch. 42). In: Principles of Neural Science, 4th Edition (Kandel ER, Schwartz JH, Jessell TM, eds): McGraw-Hill.
Gleeson P, Steuber V, Silver RA (2007) neuroConstruct: a tool for modeling networks of neurons in 3D space. Neuron 54:219-235.
Glickstein M (2007) What does the cerebellum really do? Curr Biol 17:R824-827.
Goldman DE (1943) Potential, impedance, and rectification in membranes. J Gen Physiol 27:37-60.
Goossens HH, Hoebeek FE, Van Alphen AM, Van Der Steen J, Stahl JS, De Zeeuw CI, Frens MA (2004) Simple spike and complex spike activity of floccular Purkinje cells during the optokinetic reflex in mice lacking cerebellar long-term depression. Eur J Neurosci 19:687-697.
Goossens J, Daniel H, Rancillac A, van der Steen J, Oberdick J, Crepel F, De Zeeuw CI, Frens MA (2001) Expression of protein kinase C inhibitor blocks cerebellar long-term depression without affecting Purkinje cell excitability in alert mice. J Neurosci 21:5813-5823.
Hansel C, Linden DJ, D'Angelo E (2001) Beyond parallel fiber LTD: the diversity of synaptic and non-synaptic plasticity in the cerebellum. Nat Neurosci 4:467-475.

Hausser M, Clark BA (1997) Tonic synaptic inhibition modulates neuronal output pattern and spatiotemporal synaptic integration. Neuron 19:665-678.
Hebb DO (1949) The organization of behavior : a neuropsychological theory: Wiley.
Hille B (2001) Ion Channels of Excitable Membranes. Sunderland, Massachusetts: Sinauer.
Hines ML, Carnevale NT (1997) The NEURON simulation environment. Neural Comput 9:1179-1209.
Hodgkin AL, Huxley AF (1952) A quantitative description of membrane current and its application to conduction and excitation in nerve. J Physiol 117:500-544.
Hodgkin AL, Katz B (1949) The effect of sodium ions on the electrical activity of giant axon of the squid. J Physiol 108:37-77.
Hoebeek FE, Khosrovani S, Witter L, De Zeeuw CI (2008) Purkinje cell input to cerebellar nuclei in tottering: ultrastructure and physiology. Cerebellum 7:547-558.
Hoebeek FE, Stahl JS, van Alphen AM, Schonewille M, Luo C, Rutteman M, van den Maagdenberg AM, Molenaar PC, Goossens HH, Frens MA, De Zeeuw CI (2005) Increased noise level of Purkinje cell activities minimizes impact of their modulation during sensorimotor control. Neuron 45:953-965.
Holt GR, Softky WR, Koch C, Douglas RJ (1996) Comparison of discharge variability in vitro and in vivo in cat visual cortex neurons. J Neurophysiol 75:1806-1814.
Isope P, Barbour B (2002) Properties of unitary granule cell-->Purkinje cell synapses in adult rat cerebellar slices. J Neurosci 22:9668-9678.
Ito M (2001) Cerebellar long-term depression: characterization, signal transduction, and functional roles. Physiol Rev 81:1143-1195.
Ito M, Sakurai M, Tongroach P (1982) Climbing fiber induced long term depression of both mossy fiber responsiveness and glutamate sensitivity of cerebellar Purkinje cells. J Physiol 324:113–134.
Ito M, Yoshida M, Obata K (1964) Monosynaptic inhibition of the intracerebellar nuclei induced from the cerebellar cortex. Experientia 20:575-576.
Ivry RB, Spencer RM, Zelaznik HN, Diedrichsen J (2002) The cerebellum and event timing. Ann N Y Acad Sci 978:302-317.
Izhikevich EM (2003) Simple model of spiking neurons. Neural Networks, IEEE Transactions on 14:1569-1572.
Jaeger D (2011) Mini-Review: Synaptic Integration in the Cerebellar Nuclei-Perspectives From Dynamic Clamp and Computer Simulation Studies. Cerebellum.
Jahnsen H (1986a) Electrophysiological characteristics of neurones in the guinea-pig deep cerebellar nuclei in vitro. J Physiol 372:129-147.
Jahnsen H (1986b) Extracellular activation and membrane conductances of neurones in the guinea-pig deep cerebellar nuclei in vitro. J Physiol 372:149-168.
Jirenhed DA, Bengtsson F, Hesslow G (2007) Acquisition, extinction, and reacquisition of a cerebellar cortical memory trace. J Neurosci 27:2493-2502.
Kakizawa S, Kishimoto Y, Hashimoto K, Miyazaki T, Furutani K, Shimizu H, Fukaya M, Nishi M, Sakagami H, Ikeda A, Kondo H, Kano M, Watanabe M, Iino M, Takeshima H (2007) Junctophilin-mediated channel crosstalk essential for cerebellar synaptic plasticity. Embo J 26:1924-1933.
Kleim JA, Freeman JH, Jr., Bruneau R, Nolan BC, Cooper NR, Zook A, Walters D (2002) Synapse formation is associated with memory storage in the cerebellum. Proc Natl Acad Sci U S A 99:13228-13231.
Koekkoek SK, Hulscher HC, Dortland BR, Hensbroek RA, Elgersma Y, Ruigrok TJ, De Zeeuw CI (2003) Cerebellar LTD and learning-dependent timing of conditioned eyelid responses. Science 301:1736-1739.
Kohn MC, Hines ML, Kootsey JM, Feezor MD (1994) A block organized model builder. Math Comput Model 19:75-97.
Lapicque L (1907) Recherches quantitatives sur l'excitation électrique des nerfs traitée comme une polarisation. J Physiol Pathol Gen 9:620-635.
Lavond DG (2002) Role of the nuclei in eyeblink conditioning. Ann N Y Acad Sci 978:93-105.

LeDoux MS, Hurst DC, Lorden JF (1998) Single-unit activity of cerebellar nuclear cells in the awake genetically dystonic rat. Neuroscience 86:533-545.
LeDoux MS, Lorden JF (2002) Abnormal spontaneous and harmaline-stimulated Purkinje cell activity in the awake genetically dystonic rat. Exp Brain Res 145:457-467.
Llinas R, Muhlethaler M (1988) Electrophysiology of guinea-pig cerebellar nuclear cells in the in vitro brain stem-cerebellar preparation. J Physiol 404:241-258.
Llinas R, Sugimori M (1980) Electrophysiological properties of in vitro Purkinje cell somata in mammalian cerebellar slices. J Physiol 305:171-195.
Loewenstein Y, Mahon S, Chadderton P, Kitamura K, Sompolinsky H, Yarom Y, Hausser M (2005) Bistability of cerebellar Purkinje cells modulated by sensory stimulation. Nat Neurosci 8:202-211.
London M, Hausser M (2005) Dendritic computation. Annu Rev Neurosci 28:503-532.
Luthman J (2008) Translation of a biologically realistic model of a cerebellar nuclear cell from GENESIS to NEURON. Technical Report 481School of Computer Science, University of Hertfordshire
Luthman J, Adams R, Davey N, Maex R, Steuber V (2009a) Decoding of Purkinje cell pauses by deep cerebellar nucleus neurons. BMC Neuroscience 10:P105.
Luthman J, Hoebeek FE, Maex R, Davey N, Adams R, De Zeeuw CI, Steuber V (2011) STD-Dependent and Independent Encoding of Input Irregularity as Spike Rate in a Computational Model of a Cerebellar Nucleus Neuron. Cerebellum.
Luthman J, Maex R, Adams R, Davey N, Steuber V (2009b) Decoding of regular Purkinje cell spiking based on synaptic depression in a model of a DCN neuron. Frontiers in Systems Neuroscience Conference Abstract: Computational and systems neuroscience doi: 103389/confneuro06200903240
Manni E, Petrosini L (2004) A century of cerebellar somatotopy: a debated representation. Nat Rev Neurosci 5:241-249.
Marr D (1969) A theory of cerebellar cortex. J Physiol 202:437-470.
Mauk MD, Medina JF, Nores WL, Ohyama T (2000) Cerebellar function: coordination, learning or timing? Curr Biol 10:R522-525.
Middleton FA, Strick PL (1998) The cerebellum: an overview. Trends Neurosci 21:367-369.
Mittmann W, Hausser M (2007) Linking synaptic plasticity and spike output at excitatory and inhibitory synapses onto cerebellar Purkinje cells. J Neurosci 27:5559-5570.
Mittmann W, Koch U, Hausser M (2005) Feed-forward inhibition shapes the spike output of cerebellar Purkinje cells. J Physiol 563:369-378.
Molineux ML, McRory JE, McKay BE, Hamid J, Mehaffey WH, Rehak R, Snutch TP, Zamponi GW, Turner RW (2006) Specific T-type calcium channel isoforms are associated with distinct burst phenotypes in deep cerebellar nuclear neurons. Proc Natl Acad Sci U S A 103:5555-5560.
Monsivais P, Clark BA, Roth A, Hausser M (2005) Determinants of action potential propagation in cerebellar Purkinje cell axons. J Neurosci 25:464-472.
Morishita W, Sastry BR (1993) Long-term depression of IPSPs in rat deep cerebellar nuclei. Neuroreport 4:719-722.
Morishita W, Sastry BR (1996) Postsynaptic mechanisms underlying long-term depression of GABAergic transmission in neurons of the deep cerebellar nuclei. J Neurophysiol 76:59-68.
Mouginot D, Gaehwiler BH (1995) Characterization of synaptic connections between cortex and deep nuclei of the rat cerebellum In vitro. Neuroscience 64:699-712.
Nieuwenhuys R, Voogd J, van Huijzen C (2008) The Human Central Nervous System, Fourth Edition. Berlin: Springer.
Otis TS, Mody I (1992) Modulation of decay kinetics and frequency of GABAA receptor-mediated spontaneous inhibitory postsynaptic currents in hippocampal neurons. Neuroscience 49:13-32.
Ouardouz M, Sastry BR (2005) Activity-mediated shift in reversal potential of GABA-ergic synaptic currents in immature neurons. Brain Res Dev Brain Res 160:78-84.

Palkovits M, Magyar P, Szentagothai J (1972) Quantitative histological analysis of the cerebellar cortex in the cat. IV. Mossy fiber-Purkinje cell numerical transfer. Brain Res 45:15-29.
Palkovits M, Mezey É, Hámori J, Szentágothai J (1977) Quantitative histological analysis of the cerebellar nuclei in the cat. I. Numerical data on cells and on synapses. Exp Brain Res 28:189-209.
Paxinos G, Mai JK (2004) The Human Nervous System, 2nd Edition: Elsevier.
Pedroarena CM, Schwarz C (2003) Efficacy and short-term plasticity at GABAergic synapses between Purkinje and cerebellar nuclei neurons. J Neurophysiol 89:704-715.
Purves (2004) Neuroscience, 3rd Edition: Sinauer Associates.
Raman IM, Bean BP (1997) Resurgent sodium current and action potential formation in dissociated cerebellar Purkinje neurons. J Neurosci 17:4517-4526.
Rokni D, Tal Z, Byk H, Yarom Y (2009) Regularity, variability and bi-stability in the activity of cerebellar purkinje cells. Front Cell Neurosci 3:12.
Rothman JS, Cathala L, Steuber V, Silver RA (2009) Synaptic depression enables neuronal gain control. Nature 457:1015-1018.
Rowland NC, Jaeger D (2005) Coding of tactile response properties in the rat deep cerebellar nuclei. J Neurophysiol 94:1236-1251.
Saab CY, Willis WD (2003) The cerebellum: organization, functions and its role in nociception. Brain Res Brain Res Rev 42:85-95.
Sangrey T, Jaeger D (2010) Analysis of distinct short and prolonged components in rebound spiking of deep cerebellar nucleus neurons. Eur J Neurosci 32:1646-1657.
Savio T, Tempia F (1985) On the Purkinje cell activity increase induced by suppression of inferior olive activity. Exp Brain Res 57:456-463.
Schiffmann SN, Cheron G, Lohof A, d'Alcantara P, Meyer M, Parmentier M, Schurmans S (1999) Impaired motor coordination and Purkinje cell excitability in mice lacking calretinin. Proc Natl Acad Sci U S A 96:5257-5262.
Schonewille M, Gao Z, Boele HJ, Veloz MF, Amerika WE, Simek AA, De Jeu MT, Steinberg JP, Takamiya K, Hoebeek FE, Linden DJ, Huganir RL, De Zeeuw CI (2011) Reevaluating the role of LTD in cerebellar motor learning. Neuron 70:43-50.
Schultz SR (2007) Signal-to-noise ratio in neuroscience. Scholarpedia, 2(6):2046, revision #73401
Shin SL, Hoebeek FE, Schonewille M, de Zeeuw CI, Aertsen A, de Schutter E (2007a) Regular patterns in cerebellar Purkinje cell simple spike trains. PLoS ONE 2:e485.
Shin SL, Rotter S, Aertsen A, De Schutter E (2007b) Stochastic description of complex and simple spike firing in cerebellar Purkinje cells. Eur J Neurosci 25:785-794.
Shinoda Y, Sugihara I, Wu HS, Sugiuchi Y (2000) The entire trajectory of single climbing and mossy fibers in the cerebellar nuclei and cortex. Prog Brain Res 124:173-186.
Silver RA (2010) Neuronal arithmetic. Nat Rev Neurosci 11:474-489.
Silver RA, Colquhoun D, Cull-Candy SG, Edmonds B (1996) Deactivation and desensitization of non-NMDA receptors in patches and the time course of EPSCs in rat cerebellar granule cells. J Physiol 493:167-173.
Squire LR (2008) Fundamental neuroscience, 3rd Edition: Academic Press.
Steuber V, De Schutter E (2001) Long-term depression and recognition of parallel fibre patterns in a multi-compartmental model of a cerebellar Purkinje cell. Neurocomputing 38-40:383–388.
Steuber V, De Schutter E, Jaeger D (2004) Passive models of neurons in the deep cerebellar nuclei: the effect of reconstruction errors. Neurocomputing 58-60:563-568.
Steuber V, Mittmann W, Hoebeek FE, Silver RA, De Zeeuw CI, Hausser M, De Schutter E (2007) Cerebellar LTD and pattern recognition by Purkinje cells. Neuron 54:121-136.
Steuber V, Schultheiss NW, Silver RA, De Schutter E, Jaeger D (2010) Determinants of synaptic integration and heterogeneity in rebound firing explored with data-driven models of deep cerebellar nucleus cells. J Comput Neurosci.

Stratton SE, Lorden JF, Mays LE, Oltmans GA (1988) Spontaneous and harmaline-stimulated Purkinje cell activity in rats with a genetic movement disorder. J Neurosci 8:3327-3336.
Sugihara I, Wu H, Shinoda Y (1999) Morphology of single olivocerebellar axons labeled with biotinylated dextran amine in the rat. J Comp Neurol 414:131-148.
Sultan F, Czubayko U, Thier P (2003) Morphological classification of the rat lateral cerebellar nuclear neurons by principal component analysis. J Comp Neurol 455:139-155.
Telgkamp P, Padgett DE, Ledoux VA, Woolley CS, Raman IM (2004) Maintenance of high-frequency transmission at purkinje to cerebellar nuclear synapses by spillover from boutons with multiple release sites. Neuron 41:113-126.
Telgkamp P, Raman IM (2002) Depression of inhibitory synaptic transmission between Purkinje cells and neurons of the cerebellar nuclei. J Neurosci 22:8447-8457.
Thach WT (1970) Discharge of cerebellar neurons related to two maintained postures and two prompt movements. I. Nuclear cell output. J Neurophysiol 33:527-536.
Thach WT (2007) On the mechanism of cerebellar contributions to cognition. Cerebellum 6:163-167.
Thomas A (1912) Cerebellar functions: Journal of Nervous and Mental Diseases.
Tsukada M (2008) Synaptic plasticity. In: Encyclopedia of Neuroscience, p 3961. Berlin, Heidelberg: Springer-Verlag.
Tyrrell T, Willshaw D (1992) Cerebellar cortex: its simulation and the relevance of Marr's theory. Philos Trans R Soc Lond B Biol Sci 336:239-257.
Uusisaari M, De Schutter E (2011) The mysterious microcircuitry of the cerebellar nuclei. J Physiol.
Uusisaari M, Knopfel T (2010) Functional Classification of Neurons in the Mouse Lateral Cerebellar Nuclei. Cerebellum.
Uusisaari M, Obata K, Knopfel T (2007) Morphological and electrophysiological properties of GABAergic and non-GABAergic cells in the deep cerebellar nuclei. J Neurophysiol 97:901-911.
Voogd J (2004a) Cerebellum. In: The Rat Nervous System, 3rd Edition (Paxinos G, ed), pp 205-242. Amsterdam: Elsevier Academic Press.
Voogd J (2004b) Cerebellum and precerebellar nuclei. In: The Human Nervous System, 2nd Edition (Paxinos G, Mai JK, eds), pp 321-392. Amsterdam: Elsevier Academic Press.
Voogd J, Glickstein M (1998) The anatomy of the cerebellum. Trends Neurosci 21:370-375.
Wada N, Kishimoto Y, Watanabe D, Kano M, Hirano T, Funabiki K, Nakanishi S (2007) Conditioned eyeblink learning is formed and stored without cerebellar granule cell transmission. Proc Natl Acad Sci U S A 104:16690-16695.
Walter JT, Alvina K, Womack MD, Chevez C, Khodakhah K (2006) Decreases in the precision of Purkinje cell pacemaking cause cerebellar dysfunction and ataxia. Nat Neurosci 9:389-397.
Walter JT, Khodakhah K (2009) The advantages of linear information processing for cerebellar computation. Proc Natl Acad Sci U S A 106:4471-4476.
Willshaw DJ, Buneman OP, Longuet-Higgins HC (1969) Non-holographic associative memory. Nature 222:960-962.
Woodruff-Pak DS, Disterhoft JF (2008) Where is the trace in trace conditioning? Trends Neurosci 31:105-112.
Woodruff-Pak DS, Lavond DG, Thompson RF (1985) Trace conditioning: abolished by cerebellar nuclear lesions but not lateral cerebellar cortex aspirations. Brain Res 348:249-260.
Wu HS, Sugihara I, Shinoda Y (1999) Projection patterns of single mossy fibers originating from the lateral reticular nucleus in the rat cerebellar cortex and nuclei. J Comp Neurol 411:97-118.
Yamada WM, Koch C, Adams PR (1998) Multiple Channels and Calcium Dynamics. In: Methods in Neuronal Modeling: From Ions to Networks (Koch C, Segev I, eds), pp 137-170: MIT Press.

Yoshida T, Katoh A, Ohtsuki G, Mishina M, Hirano T (2004) Oscillating Purkinje neuron activity causing involuntary eye movement in a mutant mouse deficient in the glutamate receptor delta2 subunit. J Neurosci 24:2440-2448.

Appendix – metrics of pattern recognition

The appendix lists the best DCN neuron pattern recognition metrics when those are not the number of spikes in the burst.

Parameter exploration 5

Number of parallel fibres in a pattern	Metric	Mean StoN	SEM of StoN
50	ISI of first two burst spikes	1.0	0.1
100	ISI of first two burst spikes	1.7	0.1
200	1st 50 ms, number of spikes	7.0	0.5
500	1st 50 ms, number of spikes	11.0	0.8
750	1st 50 ms, number of spikes	13.2	0.4
900-5000	Number of spikes in burst		
500	1st 50 ms, number of spikes	13.2	0.5
10000	Frequency of burst	7.8	0.3
15000	ISI of first two burst spikes	2.1	0.1
25000	8th 10 ms, number of spikes	0.03	0.01

Parameter exploration 6

Number of stored patterns in the associative net	Metric	Mean StoN	SEM of StoN
50	Number of spikes in burst	16.7	0.8
100	Number of spikes in burst	20.5	1.3
150	1st 50 ms, number of spikes	13.3	0.4
300	Number of spikes in burst	14.3	1.4
450	1st 50 ms, number of spikes	10.2	1.0
750	ISI of first two burst spikes	1.7	0.1
1500	Time of first spike after pattern presentation	0.07	0.01

Parameter exploration 9

7.3.5 spontPC

Percent of DCN $GABA_A$ receptors receiving the PC pattern readout	Metric	Mean StoN	SEM of StoN
6.7	4th 20 ms, number of spikes	0.7	0.1
13.3	3rd 20 ms, number of spikes	0.9	0.1
20	5th 20 ms, time of first spike	1.8	0.2
22.2	5th 20 ms, time of first spike	2.6	0.2
26.7	3rd 20 ms, number of spikes	2.9	0.1
30	1st 50 ms, number of spikes	8.1	0.7
33.3	3rd 20 ms, number of spikes	7.2	0.3
40	3rd 20 ms, number of spikes	8.6	0.4
50	1st 50 ms, number of spikes	7.7	0.3
60	1st 50 ms, number of spikes	8.9	0.2
66.7	1st 50 ms, number of spikes	10.4	0.5
68.9	1st 50 ms, number of spikes	13.2	0.6
70	1st 50 ms, number of spikes	13.7	1.0
71.1	1st 50 ms, number of spikes	14.2	1.2
73.3	1st 50 ms, number of spikes	12.4	0.7
75.6 - 100	Number of spikes in burst		

7.3.6 spontPC_2

Percent of DCN $GABA_A$ receptors receiving the PC pattern readout	Metric	Mean StoN	SEM of StoN
6.7	4th 20 ms, number of spikes	0.1	0.0
13.3	4th 20 ms, number of spikes	0.2	0.0
20	3rd 20 ms, number of spikes	0.5	0.0
22.2	3rd 20 ms, number of spikes	0.6	0.1
26.7	3rd 20 ms, number of spikes	0.8	0.0
30	3rd 20 ms, number of spikes	0.9	0.1
33.3	1st 50 ms, CV2 of ISIs	1.1	0.1
40	Number of spikes in burst	2.0	0.2
50	Length of burst	4.4	0.3
60 – 100	Number of spikes in burst		

7.3.7 non_spontPC

Percent of DCN $GABA_A$ receptors receiving the PC pattern readout	Metric	Mean StoN	SEM of StoN
6.7	4th 20 ms, time of first spike	0.1	0.0
13.3	2nd 50 ms, time of first spike	0.2	0.0
20	7th 10 ms, number of spikes	0.5	0.1
22.2	5th 20 ms, number of spikes	0.6	0.1
26.7	2nd 50 ms, time of first spike	0.8	0.1
30	2nd 10 ms, number of spikes	1.2	0.1
33.3	5th 20 ms, number of spikes	1.5	0.1
40	2nd 10 ms, number of spikes	2.1	0.2
50-100	Number of spikes in burst		